THE SAFETY AND COMMERCIAL IMPLICATIONS OF POLYMER SEAL DEGRADATION IN A NUCLEAR POWER GENERATION APPLICATION

A thesis submitted to the Department of Chemical and Biological Engineering, The University of Sheffield

by

Christopher Paterson Porter, BEng

In support of the application for

Degree of Philosophy (PhD)

January 2016

SUMMARY

An industrial seal manufactured from James Walker Co. and made from an acrylonitrile-butadiene based synthetic elastomer, reinforced with carbon black and incorporating glass cloth, brass wire and a sulphur based curing system has undergone a variety of tests to identify its physical and mechanical properties, how these properties change under exposure to gamma radiation and the effect pressurised CO_2 has on this radiation induced degradation.

The seal was found to have a $\Delta_{M\%}$ in toluene of $46\% \pm 2$, T_g of $-24.9°C \pm 0.7$ and a Retention Factor of $0.413\ N.N^{-1} \pm 0.004$. $\Delta_{M\%}$ decreased with radiation and T_g and RF increased suggesting crosslink formation. SEM also revealed the development of microcracks on the outside curvature of the seal. Following exposure to gamma radiation under 32 bar pressurised CO_2 the same changes were seen in all properties.

These results were compared against three commercially available nitrile rubber sheets sourced from Whitby and Chandler Ltd; at hardness grades BA40, BA50 and BA60. Analysis of peak heights found in IR spectra suggested that degradation in BA40 proceeded through the ionisation of the BDN monomer and crosslinking between *cis* C=C and $C=CH_2$ followed at higher doses by ionisation of both BDN and ACN monomers and crosslinking between *trans* C=C and C≡N groups. In BA50 it appeared that degradation of both monomers occurred concurrently. Those samples with a higher BDN content also displayed an increased proclivity for crosslink clustering, reducing the detrimental impact of gamma radiation. The IR spectra for samples irradiated under 32 bar pressurised CO_2 showed no significant change.

Service life has been simulated on a custom built Test Rig. This has shown an exponentially decaying increase in static friction with time, an increase in force required to move the seals with exposure to CO_2 and the deleterious effects of grease accumulation in flowrate sensing ports.

ACKNOWLEDGEMENTS

I can't start the discussion of this project without first extending my thanks to all those who have helped me throughout my time at the University of Sheffield.

I would first like to acknowledge my supervisors at the University of Sheffield; Bruce Ewan, Chemical and Biological Engineering (retired) without whom this would have never started, my second supervisor Neil Hyatt, Materials and Science Engineering for being available for discussion when required and my latest supervisor, Mark Ogden, Chemical and Biological Engineering. Not only has his excellent academic support and fantastically encouraging demeanour been invaluable to this project but between him and his wife, Sarah Pepper, they have kept me sane.

Secondly, I must thank those at EDF Energy for permitting this work to go ahead. Aidan Rose, Peter Tudor and Alan George have shared their expertise and knowledge and Clare Antonio has assisted with navigation through all the administrative tasks.

I am completely indebted to all the PDRA's and technicians who have helped me with selecting and organising the experiments to be run – George Dowson, Ben Palmer, Kerry Abrams, Austin Lafferty, Keith Penny, Mark Jones and also Mike O'Meara, David Palmer and Oz McFarlane for advice and construction of the Test Rig out at the Buxton facility.

Not all of this work has been possible to complete at the University of Sheffield and for their assistance in providing access to and work within their respective facilities I extend my gratitude to Kevin Warren and Ruth Edge of the Dalton Cumbrian Facility, University of Manchester and Jon Forster and Donna Zammit of AMEC in Warrington.

Lastly, but by no means least, I would like to thank my fiancée Rebecca Priddle for her continued support throughout this time, her family for those all-important periods away from the office and labs and bountiful supply of Sunday dinners, and my extended family, for always being there when needed.

These last three years have turned me into the man I am today and I owe it all to everyone who has helped me along the way. Thank you!

TABLE OF CONTENTS

LIST OF FIGURES

LIST OF NOMENCLATURE

List of Abbreviations

ACN	Acrylonitrile
AGR	Advanced Gas-Cooled Reactor
ARE	Average Relative Error
ATR	Attenuated Total Reflectance
BDN	Butadiene
BSE	Backscattered Electron
CCTV	Closed Circuit Television
CF	Closing Force
CO_2	Carbon Dioxide
DCF	Dalton Cumbrian Facility
DLO	Diffusion-Limited Oxidation
DNB	Dungeness B Power Station
DP1	Depressurisation Procedure 1
DP2	Depressurisation Procedure 2
DSC	Differential Scanning Calorimetry
DSLR	Digital Single Lens Reflex
EABS	Sum of the Absolute Errors
EDF	Électricité de France
EDX	Elemental Distribution Mapping
ERRSQ	Sum of the Error Squares
ESC	Environmental Stress Cracking
F	Applied force on a dynamic seal
FPA	Fuel Plug Assembly
FPU	Fuel Plug Unit
FRTE	Fuel Route Technical Engineer
FTIR	Fourier Transform Infrared
GCMS	Gas Chromotagraphy Mass Spectrometry
HTLS	Hunting Tooth Limit Switch
HYBRD	Composite Fractional Error Function
IFDF	Irradiated Fuel Dismantling Facility
IGA	Hiden Isochema Intelligent Gravimetric Analyser
IR	Infrared
LRSP	Leak Rate Sensing Point
MOS	Maintenance Optimisation Schedule
MPSD	A derivative of Marquardts Percent Standard Deviation
MS	Moving Surface of a dynamic seal
NBR	Nitrile Rubber
NH_3	Ammonia
NO	Nitric Oxide

NPP	Nuclear Power Plant
OPEX	Operational Experience
PFO	Pseudo-First Order
PSO	Pseudo-Second Order
PUMF	Plug Unit Maintenance Facility
SB	Seal Body of a dynamic seal
SCC	Stress Corrosion Cracking
SEI	Secondary Electron
SEM	Scanning Electron Microscopy
SF_4	Sulphur Tetrafluoride
SNE	Sum of the Normalised Errors
TA500	Lloyds Instruments Texture Analyser 500
TEM	Transmission Electron Microscopy
TGA	Thermogravimetric Analysis
TRPD	Test Rig Piston Drive
TRPH	Test Rig Piston Head
TRPV	Test Rig Pressure Vessel

List of Nomenclature

A	Arrhenius Pre-exponential Factor
a_F	Freundlich Isotherm Constant
a_L	Langmuir Isotherm Constant
a_T	Temkin Isotherm Constant
B_D	Dubinin-Radushkevic Isotherm Constant
b_T	Temkin Isotherm Constant
C_0	Initial Concentration of Solute in Solution $(kg\ m^{-3})$
C_e	Equilibrium Concentration of Solute in Solution $(kg\ m^{-3})$
D_i	Internal Diameter (m)
$\Delta_{M\%}$	Percentage Change in Mass $(\%)$
$\Delta_{V\%}$	Percentage Change in Volume $(\%)$
E	Mean Free Energy of Sorption $(kJ\ mol^{-1})$
E_A	Activation Energy $(kJ\ mol^{-1})$
e	Minimum Thickness of Pressure Vessel Wall (m)
f	Design Stress of Chosen Material at Maximum Temperature $(N\ m^{-2})$
h_0	Initial Adsorption Rate $(kg\ kg^{-1}\ s^{-1})$
K	Absorption Affinity Ratio
K_H	Henry's Law Constant $(kg\ kg^{-1}\ Pa^{-1})$
K_L	Langmuir Isotherm Constant
k_{ar}	Arrhenius Rate Constant
k_a	Adsorption Rate Constant $(m^3\ kg^{-1}\ s^{-1})$
k_d	Desorption Rate Constant (s^{-1})

k_{ID}	Intraparticulate Diffusion model Observable Rate Constant $(kg\ kg^{-1}\ s^{-1})$
k_1	Pseudo-First Order Observable Rate Constant (s^{-1})
k_2	Pseduo-Second Order Observable Rate Constant $(kg\ kg^{-1}\ s^{-1})$
L_0	Initial Recorded Length (m)
L_t	Final Recorded Length (m)
M_0	Initial Recorded Mass (kg)
M_t	Final Recorded Mass (kg)
M_W	Molecular Weight of Solute $(kg\ mol^{-1})$
$Mtoe$	Million tonnes of oil equivalent
m_c	Mass of Sorbent (kg)
n_F	Freundlich Isotherm Constant (Strength of Interaction Parameter)
P	Pressure (Pa)
P_i	Internal Pressure $(N\ m^{-2})$
q_D	Dubinin-Radushkevic Isotherm Constant
q_e	Uptake at Equilibrium $(kg\ kg^{-1})$
$q_{e,10}$	Uptake at Equilibrium at 10 bar pressure $(kg\ kg^{-1})$
q_m	Maximum Uptake $(kg\ kg^{-1})$
q_t	Uptake at Time t $(kg\ kg^{-1})$
R	Universal Gas Constant $(kJ\ mol^{-1}\ K^{-1})$
RF	Retention Factor
T	Absolute Temperature (K)
T_0	Initial Recorded Thickness (m)
T_g	Glass Transition Temperature (K)
T_t	Final Recorded Thickness (m)
t	Time (s)
$t_{1/2}$	Half-Life (s)
V	Volume of Solution (m^3)
V_r	Volume Fraction of Polymer in a Swollen Network in Equilibrium with Pure Solvent $(\%)$
V_1	Molecular Volume of Solvent $(m^3\ mol^{-1})$
W_0	Initial Recorded Width (m)
W_t	Final Recorded Width (m)
υ_e	Effective Number of Chains
χ_1	Polymer-Solvent Interaction Parameter

1 INTRODUCTION

This first chapter introduces a few concepts of Nuclear Power; its demand, its benefits and the safety orientated practices of the Nuclear Industry. A description is then given on current maintenance programmes followed by an overview of the Fuel Route, where these programmes are taking place. The chapter closes with a detailed look at the component chosen for investigation and states the aims and objectives for this thesis.

1.1 DIRECTIONS IN NUCLEAR MAINTENANCE RESEARCH

1.1.1 WHY NUCLEAR POWER

We are a generation of energy consumers. However, we are now, more than ever, becoming more conscious and sustainable in our energy use. The Department of Energy and Climate Change have released a report [1] that shows how 2014 has continued the year on year decrease in primary energy consumption (energy from fuels directly taken from natural sources) to 193.4 million tonnes of oil equivalent ($Mtoe$) which is 6.6% lower than the 2013 value and 7.0% lower than in 2012. In fact, the final energy consumption for the UK has shown a continued decrease for almost 10 years and is akin to the values observed in the mid-1980s.

Not only are we reducing our energy use but we are also being more sustainable with the fuel of choice. Fuel use has seen a significant shift away from solid fuels with the likes of gas and electricity having a greater role, Figure 1-1. Gas consumption had the highest percentage contribution in 2001 and has since begun to fall whilst electricity has shown a continuing increase at a steady pace, with an overall increase of 58% between 1970 and 2014. Electricity generation is therefore a key component when considering future energy demands and sustainability.

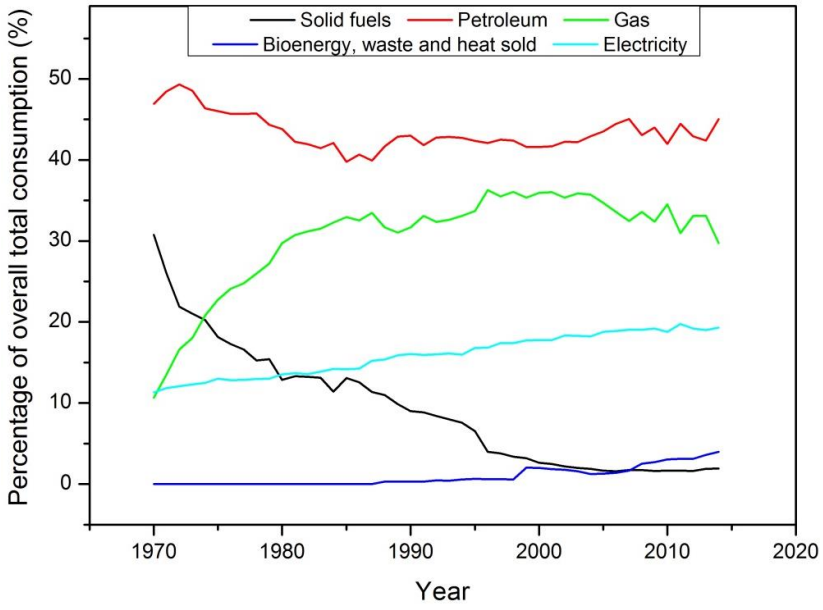

Figure 1-1: The Change in Percentage of Overall Energy Consumption for Different Production Methods [1]

Nuclear Energy is considered to be a key part of the solution to our energy demands for a number of reasons; it is the 'only readily available large-scale alternative to fossil fuels for production of a continuous and reliable supply of electricity,' and the abundance of the fuel source in the world ensures energy security and the rising prices of fossil fuel have made it 'the most cost-effective of the available base-load technologies,' [2].

However, accidents can happen and when dealing with atomic energy sources the effects can be catastrophic; Three Mile Island 1979, Chernobyl 1986 and Fukushima 2011 to name just a few.

1.1.2 Nuclear Power Plant Maintenance

EDF Energy is a UK subsidiary of Électricité de France and are the sole operators of Nuclear Power Plants (NPP) in the UK. On approach to their offices in Gloucester you are confronted with a monolith, on which is scribed the EDF Energy mantra 'Nuclear safety is our overriding priority,' Figure 1-2, which gives some insight into the public perception of Nuclear Power. Improvements to and justification of safety cases on each NPP are therefore of the utmost importance to the industry and are considered a key part of their continuous development.

Figure 1-2: The Monolith Positioned Outside EDF Energy Offices in Barnwood, Gloucester [3]

To improve equipment reliability and underpin nuclear safety and generation capacity in the NPP at Dungeness (DNB), a Maintenance Optimisation Schedule (MOS) is currently underway to ensure that the right maintenance is being carried out at the right frequency. The broad aims of the MOS when it was first set out were:

- Alignment of fuel route outages to a 3-yearly cycle
- Ensuring the specified maintenance matched the safety case requirements
- Taking Operation Experience (OPEX) from other stations and incorporation into DNB safety case
- Application of equipment reliability techniques to the fuel route

1.1.3 The Challenge, Aims and Deliverables

The Challenge

Following a review of the OPEX database provided by EDF Energy, which details any incidents that occur on site leading to disrupted service, and cross-analysis with the Safety Case Head Document [E3] a potential avenue for investigation into the Seal Plug Chevron Seals was found.

It transpired that the documentation that supports the justification of these seals for their purpose based their lifetime expectancy against that of a different base elastomer and did not take into account the combined effects of carbon dioxide (CO_2), pressure, radiation and physical wear. A further report [E4] has since been released that justifies the use of these seals for 30 $years$ based on their radiation exposure alone as opposed to the original suggestion of 6 $years$.

The Aims

The lack of understanding in this component's aging behaviour and the submission of evidence for lifetime extension lead to the decision to produce a report that defines, to an as close as is reasonably practicable level, the degradation mechanisms occurring within these seals in the unique environment seen at DNB in an effort to produce a more mechanistic understanding of their long term degradation and thus lifetime expectancy.

The original aims of the MOS as they apply to these seals can be broken down as such:

- **Alignment of Fuel Route Outages –** Chevron seal degradation is the limiting factor in Seal Plug maintenance requiring visual inspections every $2 - 3$ $years$ or whenever the Nose Unit is removed. Better prediction of the degradation mechanisms may have allowed preventative maintenance techniques or changes to operations that would prolong seal life and help achieve this aim
- **Appropriate Maintenance Regimes –** The degradation mechanism for these seals in the DNB specific environment is not clear, the sealing capability reduces as time goes on but any cliff edge effects that may be in play should be understood
- **Incorporation of OPEX –** No other stations have a similar sealing mechanism to DNB therefore there is only limited OPEX available, investigation into this seal will increase knowledge and expand the OPEX database

- **Equipment Reliability Techniques –** Modern analytical techniques should be used and knowledge updated whenever possible and appropriate.

The overall aim of this thesis can therefore be summarised as follows:

> *"To assess the degradation mechanisms on the Seal Plug Chevron Seal in the Fuelling Machine at Dungeness B as part of the Maintenance Optimisation Schedule and, where applicable, identify any potential avenues for improving service life"*

The Deliverables

A. Identify a set of characteristics that detail microscopic behaviour as well as sealing capacity;
B. Determine these sealing capacity characteristics for the industrial seal in an 'As Received' condition from the supplier;
C. Compare the characteristics found in B against those from a set of materials constructed from the same base elastomer;
D. Assess the development of these characteristics with radiation dose and determine the degradation mechanism occurring;
E. Assess the effect of a pressurised CO_2 environment on the development of these characteristics with radiation dose;
F. Design an experiment to assess mechanical wear and fatigue of seals in simulated service;
G. Determine the operational conditions that have the most detrimental effect to the seals lifetime and, where applicable, suggests potential methods for improvement through either
   i) Improvements to seal design and manufacture,
   ii) Adjustments to testing regime,
   iii) Adjustments to maintenance schedule,
   iv) Adjustments to physical and chemical environment.

1.2 Fuel Route Summary and Component Information

This section of the chapter introduces the Fuel Route and details the component chosen for investigation. Due to the confidential nature of EDF internal documents they are not in the public domain. For ease of reference they have therefore been given their own section and to distinguish between the two all EDF internal documents shall be prefixed with the letter E.

1.2.1 Fuel Route Summary

The Fuel Route describes the process of new fuel arriving at a NPP, its preparation for use, its movement around the plant and its entry into the reactor as well as its subsequent removal, handling and preparation for disposal. The two reactors at DNB (R21 and R22) are both Generation II Advanced Gas-cooled Reactors (AGRs) [E1, E2]. As with all Nuclear Reactors they rely upon a radioactive source as fuel. In the case of AGRs this fuel source is enriched uranium dioxide in the form of pellets. These pellets are arranged together to create a Fuel Stringer which, when attached to a Fuel Plug Unit, creates the Fuel Plug Assembly (FPA), Figure 1-3.

CO_2 is used to gather the heat produced by nuclear fission and transfer it to a secondary process where the heat can be used to produce steam, which then powers generators and produces electricity, Figure 1-4. However, CO_2 reacts with the radioactive environment to leave a carbon deposit on the graphite components and so a blend of various gases, with the main constituent still being CO_2, is used to more efficiently collect the fission-produced heat.

The FPAs require a method of transportation around the plant so that they can be moved from the New Build Store to the Reactor, and from there to the Buffer Store and dismantling facility. This method of transport needs to be able to control the temperature of the CO_2 leaving the Reactor, hold the fuel in a sound and secure way, facilitate charge and discharge operations and maintain the integrity of any protective components as well as the other components within the unit itself. This is done through a highly complex Fuelling Machine.

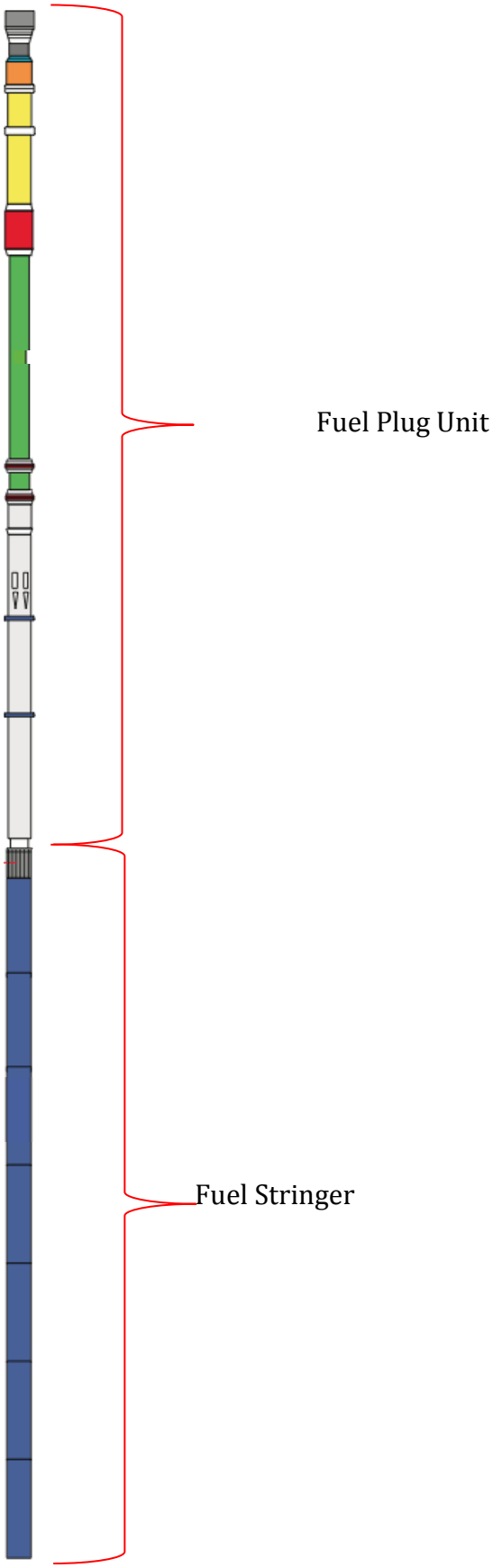

Figure 1-3: Fuel Plug Assembly [E1]

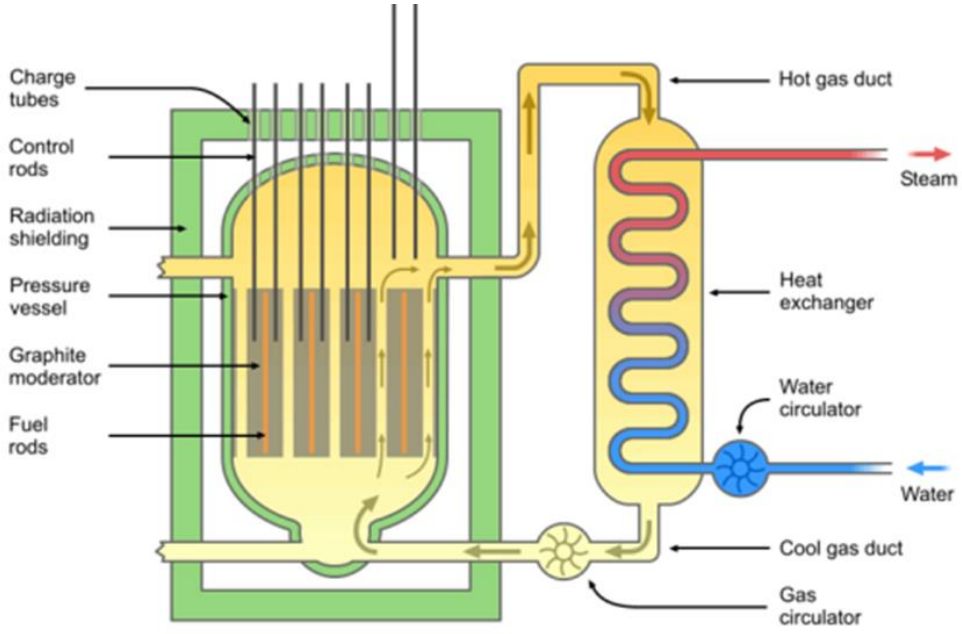

Figure 1-4: A Diagramatic Representation of an AGR Reactor [4]

The Fuelling Machine is the unit that is responsible for transporting a variety of assemblies around the Power Station. The spent fuel being removed from the Reactor Core will still be emitting radiation and a great deal of fission product heat. A Seal Plug alleviates this build up of heat by allowing pressurisation of the Fuelling Machine to reactor conditions with coolant gas and facilitates transportation under these conditions.

The Seal Plug

The Seal Plug is separated into three cylindrical steel sections that are spigot and bolted together, Figure 1-5. In the centre section of the Seal Plug there are two layers of chevron seals. It is these chevron seals that create the Pressure Boundary. There is also a slight decrease in diameter from the centre section to the lower section. This provides a lip that sits on a ledge in the Fuelling Machine and creates a back-up secondary pressure boundary.

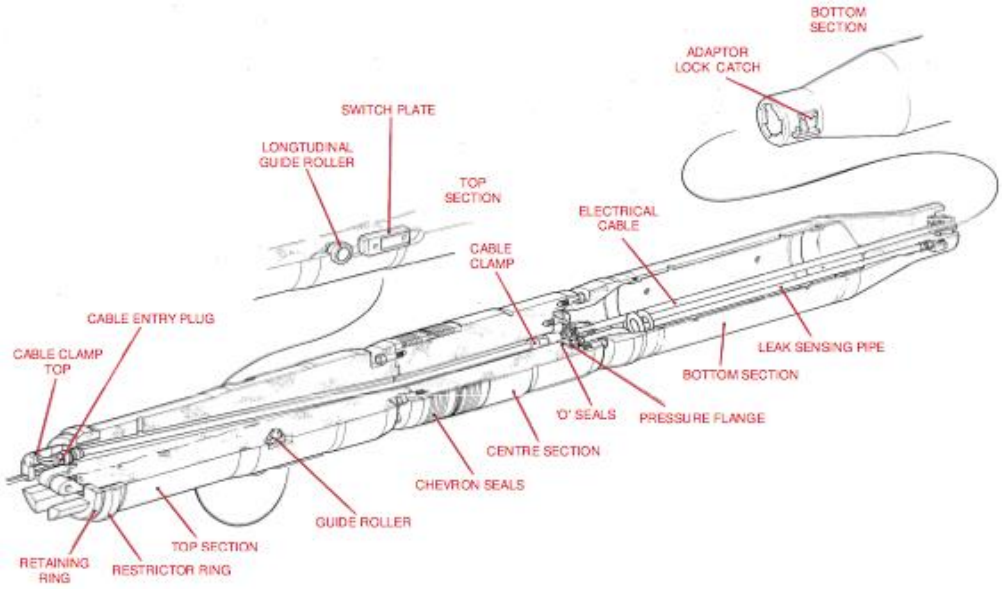

Figure 1-5: Seal Plug Assembly [E2]

1.2.2 Component Details

The Seal Plug Chevron Seals are located on the centre section of the Seal Plug and provide a pressure boundary that allows movement of the Fuelling Machine in a pressurised condition. The seals are made from an acrylonitrile-butadiene based synthetic elastomer, reinforced with carbon black and incorporating a sulphur based curing system. The cloth is a plain weave, woven glass cloth incorporating brass wire in both the warp and weft yarns with a composition of 77% glass to 23% brass wire (BS 2873, 38 SWG). The header ring is phosphor bronze containing ten spring assemblies and the endless ring is also phosphor bronze [E5]. The two seals along with their phosphor bronze ends are manufactured and supplied by James Walker Co. The full seal assembly includes a selection of spacer rings to ensure a sound fit and that permit the interspace leak checking point [E10], Figure 1-6 and Figure 1-7.

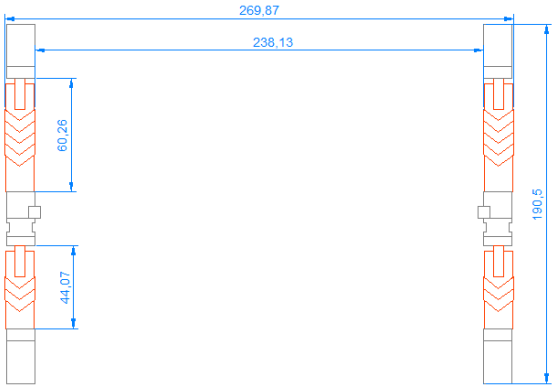

Figure 1-6: Seal Plug Chevron Seals with Dimensions (all dimensions in mm)

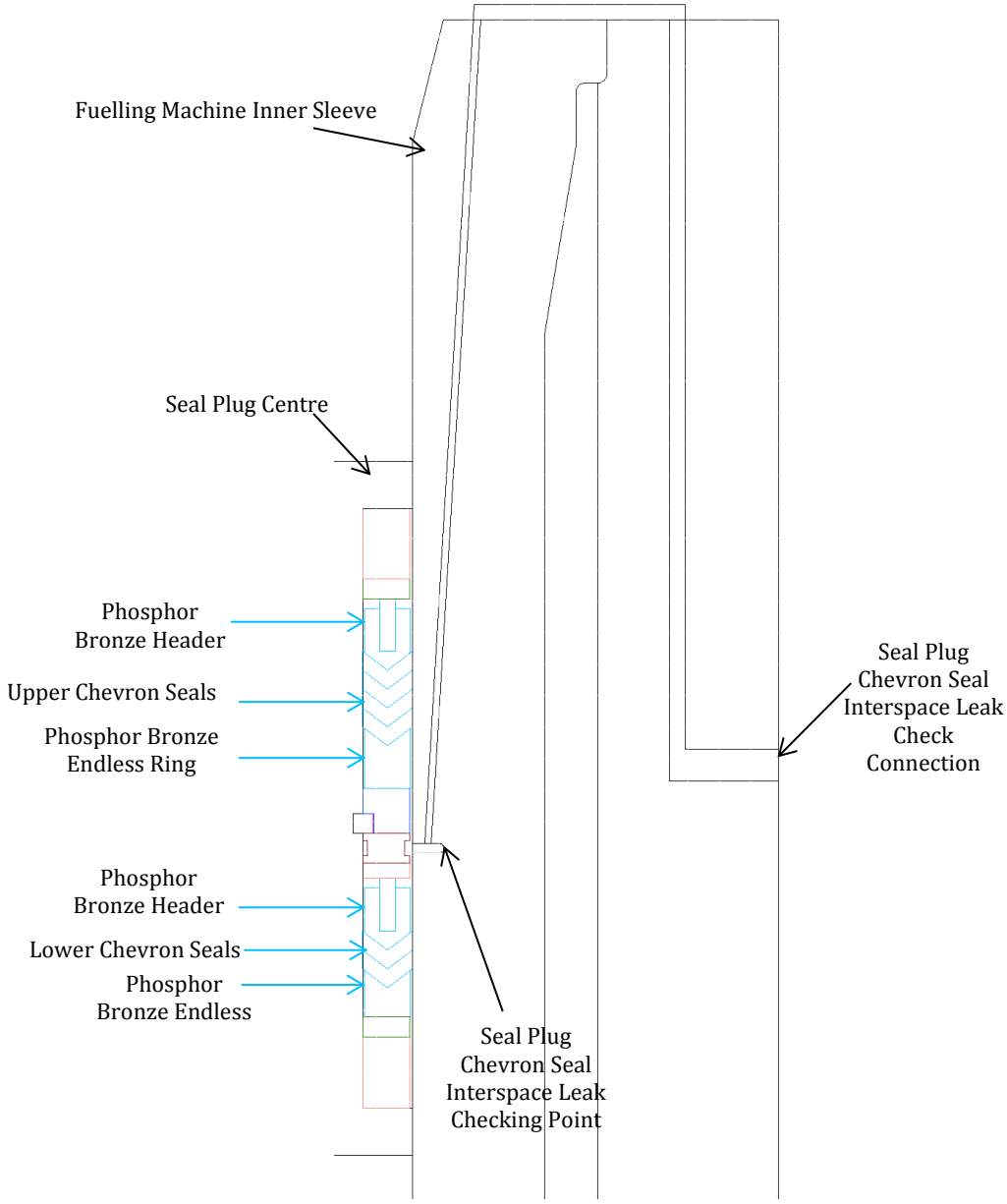

Figure 1-7: In-Service Geometry of the Full Seal Plug Chevron Seal Assembly

Knowledge of Behaviour

This section has been removed at EDF Energy's request.

1.2.2.1 CONDITIONS

This section has been removed at EDF Energy's Request

1.2.3 POTENTIAL CONSEQUENCES FROM A LOSS OF CONTAINMENT

This section has been removed at EDF Energy's request.

2 LITERATURE REVIEW

Chapter 1 identified the component for investigation as a set of chevron seals that are made up of a sulphur-cured acrylonitrile-butadiene based elastomer. The seals also comprise a reinforcing glass cloth, carbon black filler and brass wire, among other additives. This chapter reviews the available literature on lifetime prediction, degradation mechanisms and analysis techniques.

2.1 LIFETIME PREDICTION

Lifetime prediction studies on polymeric materials are often carried out through the gathering of experimental data at elevated temperatures and extrapolation of the resultant information back to ambient conditions [5]. The Arrhenius extrapolation assumes that the chemical degradation process dominates and can be expressed as:

$$k_{ar} = Ae^{-E_a/RT} \qquad \text{Equation 2-1}$$

where k_{ar} is the Arrhenius rate constant, A is the pre-exponential factor, E_a is the Activation Energy in $kJ\ mol^{-1}$, R is the Universal Gas Constant in $kJ\ mol^{-1}\ K^{-1}$ and T is the absolute temperature in K.

Providing the degradation process follows Arrhenius linearity a graph can be produced from this data that allows the reaction rate to be determined at lower temperatures. Taking the natural logarithm of the Arrhenius Equation gives:

$$\ln(k) = \frac{-E_a}{R}.\frac{1}{T} + \ln(A) \qquad \text{Equation 2-2}$$

Therefore plotting $\ln(k)$ on the y axis and $1/T$ on the x axis should yield a straight line with slope $-E_a/R$ and intercept $\ln(A)$, Figure 2-1a. However, many studies have demonstrated non-linearity in the Arrhenius plots of polymer degradation as shown in Figure 2-1b [6, 7, 8, 9, 10, 11, 12]. *Celina, Gillen and Assink* [13] review this behaviour and outline the alternative data-handling procedures as:

1. Treating the non-linearity as experimental noise
2. Using more complex kinetic schemes
3. Applying mathematical models using compensation effects
4. Diffusion Limited Oxidation (DLO) at high temperatures leading to a 'two-competing processes' situation

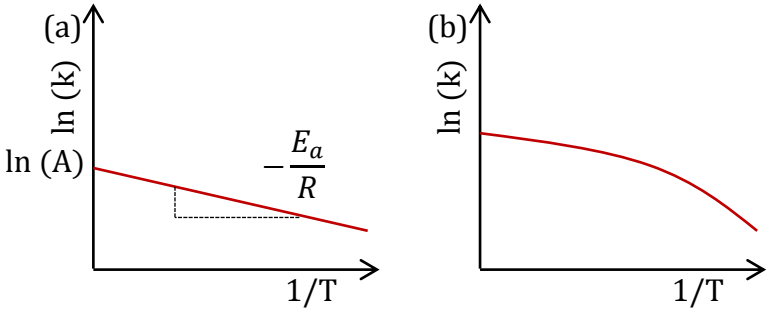

Figure 2-1: An Example of an Arrhenius Plot for (a) Linear and (b) Non-Linear Scenarios

Further to the 4th point, *Langlois, Audouin and Verdu* [14] note that overall lifetimes could be regarded as the sum of individual processes, with some degradation mechanisms having more than two competing processes. Some work has been done on the assessment of competing processes and there appears to be an excellent fit when accounting for oxygen consumption in the accelerated tests [13]. This suggests that when more than one degradation process could be occurring, extrapolation of accelerated tests to ambient conditions becomes increasingly complex and for accurate analysis, all degradation processes must be known so that the curvature of the extrapolation can be dissected into its component parts, Figure 2-2.

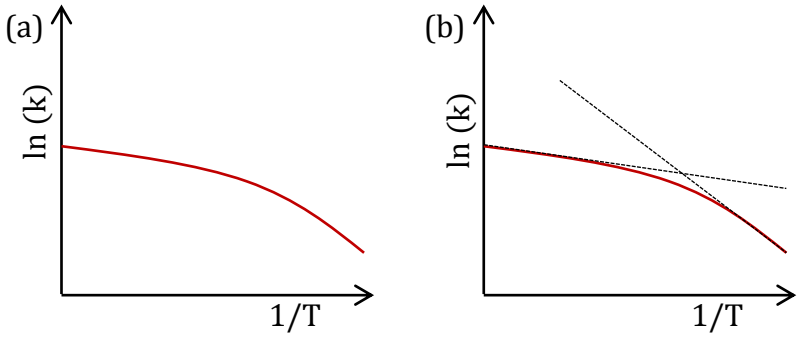

Figure 2-2: An Example of (a) Non-Linearity in Arrhenius Extrapolation and (b) its Dissection into Component Parts

Davenas et al. [15] explores the stability of polymers and discusses the complex degradation behaviour of elastomers. The diversity of organic chemistry permits a wide array of degradation mechanisms, owing to the variety of recombination schemes available following the breaking of bonds and also the high sensitivity of the elastomers to their surrounding environment. The methods utilised in manufacturing compound the complexity through the optional addition of numerous additives (anti-oxidants, plasticisers, organic and inorganic fillers, processing agents, etc.) and the heterogeneity of the molecular arrangement.

The inherently complex design of the elastomeric seals, the combination of chemical and physical degradation mechanisms [16, 17] and the limited time available for testing means that accelerated lifetime tests would not prove practical and their viability could not be assessed against real-time data. If the lifetime cannot be calculated through extrapolation tests it is important to identify the key aspects that constitute a good seal and any potential failure modes that could occur. An investigation into the effects these have on the elastomeric microstructure therefore forms the bulk of the report; the first step of which was to understand the material itself and which properties constitute a good seal.

2.2 NBR Structure and Inclusion Effects

Nitrile rubber (NBR) is a co-polymer of acrylonitrile, (ACN) and butadiene, (BDN). Figure 2-3 depicts the 1,3-BDN monomer and its associated NBR form, however, it can be made from the 1,2-BDN monomer with very limited alteration to the properties of the final material. The cyanide bond (C≡N) gives the material its polarity and thus its properties are strongly linked to the ACN content of the elastomer [18, 19]. An increase in ACN content, and thus polarity, has been shown to lead to a number of improved properties; increased resistance to swelling [20, 21], increased oil and solvent resistance [22], increased tensile strength, hardness and abrasion resistance [22], increased heat resistance [22] and increased gas impermeability [22]. However, it can also be detrimental to the material inducing decreased compression set resistance and resilience [22] and causing it to become mechanically inflexible at lower temperatures [20, 21, 22].

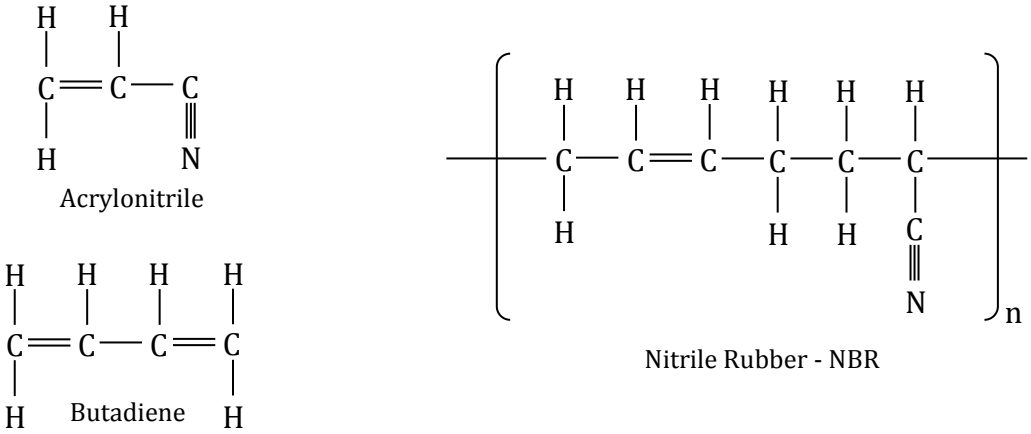

Figure 2-3: The Chemical Structure of Acrylonitrile, Butadiene and Nitrile Rubber

Because of the inevitable trade-off of properties when increasing the quantity of one particular monomer, the manufacturing procedure introduces a variety of additives. *Jackson et al.* [23] characterise the constituents of a commercial vulcanisate into four main groups:

1. Base elastomer
2. Vulcanising system
3. Protective agents
4. Reinforcing materials and/or plasticisers

It has been noted previously that carbon black has been used as a filler in the manufacture of the chevron seals. These types of fillers have been shown to induce a number of effects in the elastomers; increased material stiffness [24, 25], increased softening of an elastomer following repeated mechanical deformation (Mullins softening [25], , reduced solubility of gases into the bulk phase [26], increased Young's modulus, hysteresis and creep [23] and increased resistance to Environmental Stress Cracking (ESC) [27, 28]. The mechanisms and methods by which these act and assist in resistance against particular failure modes is explored in their relevant parts of the next section.

2.3 SEALING TECHNOLOGY

The purpose of a seal is defined as the 'control of fluid interchange between two regions sharing a common boundary' [29]. For the purposes of this project the fluid is CO_2 and the seal needs to limit the amount of leakage to as low as is reasonably practicable level. The chevron seal being investigated is on a moving component, however, it only seals once stopped and is therefore referred to as a pseudo-dynamic seal with basic concepts similar to those of a dynamic seal.

Basic Concepts of a Dynamic Seal

Figure 2-4 shows the basic principles underlining a dynamic seal. The moving surface (MS) oscillates vertically in contact with the seal body (SB). The gap between the MS and the SB is referred to as the primary sealing interface (P). The clearance between the MS and the SB at P is known as the 'seal gap' or 'film thickness' and is very small (in the order or micrometres, $10^{-6}\ m$). Between the SB and the housing, or in some cases the groove, is the secondary sealing interface (S). A force (F) is applied to the seal to create what is known as the closing force (CF), minimising the clearance at P and S to create a stronger seal.

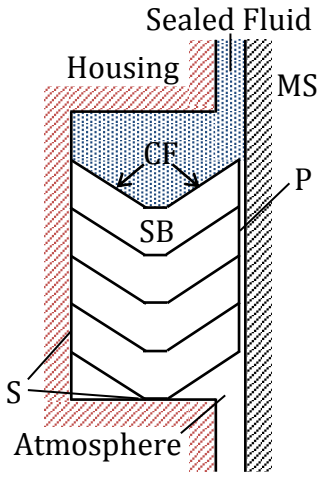

Figure 2-4: The Basic Concepts of a Dynamic Seal

Closing Force

For dynamic seals to be most effective, they need to reduce the size of the seal gap to an as low as is reasonably practicable level. This is done through the use of a CF acting on the SB in the direction of either P or both P and S. The general rule for the CF is that the total specific load (closing force ÷ sealing interface area) should exceed the sealed fluid pressure.

Elastomeric seals have a degree of deformability to them that means if a sufficient pressure is applied to the material it will contract in the direction of the force. This deformability is utilised by designing the SB slightly larger than its housing so that when in operation, the MS and housing together create a pressure on the SB that causes it to deform. This creates dimensional interference and contributes to the total specific load. If this pre-load is too high, the seal could become damaged through fatigue or wear. To prevent this occurrence, the seal is often designed so that the pressure from the sealed fluid contributes to the closing force thus allowing the pre-loading to be kept reasonably low, more commonly referred to as automatic sealing.

In terms of microstructure the pre-loading causes the polymer chains to contract and reduce the void volume within the matrix. Crosslinks that are present in the structure retain this energy forcing the chains to return to their original position and act back against the pressure creating a sealing force, Figure 2-5. Changes in the microstructure that reduce the ability of the elastomer to retain this energy can result in a decrease in the sealing force and thus contribute to the overall degradation of the materials' sealing capacity and are explored in the next section.

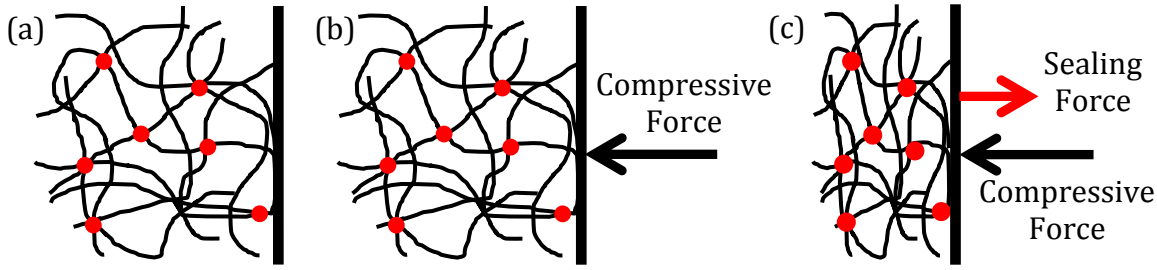

Figure 2-5: Depiction of Elastomeric Microstructure at (a) Rest, (b) In Response to a Compressive Force and (c) Crosslinks Acting Back on Compressive Force to Produce a Closing Force

2.4 Potential Failure Modes

This next section identifies the potential failure modes and determines their effects on the microstructure of the elastomer and the resulting effect this has on the sealing capacity of the component. Through an understanding of the service environment, investigated in the previous chapter, the potential failure modes that are relevant to these seals have been identified as oxidative ageing [19, 30], radiation [31, 32, 33], stretching and Mullins softening [34], absorption of gas and cavitation [26, 35]. As mentioned in the previous section elastomers are highly sensitive to their environment and synergistic effects must be taken into consideration, such as ESC [28, 36, 37].

2.4.1 Ageing

The two main processes that contribute to the ageing of elastomers are molecular scission, the dissection of the polymer backbone, and crosslinking, the formation of a chemical bond between two different sections of a polymer backbone. The susceptibility of an elastomer to a particular ageing process is dependent upon its structure and it has been previously shown that NBR typically ages through the formation of crosslinks; resulting in a more rigid network and a reduction in the mobility of the polymer chains [19, 21]. This introduces the concept of the 'gel' and 'sol' fractions within a polymer structure; the gel fractions pertaining to the portion of polymer that is crosslinked and is contained within the network whilst the remaining loose chains within the microstructure constitute the sol fraction.

A number of studies have been carried out on the ageing of elastomers and the effect increasing crosslink density has on the material properties [28, 30, 34, 38, 39, 40, 41, 42, 43, 44]. It is generally agreed that at low crosslink densities the addition of further crosslinks causes the Young's modulus, resistance to ESC and the thermal and wear resistance to all increase. It is clear that these properties are beneficial to the performance and durability of seals and as such chemical crosslinks are regularly induced in the elastomeric structure through exposure to ionising radiation.

2.4.2 RADIATION

Ionising radiation, both electron-beam and γ-rays, are used in the manufacture of elastomeric seals to induce microstructural changes in the material that improve its mechanical performance and endurance, known as vulcanisation. The literature [15, 31, 45, 46, 47, 48, 49] describes the process of radiation attack on NBR as follows:

1. High-energy incident radiation results in ionisation of either BDN or ACN pendants
2. This results in the loss of hydrogen atoms which recombine with the surrounding cage of neighbouring chains and produce radicals
3. The recombination of these radicals then follow three possible pathways in usual scenarios:
    a. The hydrogen atoms remove other hydrogen atoms and the two radicals can bind to form stable species in the allylic position – resulting in scission of the weaker chemical bonds (C-H)
    b. Due to the presence of the cyanide bond, the high-energy hydrogen atoms may also lead to the formation of conjugated polyimine radicals
    c. In the presence of oxygen and with lower quantities of ACN C-O-C crosslinks may be formed

In some cases, radiation-sensitive monomers are introduced during this vulcanising step to reduce the required dose of irradiation [31]. However, continued exposure to high-energy radiation (such as that experienced in NPPs) can begin to have a detrimental effect on the material properties. In some cases the Young's modulus can become so high that the surface of the seal can no longer compress to a sufficient degree and the sealing force is considerably diminished or the material undergoes severe embrittlement and otherwise endurable mechanical strain incurs early failure.

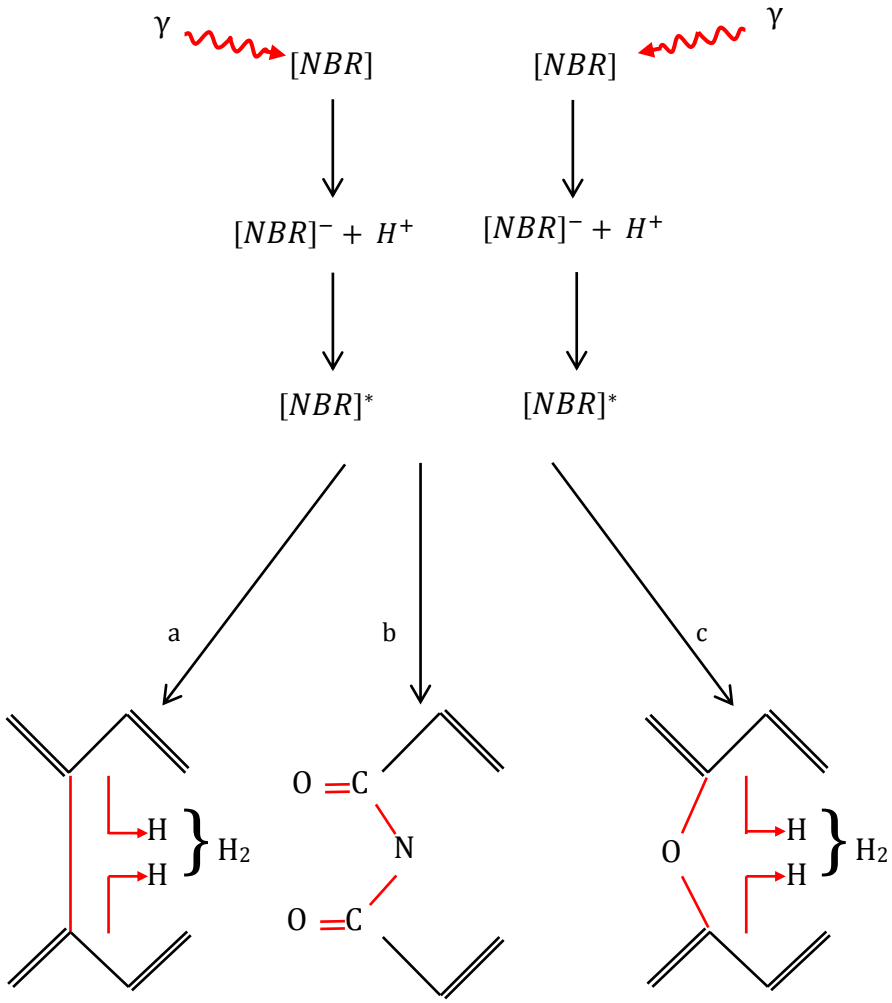

Figure 2-6: The Ionisation of NBR Following Gamma Radiation and the Subsequent Degradation Mechanisms

It has also been noted that continued radiation exposure beyond this threshold dose can lead to a reduced effect and in some cases even a reversal in the material property changes. *Vijayabaskar, Tikku and Bhowmick* [31] and *Davenas et al.* [15] witnessed increasing gel content up to a dose of $100x10^3\ J\ kg^{-1}\ s^{-1}$ at which point the effect began to cease and the gel content remained constant. Investigation into the mechanical properties saw an increase in tensile strength up to a maximum at $50x10^3\ J\ kg^{-1}\ s^{-1}$ followed by a steady decrease with increasing radiation dose. However, the glass transition temperature was found to continually increase with no change being observed at the threshold dose. These findings have been explained in the literature through the development of a 3D network in the form of crosslinking, as expected, until the crosslink density increases to the threshold

value and the network becomes so dense that there is little energy dissipation and significant segments of the polymer chains become immobile. *Davenas et al.* proposed that as the polymer backbone approaches saturation with carbon atoms, due to the formation of multiple crosslinks along the same backbone, the radiochemical yield for chain scission increases to the point it becomes significant and the change in radiation effects is due to a competition arising between crosslink formation and chain scission.

2.4.3 MECHANICAL

During its service life the seal is subject to cyclic mechanical stress through its dynamic movement into and out of its respective housing. As the seal plug is lowered the chevron wings of the seal are compressed and a pressure boundary is produced with the sealing force being applied by the recovery from this compression.

An elastomer under compression undergoes molecular rearrangements and adjustments. It is these complex deformations that give elastomers their time-dependent viscoelastic behaviour. In response to an external compressive stress the polymer chains will attempt to slide past one another and dissipate the energy being applied to the surface throughout the bulk. The portion of energy that is dissipated through the structure is not retained by the polymer chains and does not contribute to the sealing force applied at the pressure boundary. The relaxation times following release of the external stress can be used to distinguish between the various types of slippage that occur within the microstructure. Rapid relaxation has been linked to the local-scale re-adjustments of molecular bonds while the slower relaxation times have been linked to long-range-scale rearrangements of large polymer chains with respect to each other [50].

The grease that lubricates the dynamic movement of the seals will increase in viscosity as it ages and as it collects rubber debris. If the seal is housed for a period of time this thickening can cause static friction (stiction) to occur and a larger than expected force is required to begin the movement. In some situations this can lead to stretching of the elastomer and even cavitation or cavity growth near filler

particles, where substantial volume changes have previously been reported [34, 51, 52, 53, 54]. The literature [54, 55, 56] suggests one possible explanation for this as the decohesion of the polymer chains from the filler particles and the formation of vacuoles in the rubber matrix. *Merckel et al.* [34] and *Shinomura and Takahashi* [57] further support this hypothesis having shown that this effect increases with increasing filler content and that a threshold point exists below which this effect is not seen. This phenomenon is known as Mullins Softening and is reviewed in detail in [58]. It has been shown to be linearly linked with filler volume fraction, observable before the appearance of cavities and unaffected by crosslink density [25, 34].

Repeated application of stretching to an elastomer can lead to flex fatigue. This can even occur when the tensile stress that is applied is so low it would not normally induce a failure. It is widely accepted to be due to the initiation of a crack at a surface or internal defect and the subsequent propagation of that crack throughout the structure until rupture occurs, Figure 2-7 [59]. A significant portion of research exists in this area and it is concluded that there exist two different types of flex fatigue; low-cycle and high-cycle. Due to the stiction effects of the grease causing in-frequent but potentially quite significant stress values only low-cycle flex fatigue is of concern. However, the presence of reinforcement fillers such as the glass cloth helps to reduce this effect. The fibres bridge any cracks that may form and help prevent any further propagation as the stress held by the reinforcement first needs to be overcome [28, 34].

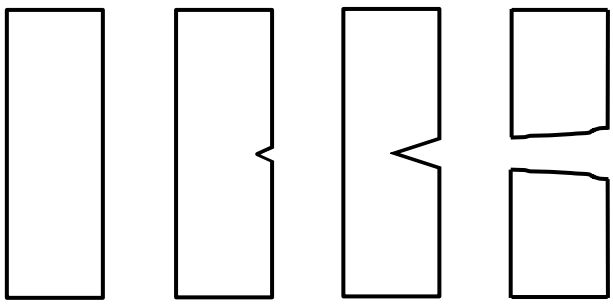

Figure 2-7: The Propagation of a Crack Through an Elastomer With Carbon Black Fillers

2.4.4 Absorption and Explosive Decompression

During its service life the seal will be exposed to high pressure CO_2 at intermittent intervals. The absorption of CO_2 into an elastomeric seal has been shown to have severe consequences for the material. The swelling of the seal following this absorption can affect dimensional tolerances [35], create stress distributions in the microstructure [26] and interfere with internal fracture mechanics that would otherwise dissipate energy. A CO_2 saturated elastomer has also been shown to have a reduced strain to failure and markedly reduced tear strength [26].

The process of this absorption has been described through the micro-Brownian motion of the polymer chains resulting in hole formation at the surface as a function of probability. The absorbing molecules can then adhere to the surface and if their location is akin to one of these 'suitably large holes' the molecule can diffuse into the bulk, Figure 2-8 [60]. The amount of gas molecules absorbed is controlled by three factors; equilibrium solubility, the surface entry coefficient and the diffusion coefficient [60]. The surface entry coefficient will dictate the probability of an absorbing molecule adhering to the surface at a location that has a sufficiently large hole available for diffusion and when significant will exhibit as a time lag in the absorption curves. The diffusion coefficient is then linked to the transport of the absorbing molecule through the bulk. However, this is a complex function of the CO_2 pressure and as such is highly non-Fickian in nature [60, 61, 62, 63, 64, 65, 66]. *Briscoe, Gritsis* and *Liatsis* [61] and *Bernier* and *Kambour* [67] attribute this to plasticisation of the polymer chains in the presence of CO_2 while Rennie and Tabor [68] discuss the external pressure reducing the free volume within the elastomeric matrix to such a degree that diffusion is arrested.

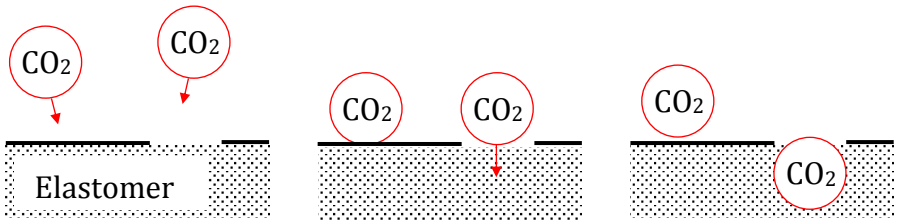

Figure 2-8: The Process of Absorption of CO_2 into an Elastomeric Matrix

The high pressure CO_2 that the seal is exposed to is cyclic in nature and rapid decompression, or pressure/temperature transients, have been linked to Explosive Decompression [26, 35, 69]. This is seen in the material as blistering and cracking, Figure 2-9 [35]. This phenomenon arises from the fact that upon rapid depressurisation or cooling the CO_2 is released from solution faster than it can diffuse to the surface of the elastomer and desorb away, resulting in bulk softening of the material, reduction in the compressed volume and a large increase in the uncompressed volume [35]. A sufficiently slow depressurisation rate will alleviate this damage, although one needs to be careful of depressurisation fatigue damage which can occur and is analogous to flex fatigue in mechanical strain of the elastomer [69].

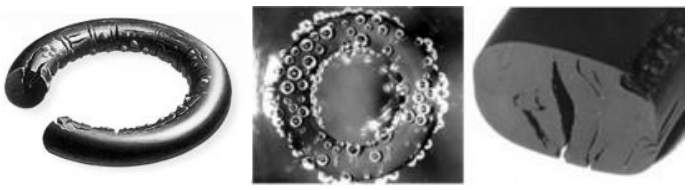

Figure 2-9: Examples of Explosive Decompression Damage Caused in Elastomers [70, 71]

2.4.5 Environmental Stress Cracking

An elastomer can experience failure below its typical design limits when in the presence of an active environment. This phenomenon, referred to as ESC, is not to be confused with Stress Corrosion Cracking (SCC) which is where an active environment reacts chemically with the structure and synergises with mechanical stress to induce early failure.

ESC is a purely physical phenomenon, has been extensively researched in the literature [60, 72, 73, 74] and its mechanism of failure has been discussed in terms of solubility parameters of solvents and polymers [67, 75, 76, 77, 78], sorption of organic liquids [79, 80], and hydrogen bonding [81, 82]. However, the most cited mechanism is that by *Gent* [83] and further work by *Bernier* and *Kambour* [67] which discusses the lowering of the glass transition temperature around the crack

tip due to dilatant stress-induced swelling permitting the propagation of the crack through viscous flow.

The work by *Hansen* [60] found that ESC is much more prominent in linear structures for both the solvent and the elastomer. It is also noted in the review by *Robeson* [28] that increased crystallinity or crosslinking within the elastomeric structure enhances its resistance to ESC failure.

2.4.6 Synergistic Effects

Throughout this chapter little reference has been given to the synergistic effects that multiple failure mechanisms could induce. This is because there is limited literature available on combined failure mechanisms as these are difficult to model and can be very selective to the environment faced by the material of choice. However, some authors comment on the possibility of synergistic effects during their research; the presence of Argon during IR radiation intensifies the restructuration of the elastomer [30], unexpected reactions could dominate degradation in high pressure situations [84] and small traces of oxygen can accelerate radiation-induced damage [15]. It is therefore prudent to ensure that any potential synergism in degradation is explored, identified and characterised where possible.

2.5 Conclusions and Analysis Techniques

The standard test carried out on elastomeric seals concerns the calculation of the materials compression set; its ability to recover following a compressive stress. Whilst this will provide some information on the potential sealing force that can be applied by the material it is not possible to infer any microstructural changes in the elastomeric matrix that will be causing the macroscopic effects. This section of the chapter explores analytical methods carried out in the literature and discusses the applicability of them to the current project.

2.5.1 Imaging and Microscopy

When assessing any elastomeric components the first stage of the process is a visual inspection. In the instance of seals this often includes splicing the material and imaging the cross-section as well. Transmission and Scanning Electron Microscopy (TEM and SEM) are often used to obtain additional information [85] as well as polarising microscopy with crossed-polar filters [37]. The latter method produces a stress profile in the visible portion of the elastomer and as the positions of stress within the structure are not an important feature of determining the degradation it is not considered worthy of investigation. TEM will prove difficult to carry out on these samples as the poor machinability of the elastomeric seals will make obtaining a sufficiently thin sample quite problematic. SEM has been proven to be a useful technique in imaging surfaces at high magnification and is regularly coupled with Elemental Distribution Mapping (EDX) for the determination of chemical elements and their locations in the visible portion of the samples. This requires a sufficiently flat portion of elastomer for reliable results, which will also prove difficult for the same reasons as the TEM. However, with due care and attention SEM microscopy will at least provide magnified images for inspection.

2.5.2 Composition and Spectroscopy

The Kjeldhal method calculates the organic nitrogen content in elastomers by heating with sulphuric acid to allow formation of ammonium sulphate, which is then captured in boric acid and back titrated to determine the ammonia, and thus nitrogen, content. This a well-established process for determination of ACN content in NBR, however it is very tedious and time consuming and there is a high chance of manual error [18]. Whilst the information gleaned from this experiment may prove useful in determination of characteristic properties, additional tests can be performed that will absolutely calculate these properties with a lower margin for error.

A number of methods have been used for the determination of additives such as liquid extraction, Soxhlet extraction, ultrasonic assisted extraction and pressurised

liquid extraction [20, 86, 87, 88, 89] but these are known to be very laborious and time consuming [90]. *Hakkarainen* [20] and *Rogalewicz, Voelkel and Kownacki* [91] suggest the combination of head-space solid-phase microextraction and Gas Chromatography Mass Spectrometry (GCMS) for the analysis of additives. Knowledge of the particular additives included could prove useful in determination of potential chemical reactions, however, the benefit of this information does not justify the time and cost involved in analysis of the complex results and the unavailability of the machines will result in the tests being difficult to carry out within the scope of this project.

Infra-red (IR) and Raman Spectroscopy are regularly used for the identification of chemical bonds within a substance. ISO 4650 details the method for rubber identification by Fourier Transform IR (FTIR) and Thermogravimetric Analysis (TGA)-FTIR has previously been used for the quantitative analysis of NBR [92]. The inclusion of numerous additives can make the resultant spectra difficult to analyse and a complicated derivatisation technique [92, 93] involving the treatment of the samples with a variety of reactive gases such as nitric oxide (NO), sulphur tetrafluoride (SF_4), ammonia (NH_3) and iodine compounds is required for modification. The use of an Attenuated Total Reflectance (ATR) attachment has been proven to improve the spectra in many applications [31, 62, 94] and can even overcome fluorescence of the IR light induced by the presence of carbon black [95, 96, 97]. Care must be taken as to the placement of the sample on the attachment as this is a near surface technique and will not record the spectra of the bulk material.

Raman spectroscopy is often used as a complimentary technique to FTIR but the presence of carbon black and impurities has proved severely problematic in the literature [23, 84, 98, 99]. The recommended techniques to alleviate this problem, such as an addition of a 'burn-out' time and photoacoustic spectroscopy, have shown limited success [100, 101].

Analysis of the spectra generated from either FTIR or Raman can lead to an understanding of the quantity of material represented by a particular peak [102], evaluation of temperature effects, catalyst influence and reaction kinetics [103, 104] plus the method proposed by *O'Donnell and Sangster* allows the calculation of

radiochemical yields for scission and crosslinking [105], which are considered to be the main result of ageing and radiation-induced damage.

2.5.3 Material Properties

2.5.3.1 Crosslink Density

To assess the extent of ageing or radiation-induced damage the crosslinking density is determined through the swelling behaviour of the elastomer. *Flory and Wall* [106, 107, 108, 109, 110] and *James and Guth* [111, 112] are recognised as the developers of the two theories that describe this swelling behaviour; the affine-network model is the work of *Wall, Flory and Rehner* and the phantom model is that of *James and Guth*. The affine network model restricts the movement of network and junctions and the microscopic deformation between any two points is therefore proportional to the macroscopic deformation. On the other hand, the phantom model suggests that crosslinks fluctuate around average positions and it is the magnitude of these fluctuations that determine the relationship between the macroscopic dilation and the deformation of the individual polymer chains. The phantom model is considered more realistic but due to the simplicity of the affine network model, and its ability to estimate the actual degree of crosslinking, they are both still in wide use today [113]. The Flory-Rehner equation is readily used to calculate the crosslink density in an elastomer, however a report by *Nandi and Winter* [113] highlights the shortfalls in the calculations; few theoretical predictions agree qualitatively with experimental data [114], the dilation modulus parameter is inconsistent with Flory-Rehner assumptions [115, 116, 117] and a number of modifications have been required to produce satisfactory results [118]. *McKenna, Flynn and Chen* [119] have since shown that the Flory-Huggins Interaction Parameter, which is required for the calculations, changes with crosslink density and would therefore pose problems in determining the change in crosslink density with increasing radiation dose. For this reason swelling tests can be used to give an indication of crosslink density and can be compared against pre and post irradiated samples but the calculation of absolute crosslink density will prove too inaccurate for correlation of results.

Another method of identifying changes in crosslink density is through Differential Scanning Calorimetry (DSC) [120, 121, 122]. The resultant plot can be used to calculate the glass transition temperature of the sample which is linked to the manoeuvrability of the polymer chains. *Davenas et al.* [15] and *Vijayabaskar, Tikku and Bhowmick* [31] have shown that an increase in crosslink density will restrict the movements of the polymer chains and will be evident as an increase in the glass transition temperature.

2.5.3.2 Mechanical Properties

A key mechanical property for elastomeric seals is the ability to create a sealing force following compression and to recover upon release of that compression. Energy dissipation throughout the elastomeric matrix is discussed above and will be evident as hysteresis in any stress-strain curve, Figure 2-10.

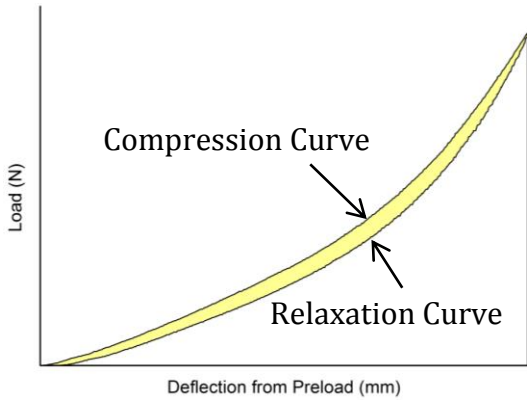

Figure 2-10: The Hysteresis in an Elastomeric Stress-Strain Curve

2.5.3.3 CO_2 Absorption Behaviour

Absorption of CO_2 into the seal will cause the elastomeric matrix to swell. This reduces the dimensional tolerances and can increase the physical wear caused by the dynamic movements of the seal. Should the crosslinks prove sufficiently localised this absorption will be hindered by their increasing density in the structure as the network junctions will prevent the movement of the polymer chains [62]. Therefore an understanding of the absorption behaviour will not only

inform as to the resilience to physical wear but also has the potential to inform as to the proximity of crosslinks from one another.

Hansen [60] has highlighted the method for identification of a significant surface entry coefficient through the plotting of uptake per original mass of elastomer against the square root of time, Figure 2-11. If a significant surface entry coefficient exists the linear portion of the plot will not pass through the origin, and its deviation from the origin will give some indication as to the magnitude of this coefficient.

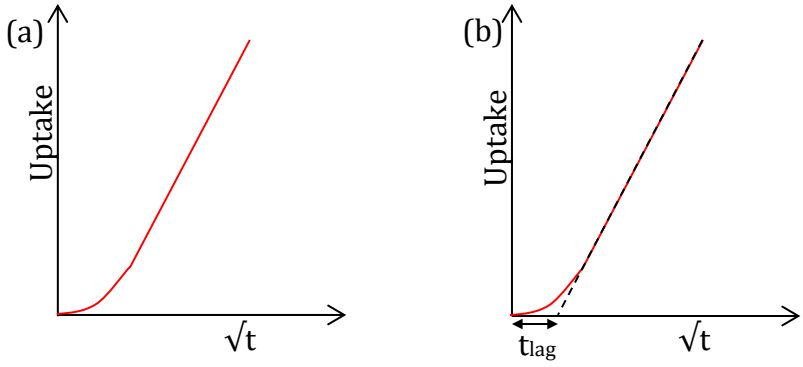

Figure 2-11: A Depiction of the Uptake vs Square Root Time Plot and Subsequent Calculation of t_{lag}

George [35] found that the uptake of CO_2 into a nitrile elastomer follows a pseudo-first order rate equation, Equation 2-3, which has been applied to other adsorption mechanisms in the literature [123, 124, 125, 126, 127, 128, 129]:

$$q_t = q_e\,(1 - e^{-k_1 t}) \qquad \text{Equation 2-3}$$

where q_t is the uptake measured at time t in $kgkg^{-1}$, q_e is the uptake at equilibrium in $kgkg^{-1}$, t is the time in s and k_1 is the observed rate constant in s^{-1}.

However, many reports have found that gas adsorption onto a solid can follow the pseudo-second order rate equation, Equation 2-4 [126, 127, 130]:

$$q_t = \frac{k_2 {q_e}^2 t}{1 + k_2 q_e t} \qquad \text{Equation 2-4}$$

where k_2 is the observed rate constant in $kgkg^{-1}s^{-1}$.

Azizian [131] discusses an alternative derivation of these well-known rate equations that allows the computation of the adsorption and desorption rate constants for the pseudo-first order model, Equation 2-5:

$$k_1 = k_a C_0 + k_d \qquad \text{Equation 2-5}$$

where k_a is the rate constant of adsorption in $m^3 kg^{-1} s^{-1}$, C_0 is the initial concentration of the solute in the solution in kgm^{-3} and k_d is the rate constant of desorption in s^{-1}.

George [35] commented on the linear relationship seen between the pressure of the CO_2 and the equilibrium uptake; this suggests ideal dilute solution behaviour and thus a fit to Henry's Law will allow the production of parameters that can be compared.

$$q_e = K_H P \qquad \text{Equation 2-6}$$

where K_H is the Henry's Law Constant in $kgkg^{-1}Pa^{-1}$ and P is the pressure in Pa.

However, this provides no information on the uptake mechanism. Adsorption studies allow plotting of uptake data to isotherm models that will produce parameters that can be compared to samples in the literature. Some typical isotherm models include those found by *Freundlich* [132], *Langmuir* [133], *Temkin* [134, 135] and *Dubinin-Radushkevic* [136, 137, 138].

Freundlich Isotherm

$$q_e = a_F {C_e}^{1/n_F} \qquad \text{Equation 2-7}$$

where a_F is the Freundlich Isotherm Constant, C_e is the equilibrium concentration of solute in solution in kgm^{-3} and n_F is the Strength of Interaction Parameter.

The Freundlich isotherm is an entirely empirical relationship and is applicable in both non-ideal sorption on heterogeneous surfaces as well as multilayer sorption cases.

Langmuir Isotherm

$$q_e = \frac{q_m a_L C_e}{1+a_L C_e} \quad \text{or} \quad q_e = \frac{K_L C_e}{1+a_L C_e} \qquad \text{Equation 2-8}$$

where a_L and K_L are the two Langmuir Isotherm Constants respectively.

A fit to the Langmuir isotherm suggests that the adsorbing molecules behave as an ideal gas and the elastomer surface behaves as an ideal solid with distinct sorption sites. A single monolayer of adsorbing molecules chemically binds to available sorption sites, permitting the calculation of the maximum volume of the monolayer, q_m, and the equilibrium constant for the chemical reaction binding the adsorbing molecule to the surface, a_L.

Temkin Isotherm

$$q_e = \frac{RT}{b_T} \ln(a_T C_e) \qquad \text{Equation 2-9}$$

where a_T and b_T are the two Temkin Isotherm Constants.

Temkin noted that the sorption sites became loaded due to solute-solute interactions, evident as decreasing heat of adsorption, and adapted the Freundlich model from a logarithmic change to a linear one.

Dubinin-Radushkevic Isotherm

$$q_e = q_D \exp\left\{-B_D \left[RT \ln\left(1 + \frac{1}{C_e}\right)\right]^2\right\} \qquad \text{Equation 2-10}$$

where q_D and B_D are the two Dubinin-Radushkevic Isotherm Constants.

This isotherm accounts for the impact a porous structure has on adsorbing molecules and the mean free energy of sorption for one mole can be calculated using the constant B_D:

$$E = \frac{1}{\sqrt{2B_D}}$$ Equation 2-11

This E value provides an indication of whether the adsorption process occurs through physical or chemical adsorption. Physical adsorption, or physisorption, arises from the development of long range weak Van der Waals forces between the solute and the sorbent. Chemical adsorption, or chemisorption, involves the attachment of the solute to the sorbent through a covalent bond. An E value less than $8x10^3\ kJ\ mol^{-1}$ indicates physisorption, whilst a higher value suggests chemisorption [139].

2.5.4 Concluding Remarks

Understanding the degradation mechanisms occurring within the seal during service life will involve a certain degree of knowledge of all the degradation mechanisms occurring from all aspects of the service history. Inherent in this is the presence of CO_2 during dynamic movements and radiation exposure. It is well known that CO_2 is an active ESC agent for nitrile elastomers causing increased deformations at lower strains, and in some cases early failure of a component, and it is therefore deemed vital to understand how CO_2 may be affecting other degradation mechanisms on which there is limited knowledge within the literature. It will therefore be key throughout this project to ascertain damage induced in the seal in air for comparison against other materials and in CO_2 to determine if CO_2 contributes to accelerated damage in other aspects of the degradation process.

3 MATERIALS AND METHODS

Chapter 2 identified the main characteristic properties of a polymer that contribute to its sealing capacity and reviews the available literature on how different environments can affect these properties. This chapter will introduce the samples that were investigated and the methods by which these characteristic properties were calculated, analysed and compared. The processes involved in each technique and any recent advances in the methodology are also discussed. It is also prudent to note at this stage that 'Standard Atmopsheric Conditions' shall be deemed a pressure of $101x10^3\ Pa$ and a temperature of 293 K.

3.1 EXPERIMENTAL SAMPLES

EDF Energy has donated a pre- and post-service seal for the purposes of this work. This has allowed the cross-comparison of the results from experiments performed under laboratory conditions with the degradation behaviour actually seen in service. Unfortunately, due to manufacturers' intellectual property rights, the information about the seal's composition and manufacturing procedure are limited. Three commercially available nitrile rubber samples of different grades were obtained to allow comparison of the seal's behaviour with other samples manufactured from the same base elastomeric component.

The three samples were grades BA40, BA50 and BA60 and were purchased from *Whitby and Chandler Ltd.* [140]. The grade values refer to their hardness ratings during Quality Assurance tests.

3.2 OPTICAL MICROSCOPY AND SPECTROSCOPY

A visual comparison of the samples provided some initial information on potential changes in the elastomer and a Nikon D3200 Digital Single-Lens Reflex (DSLR) camera was used to capture any points of interest for further discussion. Manual

handling gave a brief indication of the stiffness of the samples and any resultant embrittlement.

3.2.1 Scanning Electron Microscopy

A Hitachi TM3030 Scanning Electron Microscope was used to inspect the surface of the polymers at magnifications up to $x3500$. This SEM was able to image in both Secondary Electron Imaging (SEI) mode, which provided topographical information, and Back-scattered Electron (BSE) mode, which provided elemental information. Unfortunately due to the non-linear topography of the samples BSE was unreliable. The brass wire in the industrial seal samples provided sufficient conductivity if a sound connection was made with the SEM stub. For the *Whitby and Chandler* samples, no brass was present and therefore the samples were sputter coated with $5 - 10\ nm$ of gold.

3.2.2 Infra-Red Spectroscopy and Raman Spectroscopy

A Perkin Elmer Frontier FTIR, Figure 3-1(a), with an ATR attachment, Figure 3-1(b), was used for the obtainment of IR spectra of the samples. The ATR attachment securely held the sample against a piece of diamond through which the incident radiation was transmitted. A comparison was then made between incident radiation and the reflected radiation to determine which wavelengths had been absorbed by the surface of the sample.

(a) 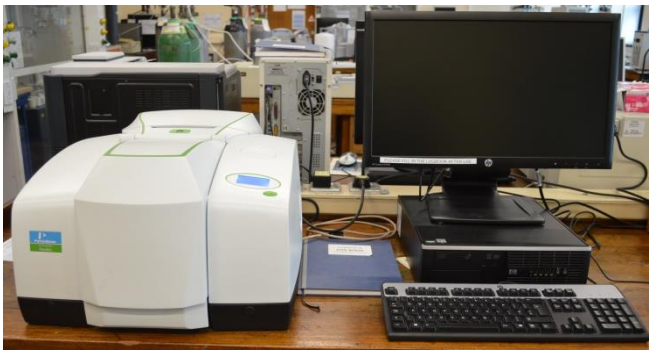 (b) 

Figure 3-1: (a) The Perkin Elmer Frontier FTIR Spectrometer and (b) ATR Attachment

Because this method of FTIR does not assess the bulk of the elastomer, each sample had a maximum of 4 mm removed from the outside edge to expose a clean fresh surface.

A Renishaw inVia Raman Microscope was used to supplement the data obtained from the IR Spectra. A 'green light' laser with a wavelength of $514.5x10^{-9}\ m$ was set to a power of $20x10^{-3}\ J\ s^{-1}$ to obtain spectra between 500 and 4000 cm^{-1}.

Spectra from both the IR and Raman were cross-analysed with the data available on the well-documented databases to assist in identification of chemical bonds present in the structure and, where possible, their configuration.

3.3 Material Properties

3.3.1 Swelling Behaviour

ASTM D6814 [141] details the procedure and calculations for determining the crosslink density of crumb rubber. The calculation involved, Equation 3-1, requires the use of the polymer-solvent interaction parameter which is unknown when the chemical and physical structure of the polymer is unknown. However, it is only the change in cross link density that is required for comparison in these experiments and thus an adaptation of these standards was used to carry out the swelling tests and calculate the percentage change in mass and volume, which gave an indication as to the change in crosslink density.

$$v_e = \frac{-\left[ln(1 - V_r) + V_r + \chi_1 {V_r}^2\right]}{\left[V_1\left({V_r}^{1/3} - V_r\right)/2\right]} \qquad \text{Equation 3-1}$$

where v_e represents the effective number of chains, V_r is the volume fraction of polymer in a swollen network in equilibrium with pure solvent (%), χ_1 is the polymer-solvent interaction parameter and V_1 is the molecular volume of the solvent ($m^3\ kmol^{-1}$).

Sample Preparation

Using a fresh sharp blade on a Stanley Knife the samples were cut into sections approximately 7 – 10 mm in both length and width and 6 mm in thickness.

Procedure

1. Acquire all apparatus and wear appropriate Personal Protective Equipment
2. Place the weighing boat on the micro-balance and tare
3. Place the first sample on the weighing boat and allow the micro-balance to equalise
4. Record the mass in mg
5. Using the callipers, record the length, width and thickness of the sample in mm
6. Place the sample in its designated test tube in the test tube rack
7. Repeat steps 2 through to 6 for each sample until the test tubes are all loaded
8. Pour 40 cm^3 of toluene into each test tube and replace the bung
9. Allow to swell for 72 $hours$, replacing solvent with fresh every 24 $hours$
10. Place the weighing boat on the micro-balance and tare
11. Remove the first sample from the test tube and quickly dip in acetone before patting dry on lint-free filter paper
12. Place the sample on the weighing boat and allow the micro-balance to equalise
13. Record the mass in mg
14. Using the callipers, record the length, width and thickness of the sample in mm
15. Return to the empty test tube and replace bung
16. Repeat steps 10 through to 15 for each sample until all have been returned to an empty test tube
17. Use Equation 3-2 and Equation 3-3 to calculate percentage mass and volume increase

$$\Delta_{M\%} = \frac{M_t - M_0}{M_0} \times 100 \qquad \text{Equation 3-2}$$

$$\Delta_{V\%} = \frac{L_t W_t T_t - L_0 W_0 T_0}{L_t W_t T_t} \times 100 \qquad \text{Equation 3-3}$$

where $\Delta_{M\%}$ is the percentage change in mass, M is the recorded mass, $\Delta_{V\%}$ is the percentage change in volume, L, W and T are the recorded length, width and thickness respectively and the subscripts 0 and t denote before and after the experiment respectively. Due to the toxicity of benzene, toluene was used as the organic solvent.

3.3.2 Glass Transition Temperature

Differential Scanning Calorimetry is regularly used to calculate the glass transition temperature, T_g, of samples. This method records the difference in heat required to raise the temperature of the sample-loaded chamber compared to an empty chamber and plots this against temperature.

The samples were prepared by using a fresh sharp blade on a Stanley Knife and dissecting approximately $4 - 5\ mg$ of sample into as small as reasonably practicable monoliths. These were placed in an aluminium pan and lid which were crimped together and loaded into the sample chamber. The system was taken down to an initial temperature of $-60\ °C$ and held for $120\ s$. The temperature was then increased at a ramp rate of $10\ °C\ min^{-1}$ up to a temperature of $20\ °C$ where it was held for $120\ s$. A typical plot from a Perkin Elmer Diamond DSC loaded with an elastomer can be seen in Figure 3-3.

Figure 3-2: The Perkin Elmer Diamond Differential Scanning Calorimeter

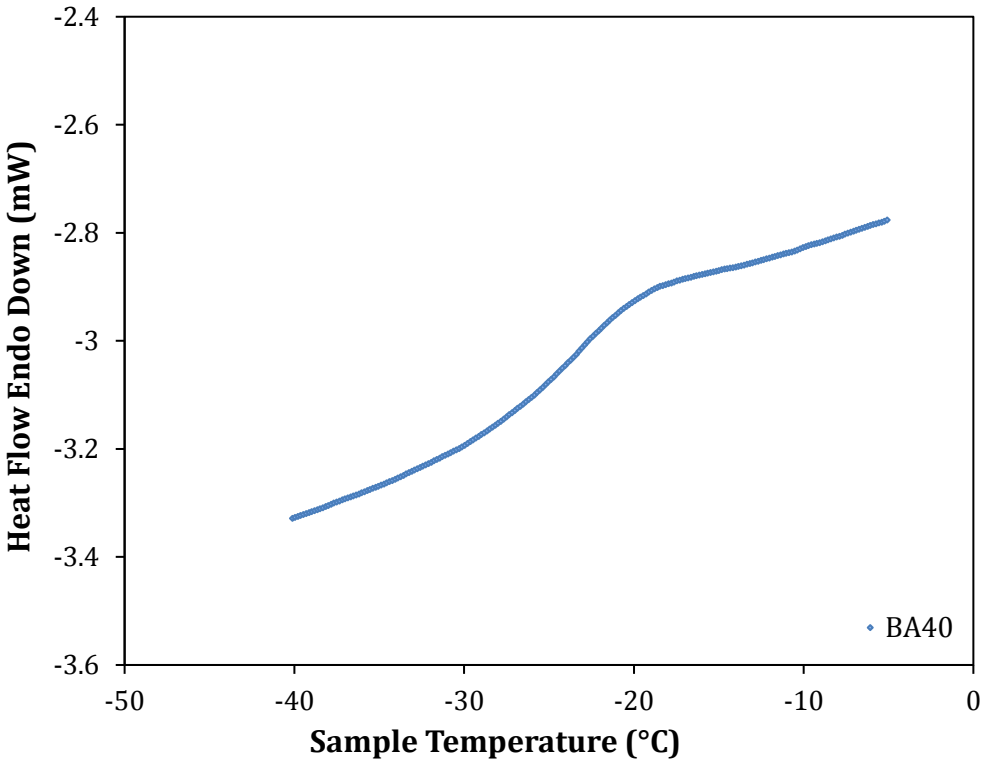

Figure 3-3: Exported Results from the Perkin Elmer Diamond DSC Depicting Heat Flow Endo Down Against Sample Temperature

There are various methods of calculating T_g but for the purposes of this report it was found at 63 % along the transition. This method, as depicted in Figure 3-4,

was used for all plots, whether the baselines were sloped or not, to produce consistent T_g data and allow for accurate comparisons.

To find the onset of the transition a line of best fit was applied to the initial baseline. A tangent line was then added to the transitioning step at the point of highest gradient. The intersection of these two lines was then deemed the onset of the transition. The same was repeated for after the transition to find the end point. The T_g was then taken at 63 % between these two points.

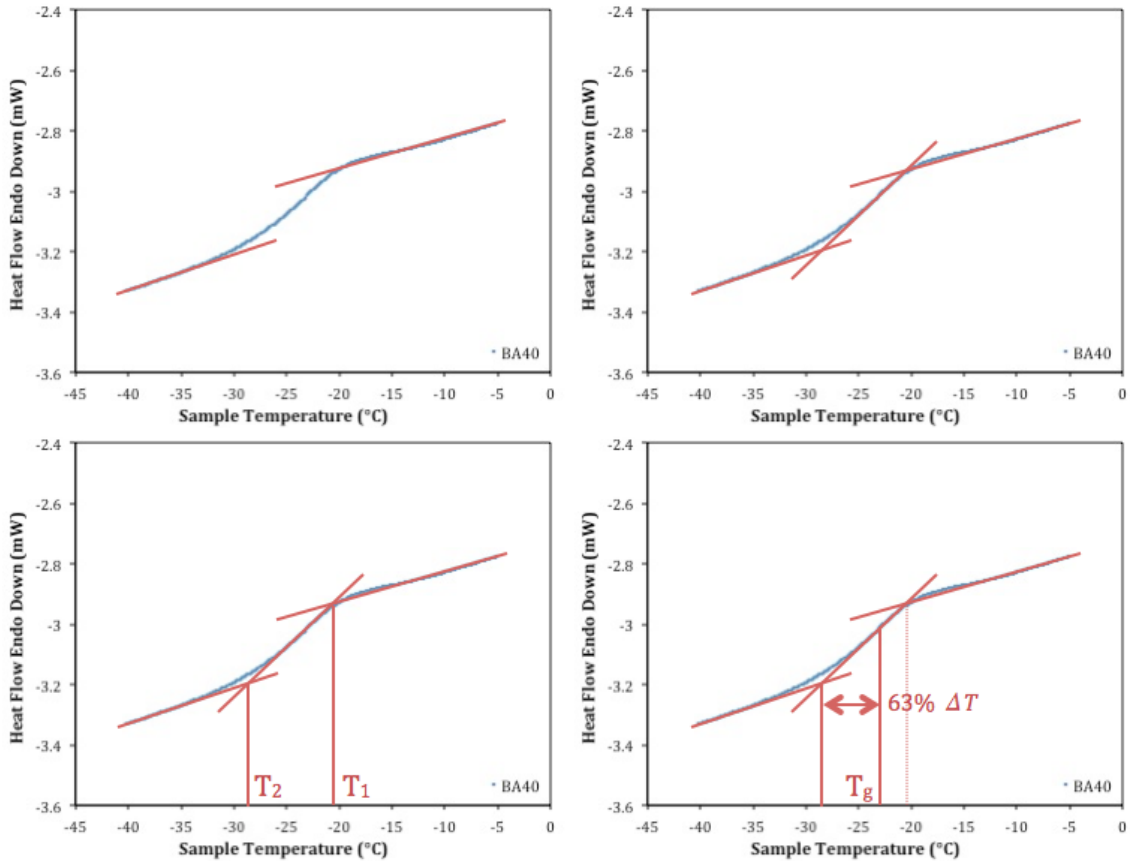

Figure 3-4: The Stepwise Procedure for Determining Glass Transition Temperature from the Perkin Elmer Diamond DSC Plots

3.3.3 Mechanical Behaviour

The Texture Analyser 500 (TA500) is an analytical apparatus from Lloyds Instruments that can perform a range of mechanical test experiments, Figure 3-5a. The generation of a standard compression curve on the TA500 involves the deflection of the samples to a pre-determined value at a rate of 1 $mm\ min^{-1}$ and

the force required to produce this deflection is recorded in a load cell attached to the moving arm. Upon reaching the pre-determined deflection, the moving arm returns to its original state at a travel rate of 1 $mm\ min^{-1}$, whilst recording the force imparted from the sample back into the load cell.

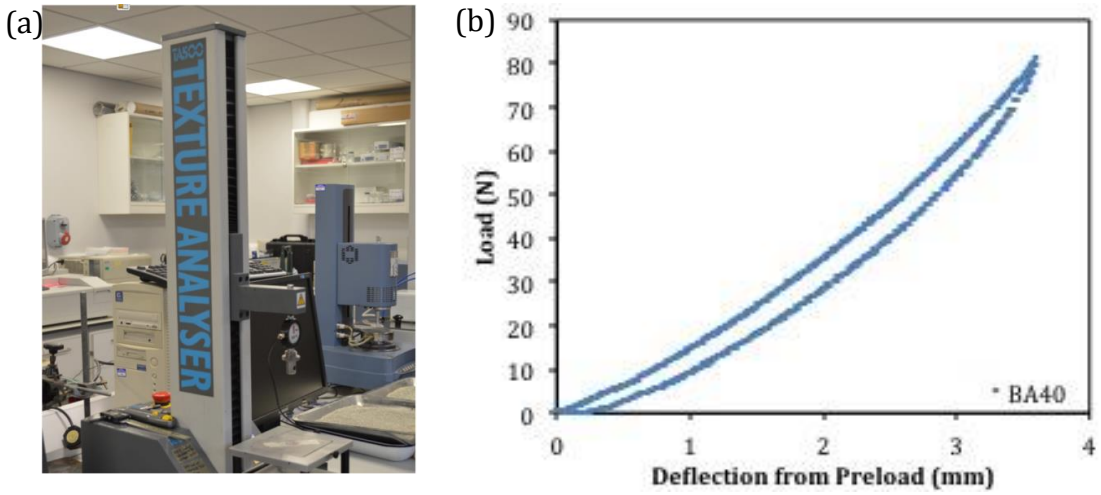

Figure 3-5: (a) A Texture Analyser 500 from Lloyds Instruments and (b) the Resultant Standard Compression Curve

A rotary drill bit was used to prep the samples into 7 mm diameter pellets. The cylindrical shape of the prepared samples limited any corner effects that may otherwise be evident in the mechanical data. A standard compression curve is shown in Figure 3-5b.

The deviation from the compression (upper) curve to the relaxation (lower) curve is referred to as the hysteresis of the sample. As explained in Chapter 2 this effect is well documented and is related to the energy dissipated through visco-elastic deformation. It can therefore be taken that the larger the hysteresis, the more energy is absorbed through internal chain movement and less is available for generating the sealing force.

To evaluate the degree of hysteresis, a 'Retention Factor' (RF) was introduced. The trapezoidal method, Equation 3-4, was used to calculate the integral of the compression curve, Figure 3-6a and the relaxation curve, Figure 3-6b. A plot of integral relaxation area vs integral compression area for different deflections generates a linear graph, Figure 3-6(c), from which a line of best fit can be taken

that passes through the origin. Equation 3-5 can then be used to find the Retention Factor.

$$Trapezoidal\ Rule = \int_a^b f(x)dx \approx (b-a)\left[\frac{f(a)+f(b)}{2}\right] \quad \text{Equation 3-4}$$

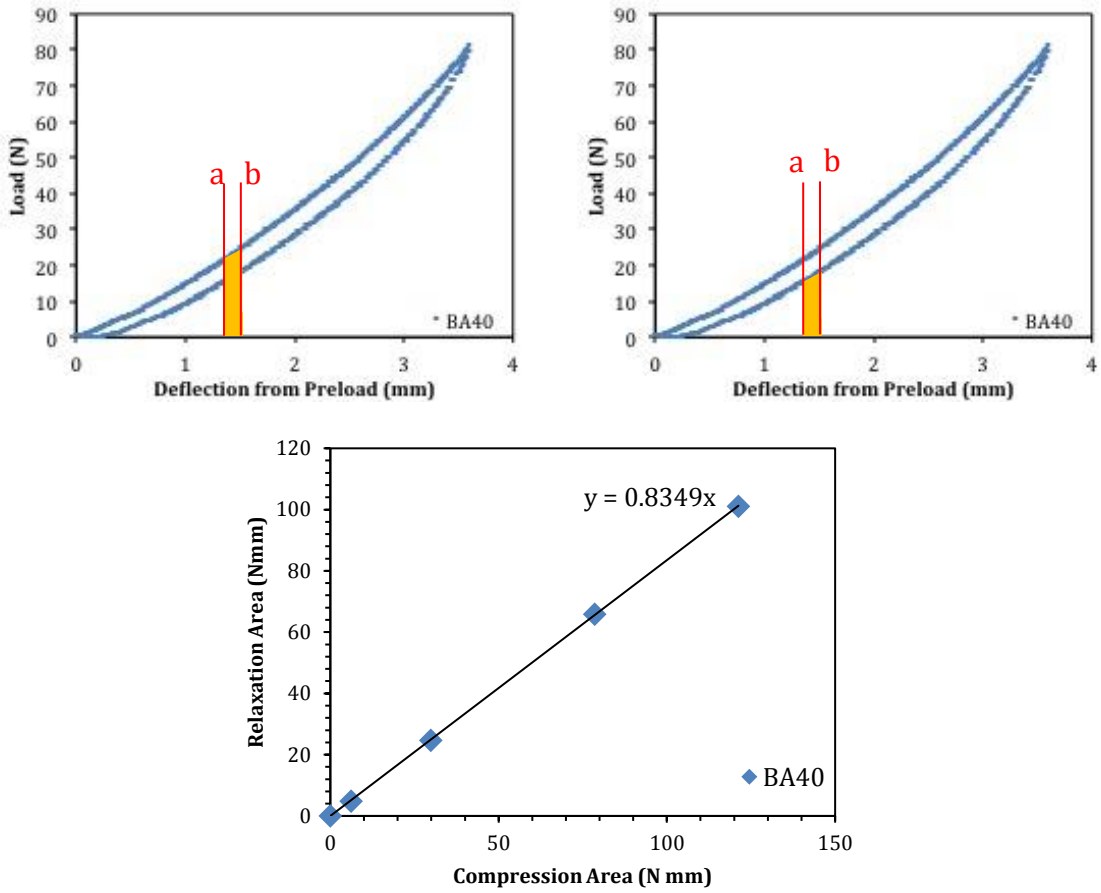

Figure 3-6: Load Against Deflection from Preload Graphs Depicting (a) The Area Under the Compression Curve, (b) The Area Under the Relaxation Curve and (c) The Linear Relation Between Compression and Relaxation

$$RF = \frac{Energy\ Returned}{Energy\ Applied} = \frac{\int Relaxation}{\int Compression} \quad \text{Equation 3-5}$$

Where RF is the dimensionless Retention Factor and is the gradient of the line of best fit plotted in Figure 3-6c.

Whilst compression set is typically regarded as the best method for determination of lifetime expectancy of an elastomer sample, calculation of RF would not only inform as to the resistance to compression of the sample, but also the restriction of

chain mobility in the elastomer bulk and thus provide more information about the mechanical properties in a shorter time frame than a compression set test.

3.3.4 CO_2 Absorption Behaviour

Hiden Isochema have manufactured an Intelligent Gravimetric Analyser (IGA) that can simultaneously measure and record the temperature, pressure and mass of a sample whilst increasing the pressure with a multitude of different gases. Accounting for buoyancy effects of increasing pressure, this allows the determination of absorption rates and loading capacities of samples in a variety of gaseous mixtures, the component under investigation in this work is exposed to a CO_2 environment and thus this was the gas that was used in the uptake experiments.

Figure 3-7: The Intelligent Gravimetric Analyser from Hiden Isochema

Using a fresh sharp blade on a Stanley Knife, approximately $50 - 100\ mg$ of each sample was cut into as small as reasonably practicable monoliths. The sample was placed in the IGA-002 mesh basket and inserted into the sample chamber and the procedure run.

Preliminary experiments were performed to study the uptake kinetics. Each sample was evacuated until equilibrium was reached and the elastomer was void

of any adsorbed gas. The chamber was then pressurised with CO_2 up to 0.5 MPa and held in an isothermal and isobaric condition for 4 $hours$. The uptake data were then fitted to the intraparticulate diffusion model, with k_{ID} representing the observable rate constant in $kg\ kg^{-1}\ s^{-1}$, and both the pseudo-first and pseudo-second order rate equations using linear regression, Table 3-2, and by non-linear regression using the SOLVER tool in Excel [142]. These rate constants were then used to calculate the half-life of the absorption mechanisms and, in the case of the PSO model, the initial adsorption rate, h_0.

Table 3-1: The Calculations for Half-life and Initial Half-life for the Pseudo-First Order and Pseudo-Second Order Rate Equations

Rate Equation	Calculation	
PFO	$t_{1/2} = \frac{\ln(2)}{k_1}$	Equation 3-6
PSO	$t_{1/2} = \frac{1}{k_2 q_e}$	Equation 3-7
PSO	$h_0 = k_2 {q_e}^2$	Equation 3-8

Where $t_{1/2}$ is the half-life in s, and h_0 is the initial adsorption rate in $kg\ kg^{-1}\ s^{-1}$.

For all subsequent samples the procedural set up for the IGA-002 was as follows:

1. Evacuate chamber for 90 min
2. Raise internal pressure by 0.1 MPa and hold for 50 min
3. Repeat until a pressure of 1 MPa has been held for 50 min
4. Reduce pressure to a vacuum and hold for 65 min

The software package that is attached to the IGA-002 allows for buoyancy discrepancies to be removed through additional calculation.

Fitting of the Thermodynamic Isotherm Models

An increase in weight was assumed to be the result of CO_2 absorption into the bulk of the elastomer and thus could be expressed in terms of moles of CO_2 in elastomer

at equilibrium against moles of CO_2 in gas, permitting the fitting of the data against known isotherm models.

The isotherm models are introduced in Chapter 2 and Table 3-2 highlights the linear regression forms of these models as well as the slopes and intercepts of the relevant plots for calculation of the unknowns. As well as the linear regression forms, the data were fitted by non-linear regression using SOLVER [142]. To assess the quality of the fit the five-error analysis procedure as previously used by *Ho, Porter and McKay* [143] was used to calculate the Sum of the Normalised Errors (SNE) and identify the isotherm model that best fits the experimental data. The equations used in the five-error analysis are:

- The Sum of the Error Squares (ERRSQ)

$$\sum_{i=1}^{p}\left(q_{e,meas}-q_{e,calc}\right)_i^2 \qquad \text{Equation 3-9}$$

- The Composite Fractional Error (HYBRD)

$$\sum_{i=1}^{p}\left[\frac{\left(q_{e,meas}-q_{e,calc}\right)^2}{q_{e,meas}}\right]_i \qquad \text{Equation 3-10}$$

- A Derivative of Marquardts Percent Standard Deviation (MPSD) [144]

$$\sum_{i=1}^{p}\left(\frac{q_{e,meas}-q_{e,calc}}{q_{e,meas}}\right)_i^2 \qquad \text{Equation 3-11}$$

- The Average Relative Error (ARE) [145]

$$\sum_{i=1}^{p}\left|\frac{q_{e,meas}-q_{e,calc}}{q_{e,meas}}\right|_i \qquad \text{Equation 3-12}$$

- The Sum of the Absolute Errors (EABS)

$$\sum_{i=1}^{p} \left| q_{e,meas} - q_{e,calc} \right|_i \qquad \text{Equation 3-13}$$

The cross analysis of the error equations is carried out as follows:

1. Identify the isotherm coefficients that reduce the value of the first error equation to a minimum
2. Identify the value of the other error equations with these first isotherm coefficients
3. Repeat for all other error equations
4. Normalise the values of the error equations via a ratio with the maximum value obtained for an error equation with the same isotherm coefficients
5. Sum the normalised values of the error equations for an overall Sum of the Normalised Errors (SNE) out of a maximum of 5

3.3.1 Handling Error

For the swelling behaviour the 'as received' samples were run in triplicate and an average taken. The standard deviation was used to calculate a percentage relative error. This allowed identification of the error boundaries in all further experiments.

Calculation of T_g has a high chance for human error due to plotting of tangential lines and interpretation of intersection points. These experiments were run in triplicate to identify the conformity of multiple experiments. As with the swelling behaviour an average was taken and the standard deviation used to calculate the percentage relative error, which was used for all further experiments.

The initial compression curve of the mechanical data was fitted to simple mathematical models to identify coefficients that could be used to determine error. Fitting of a linear model to the RF plots allowed calculation of a standard error value, from which a percentage relative error was found and used for all further experiments.

Following calculation of the kinetic model parameters the linear regression forms were plotted with both the experimental data and the model. Equation 3-14, Equation 3-15 and Equation 3-16 were used to calculate the error in the slope and the intercept respectively, [146]. Using the maximum, minimum and average values for the slope and intercept to determine the maximum, minimum and average values for all parameters allows the determination of the standard error for each. From this a percentage relative error was found and used for all further experiments. The same procedure was used for the isothermal models.

$$S = \sqrt{\frac{\sum(y_i - ax_i - b)^2}{n-2}} \qquad \text{Equation 3-14}$$

$$Slope\ Error = S \times \sqrt{\frac{n}{n\sum({x_i}^2) - (\sum x_i)^2}} \qquad \text{Equation 3-15}$$

$$Intercept\ Error = S \times \sqrt{\frac{\sum({x_i}^2)}{n\sum({x_i}^2) - (\sum x_i)^2}} \qquad \text{Equation 3-16}$$

Table 3-2: The Linear Regression Forms of the Pseudo-First and Second Order Rate Equations and Henry's Law, Freundlich, Langmuir, Temkin and Dubinin-Radushkevic Isotherm Models

Fitting Model	Equation	Linear Equation	Plot	Calculation of unknowns
Intraparticulate Diffusion	$q_t = k_{ID} t^{1/2} + C$	$q_t = k_{ID} t^{1/2} + C$	$y = q_t$ $x = t^{1/2}$	$k_{ID} = slope$
Pseudo-First Order	$q_t = q_e\,(1 - e^{-k_1 t})$	$\ln(q_e - q_t) = -k_1 t + \ln(q_e)$	$y = \ln(q_e - q_t)$ $x = t$	$k_1 = -slope$
Pseudo-Second Order	$q_t = \frac{k_2 {q_e}^2 t}{1 + k_2 q_e t}$	$\frac{t}{q_t} = \left(\frac{1}{q_e}\right) t + \left(\frac{1}{k_2 {q_e}^2}\right)$	$y = \frac{t}{q_t}$ $x = t$	$q_e = \left(\frac{1}{slope}\right)$ $k_2 = \left(\frac{1}{intercept \times {q_e}^2}\right)$
Henry's Law	$q_e = K_H P$	$q_e = K_H P$	$y = q_e$ $x = P$	$K_H = slope$
Freundlich	$q_e = a_F {C_e}^{1/n_F}$	$\ln(q_e) = \left(\frac{1}{n_F}\right)\ln(C_e) + \ln(a_F)$	$y = \ln(q_e)$ $x = \ln(C_e)$	$n_F = \left(\frac{1}{slope}\right)$ $a_F = \exp(intercept)$
Langmuir	$q_e = \frac{q_m a_L C_e}{1 + a_L C_e}$	$\frac{C_e}{q_e} = \left(\frac{1}{q_m}\right) C_e + \frac{1}{a_L q_m}$	$y = \frac{C_e}{q_e}$ $x = C_e$	$q_m = \left(\frac{1}{slope}\right)$ $a_L = \left(\frac{1}{q_m \times intercept}\right)$
Temkin	$q_e = \frac{RT}{b_T}\ln(a_T C_e)$	$q_e = \left(\frac{RT}{b_T}\right)\ln C_e + \left(\frac{RT}{b_T}\right)\ln a_T$	$y = q_e$ $x = \ln(C_e)$	$b_T = \left(\frac{RT}{slope}\right)$ $a_T = \exp\left(\frac{b_T \times intercept}{RT}\right)$
Dubin-Radushkevic	$q_e = q_D \exp\left\{-B_D\left[RT\ln\left(1 + \frac{1}{C_e}\right)\right]^2\right\}$	$\ln(q_e) = (-B_D)\left[RT\ln\left(1 + \frac{1}{C_e}\right)\right]^2 + \ln(q_D)$	$y = \ln(q_e)$ $x = \left[RT\ln\left(1 + \frac{1}{C_e}\right)\right]^2$	$B_D = -slope$ $q_D = \exp(intercept)$

4 DETERMINATION OF PHYSICAL AND MECHANICAL PROPERTIES

4.1 INTRODUCTION

Chapter 3 reviewed the samples of interest and the procedural methodology for investigating their characteristic properties. This chapter identifies the physical and spectroscopic behaviour of the industrial seal in comparison with three commercial rubber samples, followed by a discussion on how the different aspects of a materials design can be affected by different degradation mechanisms. To assist in this, key parameters such as $\Delta_{M\%}$ and $\Delta_{V\%}$ following exposure to toluene, T_g, RF, K, k_1 and k_2 values have been calculated and cross-compared.

A pre-service industrial seal was donated by EDF Energy for this work which has been manufactured from a sulphur-cured nitrile elastomer incorporating brass wire and glass cloth with carbon black filler [E5]. To allow comparison of the seal's behaviour with other samples manufactured from the same base elastomer three commercial samples of NBR at grades BA40, BA50 and BA60 have been purchased from *Whitby and Chandler Ltd.* [140]. The BA grades here represent the calculated hardness of the samples during their Quality Assurance testing.

4.2 EXPERIMENTAL

4.2.1 OPTICAL MICROSCOPY

A Hitachi TM3030 desktop SEM was used at low vacuum to inspect the surface of the samples. All images were taken in SEI mode to provide topographical information.

4.2.2 Raman and Infrared Spectroscopy

IR Spectroscopy was carried out on a Perkin Elmer Frontier FTIR with a diamond ATR attachment. The spectroscopic analysis was run with a wavelength between 4000 and 500 cm^{-1}, at a resolution of 4 $scans\ cm^{-1}$ and an accumulation of 4 $scans$, reducing the noise to acceptable levels. To ensure a fair representation of the bulk of the elastomer approximately 4 mm was removed from the surface of each sample and the runs were performed in triplicate in different sections.

Raman Spectroscopy was carried out using an invia Raman Microscope, however the runs were unsuccessful; the literature [96] suggests this is due to the presence of carbon black affecting the acquisition of spectroscopic data. As discussed by *Turrell and Corset* [147] a 'burn-out time' was attempted. Unfortunately no real practical advantage was found under the conditions tested thus Raman Spectroscopy was not carried out further.

4.2.3 Swelling Behaviour

An experiment for assessing the change in crosslink density was adapted from ASTM D6814 [141]. The samples were placed in a test tube with approximately 40 cm^3 of toluene and allowed to come to equilibrium. $\Delta_{M\%}$ and $\Delta_{V\%}$ were calculated using Equations 3-2 and 3-3 respectively.

The samples were run in triplicate and the average was taken with one standard deviation of error. It was noted during experiments that the mass dropped quickly whilst samples were weighed due to evaporation of the absorbed toluene. To minimise the effects of the evaporative loss of toluene to a low as is reasonably practicable level, the mass was recorded at the first instance of settling.

4.2.4 Glass Transition Temperature

DSC was used to identify T_g. Between 4 and 5 mg of each sample was placed in an aluminium pan with a lid crimped on top. It was placed in the DSC where the heat required to induce a temperature increase can be plotted against the temperature. To reduce the potential for error in the calculation of T_g from the line of best fit for

baselines and the steepest section of the transition, and the intersection point of these lines, all three commercial samples and the industrial seal were run in triplicate.

4.2.5 Mechanical Behaviour

Samples were cut into 7 mm diameter pellets using a rotary drill. During sample preparation it was noted that the brass wires within the industrial seal were orientated in the same direction as the compression force acted with a significant portion protruding through the upper face of the cylindrical pellet. Any protruding wires were removed using tweezers. The pellet for testing was placed under the compression arm of the TA500. A compression and relaxation programme was initialised which compressed the sample at 1 $mm\ min^{-1}$ to a deflection after preload of 1 mm, and subsequently relaxed at a rate of 1 $mm\ min^{-1}$. This was repeated with fresh sample for 2, 3, 4 and 5 mm deflections.

To calculate the experimental error associated with mechanical testing compression curves for all four plots were fitted to various models. However, none provided satisfactory results and displayed considerable error. This was attributed to the poor fit of the model to the experimental data. It was deemed that experimental error was due to the mechanical compliance of the TA500 rather than sample preparation. A visual assessment of compliance-adjusted experimental data allowed the rejection of non-conforming sets.

4.2.6 CO_2 Absorption Behaviour

A sharp fresh blade on a Stanley Knife was used to cut $50 - 100\ mg$ of sample into small monoliths, approximately 1 mm^3. Each sample underwent preliminary tests involving placement into a Hiden Isochema IGA-002 that removed any absorbed gases and raised the pressure of the chamber to 0.5 MPa CO_2. The samples were left for 4 $hours$ to ensure equilibrium. These preliminary tests allowed the identification of the best kinetic fit to the data for further analysis. Samples were then placed in the IGA and their increase in weight recorded following isothermal

0.1 MPa pressure increments between 0.1 and 1 MPa to collect data for thermodynamic analysis.

4.3 RESULTS

Visual inspection of BA40, BA50 and BA60 indicates little comparable difference, Figure 4-1. Manual handling identified BA40 as the most flaccid with increasing rigidity in BA50 followed by BA60, as expected. The industrial seal was considerably more rigid and had visible brass wire, surface dimples and internal fibres. Figure 4-2 shows the cross-section of the industrial seal, in which brass wires and fibres of glass cloth can be seen.

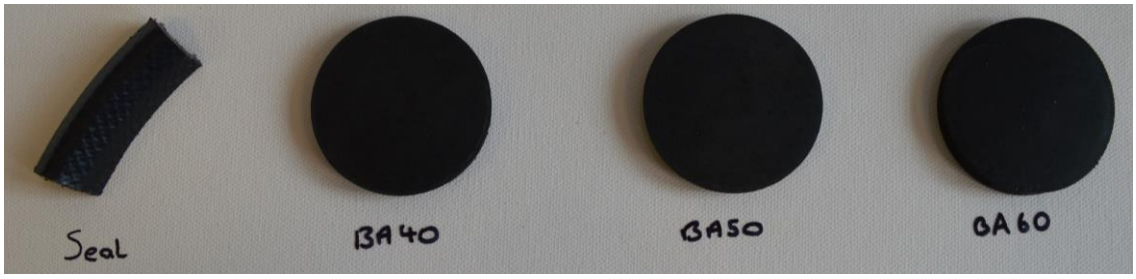

Figure 4-1: A Photograph of Samples BA40, BA50, BA60 and the Industrial Seal Depicting the Similarities Found During Visual Inspection

Figure 4-2: A Photograph of the Industrial Seal Cross-Section

4.3.1 Scanning Electron Microscopy

Surface imperfections found were due to the protrusion of brass wires, Figure 4-3a. The geometry of the different contrasting portions in Figure 4-3b highlights the different inclusions in the structure. Figure 4-3c depicts how these strengthening fibres cause defects by providing travelling paths along which cracks can propagate. In Figure 4-3d some of the material is stretched, revealing the elasticity of the sample.

It is evident from these images that inclusions used to increase the strength may inherently contribute to seal failure. Although inclusions may appear to be well distributed through the polymer, clustering of these components can be found in some locations, Figure 4-3b.

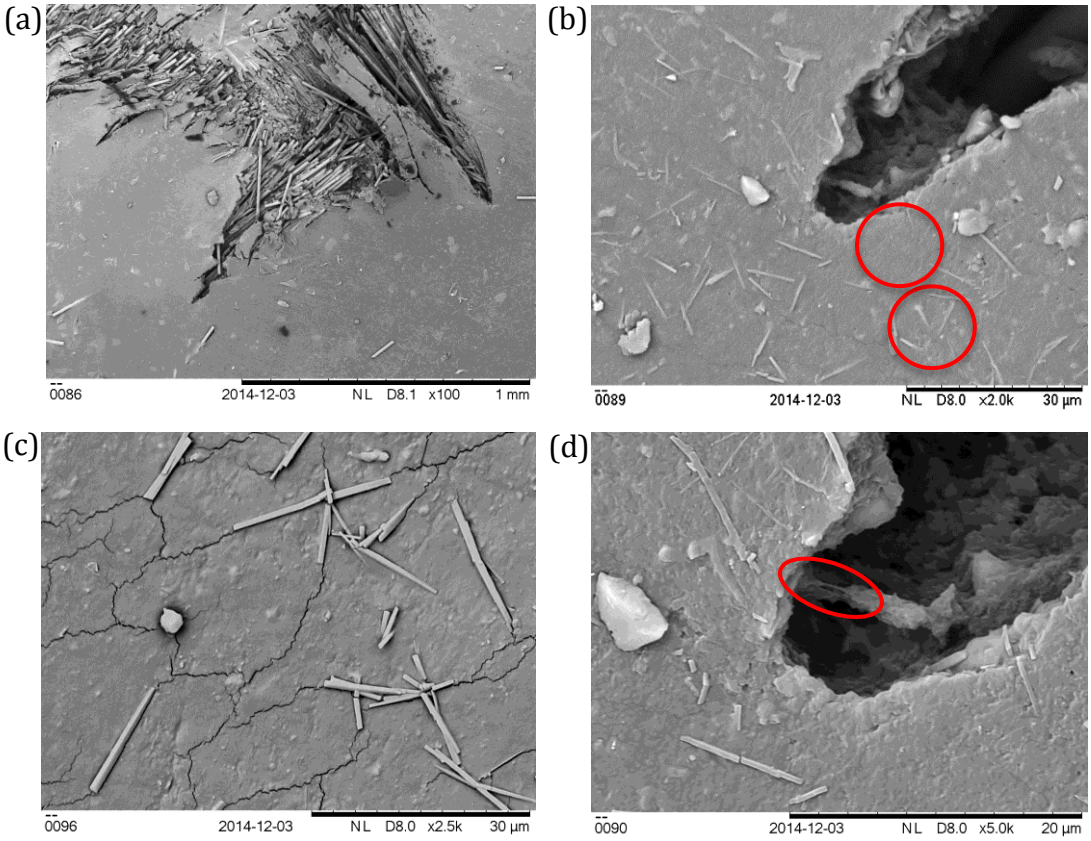

Figure 4-3: SEM Images of the Industrial Seal at (a) x100, (b) x2000, (c) x2500 and (d) x5000 Magnification Taken under Low-Vacuum Conditions and in Backscattering Mode

4.3.2 Infra-Red and Raman Spectroscopy

FTIR Spectroscopy of the industrial seal proved problematic. The clearer spectra of the commercial samples suggest that it is not the presence of carbon black causing these problems but potentially the presence of the brass wire.

The spectra were split into three separate sections to ease interpretation; 3000 to 2200 cm^{-1}, 1770 to 1150 cm^{-1} and 1150 to 730 cm^{-1}. In the 3000 to 2200 cm^{-1} range the peaks commonly seen in polymers that correspond to methylene stretches and vibrations are visible and highlighted in Figure 4-4. The additional peak at 2235 cm^{-1} was attributable to stretching of C≡N pendant in ACN.

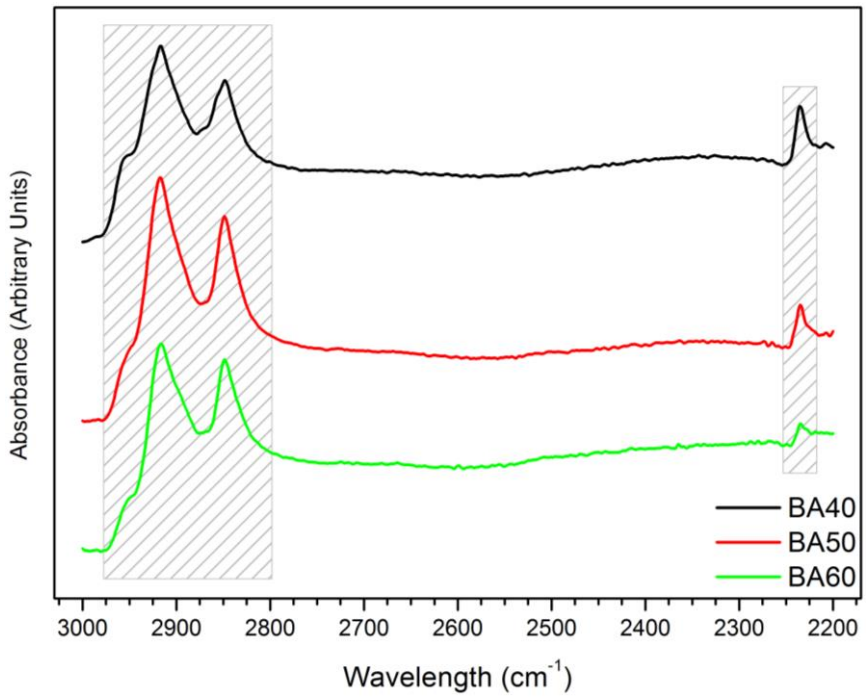

Figure 4-4: The ATR-FTIR Spectra for all Three Commercial Samples in their as Received Condition Measured Between 3000 and 2200 cm^{-1}

The next range investigated was between 1770 and 1150 cm^{-1}. The first peak in BA40 at 1720 cm^{-1} was shifted to 1736 cm^{-1} in BA50 and BA60 and is typically attributed to carbonyl stretching of oxygen containing functional groups, such as C=O. The next clean peak seen was at 1538 cm^{-1}, and is associated with deformation vibrations of the N-H bond. There was evidence of some very weak peaks before this one, which are readily linked to the double bonds in the

monomers. The broad peak range between 1436 and 1376 cm^{-1} have been shown to be due to the bending vibration of methylene groups, typically linked to BDN units, that have been deformed due to the presence of C=O groups. BA40 showed a large absorbance at 1267 cm^{-1}, which was absent in other samples. *Hassan, Aly and El-Ghandour* [45] attributed this to the stretch of the C-N bond. The spectra are shown in Figure 4-5 and their peak wavelengths, along with the associated bonds are repeated in Table 4-2.

Table 4-1:The Peaks seen in the ATR-FTIR Spectra for all Three Commercial Samples Measured Between 3000 and 2200 cm^{-1} and their Associated Bonds

Wavelength (cm^{-1})	Associated Bond	Reference
2956	-CH stretching vibration of methylene groups	[44]
2918	assymetric vibration of CH_2 in methylene (BDN units)	[31, 44, 84]
2848	symmetric vibration of CH_2 in methylene (ACN units)	[44, 84, 96, 148, 46]
2235	-C≡N Nitrile	[149, 94, 84, 62, 96, 148]

Table 4-2: The Peaks seen in the ATR-FTIR Spectra for all Three Commercial Samples Measured Between 1770 and 1150 cm^{-1} and their Associated Bonds

Wavelength (cm^{-1})	Associated Bond	Reference
1736 and 1720	carbonyl stretching of oxygen containing functional groups – linked to oxidation and crosslinks	[96, 45, 150, 151, 148]
1538	deformation vibration of N-H	[45]
1436-1376	bending vibration of CH_2 deformation due to C=O	[152, 153, 84, 62, 148, 46]
1267	-C-N stretch	[45]

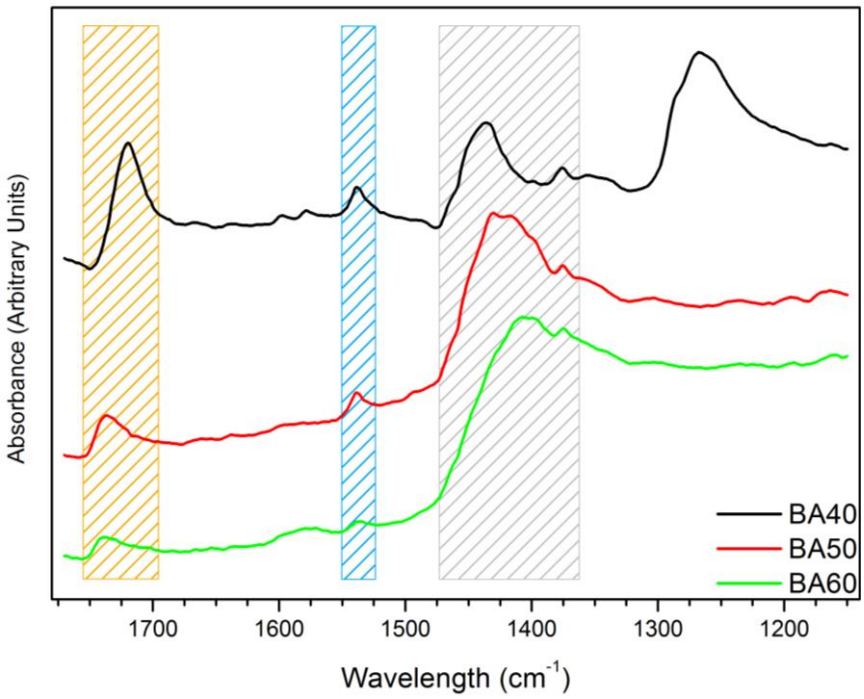

Figure 4-5: The ATR-FTIR Spectra for all Three Commercial Samples Measured Between 1770 and 1150 cm^{-1}

In the final range, 1150 to 730 cm^{-1}, BA40 showed a peak at both 1117 and 1068 cm^{-1} that were not present in the other two commercial samples. There was then a large peak at 1015 cm^{-1} for all three commercial samples and a shoulder at 1036 cm^{-1}. These peaks were not present in the spectra of previously reported NBR and it proved difficult to find a realistic match to a particular bond. The next, most prominent peak in all the spectra was at 964 cm^{-1} with a shoulder at 918 cm^{-1} and is well documented as being the C=C transvinylidene bond in the BDN unit.

Table 4-3: The Peaks seen in the ATR-FTIR Spectra for all Three Commercial Samples Measured Between 1150 and 730 cm^{-1} and their Associated Bonds

Wavelength (cm^{-1})	Associated Bond	Reference
1117-1015	inclusions and additives	[154, 148]
964 and 918	C=C transvinylidene – linked to BDN content	[155, 84, 62, 152, 45, 46]
872 and 870	artefact of N containing functional group	[156, 157]
741	cis configuration of C=C in BDN	

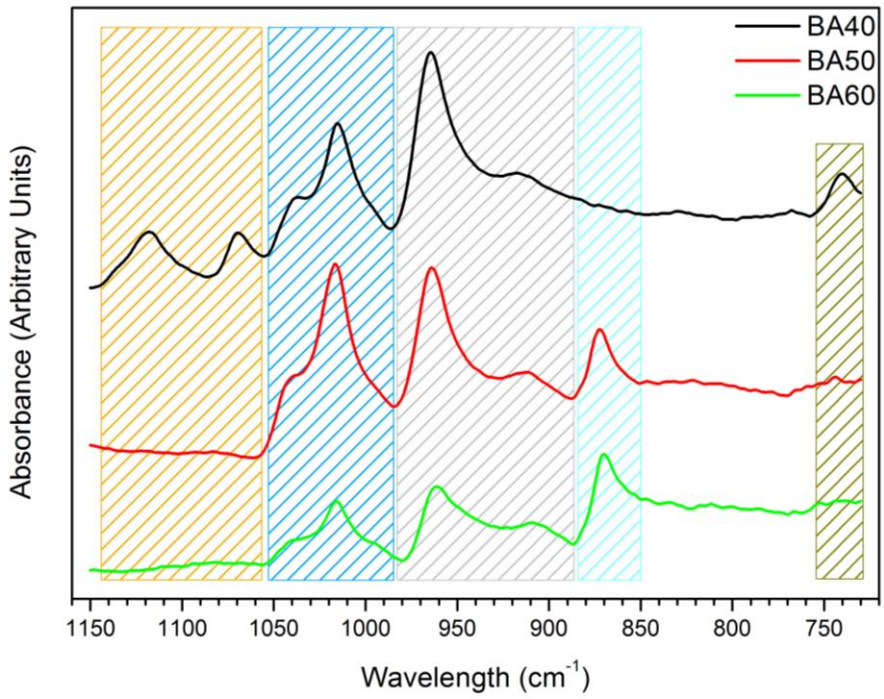

Figure 4-6: The ATR-FTIR Spectra for all Three Commercial Samples Measured Between 1150 and 730 cm^{-1}

A sharp peak was seen at 872 cm^{-1} for BA50 and at 870 cm^{-1} for BA60 with an absence of peak in BA40, possibly due to a nitrogen containing functional group. The peak at 741 cm^{-1}, strongest in BA40, weaker in BA50 and completely absent in BA60, has been attributed to the cis configuration of the double bond in BDN.

4.3.3 Swelling behaviour

The results for $\Delta_{V\%}$ were more erratic than those for $\Delta_{M\%}$ with a maximum percentage error of 18% compared to 3.7% . This was due to increased compressibility after exposure to toluene for 72 $hours$, increasing the difficulty in measuring dimensions with a calliper without compressing the sample.

Table 4-4: The Resultant $\Delta_{M\%}$ and $\Delta_{V\%}$ Values from the Swelling Tests Carried Out on the 'As Received' Samples

Sample	$\Delta_{M\%}$	Relative Error (%)	$\Delta_{V\%}$	Relative Error (%)
BA40	89.1 ± 0.3	0.35	90 ± 12	14
BA50	135 ± 3	2.3	146 ± 3	1.7
BA60	108 ± 2	2.2	140 ± 10	7.7
Industrial Seal	46 ± 2	3.7	67 ± 12	18

4.3.4 GLASS TRANSITION TEMPERATURE

Although every effort was made to remove the presence of glass cloth and brass wire from the industrial seal, partial contamination was unavoidable, as evident in the erratic DSC plots, Figure 4-7.

The increased steepness of the third run caused the removal of this data set from further analysis. The average was calculated and the error taken from one standard deviation. T_g appeared to decrease with BA rating apart from the previously mentioned erratic behaviour of the industrial seal. The largest percentage error seen was 2.7 %.

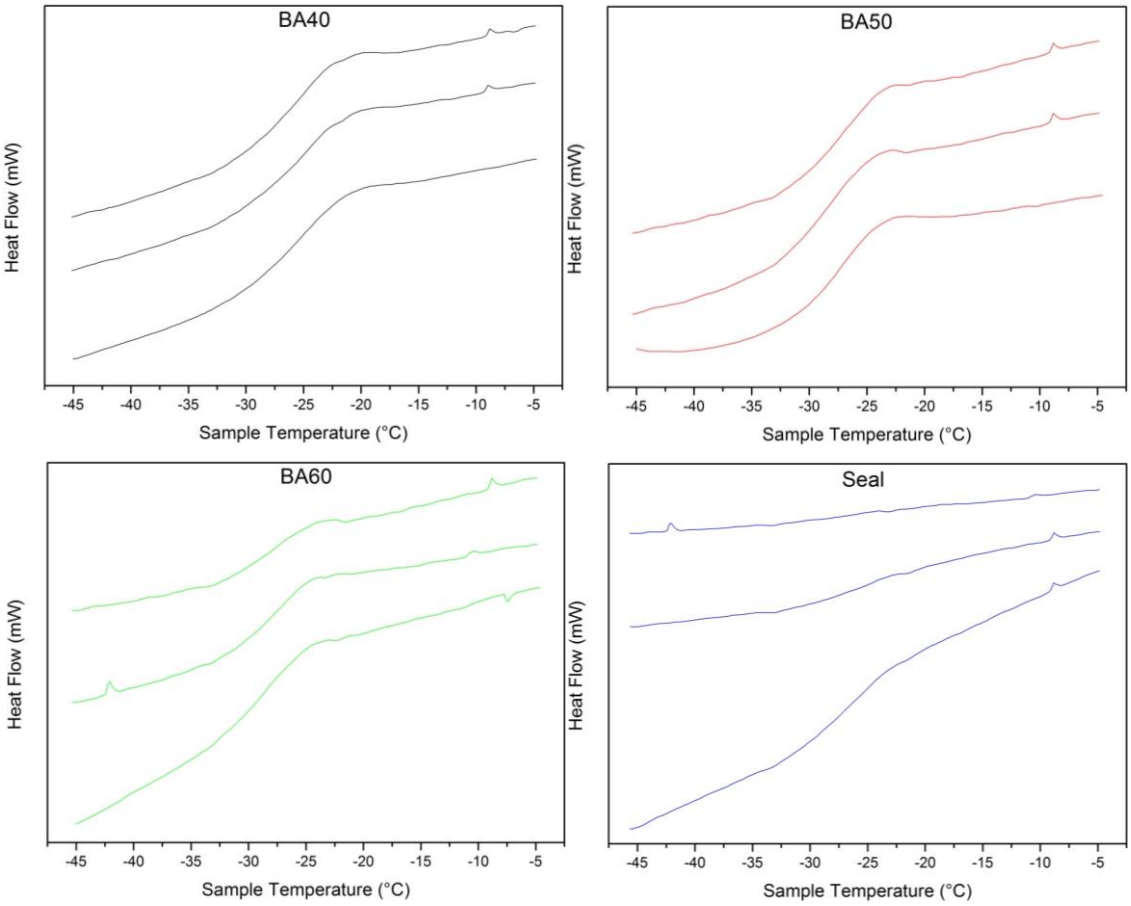

Figure 4-7: The DSC Plots as Run in Triplicate for all Three Commercial Samples and the Industrial Seal Recorded on a Perkin Elmer Diamond DSC at a Ramp Rate of 10°C min^{-1} Between -45 and -5 °C at Standard Atmospheric Conditions

Table 4-5: The Calculated Glass Transition Temperatures for all Three Commercial samples at Standaard Atmospheric Conditions

Sample	T_g (°C)	Relative Error (%)
BA40	-25.3 ± 0.3	1.4
BA50	-27.8 ± 0.4	1.5
BA60	-28.2 ± 0.4	1.4
Industrial Seal	-24.9 ± 0.7	2.7

4.3.5 Mechanical Behaviour

The 5 *mm* load-deflection curve for BA40 did not follow the same trend as the other curves and as such has been omitted from the results. However, all other load-deflection curves for the commercial samples showed very little deviation and as such all data were retained for the calculation of RF. The trapezoidal method was used to calculate the integral of the compression and relaxation portions of the load-deflection plot and the procedure outlined in Chapter 3 was followed to determine RF.

The ability to induce a 3 *mm* deflection in the commercial samples required 60, 70 and 100 *N* for BA40, BA50 and BA60 respectively. Also, the increasing disparity between the compression and relaxation curves for each load-deflection plot indicated an increasing hysteresis in the samples from BA40 to BA60. The load-deflection curves for the industrial seal showed relatively inconsistent data, Figure 4-8. The disparate load-deflection curves are considered to be due to the amount of internal brass wires that remained in the sample, as these are not necessarily evenly distributed throughout the structure of the seal and the amount of required load to induce a deflection was combating the longitudinal stress of the brass wire. The accuracy of RF for the industrial seal was therefore called into question.

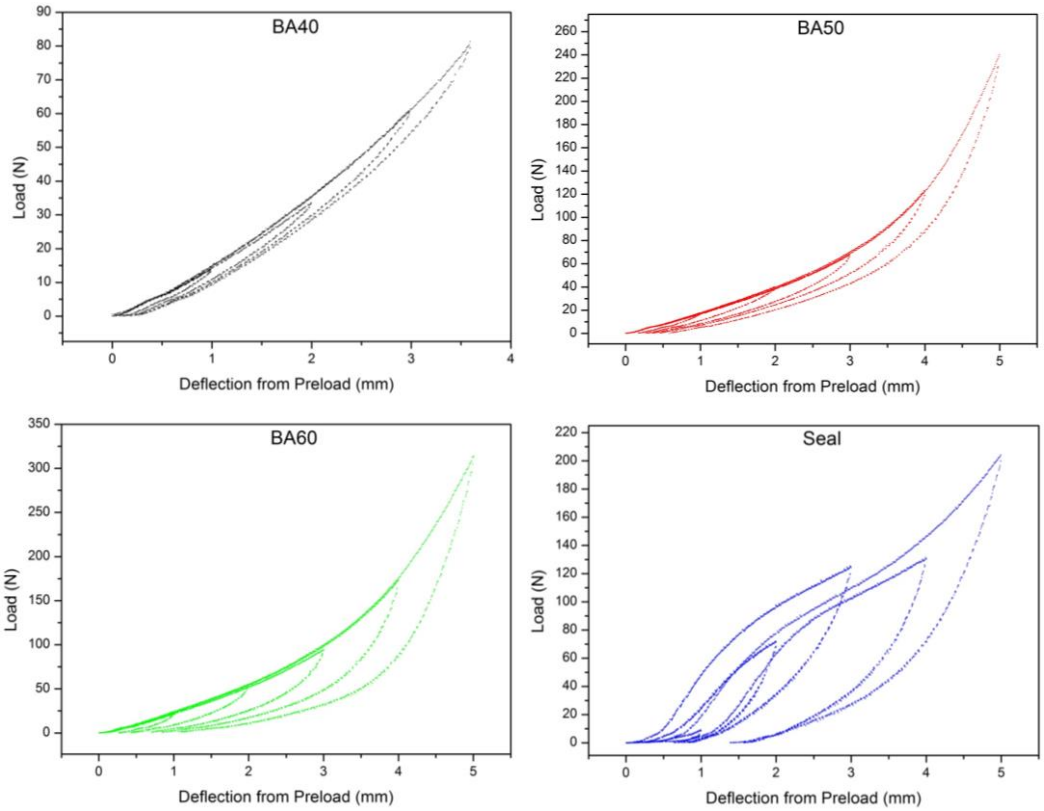

Figure 4-8: The Load-Deflection Data for all Three Commercial Samples and the Industrial Seal Measured on the TA500 under Standard Atmospheric Conditions

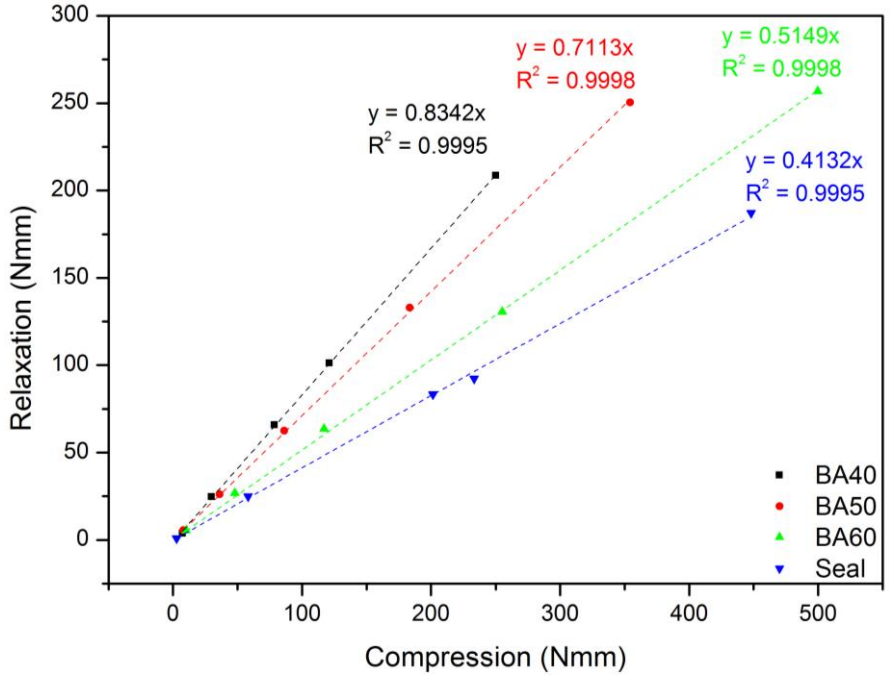

Figure 4-9: The Calculated Retention Factors for all Three Commercial Samples and the Industrial Seal

The relaxation vs compression data suggested that the BA40 had the highest RF, followed by BA50 with BA60 having the lowest. Although the load-deflection plots for the industrial seal appeared to be inconsistent, the relaxation vs compression experimental data did conform to a realistic principle.

Table 4-6: The Resultant Retention Factors Calculated from the Load-Deflection Curves Carried Out on the 'As Received' Samples

Sample	Retention Factors	Relative Error (%)
BA40	0.834 ± 0.009	1.1
BA50	0.711 ± 0.004	0.56
BA60	0.515 ± 0.004	0.68
Industrial Seal	0.413 ± 0.004	1.0

4.3.6 CO_2 Absorption Behaviour

4.3.6.1 Preliminary Experiments

Assuming an increase in mass correlated to the absorption of CO_2 BA40 exhibited the highest uptake with a q_e of approximately $11.7x10^{-3}\ kg\ kg^{-1}$ followed by BA50, $9.91x10^{-3}\ kg\ kg^{-1}$ and BA60, $7.65x10^{-3}\ kg\ kg^{-1}$. The industrial seal exhibited anomalous behaviour undergoing an initial increase in weight with ramping CO_2 pressure but at the set pressure of 0.5 MPa the weight steadily decreased over time. This made it impossible to carry out kinetic uptake calculations and thus was removed from further analysis.

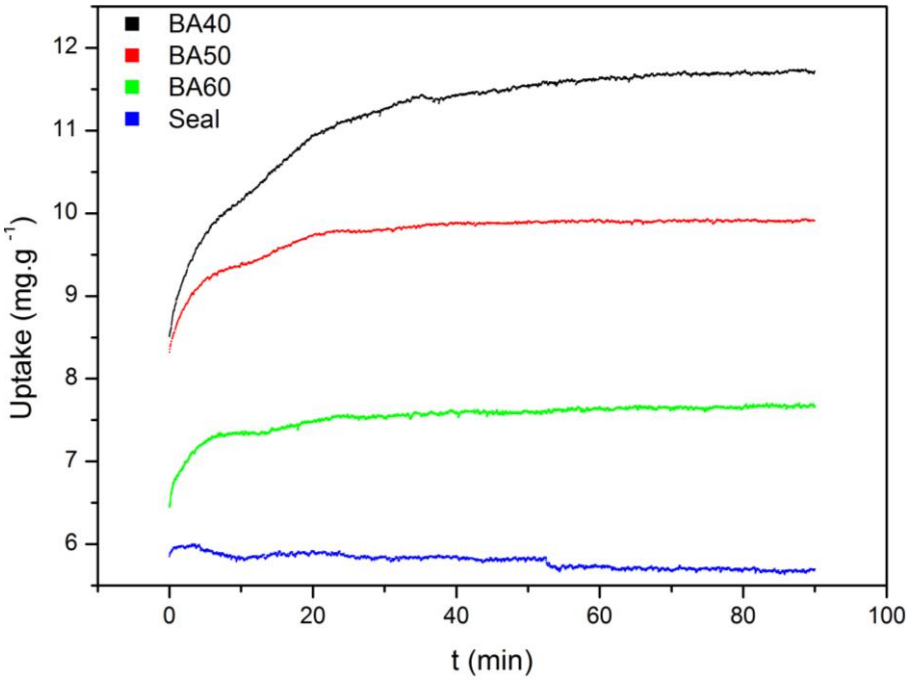

Figure 4-10: The Uptake Data for All Three Commercial Samples and the Industrial Seal in 0.5 MPa CO_2 at 20 °C

4.3.6.2 Absorption Kinetics

The time lag appeared to decrease with increasing BA rating, however significant error was found in these values.

Table 4-7: The Calculated Time-Lag Coefficients for All Three Commercial Samples in 0.5 MPa CO_2 at 20 °C

Sample	Time Lag (s)	Relative Error (%)
BA40	4.7 ± 0.1	3.05
BA50	2.8 ± 0.3	9.72
BA60	0.08 ± 0.04	56.9

Replotting with dimensionalised uptake provides the linear regression plot for intraparticulate diffusion. However, the data only shows a straight line in the initial portion of the graph and therefore the observed rate constant, k_{ID}, has only been found up to a time of 6 minutes.

Table 4-8: The Observed Rate Constant for the Intraparticulate Diffusion Model for All Three Commercial Samples in 0.5 MPa CO_2 at 20 °C

Sample	$k_{ID}(kg\ kg^{-1}\ s^{-1})$	Relative Error (%)	Intercept
BA40	10.4 ± 0.03	0.32	8.33 ± 0.0035
BA50	7.12 ± 0.05	0.74	8.24 ± 0.0055
BA60	5.9 ± 0.03	0.55	6.46 ± 0.0034

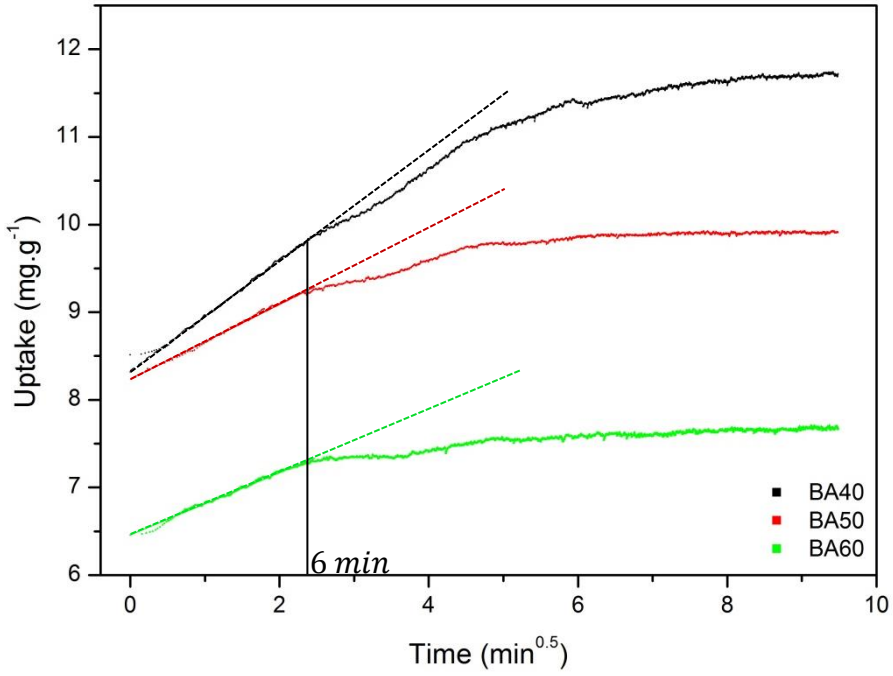

Figure 4-11: The Intraparticulate Diffusion Model Fit for All Three Commercial Samples in 0.5 MPa CO_2 at 20 °C

Linear regression of the Pseudo-First Order (PFO) model depicted an almost linear trend in the earlier portions of the graph, with increasing disparity over time and the linear regression plots for the Pseudo-Second Order (PSO) model showed a linear trend at later times. The non-linear least squares method using SOLVER allowed fitting of the PFO and PSO rate equations to the uptake data and the five-error analysis procedure [158] was used to calculate SNE for comparison, Figure 4-12.

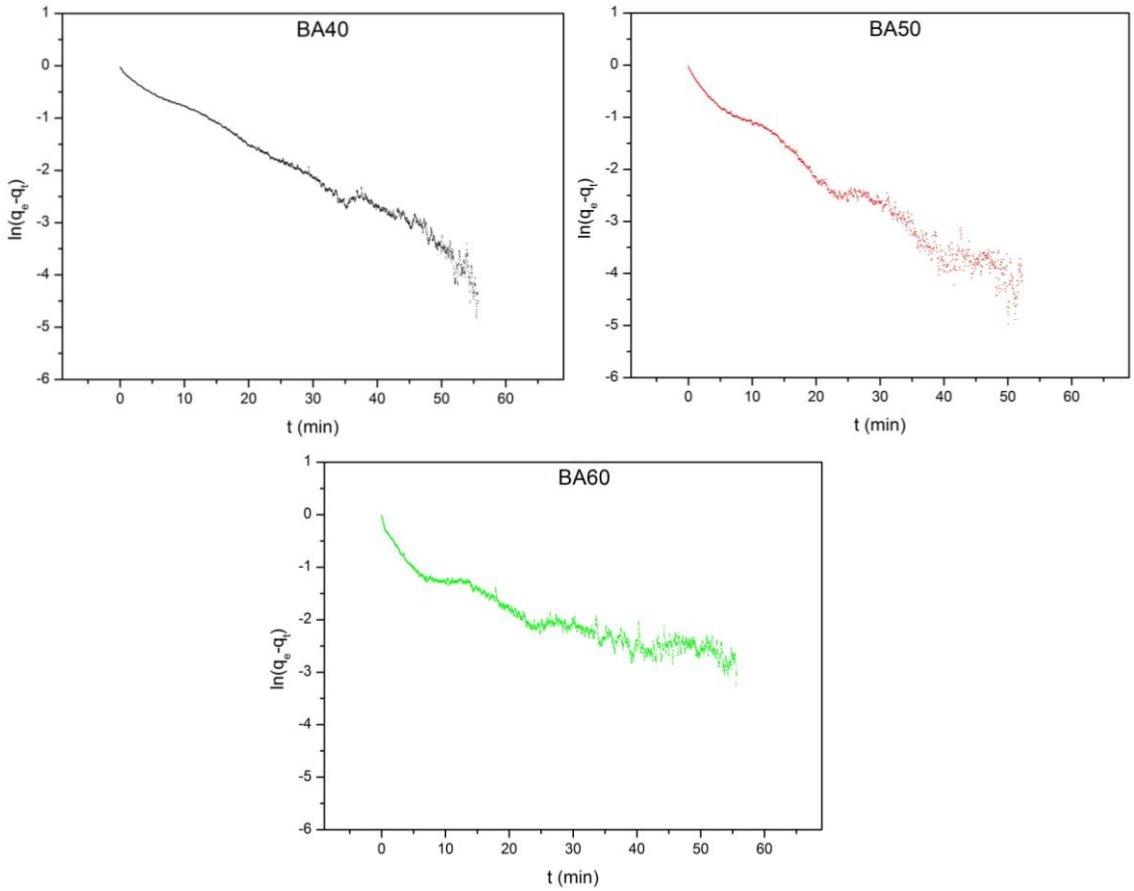

Figure 4-12: The Pseudo-First Order Linear Regression Plots for All Three Commercial Samples in 0.5 MPa CO_2 at 20 °C

Table 4-9: The Resultant SNE Values from the Five-Error Function Procedure Carried out on the Pseudo-First and Pseudo-Second Order Rate Equation Fits Using Non-linear Least Squares fit for All Three Commercial Samples

Rate Equation-Fit	SNE VALUES		
	BA40	BA50	BA60
PFO-Nonlinear	0.212272	0.37216	0.806658
PSO-Nonlinear	0.478171	0.503058	0.270596

The data for BA40 and BA50 fitted the PFO rate equation better whilst the PSO rate equation was the best fit for the BA60 data. The calculated coefficients, Table 4-10, show that the PSO order rate equations had a much lower error with a maximum of 0.81%.

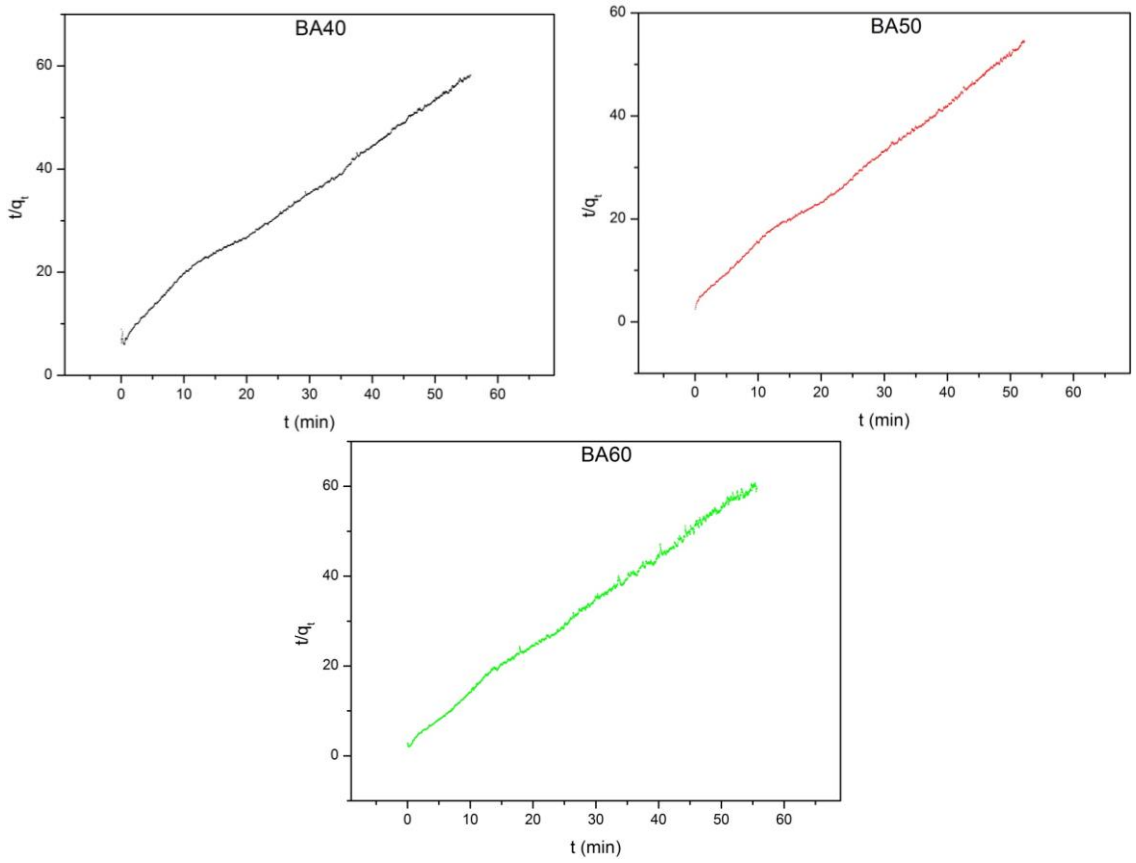

Figure 4-13: The Pseudo-Second Order Linear Regression Plots for All Three Commercial Samples in 0.5 MPa CO_2 at 20 °C

Table 4-10: The Calculated Kinetic Coefficients for Pseudo First and Second Order Models.

Non-Linear Fitting of the PFO Rate Equation				
Sample	$q_e\ (kg\ kg^{-1})$	Relative Error (%)	$k_1(s^{-1})$	Relative Error (%)
BA40	0.118 ± 0.00003	0.21	0.0561 ± 0.0003	0.56
BA50	0.099 ± 0.0001	1.1	0.129 ± 0.003	2.1
BA60	0.078 ± 0.0003	3.5	0.204 ± 0.005	2.7
Non-Linear Fitting of the PSO Rate Equation				
Sample	$q_e(kg\ kg^{-1})$	Relative Error (%)	$k_2(kg\ kg^{-1}\ s^{-1})$	Relative Error (%)
BA40	$0.122x10^{-3} \pm 0.003x10^{-3}$	0.02	0.792 ± 0.002	0.14
BA50	$0.101x10^{-3} \pm 0.002x10^{-3}$	0.02	2.69 ± 0.001	0.49
BA60	$0.077x10^{-3} \pm 0.001x10^{-3}$	0.01	5.35 ± 0.05	0.81

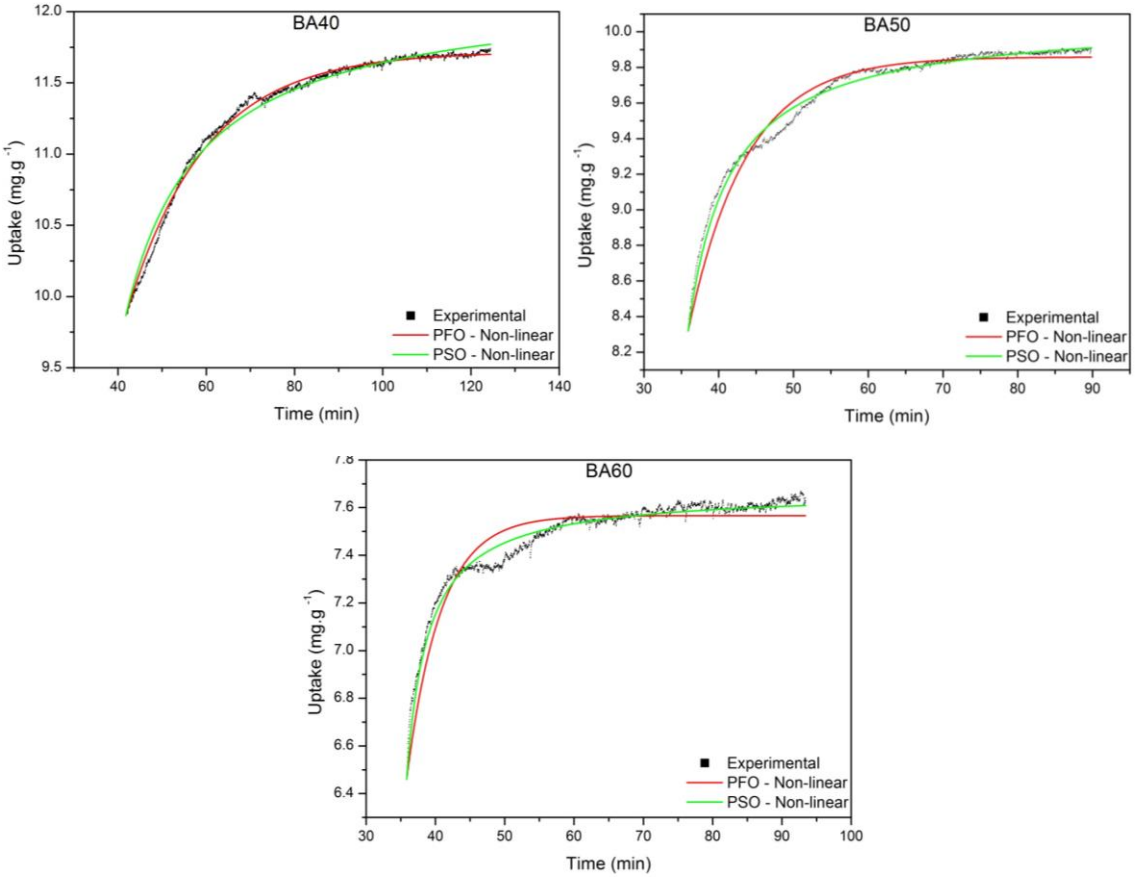

Figure 4-14: Fitting of the Pseudo First and Second Order Models to All Three Commercial Samples in 0.5 MPa CO_2 at 20 °C

4.3.6.3 ISOTHERMAL MODELS

As the PSO rate equation showed a better fit for later times and had the lowest overall SNE values, this rate equation was used to fit the kinetic data at 0.1 MPa pressure increments between 0.1 and 1 MPa and collect the systems thermodynamic data, Figure 4-15.

It can be seen that unlike the preliminary experiments, BA40 and BA50 absorbed very similar amounts of CO_2, whilst BA60 absorbed the least. $q_{e,10}$ for BA40, BA50 and BA60 was 20.0, 20.1 and 15.6 $g.kg^{-1}$ respectively, measured in 1 MPa CO_2 at 20 $°C$.

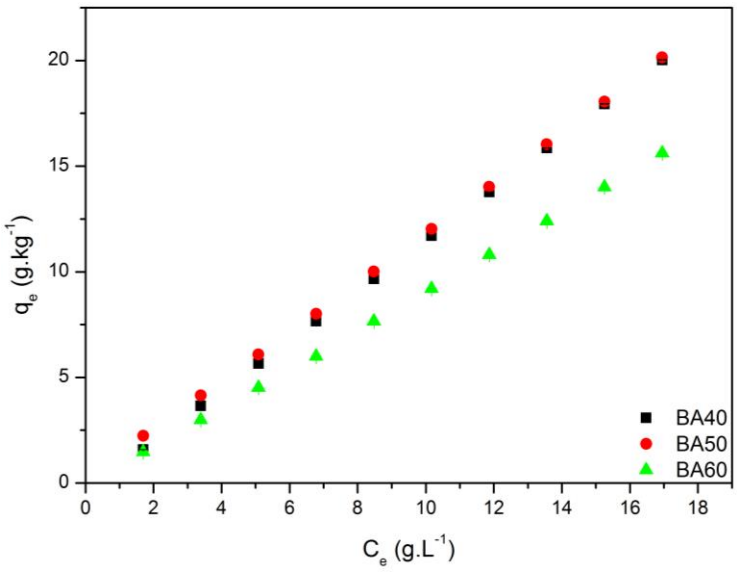

Figure 4-15: The Equilibrated Mass Uptake against Solute Concentration for All Three Commercial Samples in CO_2 at 20 °C

The five-error analysis procedure explained in Chapter 3 and used by *Ho, Porter and Mckay* [158] was used in conjunction with non-linear regression using SOLVER in Excel to find the error equations that provided the best fits for the different isotherms and Table 4-11 depicts the results along with the respective R^2 values. The isotherm coefficients calculated from the best error function fits, highlighted, are repeated in Table 4-12 and their isotherm plots are shown in Figure 4-16. During this procedure the Langmuir models did not converge on any particular values and have therefore been omitted.

Table 4-11: The Error Equations that Provide the Best Fit Isotherms and the Resultant R^2 Value for all Three Commercial Samples as Received and Measured at 20 °C

Isotherm Model	BA40		BA50		BA60	
	Error Equation	R^2 Value	Error Equation	R^2 Value	Error Equation	R^2 Value
Henry's Law	EABS	0.998	ERRSQ	0.999	HYBRD	0.999
Freundlich	ARE	0.999	HYBRD	0.999	EABS	0.999
Temkin	HYBRD	0.859	HYBRD	0.863	HYBRD	0.859
Dubinin-Radushkevic	HYBRD	0.898	HYBRD	0.878	ERRSQ	0.914

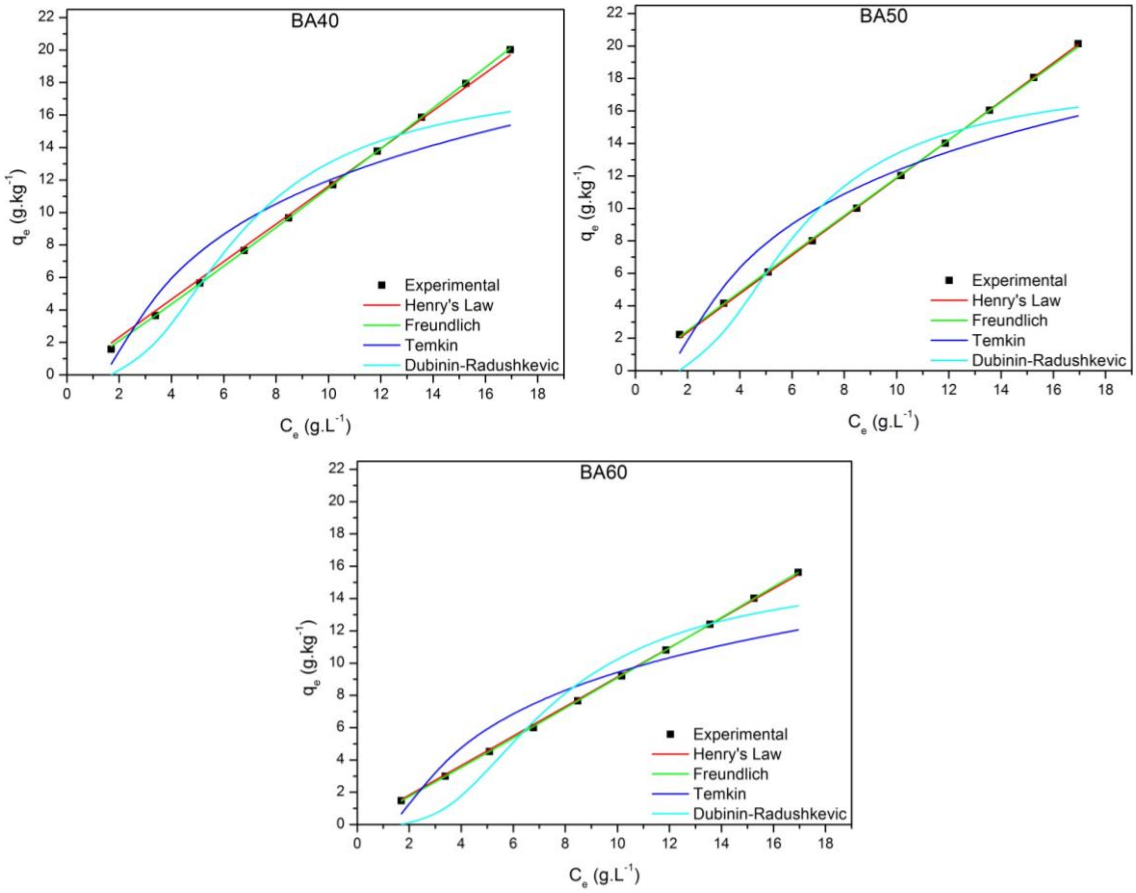

Figure 4-16: Fitting of the Thermodynamic Uptake Data for BA40, BA50 and BA60 to Henry's Law, Freundlich, Temkin and Dubinin-Radushkevic Isotherm Models in their As Received Condition in CO_2 Between 0.1 and 1 MPa

The R^2 values suggest that either Henry's Law or the Freundlich Isotherms best explain the experimental data.

Table 4-12: The Calculated Isotherm Constants for All Three Commercial Samples in their 'As Received' Condition Measured at 20 °C

Isotherm Model	Parameter	BA40	BA50	BA60
Henry's Law	K_H	1.97 ± 0.03	2.01 ± 0.01	1.55 ± 0.01
Freundlich	a_F	1.00 ± 0.04	1.25 ± 0.03	0.85 ± 0.01
	n_F	0.94 ± 0.01	1.02 ± 0.01	0.972 ± 0.003
Temkin	b_T	382 ± 81	384 ± 78	492 ± 104
	a_T	0.66 ± 0.29	0.70 ± 0.31	0.67 ± 0.30
Dubinin-Radushkevic	$B_D(x10^{-6})$	6.1 ± 1.7	5.5 ± 1.5	7.9 ± 2.4
	q_D	18 ± 19	18 ± 17	16 ± 29

4.4 Discussion

4.4.1 Spectroscopy

The presence of the C=O peaks at $1736 - 1720\ cm^{-1}$ suggests oxidation of the elastomers and the formation of crosslinks in the imide position, as well as the presence of ester-containing additives. The disparity in peak position indicates the use of different additives with similar chemical structures. These artefacts could also be inducing the shift in position seen in the BDN-methylene vibrations between 1436 and 1376 cm^{-1}. These crosslinks are most likely the result of the vulcanisation procedure carried out during manufacture.

There has been no bond directly linked to the presence of the peaks at 1117 and 1036 cm^{-1}. The closest in the literature were those found by *Coates* [154], who noticed that the presence of carbon black caused a peak at 1092 cm^{-1}, and the work by *Vijayabaskar, Tikku and Bhowmick* [148], which attributed a peak at 1050 cm^{-1} to a C-O-C stretch. BA40 was the only sample to display these peaks and therefore it can be assumed they were not due to the presence of carbon black, as all samples were expected to contain it and would have all displayed the peaks. These therefore must be due to the inclusion of some additives that were only used in the manufacture of BA40. However, the peaks between 1036 and 1015 cm^{-1} appeared in all samples and are most likely due to the use of a common additive or inclusion that has been used in the manufacture of all three commercial samples. The peaks between 872 and 870 cm^{-1} appear to be present in the literature although no attempt has been made at attributing them to a particular bond in NBR. However, other reports have identified this region as being the result of a nitrogen containing functional group, which means it could have possibly indicated part of the imide crosslink or an out of plane N-H deformation, potentially owing to an additive or inclusion.

The peaks at 964, 918 and 741 cm^{-1} have been linked to the BDN content within the sample and the diminishing height of the peak with increasing hardness in the samples would suggest higher ACN:BDN ratios in the harder samples. In a paper by *Chakraborty et al.* [155] the ratio of the C≡N peak at 2235 cm^{-1} to the C=C peak

at 964 cm^{-1} was found to fit a linear trend, against which the results from this work have been compared and the ACN content has been calculated as 50.1, 50.0 and 49.6% for BA40, BA50 and BA60 respectively. However, *Chakraborty et al.*'s [155] C≡N peak is considerably sharper than the one seen in this work. *Seehra, Yalamanchi and Singh* [62] showed a similar diminished peak height and attributed it to the presence of additives and fillers affecting the bond vibrations, and also the cleaving of the nitrile bond in the curing process of manufacture.

4.4.2 Swelling Behaviour

The calculated $\Delta_{M\%}$ values of 89.1, 135, 108 and 46% for BA40, BA50 and BA60 and the industrial seal respectively are in good agreement with those found by *Seehra, Yalamanchi and Singh* [62], 90.3 and 75.9% for nitrile elastomers of 70 and 75-durometer hardness respectively.

Their work also discussed the contributing factor of BDN content to the swelling capacity and as such it can be inferred that BA50 had the lowest ACN:BDN ratio due to its higher $\Delta_{M\%}$ value and, inversely, BA40 had the highest.

The swelling capacity of the sample is related to the gel content and crosslink density within the structure; as more chains are interconnected with one another the propensity for them to spread apart due to diffusing molecules will diminish. This means that their geometric dimensions will remain closer to their original values and the increased friction, seen as a result of a swelling dynamic component within its restrictive housing, will be reduced.

4.4.3 Glass Transition Temperature

T_g has also been shown to be closely linked to the gel content within the elastomer; if a greater portion of the polymer chains are bound into the gel network a larger heat is required to induce a change in transition and thus T_g is subsequently raised. The extremely close T_g values between all four samples, which are in general agreement with those in the literature, would therefore suggest similar gel contents.

A number of papers [148, 15] suggest that there is a trend between T_g of NBR and its ACN:BDN ratio. The T_g values found by *Vijayabaskar, Tikku and Bhowmick* [148] and *Kucukpinar and Doruker* [159] are plotted against their ACN content along with the ACN contents calculated from the data found in this report, Figure 4-17.

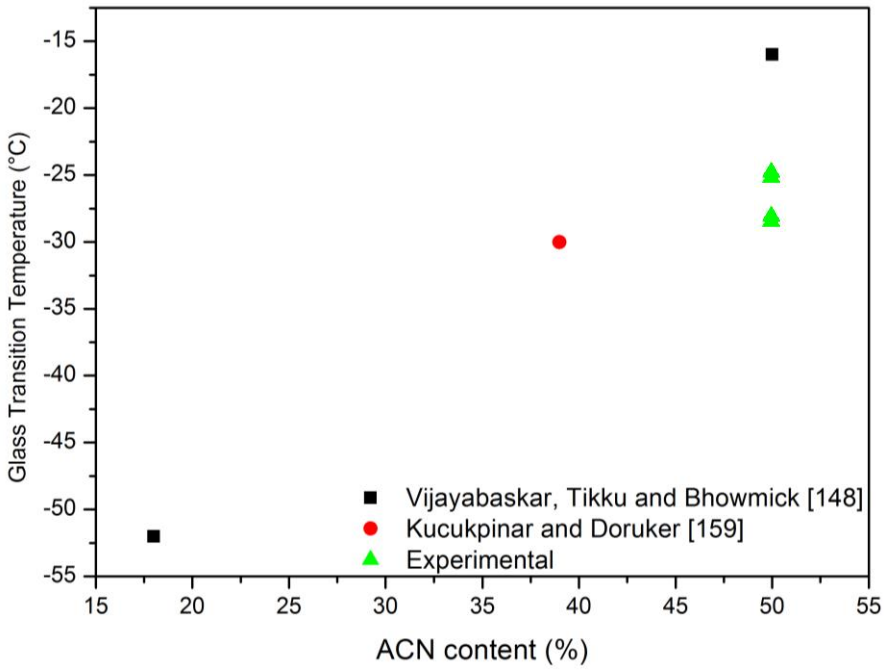

Figure 4-17: A Comparison of the Estimated Tg Values for All Three Commercial Samples and the Industrial Seal Against Those Found in the Literature

4.4.4 Mechanical Behaviour

The mechanical compression data collected here have been compared against those by *Hassan et al.* [160] and a good agreement between the two has been found, Figure 4-18.

As discussed in Chapter 2, when a force is applied to the surface of the elastomer the chains will move in the direction of the applied force. If the chains are free to move then a portion of this initially applied force is exhausted in the chain motion (energy is dissipated), however, if there are significant restrictions to motion, most commonly due to the presence of crosslinks, then a portion of the initial force applied to produce the deformation will be retained by these restrictions. Upon

release of the applied force, this retained force provides the energy that allows the chains to return to their original positions. The RF calculated provides the ratio of the energy retained against the energy applied to the elastomer and due to the immediate discontinuation of the measurements upon the return of the moving arm to its original position this value only considers the rapid recovery mechanism, which has been linked to the local-scale readjustments of molecular bonds.

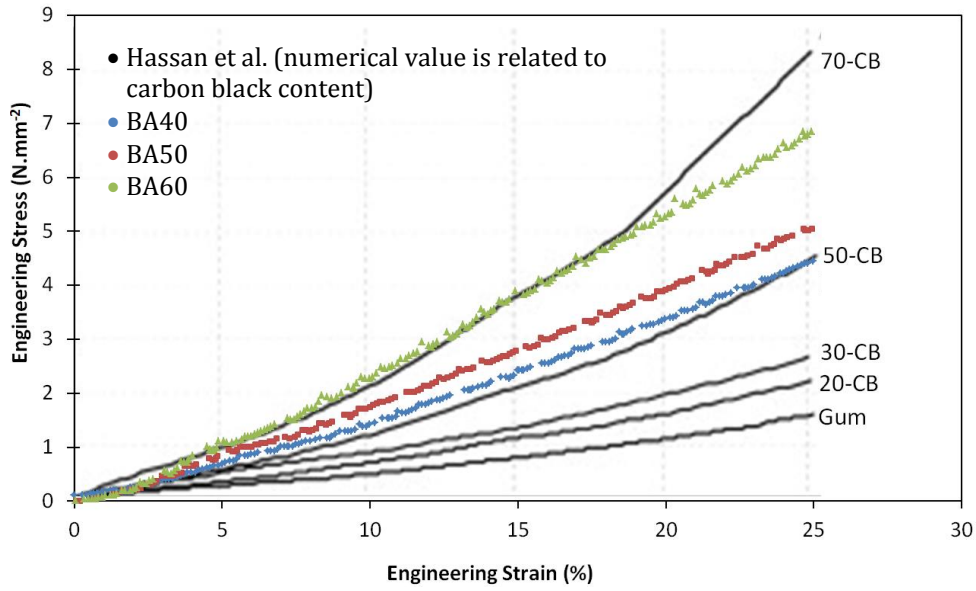

Figure 4-18: A Comparison of the Mechanical Compression Data for all Three Commercial Samples (in colour) Against Those Found in Literature [160] (in black)

The higher RF in BA40 would therefore suggest that the internal chains in this sample have a lower degree of mobility, i.e. there are more restrictions to movement in the sample that prevent chain motion and assist in their relocation. However, one must consider the possibility that this is due to the faster recovery of the softer samples. The RF therefore does not give absolute values of overall internal chain mobility due to the time dependence of the different recovery mechanisms but measurement of the change in RF with radiation dose will give a good insight into the change in the fast-recovery-mechanisms and hence the ability of the material to create a sealing force as it is acting back against the compressing component.

As RF provided the material characteristic that would be most closely linked to the components sealing capacity, the other properties have been compared for each sample against this, Figure 4-19. Taking into consideration that the far left points belong to those of the industrial seal and therefore include glass cloth and brass wire which may affect other properties, the data suggests that a higher RF lends itself to a higher T_g and lower swelling capacity.

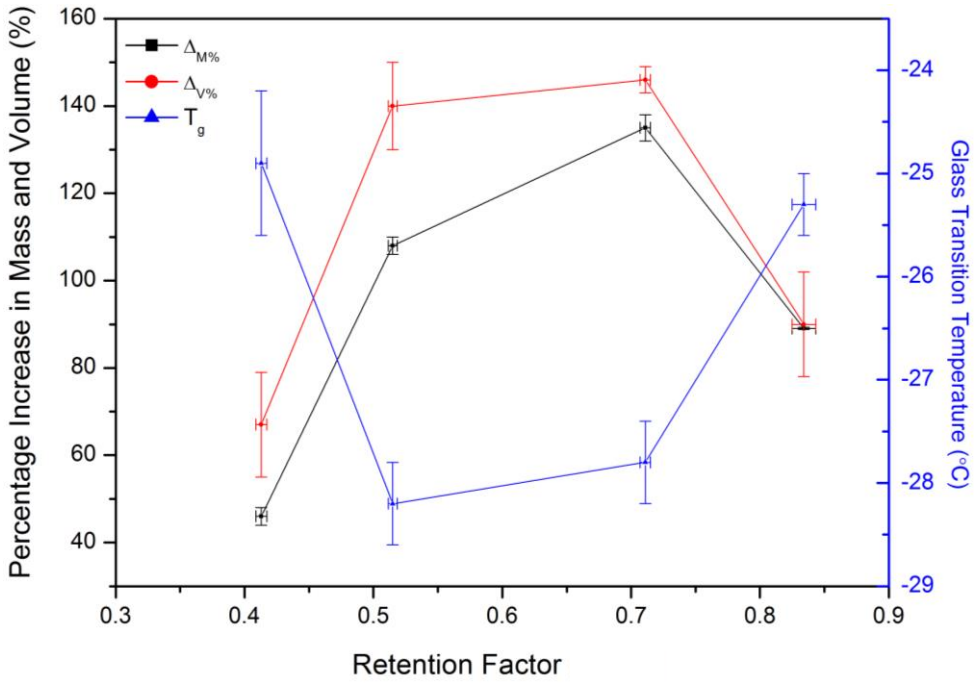

Figure 4-19: A Comparison of $\Delta_{M\%}$, $\Delta_{V\%}$ and T_g Against Retention Factor for All Samples

4.4.5 CO_2 Absorption Behaviour

4.4.5.1 Absorption Kinetics

The decreasing mass with respect to time seen in the industrial seal is most likely due to the presence of brass wires introducing channels through which the CO_2 can escape.

Even though T_{lag} is seen to decrease with increasing hardness, the results are of a sufficiently low value that when compared to the time to equilibrium they can be considered negligible. k_{ID} decreased with increasing BA rating whilst k_1 and k_2 increased, Table 4-13. This can be explained through the swelling behaviour of

NBR in a CO_2 environment. The increased chain movement in the softer samples allows an increased expansion in the polymer chain matrix and thus the particles can diffuse through the system at a faster rate. However, as the material swells to its full capacity the chain movements become restricted and diffusion is slowed. This also explains the decreasing trend seen in the $t_{1/2}$ values for the PSO rate equation, Table 4-14; as the material swells its capacity will increase and thus a system that continues to swell for longer will have a longer time to equilibrium and thus larger $t_{1/2}$.

Table 4-13: The Calculated Observable Rate Constants for the Intraparticule Diffusion, PFO and PSO Models for All Three Commercial Samples Measured at 20 °C and 0.5 MPa CO_2

Sample	$k_{ID}(kg\ kg^{-1}\ s^{-1})$	$k_1\ (s^{-1})$	$k_2(kg\ kg^{-1}\ s^{-1})$
BA40	10.4 ± 0.03	0.0561 ± 0.0003	0.792 ± 0.002
BA50	7.12 ± 0.05	0.129 ± 0.003	2.69 ± 0.001
BA60	5.9 ± 0.03	0.204 ± 0.005	5.35 ± 0.05

Table 4-14: The Calculated Half-life and Initial Half-life Values for All Three Commercial Samples Measured at 20 °C and 0.5 MPa CO_2

Sample	PFO	PSO	
	$t_{1/2}\ (min)$	$t_{1/2}\ (min)$	h_0
BA40	13.79 ± 0.04	1.730 ± 0.003	7.03 ± 0.01
BA50	8.5 ± 0.05	0.615 ± 0.003	16.38 ± 0.09
BA60	14.41 ± 0.09	0.406 ± 0.003	18.9 ± 0.2

When compared to RF, Figure 4-20, it can be seen that higher force retention equates to slower absorption.

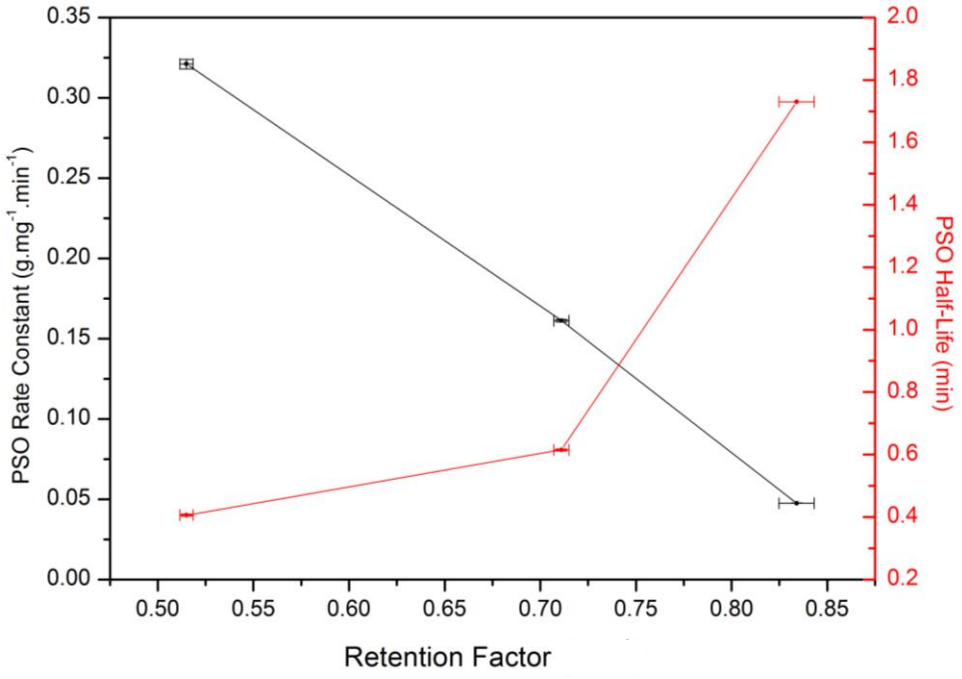

Figure 4-20: PSO Rate Constant and Half-life against RF for All Three Commercial Samples

Following the second run in the IGA at various pressures, the absorption and desorption kinetic coefficients, k_a and k_d, and the absorption affinity ratio, K, were calculated from the observable rate constant in the PFO rate equation, k_1, as per Equations 4-5 and 4-6, Table 4-15 and Table 4-16.

Table 4-15: The Calculated k_a and k_d Values for All Three Commercial Samples in CO_2 at 20 °C

Sample	k_a $(m^3\ kg^{-1}\ s^{-1})$	Relative Error (%)	k_d (s^{-1})	Relative Error (%)
BA40	0.0046 ± 0.0004	8.1	0.071 ± 0.004	5.0
BA50	0.0052 ± 0.0005	10	0.069 ± 0.005	7.5
BA60	0.0034 ± 0.0006	18	0.070 ± 0.006	8.8

Table 4-16: The Ratio of k_a to k_d for All Three Commercial Samples in CO_2 at 20 °C

Sample	K $(m^3\ kg^{-1})$	Relative Error (%)
BA40	0.064 ± 0.009	14
BA50	0.076 ± 0.015	20
BA60	0.049 ± 0.014	30

A sample will have a higher affinity for absorption over desorption, represented by a higher K value, when the absorbing substance has a higher affinity to the solid sample. This affinity is most likely due to polarity; CO_2 is a non-polar molecule and

a very well-known mantra in the scientific community is that 'like dissolves like' suggesting that non-polar molecules will have a higher affinity to CO_2 than polar ones. One can therefore derive that the samples with a higher K value, will have a lower polarity and thus lower ACN content.

A slower absorbing material will require a longer soak time in the CO_2 environment before the swelling reaches the point at which it becomes detrimental. Therefore, slower rate constants indicate a more resistant material to CO_2 swelling. The affinity of the material to the CO_2 will also have an impact on its swelling behaviour as a higher affinity will result in increased absorption over desorption and thus the material will retain the CO_2 molecule for longer and the swelling will be more detrimental.

4.4.5.2 Isothermal Models

A brief glance at Figure 4-15 will reveal the linearity to the thermodynamic data for all the commercial samples. This is in agreement with the work done by *George* [35] who investigated swelling and absorption effects up to 4.1 MPa pressure on a similar elastomer. When compared against the work by *Briscoe and Zakaria* [161] and *Fleming and Koros* [162], the 15, 14 and $11x10^{-6}\ m^3(STP)\ m^{-3}\ Pa$ values found for BA40, BA50 and BA60 respectively are similar to the $25x10^{-6}\ Pa\ m^3(STP)\ m^{-3}$ value found for the silicone elastomers at lower pressures. However, in their work they discuss how the linearity is seen at low pressures and it is only at much higher pressures, greater than 5 MPa, that any deviation from linearity is evident. This is perhaps one explanation as to why the Langmuir fit did not converge; the model was fitting to the initially linear section but had no indication of the point at which uptake begins to tail off and so could not provide an accurate fit. It could also explain the large errors seen in the Temkin and Dubinin-Radushkevic models. If the data found in this work are simply in the beginning stages of these models and at higher pressures show a similar trend to that seen in the work by *Briscoe and Zakaria* then these models would have perhaps had a much better fit.

The K_H values can be interpreted as the uptake in the elastomers as it simply represents the gradient by which the q_e vs C_e plot increases. This would suggest that BA40 and BA50 had similar uptake characteristics whilst the absorption in BA60 was somewhat hindered.

The Freundlich model has a slightly better fit than the Henry's Law model, which is to be expected due to the addition of the n_F parameter, commonly termed the 'Strength of Interaction Parameter.' The a_F parameter determines the gradient of the straight line, much like the K_H parameter in the Henry's Law model, and the n_F parameter determines the amount of curve that line has away from linearity. For n_F values of 1 the trend is linear, if the value is above 1 the gradient decreases, suggesting a limiting factor on absorption capacity, if the value is below 1 the gradient increases.

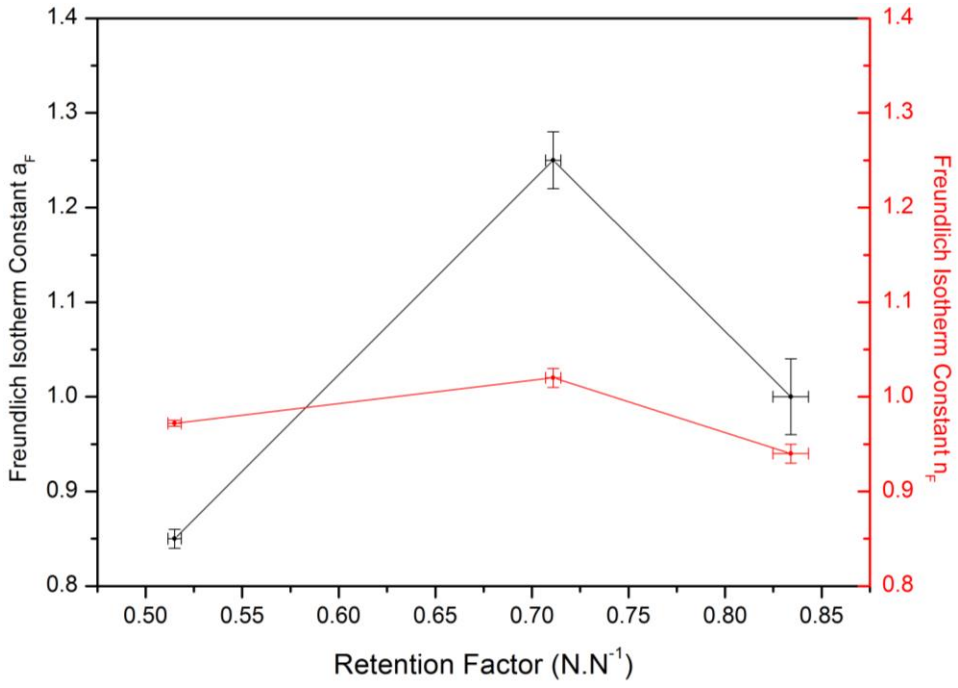

Figure 4-21: Freundlich Isotherm Constants against RF for All Three Commercial Samples

n_F exhibits lower change with RF than a_F suggesting the interaction between CO_2 molecules and the elastomers is minimal. The mean free energy of sorption for one mole, E $(kJ\ mol^{-1})$, has been calculated from the Dubinin-Radushkevic

Isotherm as this provides some insight into whether the adsorption process is through a physisorption or chemisorption mechanism.

Table 4-17: Calculated Mean Free Energy of Sorption Values for All Three Commercial Samples in CO_2 at 20 °C

Sample	E $(kJ\ mol^{-1})$	Relative Error (%)
BA40	0.29 ± 0.05	17
BA50	0.30 ± 0.05	17
BA60	0.25 ± 0.05	20

An E value below 8 indicates physisorption and even with the large relative error the values calculated here fall well below that value. This means that any interaction between the diffusing molecule and the material is physical in nature and not chemical. As the n_F values are not equal to 1 it is known that there is some interaction between CO_2 and the elastomers, all be it small, and it can therefore be inferred that this is to do with the intermolecular structure of the elastomeric matrix. A change in the structure, through radiation exposure for example, will therefore cause a change in these parameters which can be directly linked to the materials ability to absorb CO_2 and will ultimately affect the CO_2 loading capacity of the material, and thus its swelling capacity.

4.4.6 Crosslink Density

The crosslink density within an elastomer is regularly assessed by its swelling behaviour. However, for direct calculation of crosslink density one must know the polymer-solvent interaction parameter, which is unique for each absorbing system and has been shown to change with radiation dose [163] thus rendering this calculation useless in later sections. The swelling tests will, nevertheless, provide a degree of understanding of the crosslink density, as the formation of crosslinks is expected to hinder the expansion of the polymer network. As discussed earlier in the chapter, crosslink formation is either through ionisation and subsequent degradation of the BDN units or the ACN units and this selection will not affect the crosslink density. A comparison of the affinity of the CO_2 to the elastomer, as derived from the K values, with the $\Delta_{M\%}$ values from the swelling tests and data gathered from the IR spectra may provide additional information not only on the

comparable crosslink density with the 'as received' samples but also the positioning and affect it has on the absorption of CO_2 gas.

4.5 CONCLUSIONS

The visual inspection of the samples found no discernible difference between the commercial samples but the increasing hardness as denoted by the BA values is evident on manual handling. The industrial seal is considerably tougher and has visible brass wires, surface dimples and internal fibres. SEM found the fibres that are incorporated into the structure for their strengthening benefits may potentially produce propagation channels along which the damage from cracks may accelerate. There is also evidence of some potential clustering of components within the structure of the commercial samples.

The ATR-FTIR data suggests decreasing BDN content ratios from BA40 to BA60 but due to the inclusions and additives in BA50 and BA60 causing some bond vibration disturbances the validation of content ratios will be less accurate. However, comparison of the IR data with increasing radiation dose may prove useful in assessing the potential changes in the internal structure.

$\Delta_{M\%}$ for BA40, BA50, BA60 and the industrial seal was found to be 89.1, 135.4, 108.3 and 46.4 % respectively with an error of 2 %. $\Delta_{V\%}$ for the samples was found to be 99.3, 145.5, 141.9 and 67.3 % respectively with an error of 30 %. The larger error in the $\Delta_{V\%}$ values is attributed to the increased compressibility of the samples following exposure to toluene producing additional error upon measurement of their dimensions when using a calliper. The $\Delta_{M\%}/\Delta_{V\%}$ ratios are larger than the density of toluene suggesting that toluene molecules locate inside void spaces in the elastomeric structure. The lower values of the industrial seal are expected to be due to the brass wire and glass cloth in the structure, contributing to its mass whilst not providing an absorption medium into which the toluene can travel.

T_g for BA40, BA50, BA60 and the industrial seal was found to be $-25.3, -27.8, -28.2$ and $-24.9\ °C$ respectively with an error of 2%. The

assessment of the industrial seal proved particularly problematic in that possible contamination of the brass wire or glass cloth into the sample pan was difficult to remove. T_g is expected to increase with increasing ACN content, however this trend was not seen in the data. One main contributing factor to this may be the presence of additives in the elastomer structures affecting T_g. However, comparison of change in T_g with increasing radiation dose will prove useful in assessment of the change in gel content and molecular mobility within the microstructure.

The force required to induce a 3 mm deflection in all the samples was found to be 60, 70, 100 and 120 N respectively. The leaf-shaped load-deflection curves for the industrial seal are most likely due to the presence of brass wire and their orientation congruent to the deflection direction. RF for the samples was found to be 0.8342, 0.7113, 0.5149 and 0.4132 respectively. These values suggest that BA40 provided the largest sealing force and as such has the highest crosslink density. This is in agreement with the IR peak intensity at 1736 and 1720 cm^{-1} which showed a reduction with increasing hardness in the samples, suggesting either a decrease in the concentration of C=O containing additive or decreasing crosslink density.

In the CO_2 absorption behaviour tests, the industrial seal did not follow an expected trend in that following the step-wise pressure increase in the preliminary experiments, it began to decrease in weight over time. This has been attributed to the brass wire within the structure providing a channel through which CO_2 that has been absorbed into the bulk of the elastomer can then escape. The kinetics of the commercial samples was found to best fit the PSO model. K for BA40, BA50 and BA60 calculated from the PFO model was found to be 0.0715, 0.0643 and 0.0338 respectively. CO_2 is a non-polar molecule and thus non-polar substances will have an increased affinity towards it. The lower K values seen in the harder samples suggested a higher ACN content and thus affinity to absorb the CO_2. The Freundlich isotherm was found to best fit the thermodynamic data with calculated a_F values of 0.9112, 1.172 and 0.7910 respectively and calculated n_F values of 0.9151, 0.9997 and 0.9504 respectively. Whilst these are simple mathematical

constants and do not give any description as to the absorption mechanism, their change following irradiation dose may provide some insight into the changes in the microstructure. It is also worthwhile noting that the n_F constant, commonly referred to as the 'Strength of Interaction Parameter' follows a similar trend to that seen in $\Delta_{M\%}$; BA50 had the highest value, followed by BA60 and finally BA40.

5 EFFECTS OF GAMMA RADIATION ON PHYSICAL AND MECHANICAL PROPERTIES

5.1 INTRODUCTION

During their service lifetime the seals travel in close proximity to Spent Nuclear Fuel, exposing them to approximately 30 Gy of ionising radiation in the form of gamma rays. Chapter 3 identified the main degradation following this exposure to be the ionisation of either the BDN or ACN units and subsequent formation of crosslinks through one of three mechanisms; the ejection of hydrogen and crosslinking in the allylic position, the formation of imide crosslinks or the formation of C-O-C crosslinks.

Chapter 4 reported a series of experiments to determine the physical and mechanical properties of the industrial seal and compared these against three commercially available samples made from the same base elastomer. This chapter discusses the method of radiation exposure utilised for the experiments and the development of the sealing capacity characteristics for all samples following radiation exposure under standard atmospheric conditions. These results are then cross-analysed between all samples to determine the effect of radiation on the material properties and their susceptibility to radiation-induced damage.

5.2 EXPERIMENTAL

5.2.1 RADIATION EXPOSURE

The seals are exposed to a radiation dose rate of approximately 0.053 $Gy\ s^{-1}$ in service, [E4]. The cobalt-60 irradiator at the Dalton Cumbrian Facility (DCF) was used to achieve a dose rate of 1.67 $Gy\ s^{-1}$, which allowed samples to be exposed to $10, 50, 100, 250$ and $500\ kGy$ in the available time frame and permitted the use of a turntable mechanism ensuring an even dose across the samples.

Each sample was cut using a rotary drill into approximately 55 mm discs and placed on the 'Sample Stand' seen in Figure 5-1. This provided ample clearance between sample discs and eased their identification post-exposure without the need to deface the samples.

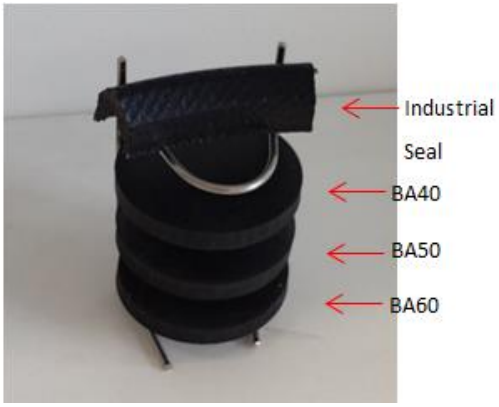

Figure 5-1: The Sample Stand used during Radiation Exposure

5.2.2 Optical Microscopy

A Hitachi TM3030 desktop SEM was used at low vacuum to inspect the surface of the samples. All images were taken in SEI mode to provide topographical information.

5.2.3 Infrared Spectroscopy

FTIR Spectroscopy was carried out on a Perkin Elmer Frontier FTIR with a diamond ATR attachment between 4000 and 500 cm^{-1} at a resolution of 4 $scans\ cm^{-1}$ and an accumulation of 4 $scans$. The spectra were taken approximately 4 mm into the bulk of the sample negating any surface effects.

5.2.4 Swelling Behaviour

The experimental procedure outlined in Chapter 3 was used to find $\Delta_{M\%}$ and $\Delta_{V\%}$ following 72 $hours$ soaking in toluene.

5.2.5 Glass Transition Temperature

A Perkin Elmer Diamond DSC was used to find the heat flow against temperature data for the samples. From this T_g was manually determined.

5.2.6 Mechanical Behaviour

7 mm diameter pellets were run through a compression and relaxation programme on a TA500 at a rate of 1 $mm\ min^{-1}$ at pre-set deflections of 1, 2, 3, 4 and 5 mm.

5.2.7 CO_2 Absorption Behaviour

$50 - 100\ mg$ of sample was cut into small monoliths of approximately 1 mm^3 volume. Each sample was placed into a Hiden Isochema IGA-002 and taken down to vacuum for 90 $mins$ before their increase in weight was recorded following isothermal $0.1x10^6\ Pa$ pressure increments between $0.1x10^6$ and $10x10^6\ Pa$.

5.3 Results

5.3.1 Visual Inspection and Manual Handling

After removal from the irradiator there was no visible change to the samples, although an increase in rigidity was noticeable with increasing radiation dose.

5.3.2 Scanning Electron Microscopy

The SEM revealed the development of micro-cracks in the industrial seal. These were found to all be parallel and are located on the outer edge of the seal travelling perpendicular to the direction of curvature, Figure 5-2.

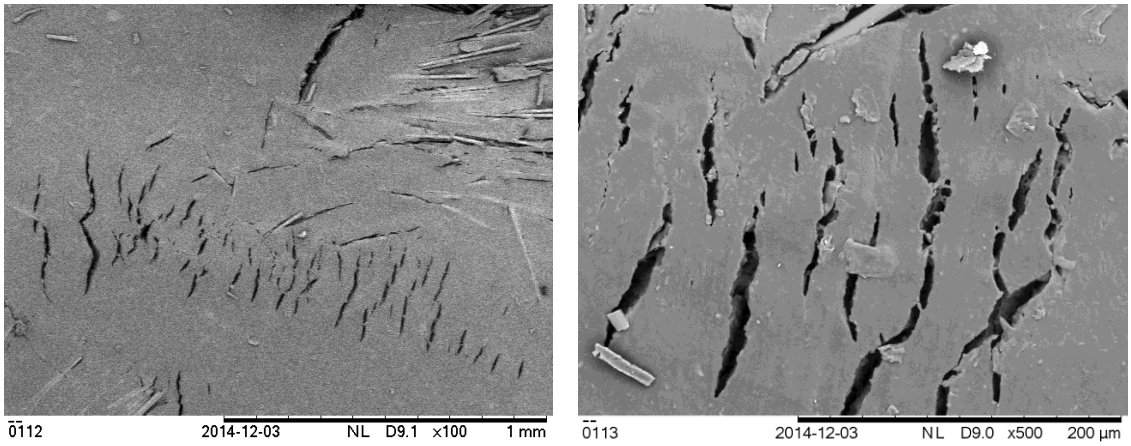

Figure 5-2: SEM Micrographs at x100 and x500 Magnification of the Industrial Seal Following Exposure to 500 kGy of Gamma Radiation under Standard Atmospheric Conditions

5.3.3 Infra-Red Spectroscopy

A comparison of the IR spectra for each sample in an as received condition and following 500 kGy of irradiation under standard atmospheric conditions can be seen in Figure 5-3.

The most notable change was the decrease in peak height at 1015 cm^{-1}.

5.3.4 Swelling Behaviour

All samples exhibited a decreasing trend in $\Delta_{M\%}$ with increasing radiation dose, Figure 5-4 and Table 5-1.

For comparison the percentage change in $\Delta_{M\%}$ is plotted in Figure 5-5. BA50 exhibited the highest resistance to radiation-induced crosslinking displaying the least percentage change with radiation dose, a maximum of -20% at 500 kGy, whilst BA40 and BA60 showed a very similar reaction to ionising radiation with maximum percentage changes of -25.5 and -25.6% respectively. The industrial seal exhibited the strongest reaction to ionising radiation in these experiments with a percentage change of -35.9% after 500 kGy.

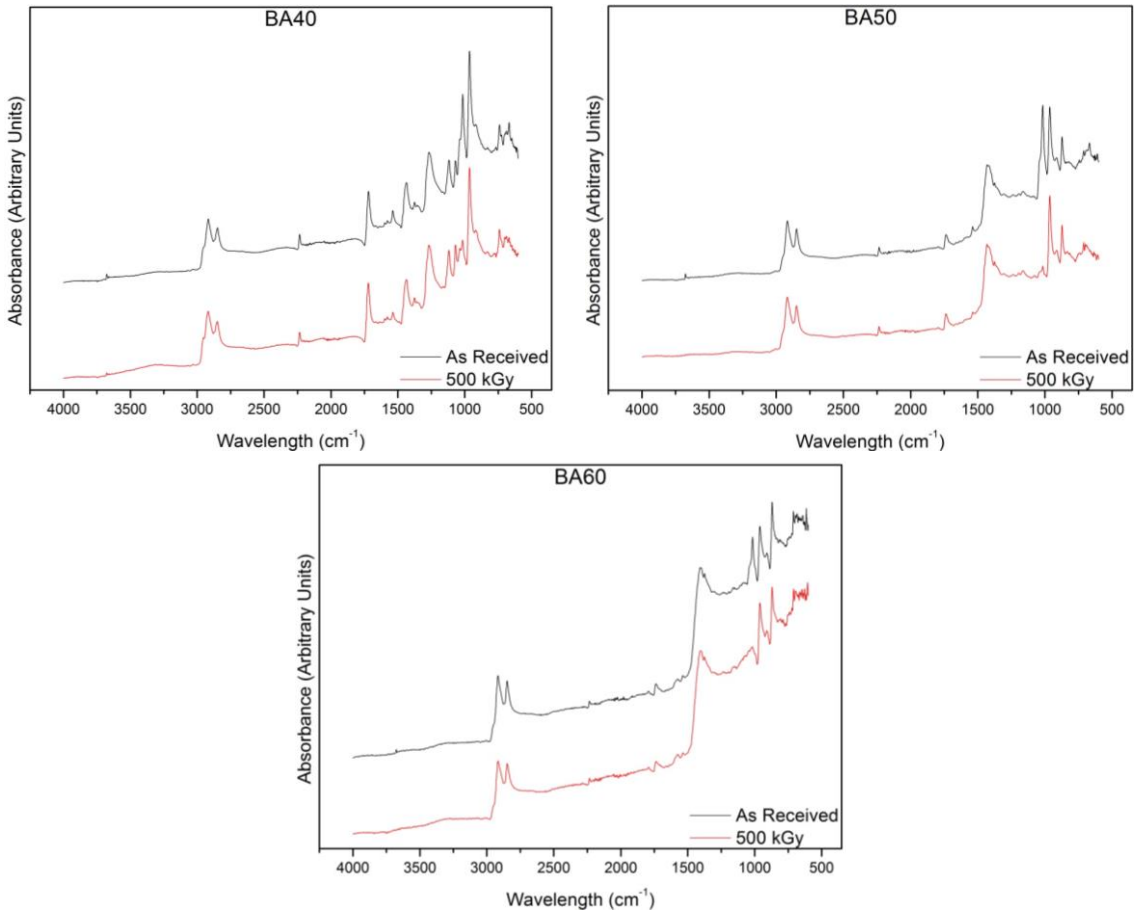

Figure 5-3: ATR-FTIR Spectra for All Three Commercial Samples Following Exposure to Gamma Radiation under Standard Atmospheric Conditions

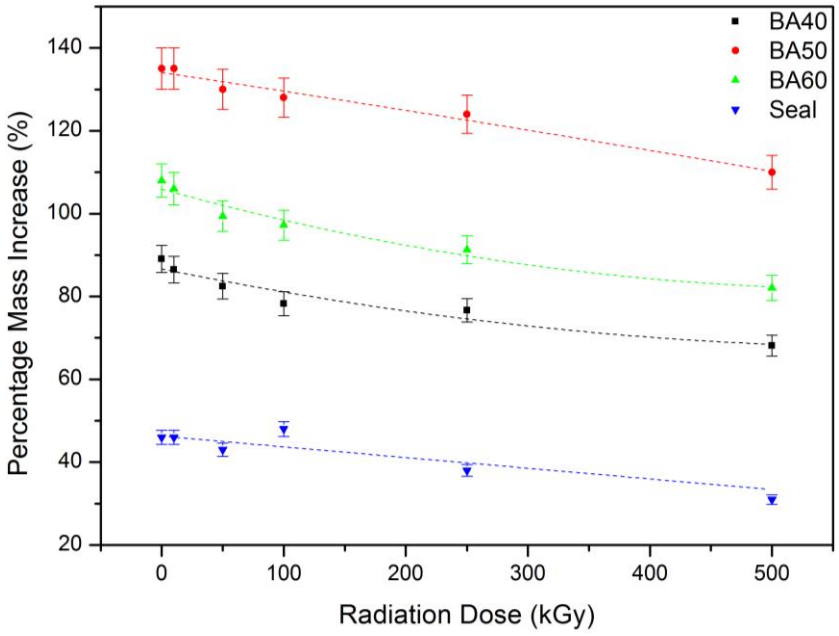

Figure 5-4: The Change in $\Delta_{M\%}$ for All Three Commercial Samples and the Industrial Seal Following Exposure to Gamma Radiation under Standard Atmospheric Conditions

Table 5-1: The Change in $\Delta M_{\%}$ for All Three Commercial Samples and the Industrial Seal Following Exposure to Gamma Radiation under Standard Atmospheric Conditions

Radiation Dose (kGy)	**Percentage Mass Increase (%)**			
	BA40	**BA50**	**BA60**	**Seal**
0	89.1 ± 3.3	135 ± 5.0	108 ± 4.0	46.4 ± 1.7
10	86.5 ± 3.2	135 ± 5.0	106 ± 3.9	45.9 ± 1.7
50	86.5 ± 3.1	130 ± 4.8	99.4 ± 3.7	43.2 ± 1.6
100	78.3 ± 2.9	128 ± 4.7	97.2 ± 3.6	48.2 ± 1.8
250	76.7 ± 2.8	124 ± 4.6	91.3 ± 3.4	38.1 ± 1.4
500	68.1 ± 2.5	110 ± 4.1	82.1 ± 3.0	31.2 ± 1.1

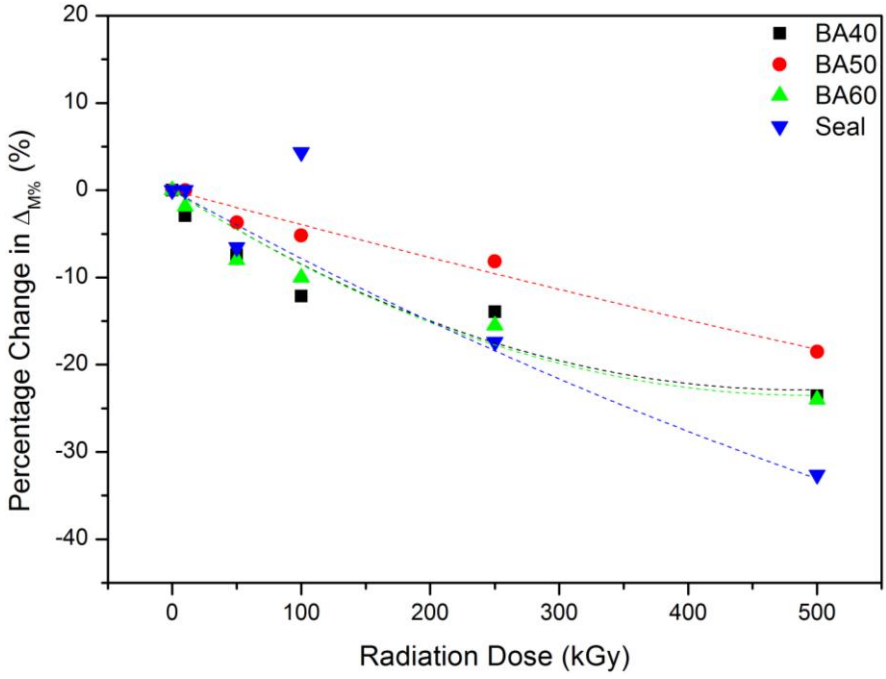

Figure 5-5: The Percentage Change in $\Delta_{M\%}$ for All Three Commercial Samples and the Industrial Seal Following Exposure to Gamma Radiation under Standard Atmospheric Conditions

5.3.5 Glass Transition Temperature

The three commercial samples exhibited a general increase in T_g with increasing radiation dose, Table 5-2 and Figure 5-6. However, BA50 and BA60 showed an initial decline in T_g up to a radiation dose of 10 kGy before their respective increases. The industrial seal showed a steady decline in T_g with radiation dose although the change was minimal and within error boundaries.

Table 5-2: The Change in T_g for All Three Commercial Samples and the Industrial Seal Following Exposure to Gamma Radiation under Standard Atmospheric Conditions

Radiation Dose	**Glass Transition Temperature** $(°C)$			
(kGy)	**BA40**	**BA50**	**BA60**	**Seal**
0	-25.3 ± 0.4	-27.8 ± 0.4	-28.2 ± 0.4	-24.9 ± 0.7
10	-24.6 ± 0.3	-28.9 ± 0.4	-29.5 ± 0.4	-24.9 ± 0.7
50	-24.1 ± 0.3	-27.5 ± 0.4	-28.9 ± 0.4	-25.4 ± 0.7
100	-23.8 ± 0.3	-27.8 ± 0.4	-28.4 ± 0.4	-25.7 ± 0.7
250	-22.0 ± 0.3	-26.3 ± 0.4	-26.7 ± 0.4	
500	-21.0 ± 0.3	-23.8 ± 0.4	-25.8 ± 0.4	-26.0 ± 0.7

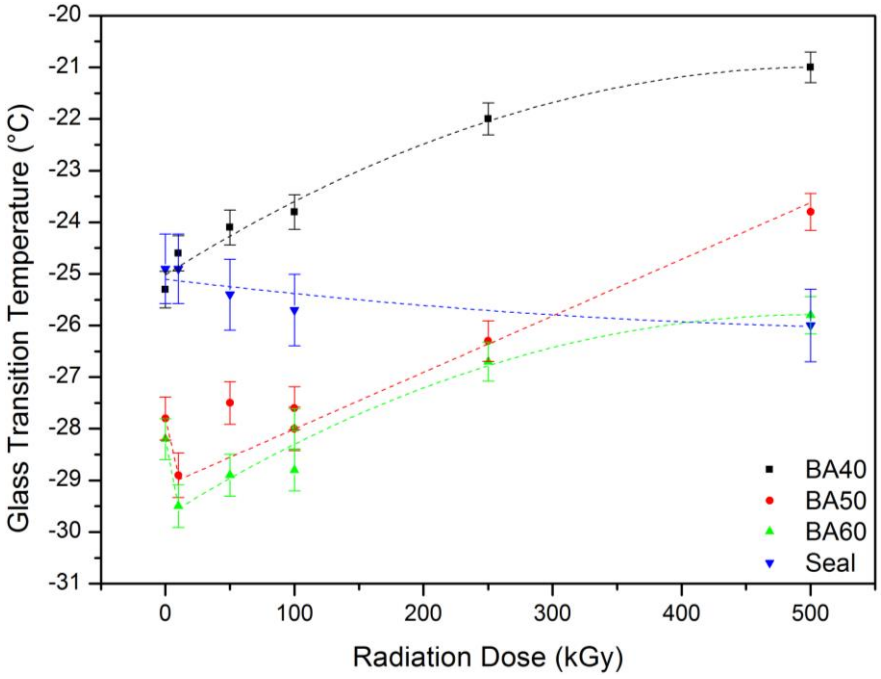

Figure 5-6: The Change in T_g for All Three Commercial Samples and the Industrial Seal Following Exposure to Gamma Radiation under Standard Atmospheric Conditions

The percentage change in T_g has been plotted in Figure 5-7, where it can be seen that following the initial decrease in T_g all three commercial samples increased at approximately the same rate, as opposed to the seal which decreased continually.

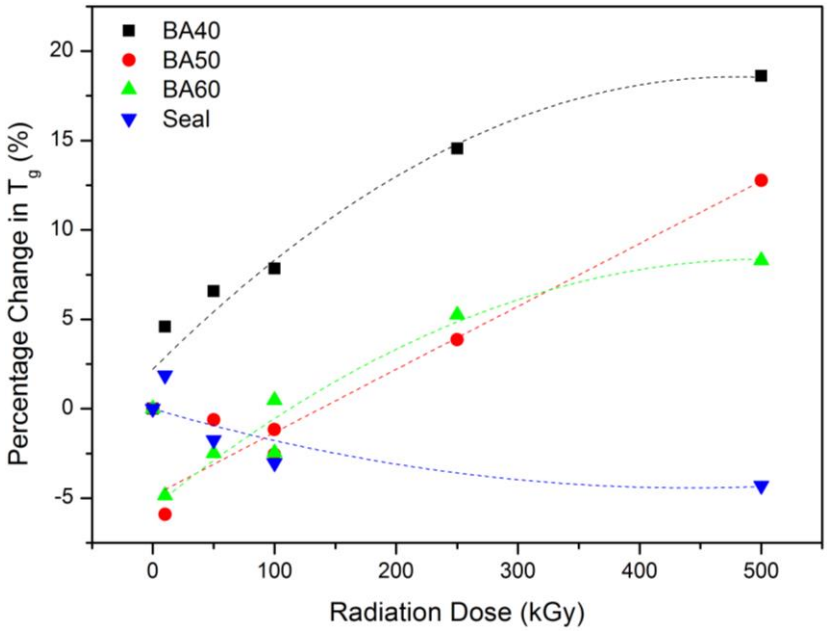

Figure 5-7: The Percentage Change in T_g for All Three Commercial Samples and the Industrial Seal Following Exposure to Gamma Radiation under Standard Atmospheric Conditions

5.3.6 Mechanical Behaviour

Exposure to 10 kGy of radiation made little change to the required load to induce a set deflection in BA40, Figure 5-8. However at higher radiation doses the required load increased respectively.

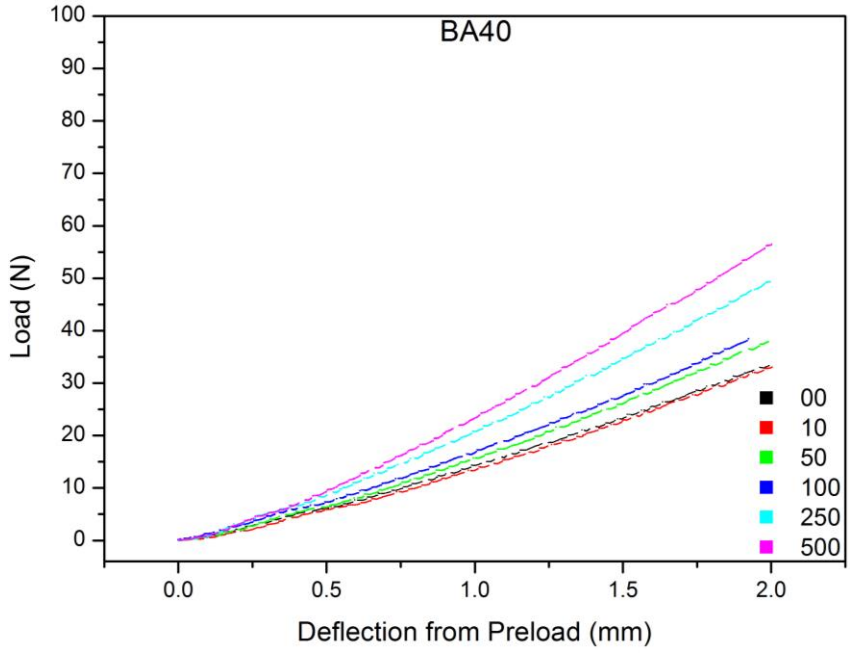

Figure 5-8: The Load-Deflection Plots for the Compression Regime on BA40 Following Exposure to Gamma Radiation under Standard Atmospheric Conditions

BA50 and BA60 exhibited an initial decrease in required load up to a radiation dose of 10 kGy before the required load increased with radiation dose, Figure 5-9.

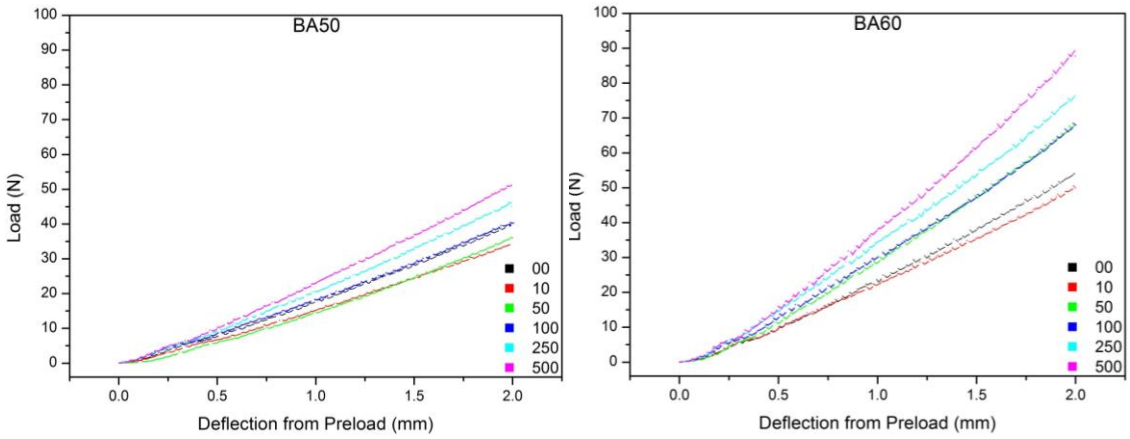

Figure 5-9: The Load-Deflection Plots for the Compression Regime on BA50 and BA60 Following Exposure to Gamma Radiation under Standard Atmospheric Conditions

RF for all samples increased steadily with increasing radiation dose, Table 5-3 and Figure 5-10. The percentage change in RF has been plotted in Figure 5-11. BA40 and BA50 showed the lowest percentage change whilst the industrial seal exhibited the largest.

Table 5-3: Change in RF for All Three Commercial Samples and the Industrial Seal Following Exposure to Gamma Radiation under Standard Atmospheric Conditions

Radiation Dose (kGy)	**Retention Factor**			
	BA40	**BA50**	**BA60**	**Seal**
0	0.834 ± 0.017	0.711 ± 0.014	0.515 ± 0.010	0.413 ± 0.008
10	0.823 ± 0.016	0.699 ± 0.014	0.507 ± 0.010	0.413 ± 0.008
50	0.843 ± 0.017	0.712 ± 0.014	0.534 ± 0.011	0.473 ± 0.009
100	0.856 ± 0.017	0.719 ± 0.014	0.543 ± 0.011	0.457 ± 0.009
250	0.870 ± 0.017	0.735 ± 0.015	0.576 ± 0.012	0.483 ± 0.010
500	0.881 ± 0.018	0.779 ± 0.016	0.609 ± 0.012	0.536 ± 0.011

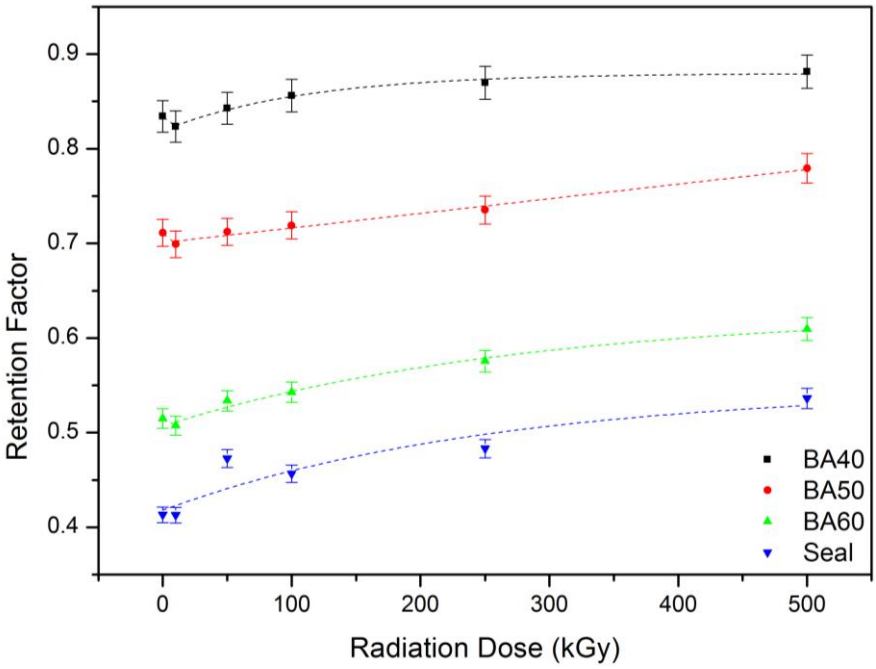

Figure 5-10: The Change in RF for All Three Commercial Samples and the Industrial Seal Following Exposure to Gamma Radiation under Standard Atmospheric Conditions

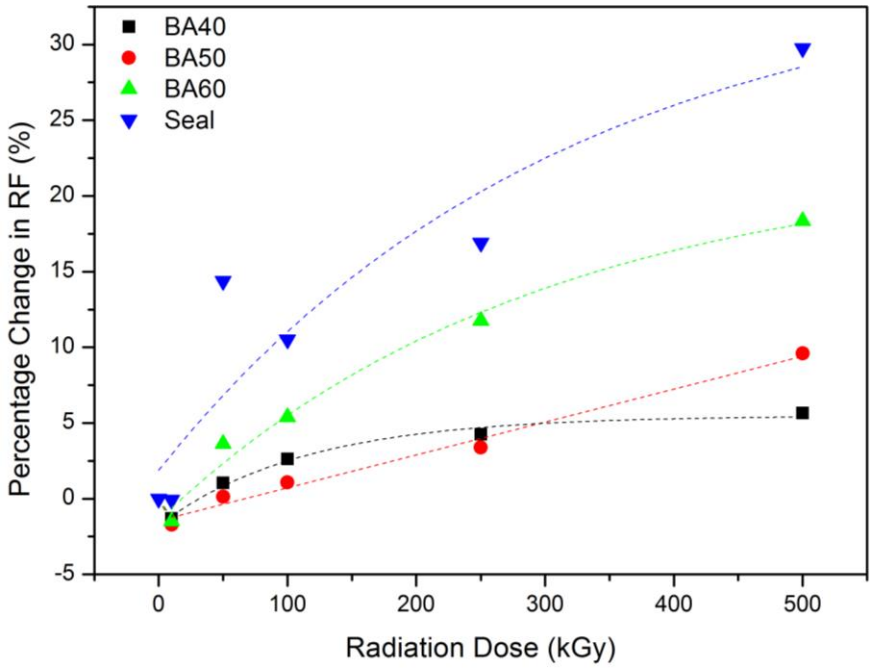

Figure 5-11: The Percentage Change in RF for All Three Commercial Samples and the Industrial Seal Following Exposure to Gamma Radiation under Standard Atmospheric Conditions

5.3.7 CO_2 Absorption Behaviour

5.3.7.1 Absorption Kinetics

Intraparticulate Diffusion

Whilst all samples showed an increase in k_{ID} with solute concentration there was no apparent trend with radiation dose, Figure 5-12.

Pseudo-Second Order

BA40 exhibited the largest change in k_2 values followed by BA50 with BA60 presenting the greatest resistance.

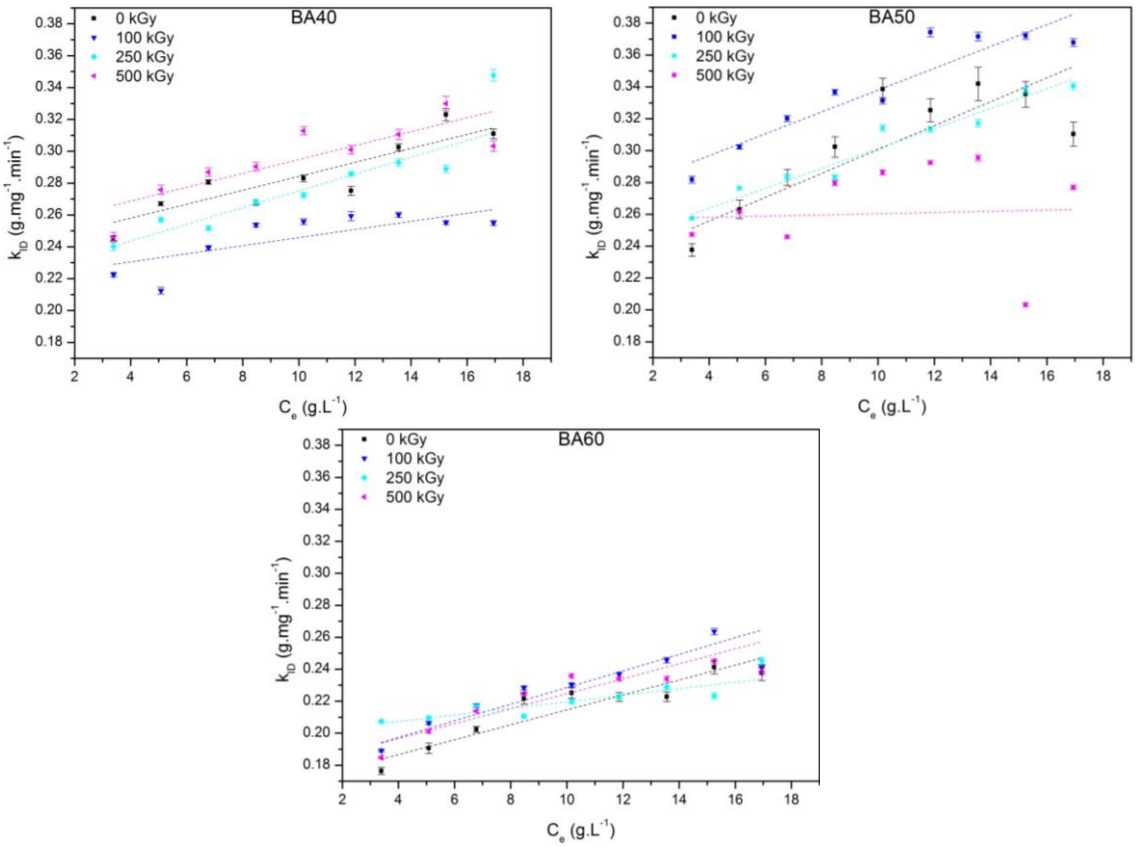

Figure 5-12: The Plots of k_{ID} for All Three Commercial Samples against Solute Concentration Following Various Doses of Gamma Radiation under Standard Atmospheric Conditions

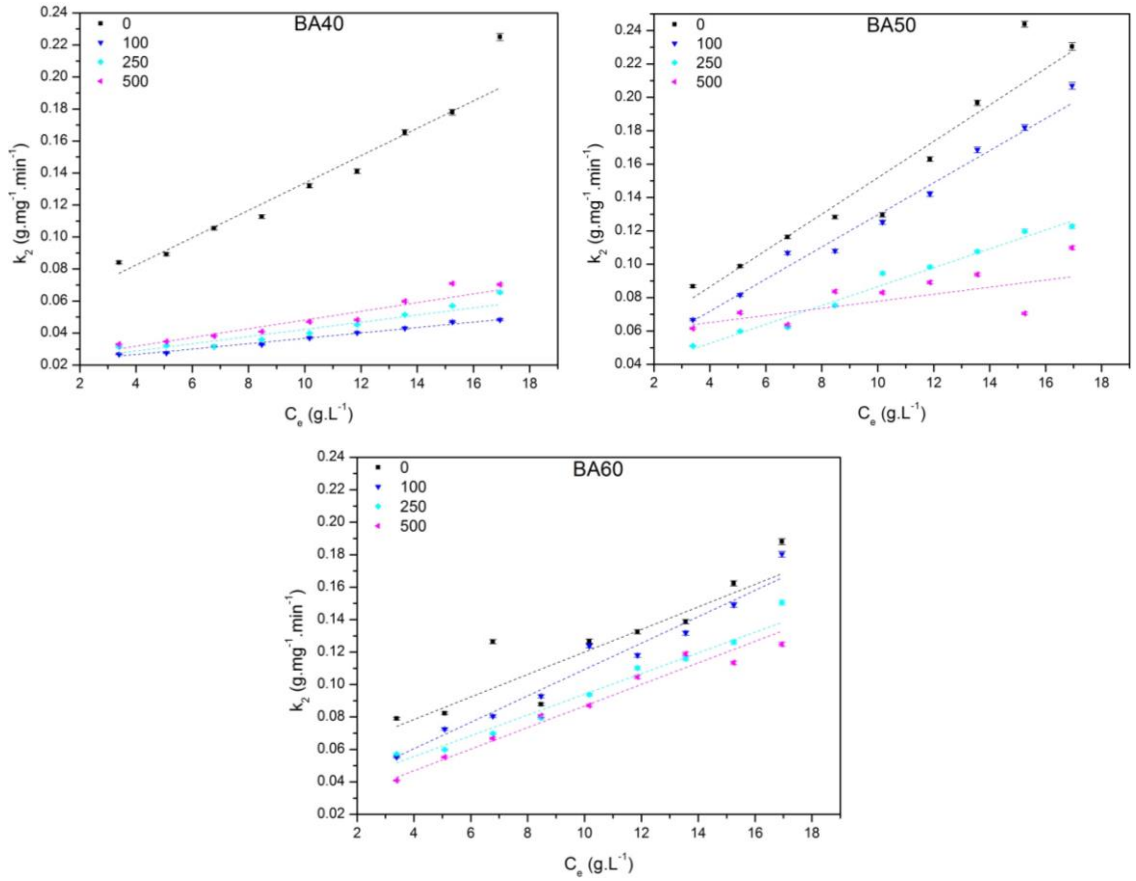

Figure 5-13: The Plots of k_2 for All Three Commercial Samples against Solute Concentration Following Various Doses of Gamma Radiation under Standard Atmospheric Conditions

5.3.7.2 Isothermal Models

For BA40 and BA60 $q_{e,10}$, the equilibrated mass of CO_2 absorbed into the elastomer at 10 bar pressure, increased with radiation dose, Table 5-4 and Figure 5-14. However, for BA50 the value initially increased before decreasing below its original value.

Table 5-4: Change in $q_{e,10}$ for All Three Commercial Samples and the Industrial Seal Following Exposure to Gamma Radiation under Standard Atmospheric Conditions

Radiation Dose (kGy)	$q_{e,10}$ $(x10^{-3}\ kg\ kg^{-1})$		
	BA40	**BA50**	**BA60**
0	20.024 ± 0.006	20.140 ± 0.006	15.625 ± 0.005
100	23.293 ± 0.007	21.234 ± 0.006	17.973 ± 0.005
250	22.481 ± 0.007	20.058 ± 0.006	17.289 ± 0.005
500	22.608 ± 0.007	19.167 ± 0.006	17.596 ± 0.005

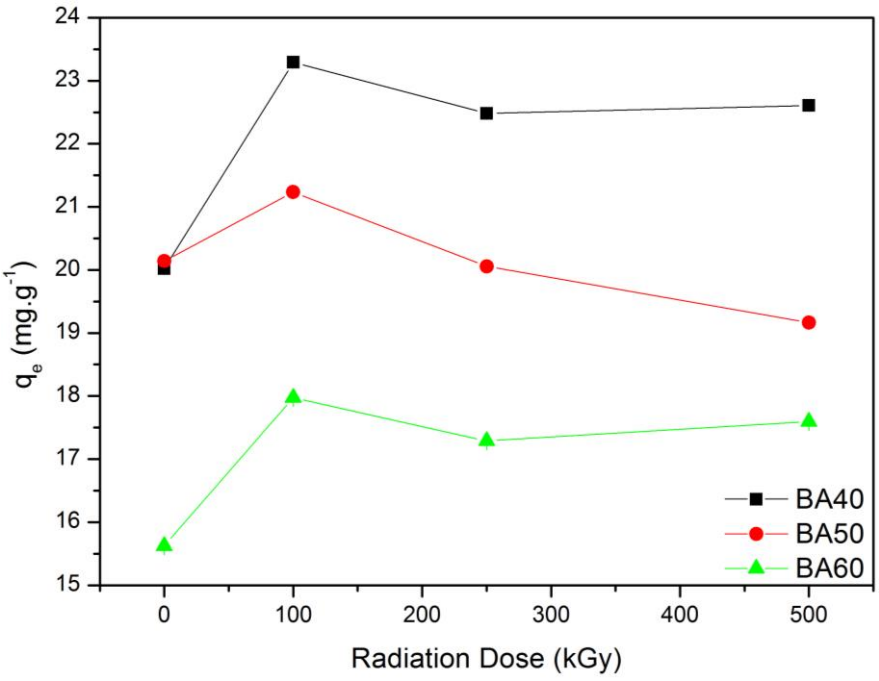

Figure 5-14: The Change in $q_{e,10}$ for All Three Commercial Samples Following Gamma Radiation under Standard Atmospheric Conditions

The percentage change plots reveal the similarity between the changes in BA40 and BA60, Figure 5-15.

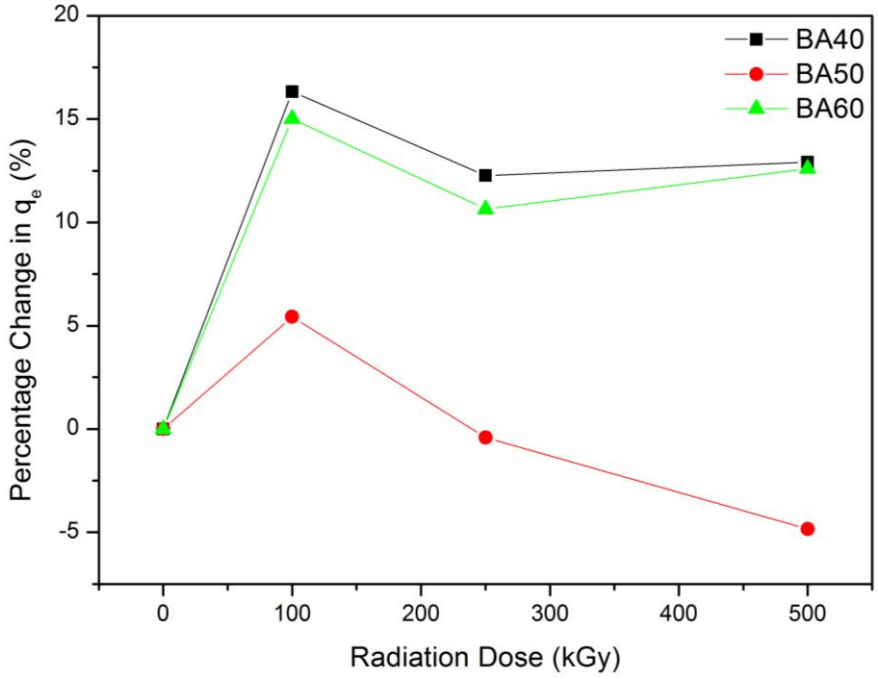

Figure 5-15: The Percentage Change in $q_{e,10}$ for All Three Commercial Samples Following Gamma Radiation under Standard Atmospheric Conditions

After fitting to Freundlich isotherms, n_F showed little change with increasing radiation dose. a_F exhibited a general increase in both BA40 and BA60 whilst this initial increase was followed by a decrease in BA50, Figure 5-16.

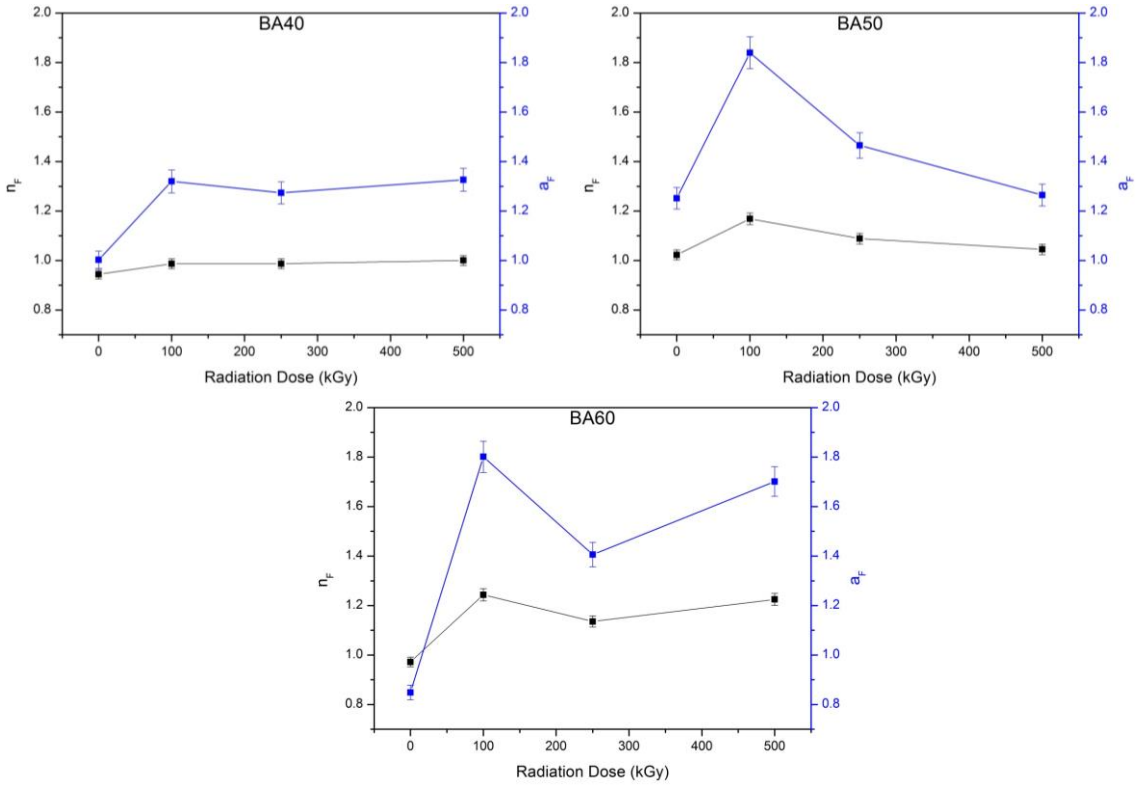

Figure 5-16: The Change in n_F and a_F for All Three Commercial Samples Following Gamma Radiation under Standard Atmospheric Conditions

The percentage change plots highlight the larger effect on BA60, Figure 5-17.

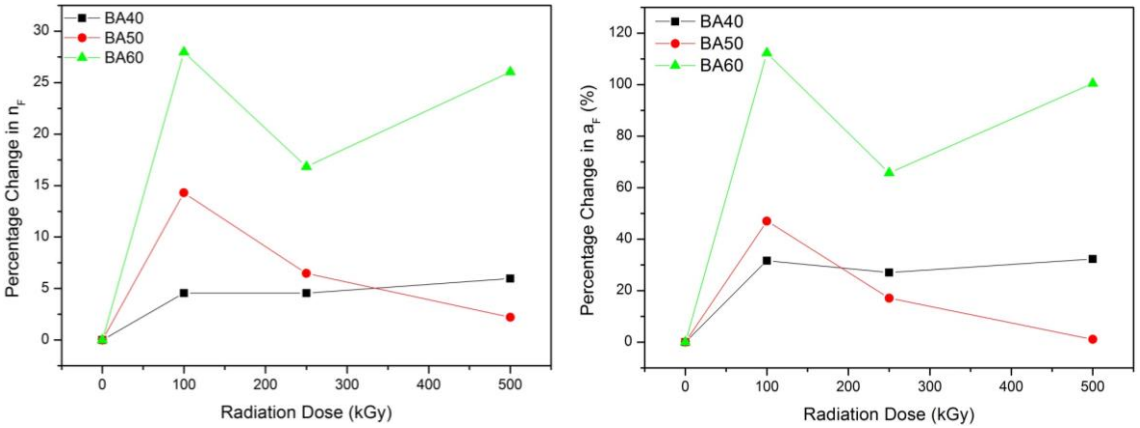

Figure 5-17: The Percentage Change in n_F and a_F for All Three Commercial Samples Following Gamma Radiation under Standard Atmospheric Conditions

5.4 DISCUSSION

5.4.1 SPECTROSCOPY

During manufacture built-in stresses can occur across the microstructure of the elastomer. These will be especially prevalent in a formed shape such as a circular seal. During exposure ionising radiation has resulted in the embrittlement of the surface and these built-in stresses have caused the initiation of multiple cracks.

This crack initiation at the outside curvature of the seal will not only result in crack propagation through external stress but, due to the repeated dynamic movements of the seal, may also provide an escape point for internal fibres. Whilst the embrittlement of the seals through radiation exposure is known and can be accounted for, the development of these micro-cracks will cause it to begin to deteriorate and weaken through a previously un-realised mechanism. This could result in the event of early and unexpected failure if sufficient crack formation has occurred.

The minimal change in IR spectra seen above is in agreement with the work by [148, 49, 164] who found no change in the peak height at 2235 cm^{-1} and the work by *Hassan et al.* [45] who showed only very minor variations in peak height throughout the whole spectra.

For BA40, Figure 5-18, the similar decrease in peak heights up to 50 kGy of gamma radiation seen in the *cis* configuration of C=C and the chain-end vinylidene group $C{=}CH_2$ at 741 and 918 cm^{-1} respectively suggest that it is these two functional groups of the BDN unit that have undergone ionisation and subsequent degradation. However, at higher doses the *trans* configuration of C=C at 964 cm^{-1} and the C≡N at 2235 cm^{-1} begin to decrease, suggesting a crossover point at which the ACN unit begins to degrade through interaction with the *trans* vinyl functional groups on the BDN unit. The CH_2 methylene group showed very little change across all radiation doses, as expected. A significant portion of the bonds attributable to additives and inclusions have undergone dramatic reductions with the most notable being that at 1015 cm^{-1}, which suggests these compounds have leached out of the material during the exposure.

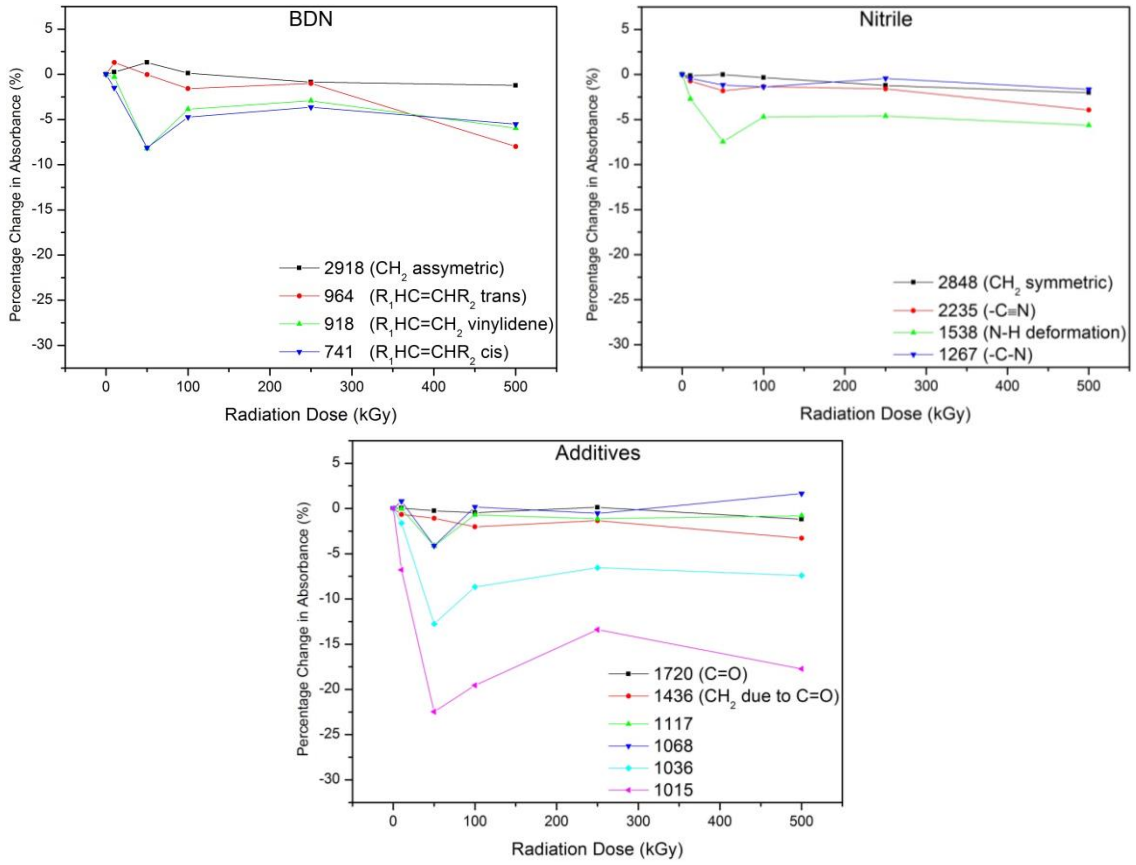

Figure 5-18: The Change in Absorbance for the Bonds that are Attributed to BDN, Nitrile and Additive Content Respectively in BA40 Following Exposure to Gamma Radiation under Standard Atmospheric Conditions

The spectra for BA50, Figure 5-19a showed more complex behaviour with degradation of the *cis* C=C and chain-end vinylidene group C=CH_2 up to 10 kGy followed by the *trans* C=C up to 50 kGy, after which degradation of the *cis* and chain end groups resumed. However, the C≡N appeared to degrade at higher radiation doses as well. With the general decrease in peak height being lower than that seen in BA40 it is possible that in BA50 both the BDN and ACN units were becoming ionised concurrently during radiation exposure.

In BA60 all backbone-attributable peak heights increased, Figure 5-19b, suggesting leaching of a substance that previously hindered the visibility of bond vibrations.

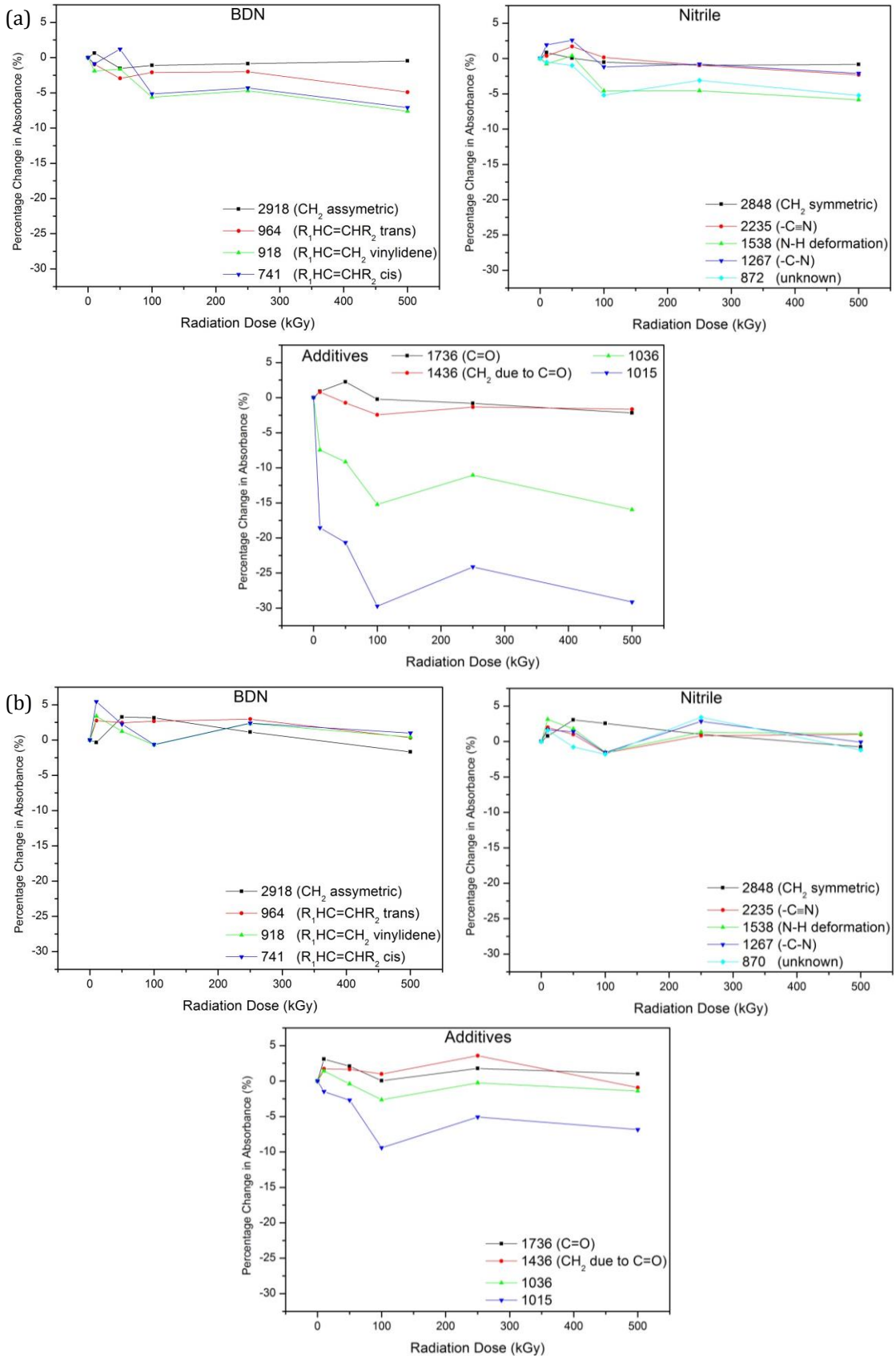

Figure 5-19: The Change in Absorbance for the Bonds that are Attributed to BDN, Nitrile and Additive Content Respectively in (a) BA50 and (b) BA60 Following Exposure to Gamma Radiation under Standard Atmospheric Conditions

5.4.2 Swelling Behaviour

The decrease in $\Delta_{M\%}$ with radiation dose is expected due to the formation of crosslinks in the structure and the resultant restriction to structure expansion. BA40 and BA60 exhibited similar changes in $\Delta_{M\%}$ with radiation dose whilst BA50 showed a reduced effect suggesting that either the component responsible for inducing swelling-restrictive crosslinking following gamma radiation is more prevalent in BA40 and BA60 or there is a factor in BA50 that reduces the effect of swelling-restrictive crosslinking.

The industrial seal exhibited the largest change in $\Delta_{M\%}$ with radiation dose, suggesting there is a component within the material that makes it more susceptible to gamma radiation attack. However, to incur a 5% change in swelling capacity a radiation dose of over 50 kGy is required, which is significantly larger than the 30 kGy calculated for a full 6 $year$ service life and thus radiation damage alone is considered insufficient to affect the swelling behaviour of the seal.

5.4.3 Glass Transition Temperature

When compared to the literature [148] the results in this work show a congruent but reduced relationship with radiation dose Figure 5-20. However, the experiments carried out in [148] used an electron beam radiation source at a dose rate of approximately 9.3 $Gy\ s^{-1}$. It is possible that the dose rate is having an effect as for crosslinking to occur two units will need to be ionised within close proximity to one another; a higher dose rate will increase the likelihood of neighbouring units to become ionised within the same time frame and would therefore lead to an increase in crosslinking.

Following the initial decrease in T_g seen in BA50 and BA60 all three commercial samples increased at the same rate suggesting that the gamma-induced crosslinking is having the same effect on the gel content within all samples.

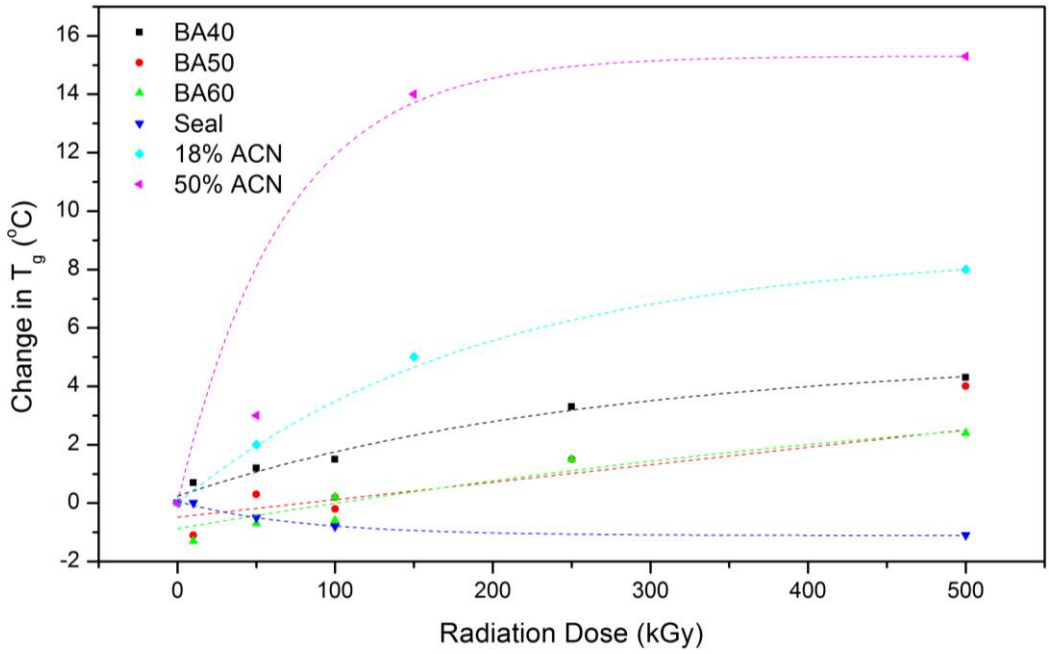

Figure 5-20: The Absolute Change in T_g for All Three Commercial Samples and the Industrial Seal Following Exposure to Gamma Radiation under Standard Atmospheric Conditions Compared to Data Found in the Literature [148]

The industrial seal exhibited a minimal decreasing trend in T_g with radiation dose that is not seen in other samples. This could be due to the presence of the brass wire and glass cloth that may be obstructing the formation of larger gel networks, however, these changes are within the margin of error and so limited conclusions can be drawn from these results.

5.4.4 Mechanical Behaviour

The initial decrease and subsequent increase in required load to induce deflection seen in BA50 and BA60 would suggest initial chain scission followed by crosslinking. This is supported by the similar trend seen in RF and the decreasing trend seen in the deviation of the relaxation curve from the origin, Figure 5-21.

Relaxation deviation decreased with increasing radiation dose, although BA40 showed an initial sharp increase, Figure 5-22. The industrial seal exhibited anomalous behaviour at 10 and 50 kGy before returning to an observable trend.

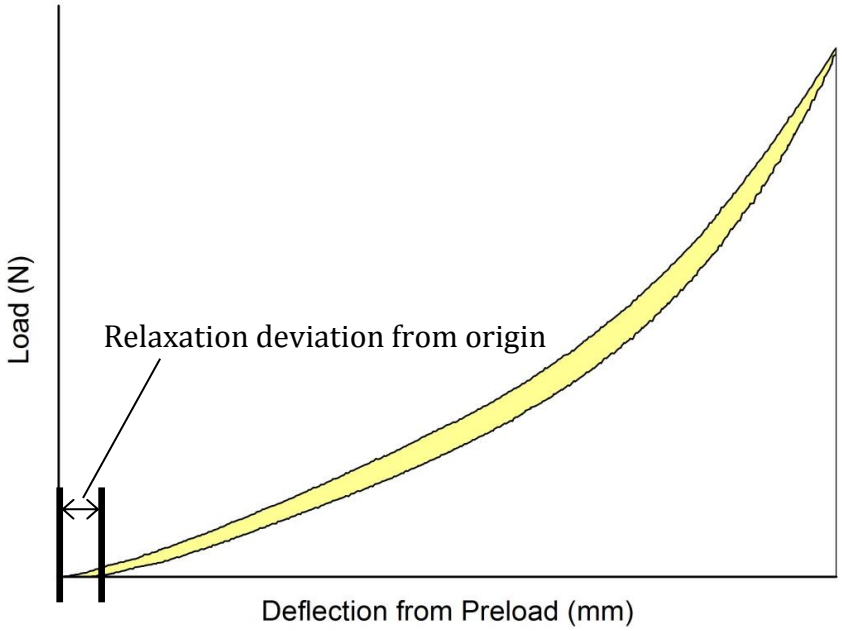

Figure 5-21: Calculation of Relaxation Deviation from the Origin

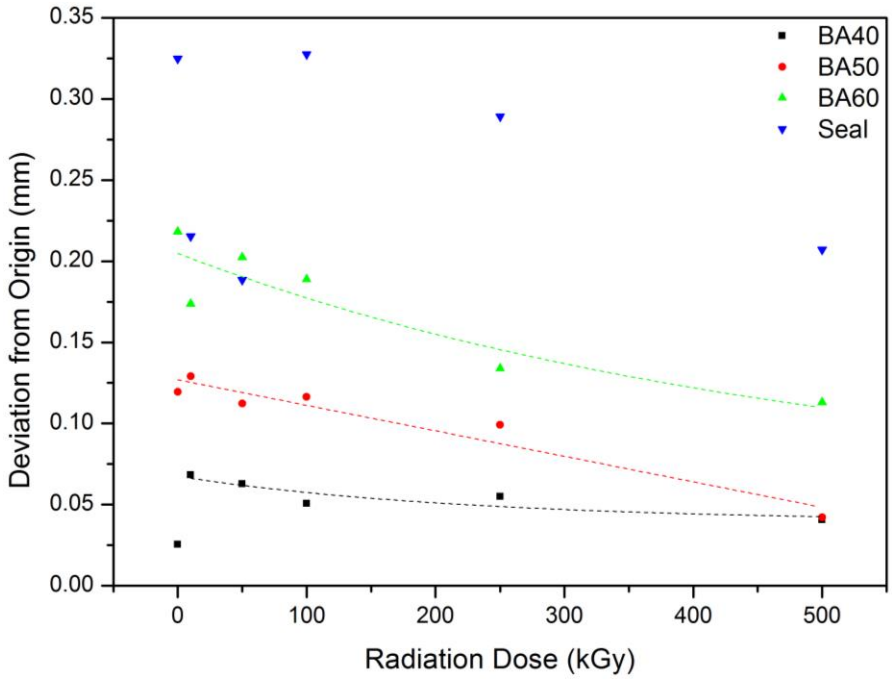

Figure 5-22: The Change in Relaxation Deviation for All Three Commercial Samples and the Industrial Seal Following Exposure to Gamma Radiation under Standard Atmospheric Conditions

Comparison of the increasing RF against the decreasing relaxation deviation reinforces the principle that long-range scale rearrangements are restricted by the

increasing crosslink density and recovery from mechanical deformation is increasingly through local-scale readjustments of molecular order.

The mechanical behaviour of the industrial seal is difficult to analyse due to the abnormal behaviour under compression and relaxation, discussed in Chapter 4. However, the microstructural changes discussed above will be prevalent in the industrial seal albeit to a somewhat lesser extent owing to the presence of brass wire and glass cloth and the potential disturbances they may induce.

5.4.5 CO_2 Absorption Behaviour

5.4.5.1 Absorption Kinetics

The lack of change in k_{ID} following exposure to gamma radiation under standard atmospheric conditions and the reducing effect it has on k_2 suggests the CO_2 molecules initially diffuse through the microstructure following the intraparticulate model before shifting to the pseudo-second order model as the material expands. It is in this later stage of absorption where the crosslinks begin to have a restrictive effect on the microstructural expansion of the polymer matrix and therefore reduce the rate of uptake. The dose effect has been determined through the calculation of the integral of the k_2 linear fits between 3 and 17 $kg\ m^{-3}$ CO_2 in the gaseous phase; a decreasing integral therefore relates to a lowering of the k_2 values, Figure 5-23. The declines in all values show that crosslinks are hindering the expansion of the matrix and have a more pronounced effect in BA40 and the lowest effect in BA60.

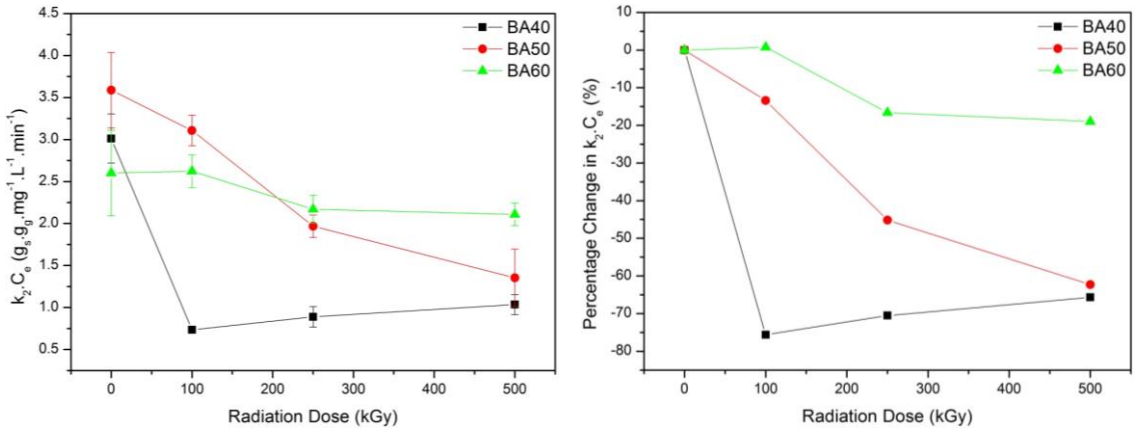

Figure 5-23: Integral k_2 Plots and Percentage Change of Integral k_2 Plots

5.4.5.2 Isothermal Models

$q_{e,10}$ showed an initial increase with radiation exposure up to a dose of 100 kGy before a decrease in all commercial samples suggesting a competition between crosslinking effects reducing the absorption capacity and the increasing dominance of non-polar compounds, such as BDN, increasing the chemical affinity.

BA40 and BA60 exhibited similar percentage changes in $q_{e,10}$whilst BA50 showed almost a 30% lower increase up to 100 kGy and a much larger subsequent decrease suggesting that the crosslinking behaviour has a much more dominating effect in BA50 compared to BA40 and BA60.

n_F, or the 'Strength of Interaction' parameter, and a_F both increased for all commercial samples up to a dose of 100 kGy where they remained fairly constant. n_F determines the curvature of the q_e vs C_e plot and its increase with radiation dose details the decreasing gradient of this plot whilst a_F determines the initial gradient. The similar behaviour of the two parameters but contrasting effects on CO_2 uptake suggest that a_F can be related to the materials affinity to absorption of CO_2 and n_F to the limiting effects of gamma-induced crosslinks. The much larger changes seen in a_F therefore show that gamma radiation has a greater effect on the affinity of the material to CO_2 than the 'road-block' effects resulting from crosslinking.

5.4.6 Cross-Analysis of Samples

Exposure to gamma radiation has caused a fairly similar change in all samples when comparing their RF against their crosslink determining properties, Figure 5-24.

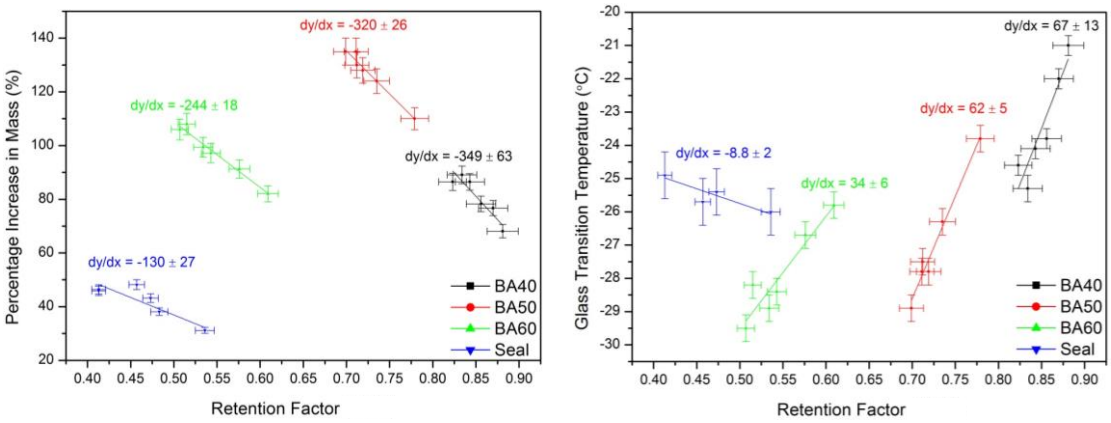

Figure 5-24: Comparison of Change in $\Delta_{M\%}$ and T_g against RF for All Three Commercial Samples and the Industrial Seal Following Exposure to Gamma Radiation under Standard Atmospheric Conditions

Gamma radiation induced a similar change in T_g with each sample whilst exhibiting a larger change in RF with the harder samples. This suggests that, following exposure to gamma radiation, the gel network increased at the same rate in each sample whilst the crosslink density increased at a higher rate in the harder samples. One explanation for this behaviour is the interaction between the elastomer chains and the larger proportion of fillers used to increase the hardness in BA60 resulting in an increased number of chains becoming part of the gel network. Therefore the chains involved in the new crosslinks were already part of the gel network and therefore did not increase this value. BA50 showed a considerably larger decrease in the deviation from origin, indicating a more rapid relaxation and a preference in the sample towards local-scale readjustments of molecular order over long-range-scale rearrangements of large polymer chains.

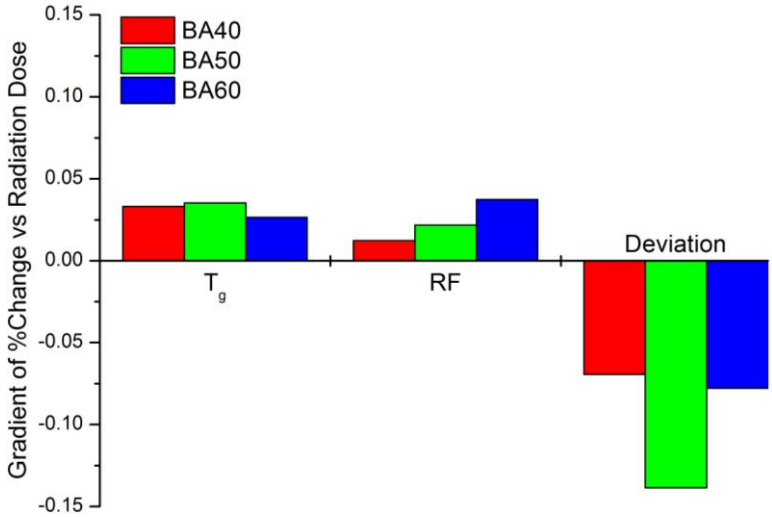

Figure 5-25: The Gradients of the %Change vs Radiation Dose Plots for T_g, RF and Deviation from the Origin Characteristic Properties for all Three Commercial Samples Following Exposure to Gamma Radiation under Standard Atmospheric Conditions

A comparison between the ability of the materials to absorb CO_2 and to absorb toluene reveals a further similarity between BA40 and BA60, Figure 5-26. This is interesting behaviour as the development of crosslinks would result in a restriction of the molecular matrix to expand and thus reduce the ability of all samples to absorb toluene, as seen, yet the data also highlights the increased ability of BA40 and BA60 to absorb CO_2.

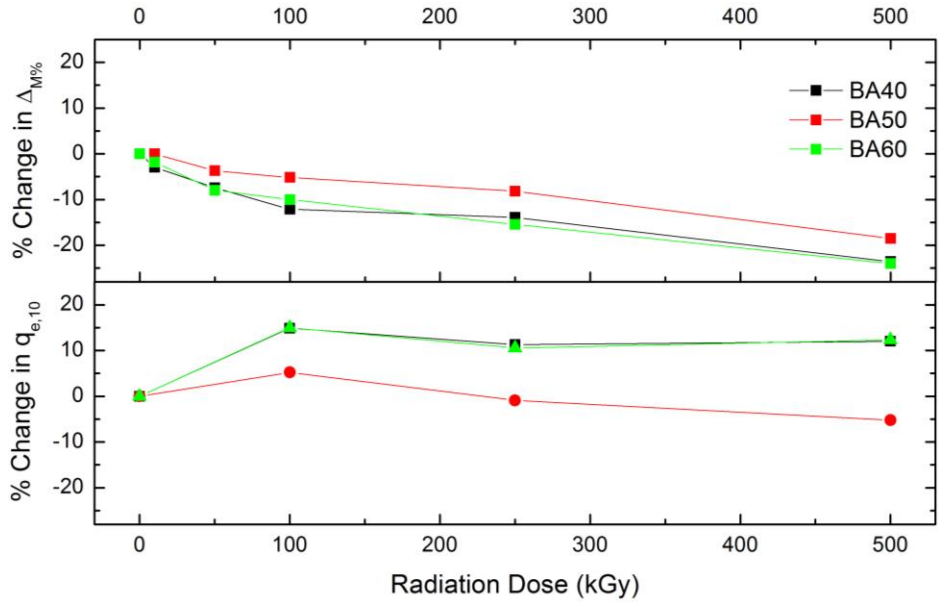

Figure 5-26: The Percentage Change in $\Delta_{M\%}$ and $q_{e,10}$ for All Three Commercial Samples Following Exposure to Gamma Radiation under Standard Atmospheric Conditions

Vijayabaskar, Tikku and Bhowmick [148] exposed NBR samples to electron beam radiation and found that those with a higher BDN content exhibited larger changes in all characteristic properties, except T_g, than those with a higher ACN content. NMR analysis also revealed an increase in spectroscopic crosslink densities for samples with larger C-C linkages i.e. the higher BDN-containing samples. One can therefore infer that the propensity for the crosslink density of NBR samples to be affected by radiation is proportional to their BDN content. However for T_g, and the portion of chains included in the gel network, it is their ACN content that determines the degree of change induced by radiation. This can be explained by higher BDN contents instilling a greater proclivity for crosslink clustering. This clustering mechanism explains the reduced dose effect seen in BA50 for $\Delta_{M\%}$ and $q_{e,10}$ and also the increased penchant for rapid relaxation.

5.5 Conclusions

A nitrile rubber chevron seal and three commercially available nitrile rubber samples at grades BA40, BA50 and BA60 have been exposed to gamma radiation at a dose rate of approximately 1.67 $Gy\ s^{-1}$ to total absorbed doses of $10, 50, 100, 250$ and $500\ kGy$.

SEM revealed the embrittlement of the seal surface through the development of microcracks perpendicular to the curvature of the seal.

From the IR spectra it was suggested that BA40 initially degraded through ionisation of the BDN monomers which caused crosslinking between the *cis* C=C in BDN and the C=CH_2 vinylidene groups. However, at higher radiation doses this was believed to shift towards a breakdown of the ACN monomers through an interaction between the *trans* C=C in BDN and the C≡N in ACN. BA50 appeared to degrade both monomers simultaneously.

The decrease of $\Delta_{M\%}$ and increase in T_g, required load for a set deflection and RF with radiation dose suggested the formation of crosslinks, which only began to hinder absorption in the latter phase of expansion, when a PSO model describes

the rate of uptake. However, they have been shown to affect the affinity of the samples more than they affect the expansion of the network.

A comparison between the samples suggests an interaction between the strengthening filler particles and the polymer chains that negatively affects the rate of gel formation within the microstructure. A trend has been identified between BDN content and the potential for crosslink clustering that will reduce the dose effect and potentially increase radiation resistance in terms of physical and mechanical properties.

6 PRESSURISED CO_2 EFFECTS ON GAMMA-INDUCED DEGRADATION OF NBR

6.1 INTRODUCTION

Chapter 5 investigated the effects of radiation exposure on the industrial seal and the commercial samples. However, in service the seals are under a pressurised CO_2 environment during the radiation exposure and this environment may affect the damage seen. To assess the affect of the CO_2 environment on the radiation-induced damage a 'Pressure Pot' was designed and manufactured by the University of Sheffield for carrying out irradiation experiments whilst under pressure. Each set of samples were placed in separate pots and the chambers pressurised up to $3.2x10^6\ MPa$ of CO_2. Each pot was irradiated to its pre-set dose level, ensuring the same dose rate was met with the same source radiation as the samples in Chapter 5. The results were then cross-analysed against those in Chapter 5 to identify any similarities and differences.

6.2 EXPERIMENTAL

6.2.1 RADIATION EXPOSURE AT HIGH PRESSURES

Elastomeric seals are the most common component used to create a pressure boundary. Unfortunately this poses a problem in the manufacture of pressure pots for irradiating samples as the elastomers will embrittle and the pressure boundary will be compromised. This was tackled through the use of a brass pip and compressing bolt, Figure 6-1. Figure 6-2 shows a schematic diagram of the completed pot and a digital photograph.

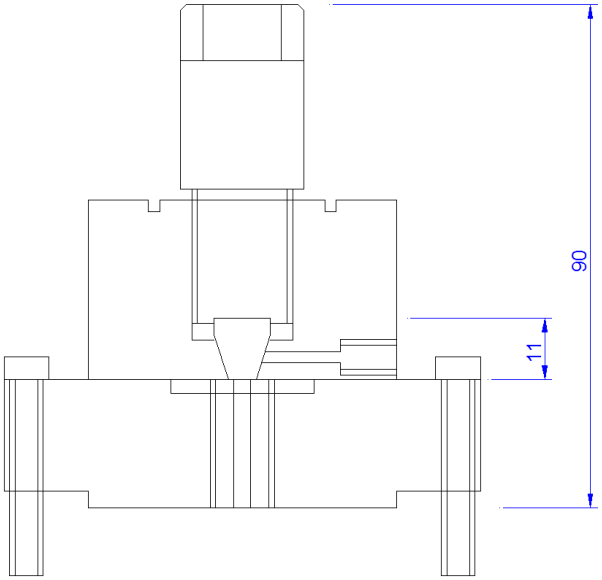

Figure 6-1: Diagram of Pressurising Valve and Assembly Lid (All Dimensions are in mm)

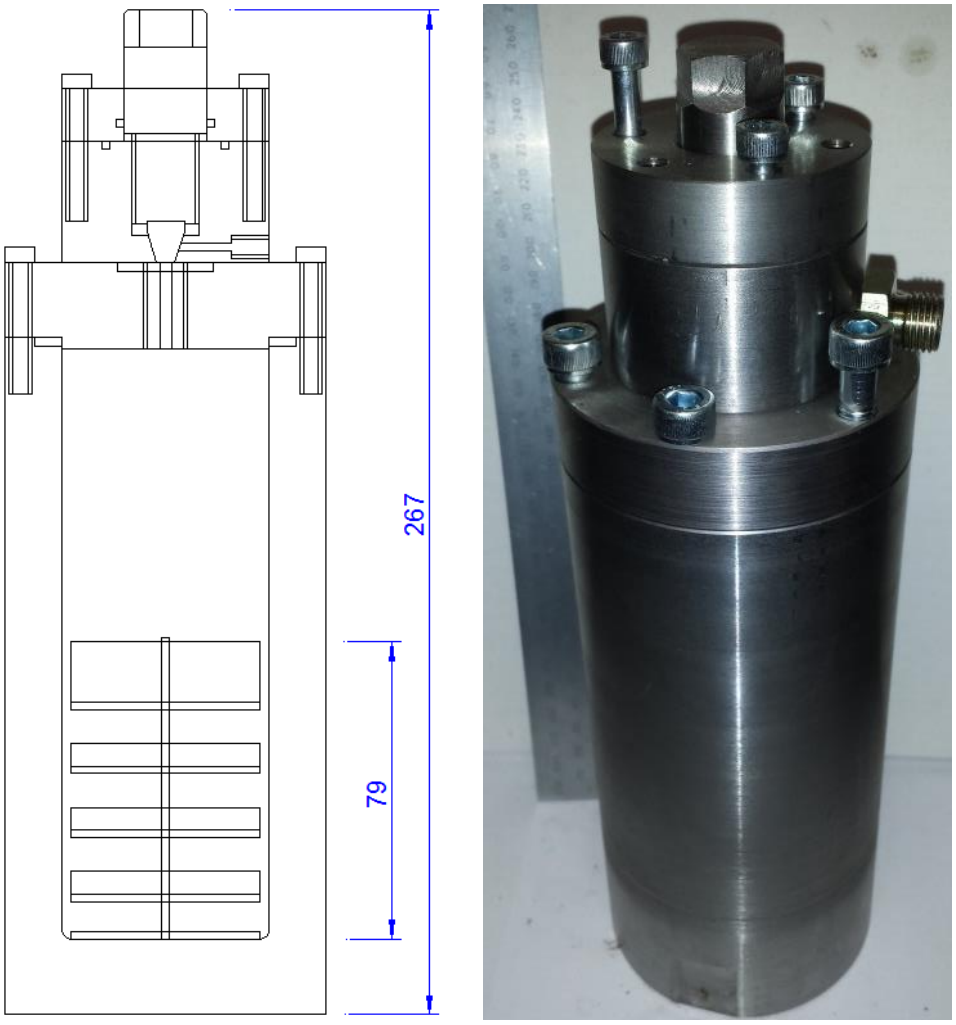

Figure 6-2: Diagram and Photograph of Complete Pressure Pot (All Dimensions are in mm)

To ensure the samples were exposed to the same dose rate as those in Chapter 5 when in the cobalt irradiator, the pots were placed on a turntable closer to the radiation source that, when accounting for linear absorption, resulted in a dose rate of approximately 1.67 $Gy\ s^{-1}$.

6.2.2 Optical Microscopy

A Hitachi TM3030 desktop Scanning Electron Microscope was used at low vacuum to inspect the surface of the samples. All images were taken in SEI mode to provide topographical information.

6.2.3 Infrared Spectroscopy

FTIR Spectroscopy was carried out on a Perkin Elmer Frontier FTIR with a diamond ATR attachment between 4000 and 500 cm^{-1} at a resolution of 4 $scans\ cm^{-1}$ and an accumulation of 4 $scans$. The spectra were taken approximately 4 mm into the bulk of the sample negating any surface effects.

6.2.4 Swelling Behaviour

The experimental procedure outlined in Chapter 3 was used to find $\Delta_{M\%}$ and $\Delta_{V\%}$ following 72 $hours$ soaking in toluene.

6.2.5 Glass Transition Temperature

A Perkin Elmer diamond DSC was used to find the heat flow against temperature data for the samples. From this T_g was manually determined.

6.2.6 Mechanical Behaviour

7 mm diameter pellets were run through a compression and relaxation programme on a TA500 at a rate of 1 $mm\ min^{-1}$ at pre-set deflections of 1, 2, 3, 4 and 5 mm.

6.2.7 CO_2 Absorption Behaviour

$50 - 100\ mg$ of sample was cut into small monoliths of approximately 1 mm^3 volume. Each sample was placed into a Hiden Isochema IGA-002 and taken down to vacuum for 90 $mins$ before their increase in weight was recorded following isothermal $0.1x10^6\ Pa$ pressure increments between $0.1x10^6$ and $1x10^6\ Pa$.

6.3 Results

6.3.1 Visual Inspection and Manual Handling

6.3.1.1 CO_2 Exposure

To assess the effects of depressurisation procedure a set of samples were loaded into two of the above described pots and pressurised to $3.2x10^6\ Pa$ CO_2. After 72 hours in this environment the pots were depressurised following two procedures:

1. $0.34x10^6\ Pa$ pressure drop with subsequent 10 $minute$ wait until the pressure reads below $1.5x10^6\ Pa$ at which point the pressure is dropped to atmospheric
2. A continuous pressure drop of approximately $2.5x10^3\ Pa\ s^{-1}$

Within 30 $minutes$ of Depressurisation Procedure 1 (DP1) bubble formation was evident in both BA40 and BA50, Figure 6-3 and Figure 6-4. The bubbles grew in size with the passing of time and some intersected and combined. BA40 generally produced smaller bubbles than BA50 as opposed to BA60, which did not form any singular bubbles but did enlarge in size.

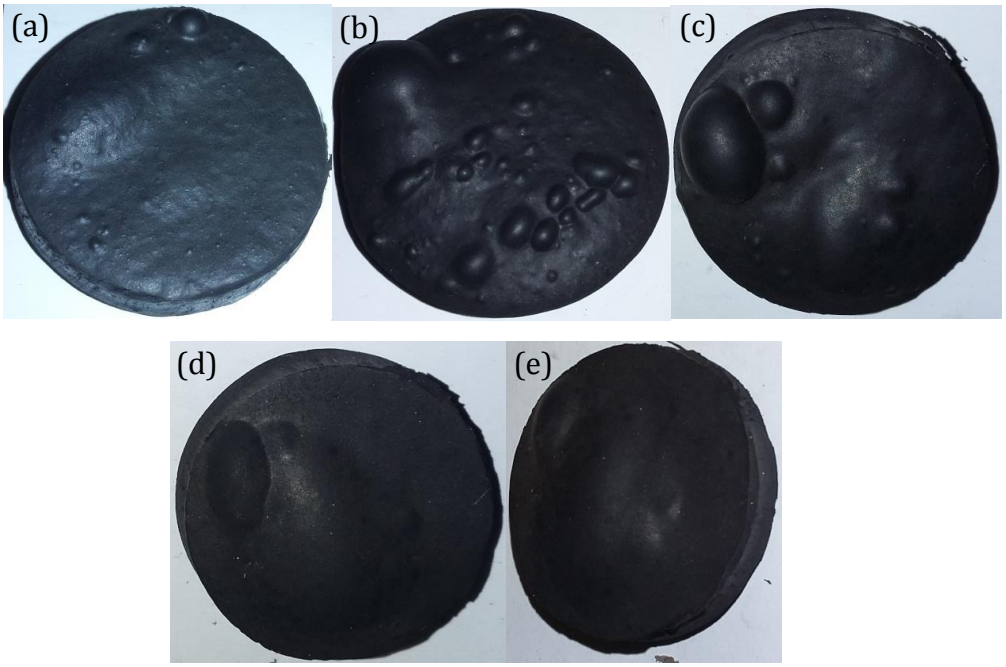

Figure 6-3: Photographs of BA40 at (a) 30, (b) 90, (c) 270, (d) 2730 and (e) 4560 Minutes after Step-Down Depressurisation from 3.2 MPa CO_2

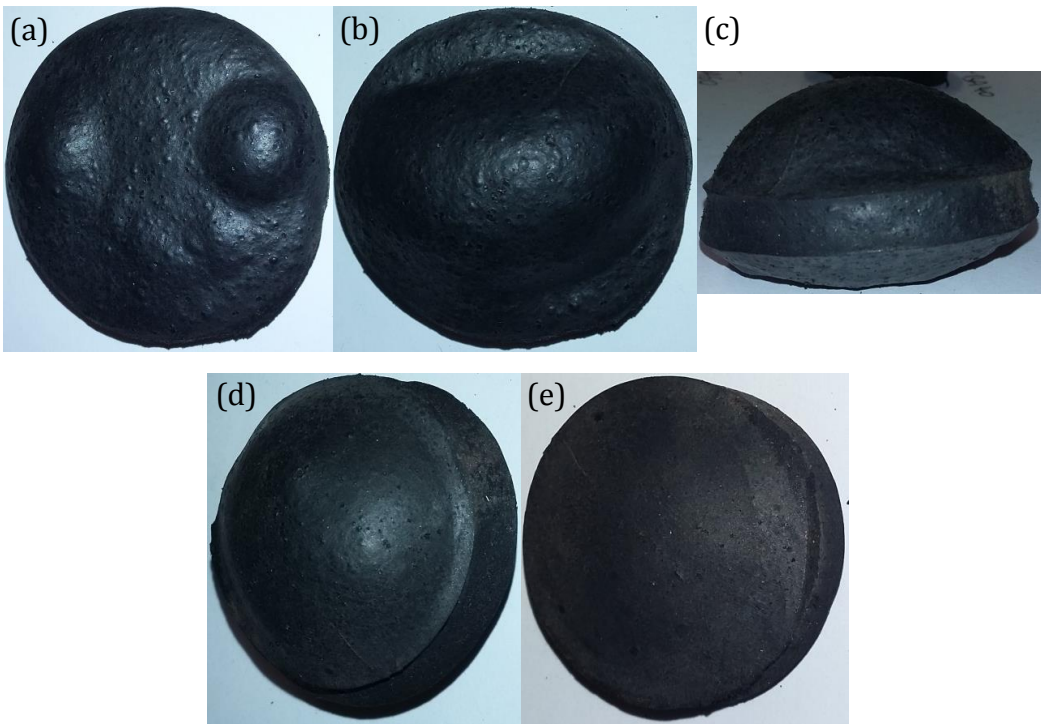

Figure 6-4: Photographs of BA50 at (a) 75, (b) 105, (c) 105, (d) 270 and (e) 2730 Minutes after Step-Down Depressurisation from 3.2 MPa CO_2

Following Depressurisation Procedure 2 (DP2) the bubbles that were formed were of significantly smaller size in both BA40 and BA50, Figure 6-5 and Figure 6-6.

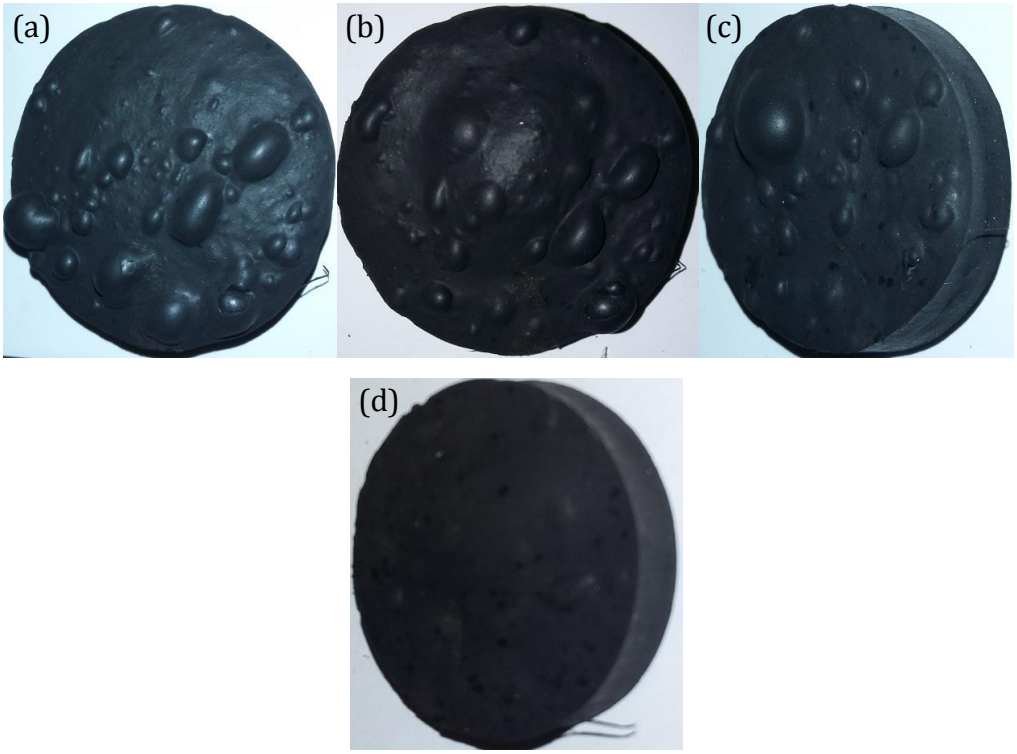

Figure 6-5: Photographs of BA40 at (a) 90, (b) 160, (c) 330 and (d) 4620 Minutes after Continuous Depressurisation from 3.2 MPa CO_2

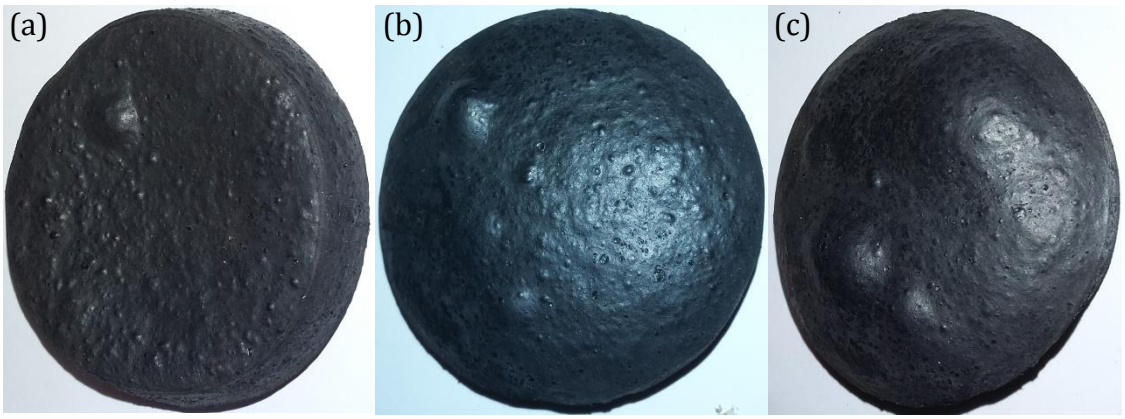

Figure 6-6: Photographs of BA50 at (a) 60, (b) 160 and (c) 330 Minutes after Continuous Depressurisation from 3.2 MPa CO_2

6.3.1.2 FOLLOWING RADIATION

All three commercial samples showed little change after 10 kGy radiation at high pressure, apart from the appearance of some darker spots on BA40, Figure 6-7.

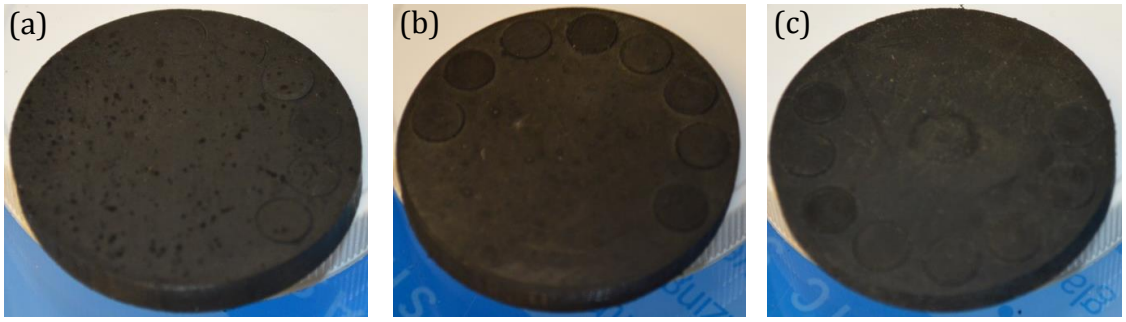

Figure 6-7: Digital Photographs of (a) BA40, (b) BA50 and (c) BA60 Following 10 kGy Gamma Radiation under 3.2 MPa CO_2 After a Significant Waiting Period

After 100 kGy radiation there was evidence of some bubbling in BA40 and BA50, Figure 6-8.

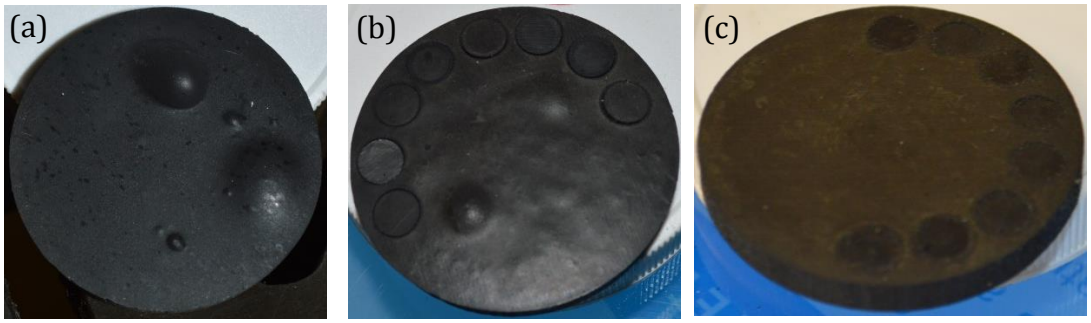

Figure 6-8: Digital Photographs of (a) BA40, (b) BA50 and (c) BA60 Following 100 kGy Gamma Radiation under 3.2 MPa CO_2 After a Significant Waiting Period

Figure 6-9 shows the state of all commercial samples following immediate removal from the pressure pots after 250 kGy radiation exposure. Severe bubbling can be seen in BA40 whilst BA50 and BA60 show doming.

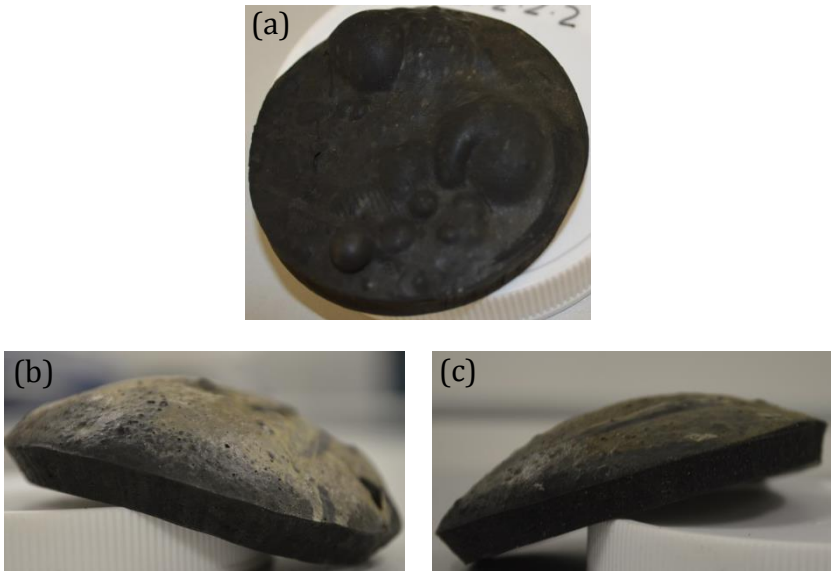

Figure 6-9: Digital Photographs of (a) BA40, (b) BA50 and (c) BA60 Following 250 kGy Gamma Radiation under 3.2 MPa CO_2 Immediately After Removal from Pressure Pots

After one week BA50 and BA60 returned to their original shape whilst BA40 still had some slight bubbling. The marks on Figure 6-10 b and c suggest that a substance leached out of BA50 and BA60.

Figure 6-10: Digital Photographs of (a) BA40, (b) BA50 and (c) BA60 Following 250 kGy Gamma Radiation under 3.2 MPa CO_2

Following 500 kGy of gamma radiation no bubbling was seen in any of the commercial samples but the surface of BA50 and BA60 did have a much shinier finish, Figure 6-11.

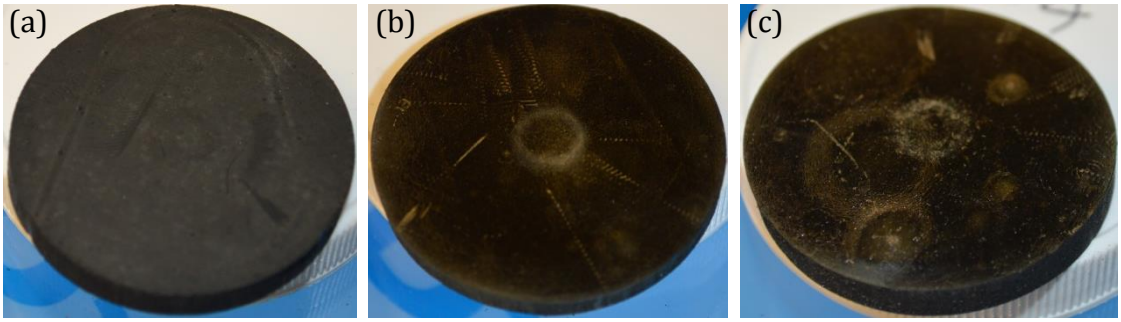

Figure 6-11: Digital Photographs of (a) BA40, (b) BA50 and (c) BA60 Following 500 kGy Gamma Radiation under 3.2 MPa CO_2

6.3.2 Scanning Electron Microscopy

SEM revealed no further changes to the structure.

6.3.3 Infra-Red Spectroscopy

As with irradiation under atmospheric conditions the main difference in the IR spectra was elimination of the peak at 1015 cm^{-1}.

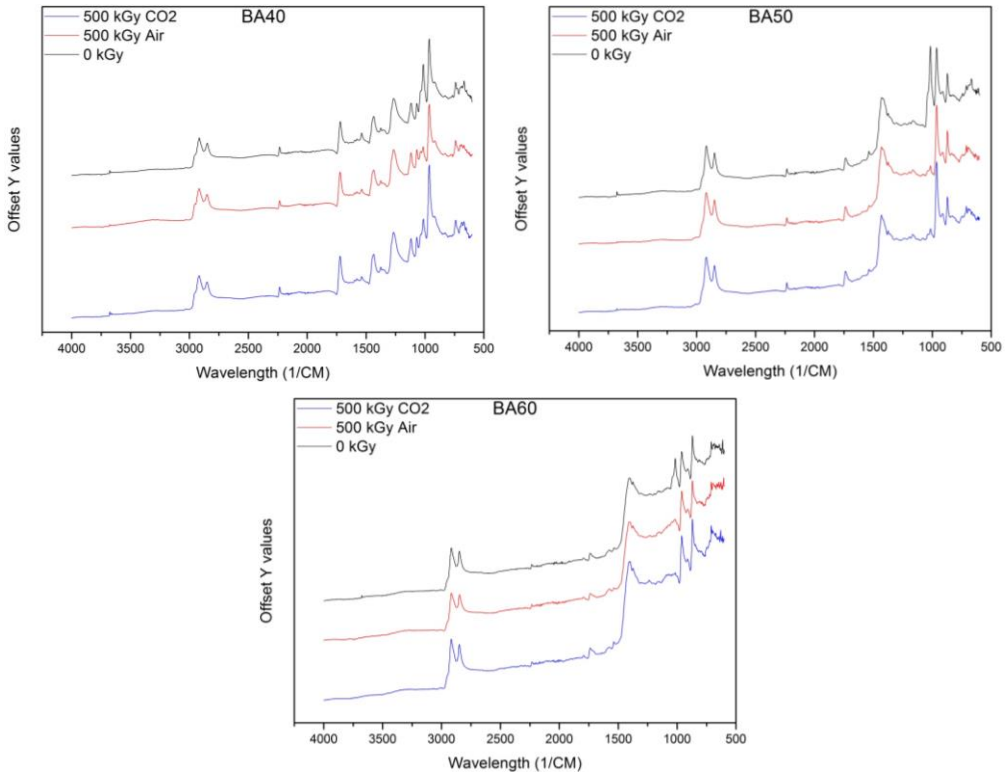

Figure 6-12: ATR-FTIR Spectra of BA40, BA50 and BA60 in an As Received Condition and Following 500 kGy of Gamma Radiation under Standard Atmospheric Conditions and 3.2 MPa CO_2

6.3.4 Swelling Behaviour

$\Delta M_{\%}$ for all three commercial samples showed marginally higher values at lower radiation doses when exposed to gamma radiation under $3.2x10^6\ Pa$ CO_2 than under standard atmospheric conditions, however, the changes do fall within the margin of error.

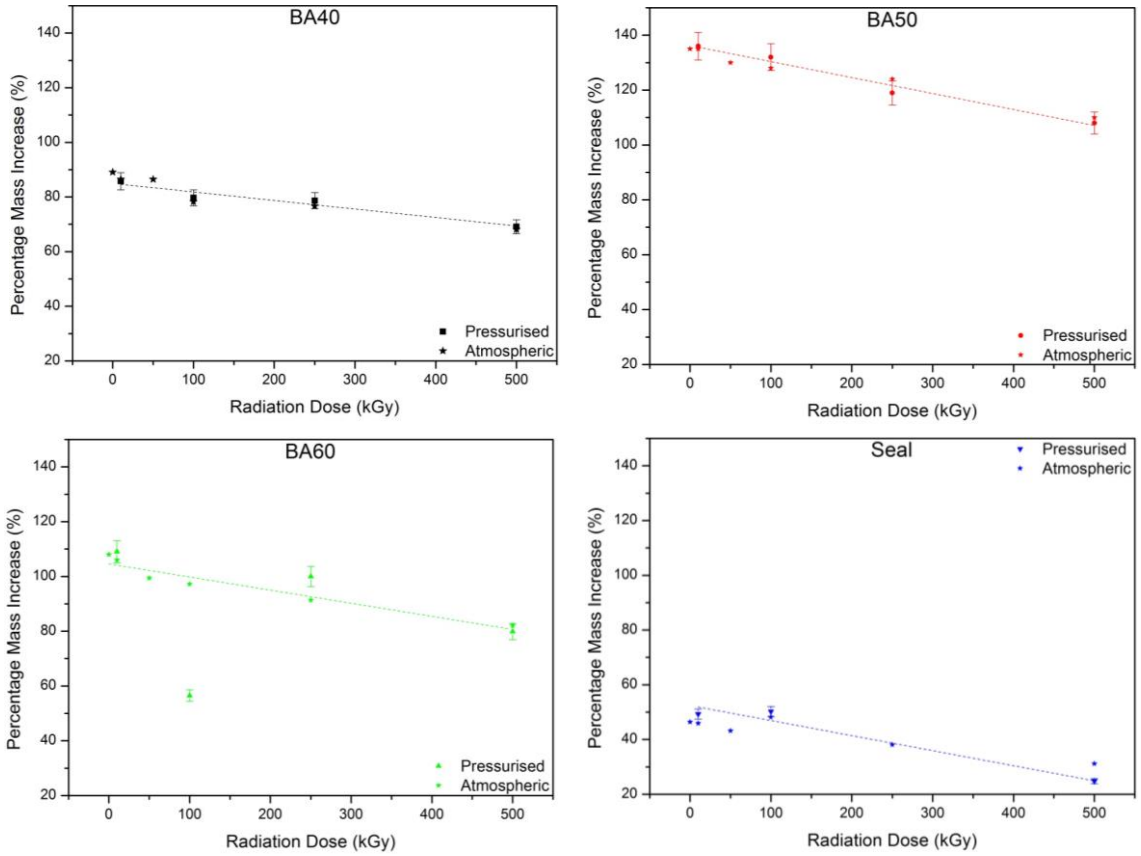

Figure 6-13: The Change in $\Delta_{M\%}$ for All Three Commercial Samples and the Industrial Seal Following Exposure to Gamma Radiation under 3.2 MPa CO_2 Compared against Exposure under Standard Atmospheric Conditions

6.3.5 Glass Transition Temperature

The calculated T_g values showed a decreased change in BA40 with radiation exposure under $3.2x10^6\ Pa$ CO_2 compared to those found in Chapter 5. However BA50 and BA60 showed no change and the seal displayed significantly erratic results.

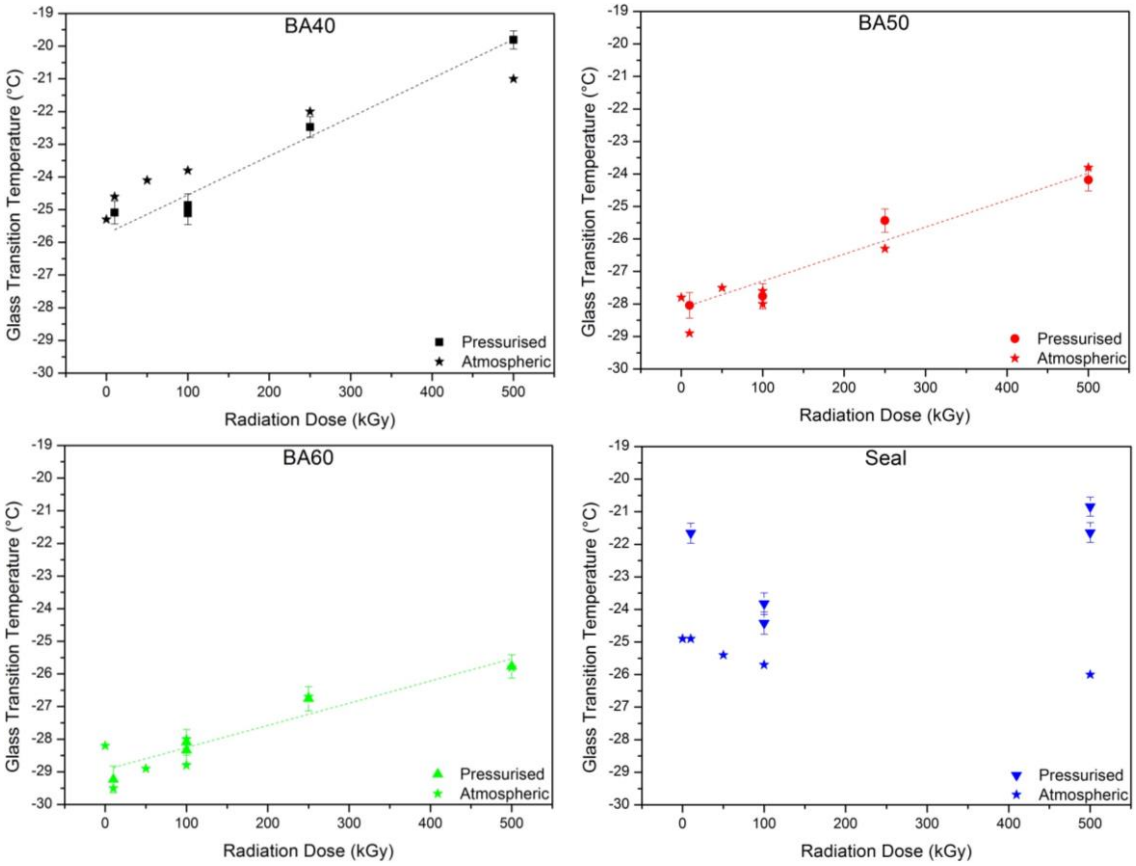

Figure 6-14: The Change in T_g for All Three Commercial Samples and the Industrial Seal Following Exposure to Gamma Radiation under 3.2 MPa CO_2 Compared against Exposure under Standard Atmospheric Conditions

6.3.6 Mechanical Behaviour

The presence of high pressure CO_2 during the irradiation procedure resulted in generally lower RFs for BA50 whilst BA40 and BA60 showed similar behaviour to that in Chapter 5.

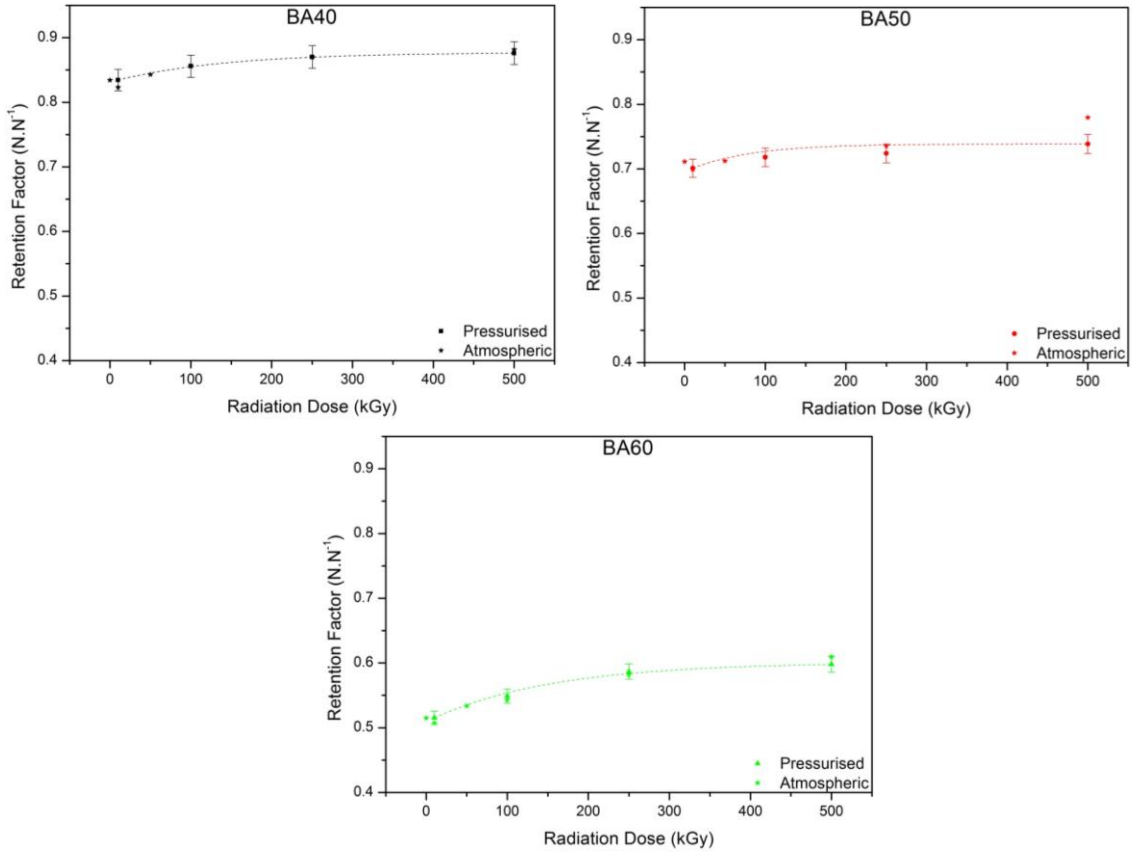

Figure 6-15: The Change in RF for All Three Commercial Samples Following Exposure to Gamma Radiation under 3.2 MPa CO_2 Compared against Exposure under Standard Atmospheric Conditions

6.3.7 CO_2 Absorption Behaviour

Due to unforeseen circumstances and technical problems with the IGA-002 it was not possible to complete the CO_2 absorption behaviour experiments within the scope of this report.

6.4 Discussion

6.4.1 Visual Inspection

CO_2 gas is released from solution at a faster rate than it can diffuse to an external boundary, causing the formation of bubbles in the samples. If we consider an external component creating a compression in a sample to be an inward-driving force then these gas molecules can be considered to be creating an outward-driving force. *Merckel et al.* [34] describe an elastomer as consisting of hard and

soft domains. Under compression the quantity of these harder domains will determine the observable hardness of the sample and as such one can infer that BA40 has the fewer harder domains ranging up to BA60 with the most. Under expansion these harder domains will act as restrictions whilst the softer domains will able to deform to a greater extent, thus explaining the smaller yet more frequent bubble formation seen in the softer samples and as shown in Figure 6-16.

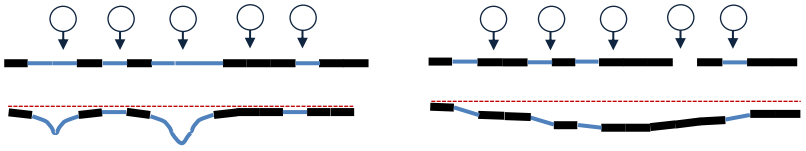

Figure 6-16: A Diagram Representing Hard and Soft Domain Deformation Whilst Under Expansion

Due to the step down depressurisation of DP1 there will be numerous gradients of pressure throughout the structure and so a layer-like effect will occur and the visible outcome of smaller bubbles would be weakened as the higher layers may have a hard domain in the corresponding lower soft domain location.

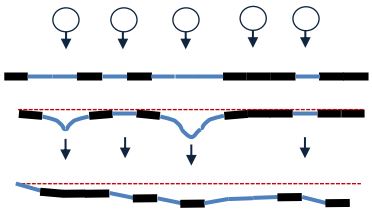

Figure 6-17: A Diagram Representing the Layer Effect of Step-Down Depressurisation

Following irradiation, the bubbles remained for a significantly longer period of approximately one week, suggesting crosslink formation has resulted in a reduction in the rate of release. It was also noticed that a substance appeared to have leached out of BA50 and BA60 but surface IR revealed the same spectra as that seen in ATR-IR of the bulk. The shiny surface of BA50 and BA60 following 500 kGy fractured upon application of a sharp Stanley Knife indicating glassification.

6.4.2 SPECTROSCOPY

A closer inspection of the ATR-IR Spectra, Figure 6-18, reveals more subtle differences. The very broad absorption around $3400 - 3300\ cm^{-1}$ does not appear in the pressurised samples. There also slight differences in the range $1800 - 950\ cm^{-1}$; an increase in peak growth at 1720 and 1436 cm^{-1}, suggesting an increase in carbonyl bonds, and at 1267 cm^{-1}, suggesting an increase in the –C-N bond. There is also evidence of a decrease in peak growth at 1068 cm^{-1} and a decrease in peak decay at 1015 cm^{-1} suggesting a reduction in the amount of compound leaching during radiation exposure.

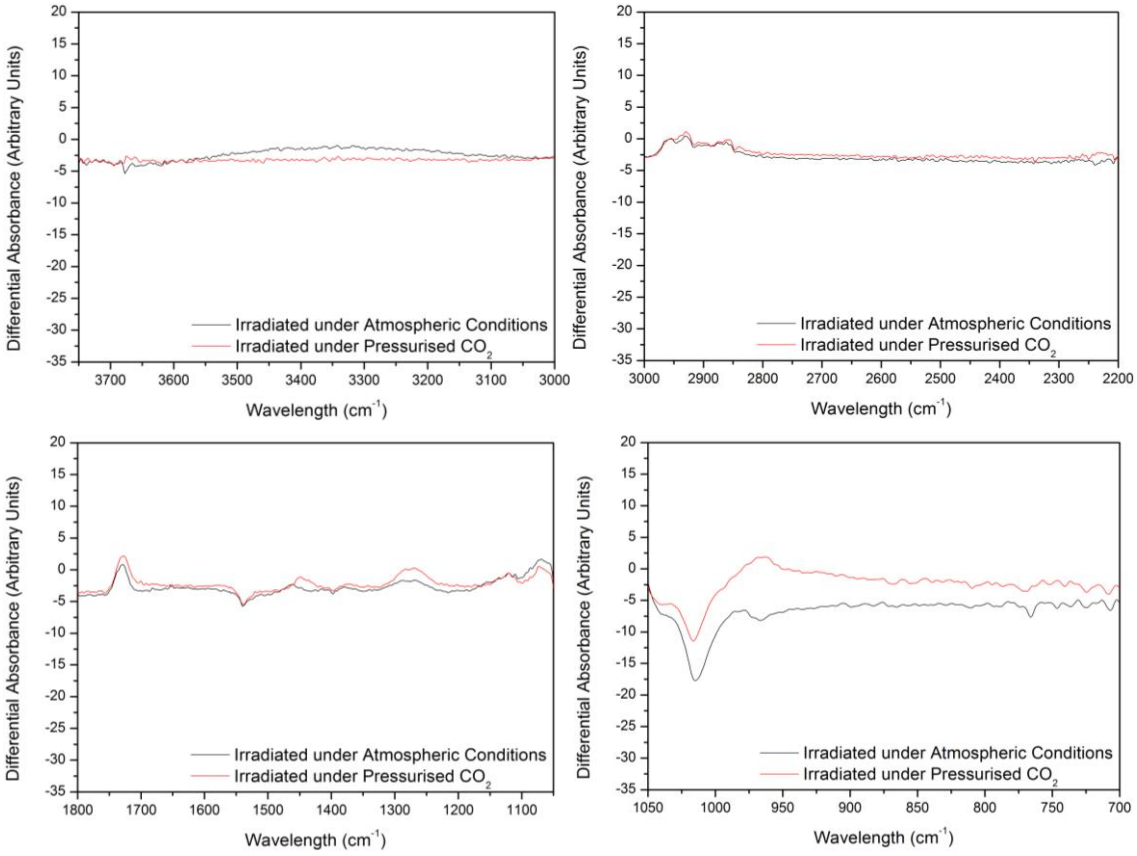

Figure 6-18: A Comparison of the ATR-IR Spectra for BA40 Following Exposure to 500 kGy Gamma Radiation under Atmospheric Conditions and under 3.2 MPa Pressurised CO_2 Between 3750-3000 cm^{-1}, 3000-2200 cm^{-1}, 1800-1050 cm^{-1} and 1050-700 cm^{-1}

The comparison of the spectra for BA50 showed very little difference between irradiation under atmospheric conditions and under pressurised CO_2, Figure 6-19.

There may be some slight discrepancies in the range $1800 - 950\ cm^{-1}$ but the variances are within the scope of experimental error.

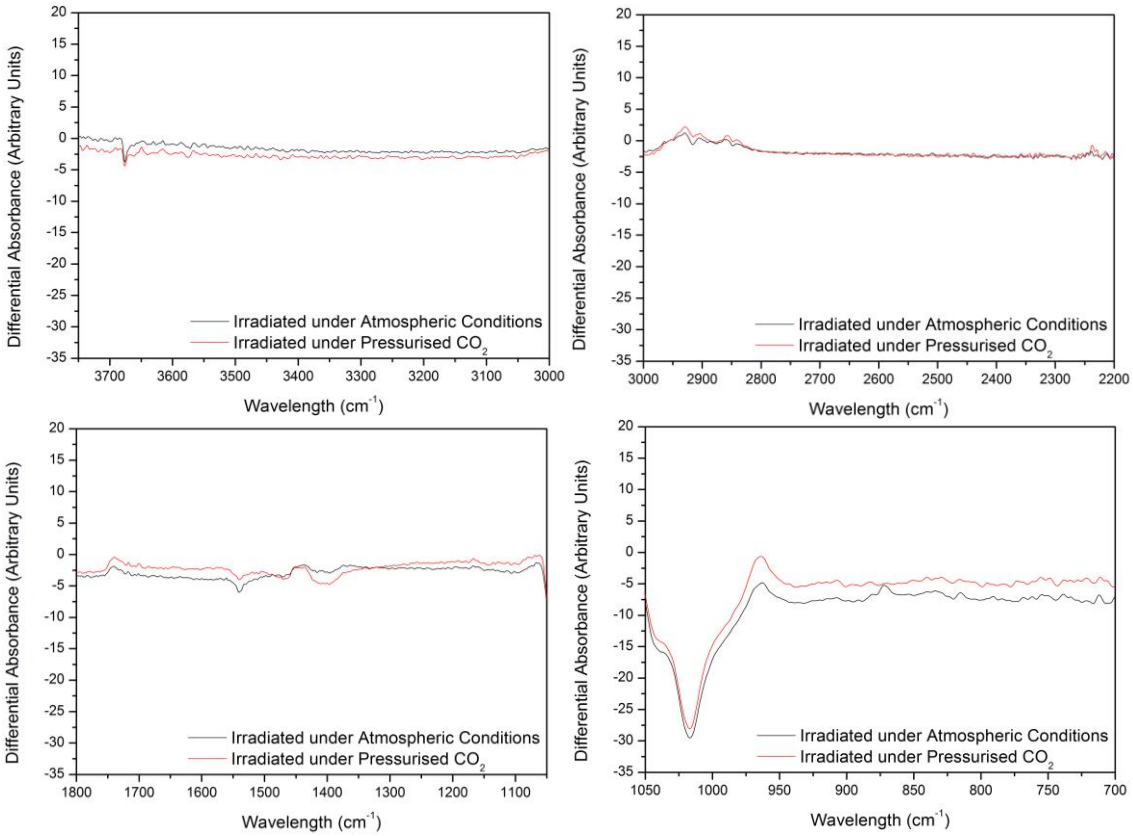

Figure 6-19: A Comparison of the ATR-IR Spectra for BA50 Following Exposure to 500 kGy Gamma Radiation under Atmospheric Conditions and under 32 Bar Pressurised CO2 Between 3750-3000 cm^{-1}, 3000-2200 cm^{-1}, 1800-1050 cm^{-1} and 1050-700 cm^{-1}

However, the results for BA60 showed slightly more dominant differences. In the range $3000 - 2800\ cm^{-1}$ the peaks associated with methylene stretches decreased following irradiation under atmospheric conditions whilst the presence of pressurised CO_2 during the irradiation procedure has apparently reversed this phenomenon and an increase in peak height can be seen. The same can be said for the large shift in baseline at wavelengths below $1500\ cm^{-1}$; following irradiation under atmospheric conditions the baseline was reduced, whilst the presence of pressurised CO_2 during the irradiation procedure has resulted in an increased baseline below this point.

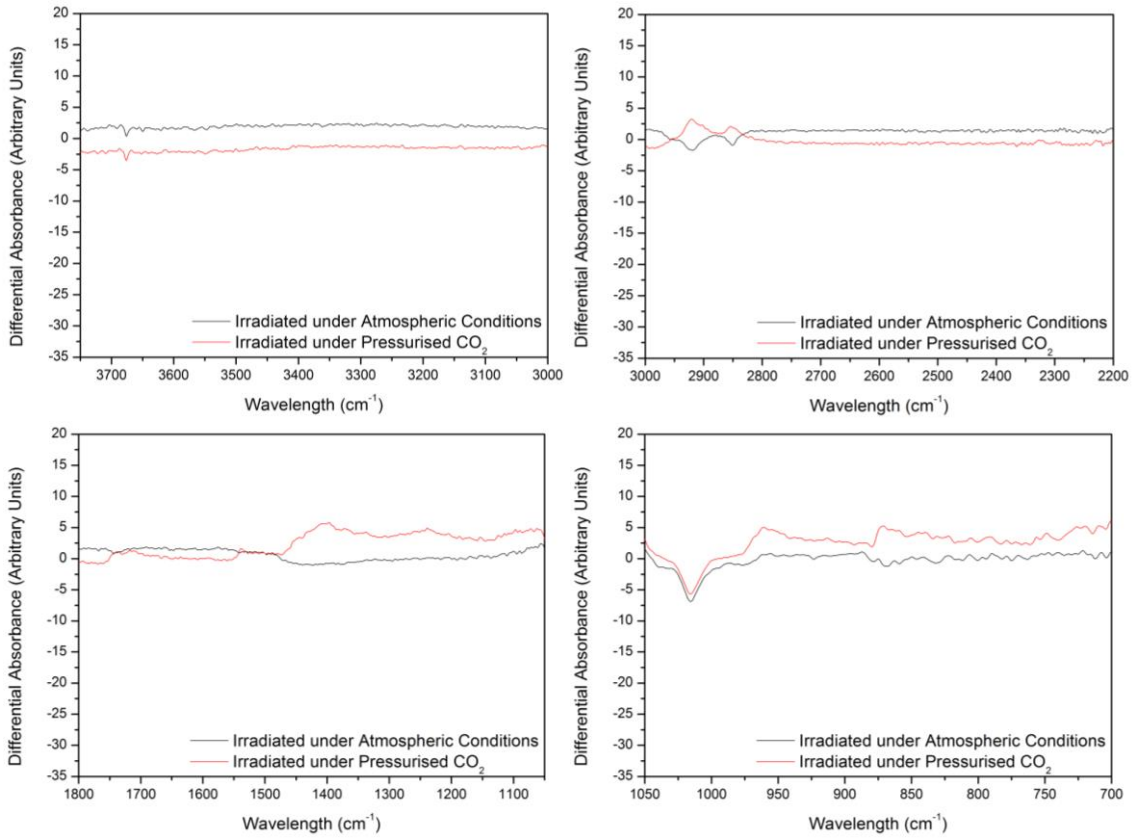

Figure 6-20: A Comparison of the ATR-IR Spectra for BA60 Following Exposure to 500 kGy Gamma Radiation under Atmospheric Conditions and under 32 Bar Pressurised CO2 Between 3750-3000 cm^{-1}, 3000-2200 cm^{-1}, 1800-1050 cm^{-1} and 1050-700 cm^{-1}

6.4.3 Physical and Mechanical Properties

The material properties of the samples show no significant difference between those irradiated under atmospheric conditions and those under pressurised CO_2. One explanation for this is that the comparable size of the CO_2 molecules and the NBR elastomer chain means that they do not interfere physically with the mechanism of crosslinking. Whilst the spectroscopy results do differ slightly than those from Chapters 4 and 5, the variations are so minimal that negligible changes can be assumed.

6.5 Conclusions

A nitrile rubber chevron seal and three commercially available nitrile rubber samples at grades BA40, BA50 and BA60 have been exposed to gamma radiation

whilst under $3.2x10^6\ Pa$ pressurised CO_2 at a dose rate of approximately $1.67\ Gy\ s^{-1}$ to total absorbed doses of $10, 100, 250$ and $500\ kGy$.

Softer samples of NBR undergo explosive decompression in the form of small bubbles. When step-down depressurisation is utilised these smaller bubbles are evened out through a multi-layer effect and larger bubbles are seen. Crosslinking from gamma radiation resulted in a reduction in the rate of CO_2 release.

The presence of pressurised CO_2 during the radiation exposure does not affect the rate nor position of crosslink formation within NBR.

7 INVESTIGATION INTO SERVICE LIFE

Chapters 4 through 6 worked towards the development of a mechanistic understanding of how gamma radiation affects the microstructure of nitrile rubber and the effect the environment has on the degrading consequences of gamma radiation. However, physical wear and friction effects are known to be a leading factor in the damage of dynamic elastomeric seals during service. For this reason a test rig has been designed and constructed at the Harpur Hill Facility in Buxton for carrying out a number of physical wear tests on seal specimens, covering stiction, environmental effects on friction and reciprocating dynamic movement. This chapter introduces the requirements of the test rig based on operation of the DNB Fuelling Machine and the resultant design and construction. The results obtained from the rig have been analysed and discussed and a comparison between post-experimental seals and post-service seals has been carried out.

7.1 TEST RIG DESIGN REQUIREMENTS & OPERATIONAL PROTOCOL

General Design Requirements:

G1. To hold the seal securely in place
G2. To have the ability to remove the seal with relative ease in order to carry out any exploratory investigations
G3. To meet all safety precautions as laid out by British Safety Standards, the Health and Safety Executive and EDF Energy

This section has been removed at EDF Energy's request.

These result in the following operational requirements for the test rig:

This section has been removed at EDF Energy's request.

Following discussion with the interested parties a number of additional requirements were considered key in the design of the test rig:

A1. To permit deconstruction and reassembly with different component parts for future testing of alternate specimens
A2. To record the power required to lift the seals out of their seating as an investigation into friction / stiction properties

7.2 Test Rig Design and Construction

The requirements outlined in the previous section have been met through collaboration between the author and the technicians at the Harpur Hill Facility, who have been previously recognised in the acknowledgements for their outstanding expertise and unrelenting assistance. Figure 7-1 depicts a photograph of the completed design.

Figure 7-1: A Photograph of the Completed Test Rig at the Buxton Facility

7.2.1 Test Rig Piston Head

This section has been removed at EDF Energy's request.

7.2.2 Test Rig Pressure Vessel

[E12] details the geometry of the Fuelling Machine Nose Unit in which the Seal Plug Chevron Seals seat. The internal diameter and surface finish have therefore been taken and replicated on the Test Rig Pressure Vessel (TRPV). As with the TRPH the standards to which the engineering drawing has been designed are now

obsolete and the updated material specification has been used. The engineering drawings also show a lead to permit the easy entry of the Seal Plug Chevron Seals into their seating position and the location and size of a small notch in the Nose Unit wall that allows the attachment of a flow meter to determine the leak rate past the seals, known as the Leak Rate Sensing Point (LRSP). These two features have also been replicated in the final design as they may prove imperative in the seal's degradation mechanisms.

Requirements O2 – O4 and O7 detail the minimum and maximum pressure the TRPV will experience during operation. Equation 2-1 was taken from [165] and was used to calculate the minimum thickness of the TRPV as 10 mm, including an allowance for corrosion. This thickness is also considered suitable for taking the TRPV down to 0.03 MPa. Flat bolted cover plates were used for their cost effectiveness and proved sufficient for the design criteria. This design contributes to A1, O2-4 and O7.

$$e = \frac{P_i D_i}{2f - P_i} \qquad \text{Equation 7-1}$$

where e is the minimum thickness of the pressure vessel in m, P_i is the internal pressure in $N\ m^{-2}$, D_i is the internal diameter in m and f is the design stress of the chosen material at the maximum temperature the component will be exposed to in $N\ m^{-2}$.

7.2.3 Test Rig Piston Drive

Requirements O5, O8 and O9 detail the reciprocal motion of the piston and the ability to increase the frequency of these movements. Requirement A1 also covers the ability to change all aspects of the test rig, such as TRPH and TRPV design as well as speed of reciprocating movements. With these constraints placed on the design consideration of the Test Rig Piston Drive (TRPD) it was decided to implement a motor and drive chain system. This facilitates the changing of gears to adjust speeds and torque requirements of the rig and, with the use of limit switches, can produce reciprocating motion with limited operator input. A load cell was added to the Piston Shaft to record the tension and compressions being

applied through the piston drive to induce both lift and lower of the seals, completing O9, A1 and A2 and contributing to O5 and O8.

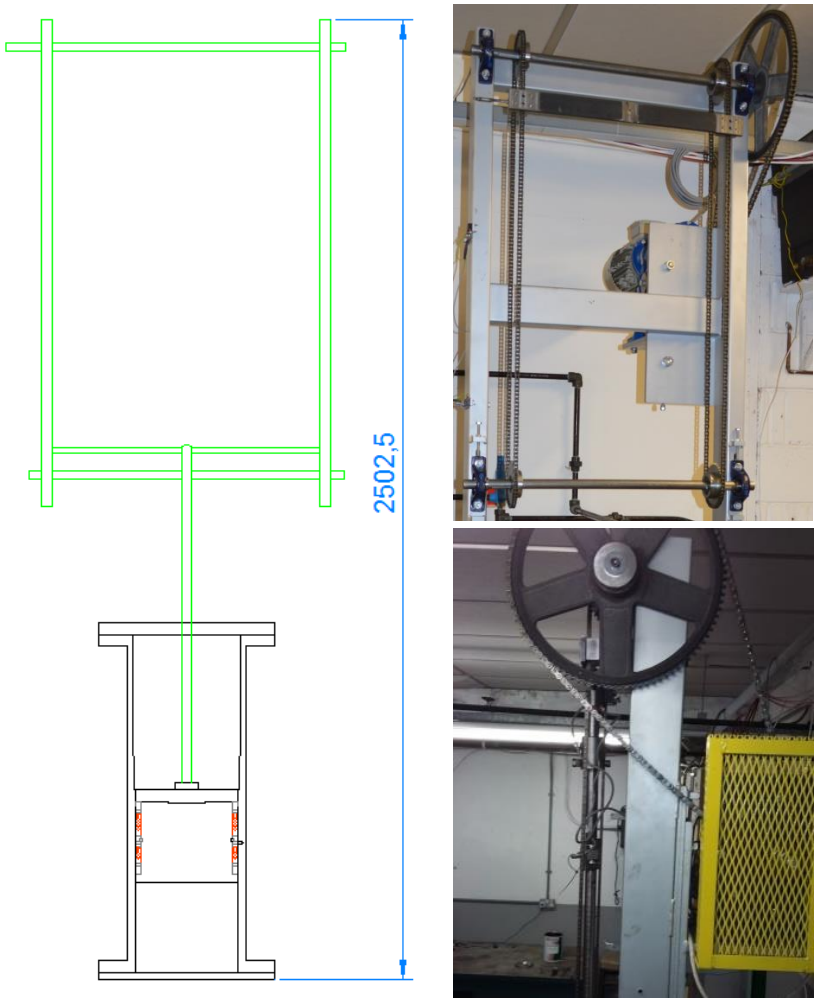

Figure 7-2: An AutoCAD Drawing and Photograph of the Test Rig Piston Drive with Dimensions (all dimensions are in mm)

7.2.4 Test Rig Support Structure

A support structure constructed from 2 inch box section has been used to provide stability to the system and house all the previously mentioned components. This also contributes to requirement A1 in its ability to house larger or smaller components at all parts of the design.

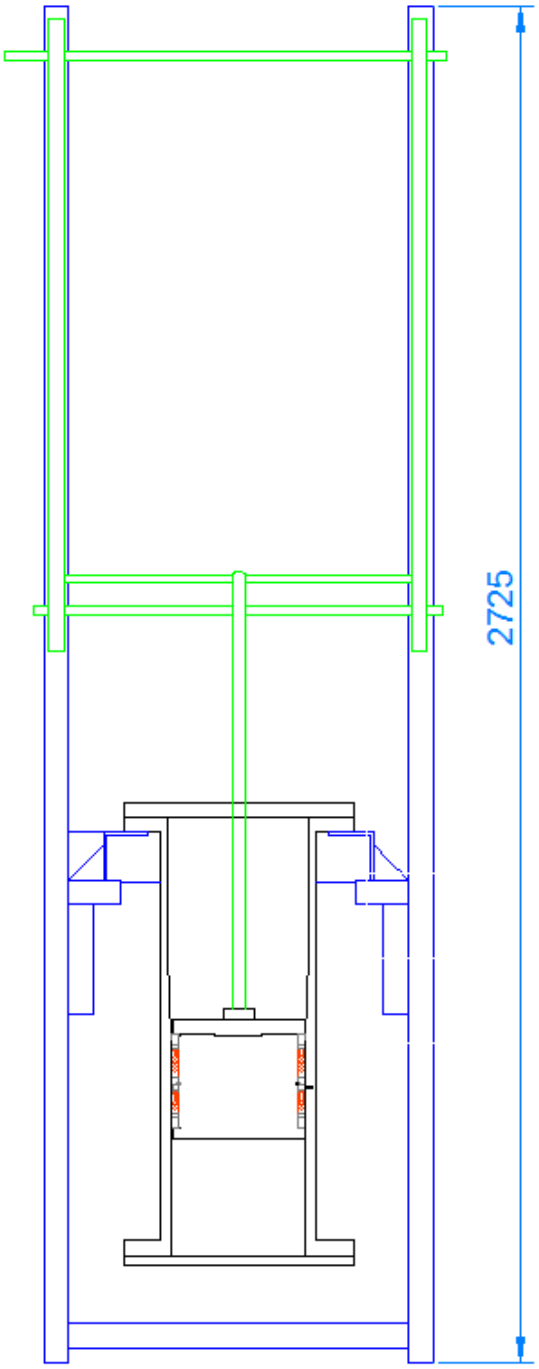

Figure 7-3: An AutoCAD Drawing of the Test Rig Support Structure with Dimensions (all dimensions are in mm)

7.2.5 Piping and Instrumentation

A bypass pipe has been installed to permit movement of the gas from the top section of the TRPV to the bottom section during seal movement with the inclusion of a bypass valve which will allow pressurisation of the top section separate to the bottom. Due to the changing environment the seal is to be exposed to, a number of

connections need to be established such as a high pressure CO_2 line, a vacuum line and a vent to atmosphere line. However, to limit the intrusions into the TRPV it was decided to have all lines connect into this bypass pipe above the bypass valve; this is because the environment in the top section is always changed first before equalising with the bottom section. Two pressure gauges, one for high pressure and one for a low vacuum, have been attached to the top section, which electronically inform the operator about the pressure as well as an additional high pressure valve on the bottom section. These are all protected by pneumatic valves so that the high pressure gauges are not damaged by the low vacuum and vice-versa. This design completes O1 and contributes to O2-8.

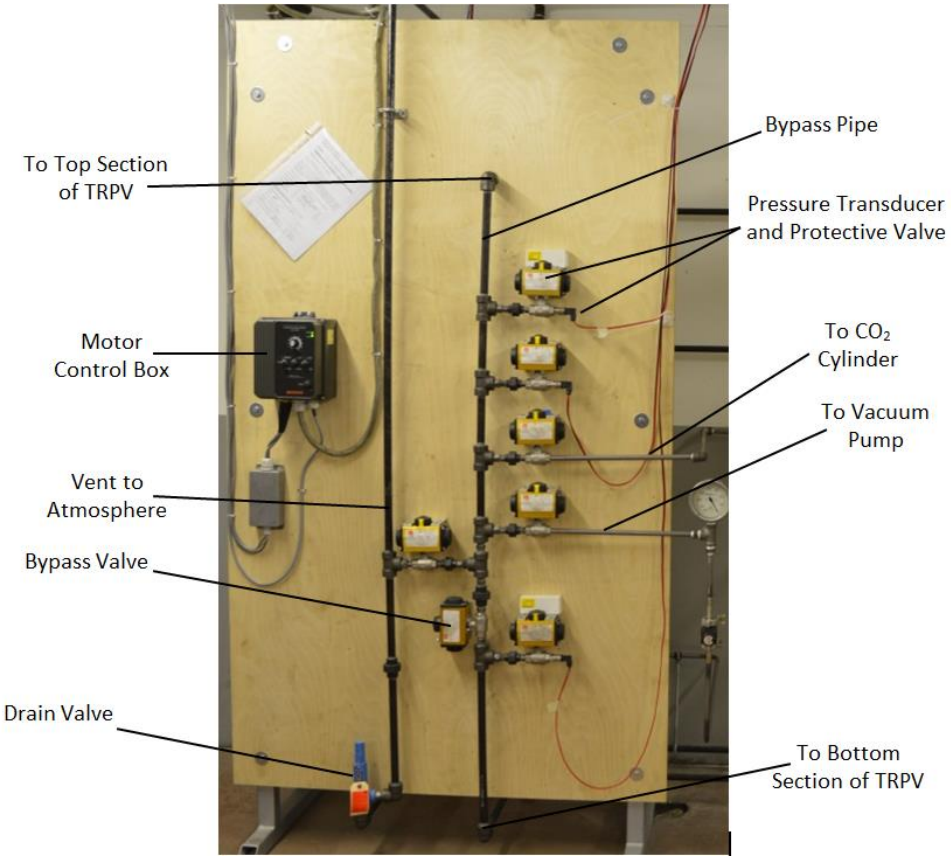

Figure 7-4: The Piping and Instrumentation Control Board

7.2.6 Operator Control System

LabView was used, both as a control program and results collector, that allowed complete control of the Test Rig from a separate control room. This was used in conjunction with an NAQ Data board to remotely control the electro-pneumatic

valves in the set-up shown in Figure 7-6. The NAQ board provided a 5 V signal that tripped a TIP122 transistor, triggering a 24 V circuit that could then activate the electro-pneumatic valves, providing the $0.7x10^6$ Pa pressurised air which is required to operate the valves on the Test Rig. This design completes O2-8.

All sensors were set to output in current to minimise the loss in signal from travelling from the source to the control room where they were put through a two-wire current loop system to revert the signals back to voltage. The NAQ Data board then converted these voltage readings into pressure and weight readings where they were displayed and recorded in LabView.

A nylon hose was attached to the LRSP on the TRPV that could be connected to a series of flowrate sensors of different capacities in the control room. During leak-testing the hose could be attached to the lowest capacity flowrate sensor and the reading recorded. If the flowrate exceeded the capacity of this sensor the hose could be moved up to the next highest capacity and so on until a value could be read and recorded.

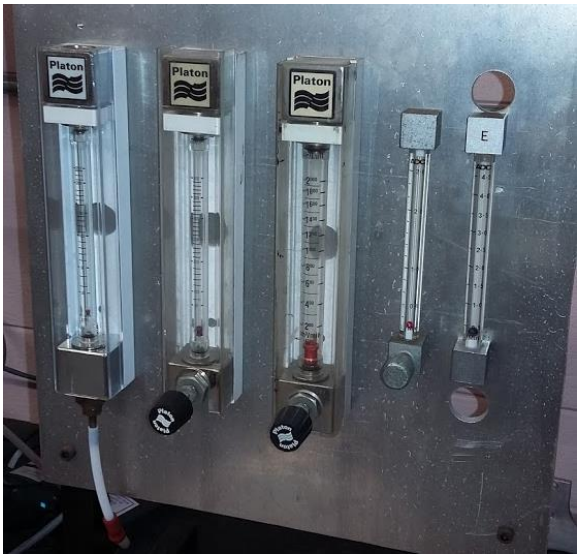

Figure 7-5: The Series of Flowrate Sensors

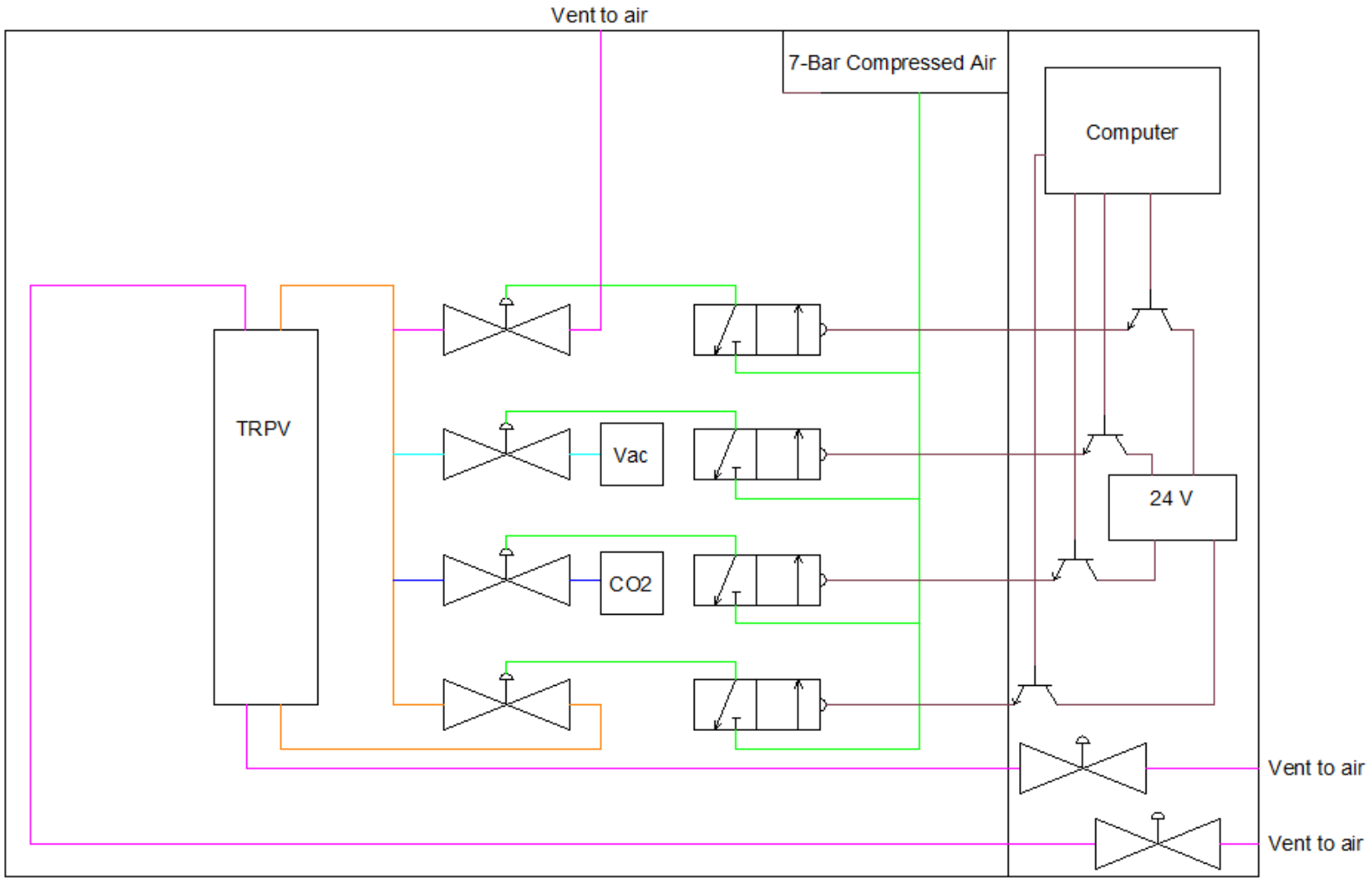

Figure 7-6: A Schematic of the Control System for the Pneumatic Valves on the Test Rig

7.3 Test Rig Experimental Results

7.3.1 Preliminary Testing

A single lift and lower on the Test Rig has been run and the resulting load cell readings against time are depicted in the below series of figures, as well as a simplified graphical representation of the TRPH location within the TRPV at the relevant points on the graphs.

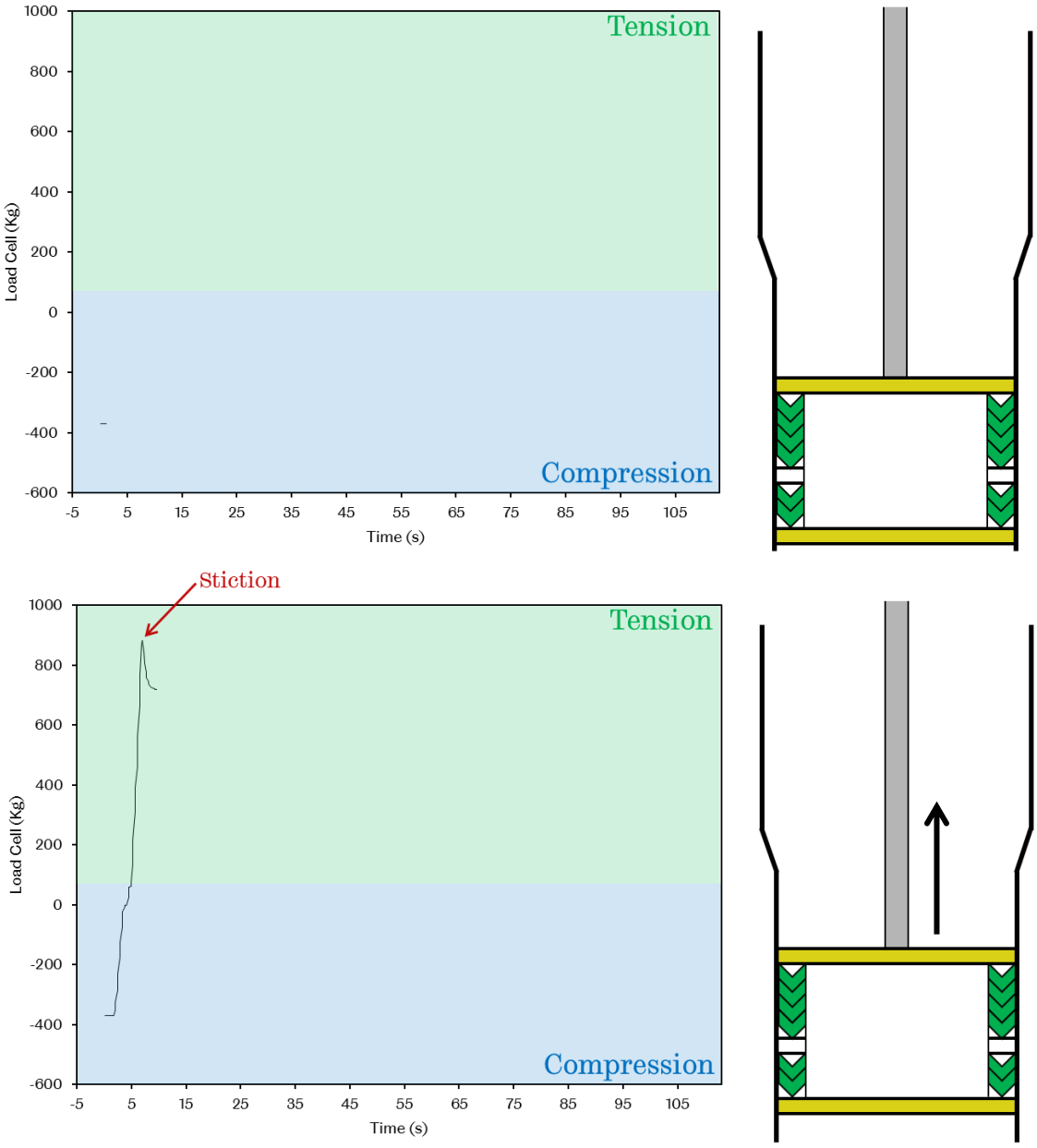

Figure 7-7: Load Cell against Time for a Single Run on the Test Rig with a Graphical Representation of the TRPH Location within the TRPV - Part A

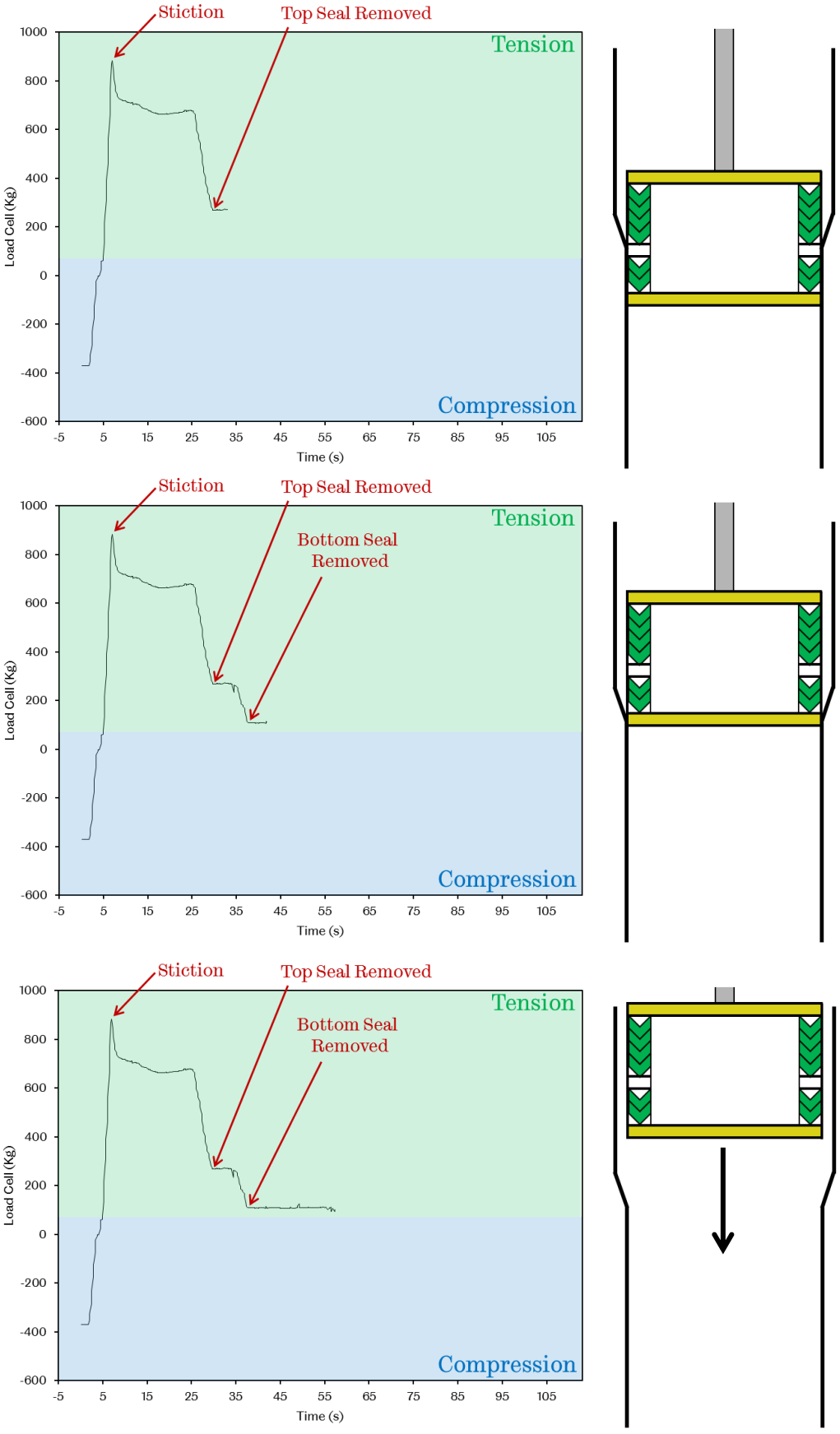

Figure 7-8: Load Cell against Time for a Single Run on the Test Rig with a Graphical Representation of the TRPH Location within the TRPV - Part B

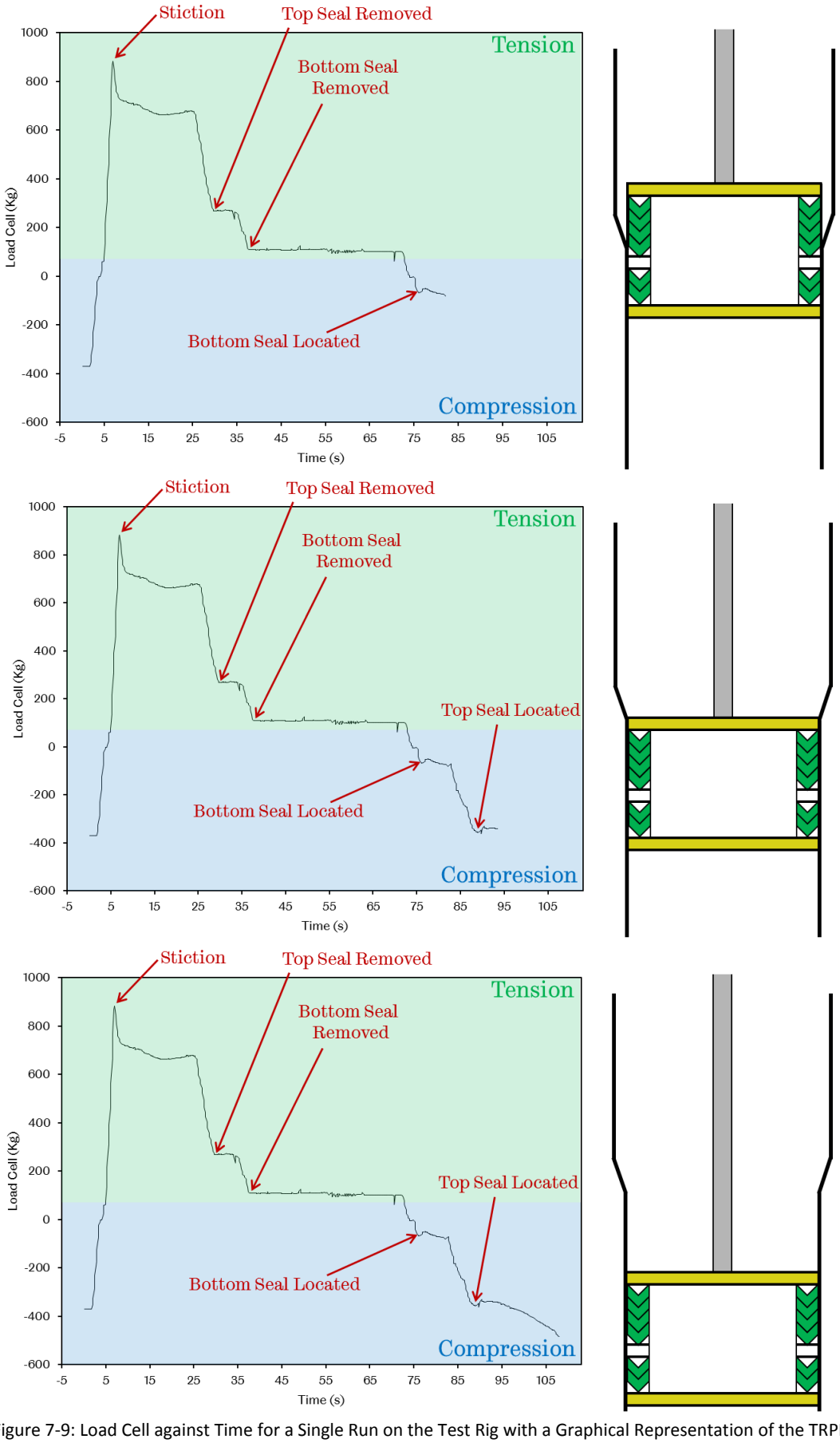

Figure 7-9: Load Cell against Time for a Single Run on the Test Rig with a Graphical Representation of the TRPH Location within the TRPV - Part C

7.3.2 STICTION

The development of stiction with time has been measured through the application of a fresh coat of grease on the seals, lowering the TRPH into the seated position and allowing the system to settle for a pre-determined waiting period. The stiction is then defined as the initial peak of the load cell vs time plot that describes the tension applied through the load cell to start the seal moving. This was repeated at 10 minute intervals until no change was observed or the load cell capacity had been reached, Figure 7-10.

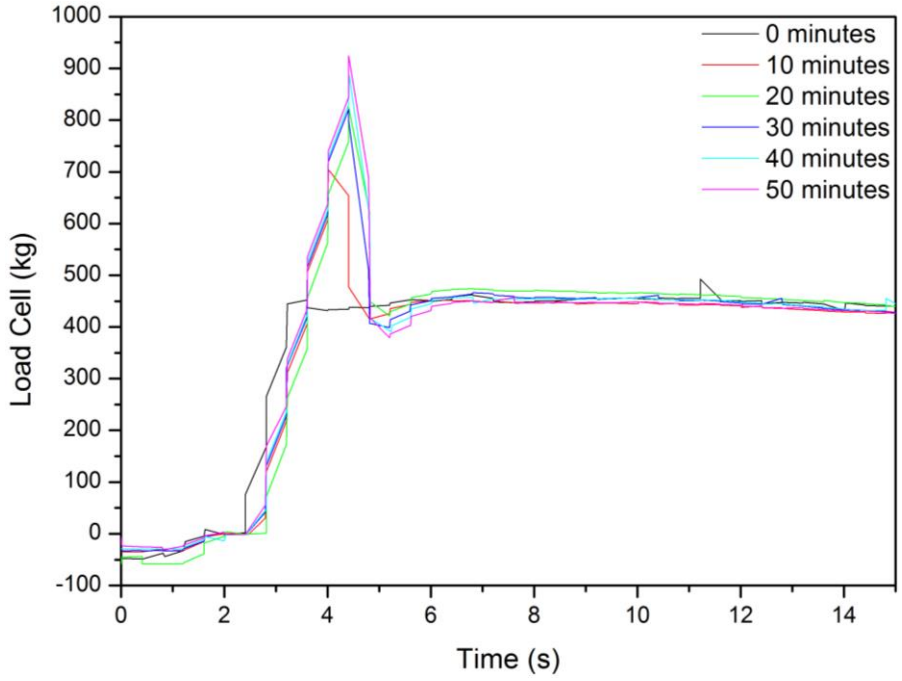

Figure 7-10: Load Cell Readings between 0 and 15 Seconds for Waiting Periods of 0, 10, 20, 30, 40 and 50 Minutes

The stiction shows an increase with waiting time up to 50 minutes after which the load cell maximum is reached and thus the recorded maximum is not accurate. Figure 7-10 also shows that the required tension force to induce lift when both seals are in contact with the TRPV remains constant regardless of the stiction value.

7.3.3 Environmental Effects on Friction

The design of the Test Rig allows pressurisation with CO_2. Figure 7-11 depicts the procedure, beginning with the evacuation of air. The high pressure CO_2 is then used to bring the total pressure back to atmospheric at which point the protective pneumatic valves can be opened and closed respectively and the high pressure CO_2 then used to bring the pressure of the top section to $3.2x10^6\ Pa$. Safety checks are then carried out to ensure there are no leaks and all sensors (both mechanical and electrical) are working correctly. The high pressure CO_2 line is then opened again with the bypass valve to allow the equalising of pressure between the top and bottom sections of the TRPV to approximately $3.2x10^6\ Pa$.

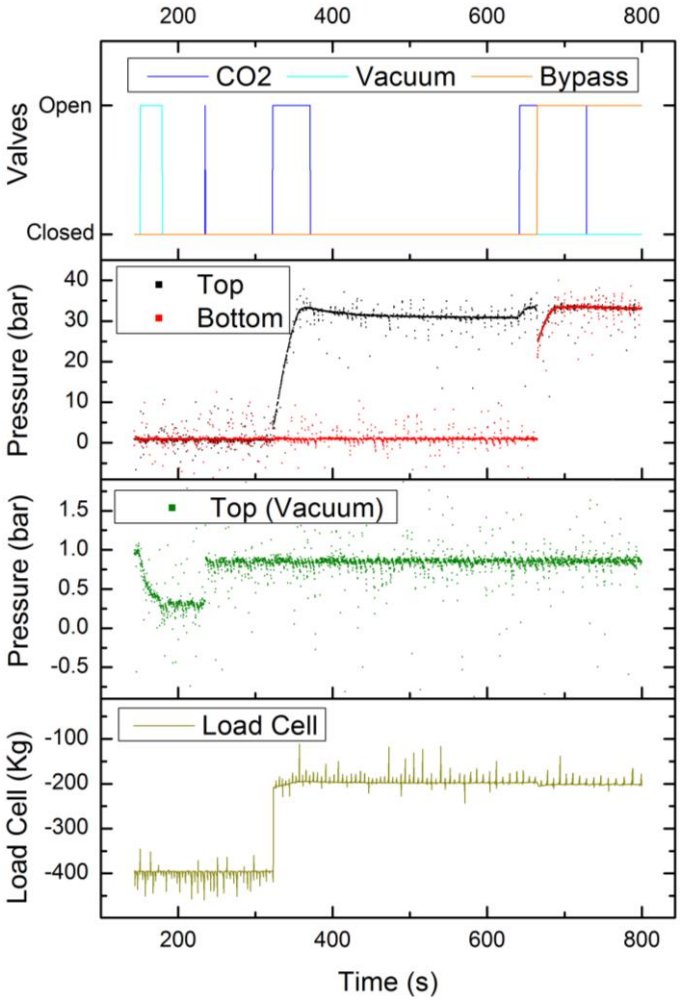

Figure 7-11: Pressure Gauges and Load Cell against Time during Pressurisation of the Test Rig

From Figure 7-11 one notices that the load cell reading reduces from approximately 400 kg in compression to approximately 200 kg during the pressurisation of the top section of the TRPV. It can also be seen that the compression increases very slightly at the point of equalising the pressure between the two sections of the TRPV. The system was evacuated through the step-down procedure specified in [E15] and then re-pressurised.

A 4-run cycle was performed immediately following pressurisation and subsequently every 10 min until the 4-run cycle showed limited change. The results are shown below, Figure 7-12. It was found that the presence of high pressure CO_2 in the TRPV resulted in a higher required tension force to lift the seals and a much larger compressive force to push the seals out of and into the respective housing. This appeared to increase with increasing time in the CO_2 environment. Some runs also showed an anomalous increase in tension following the removal of the upper seals during the lifting process.

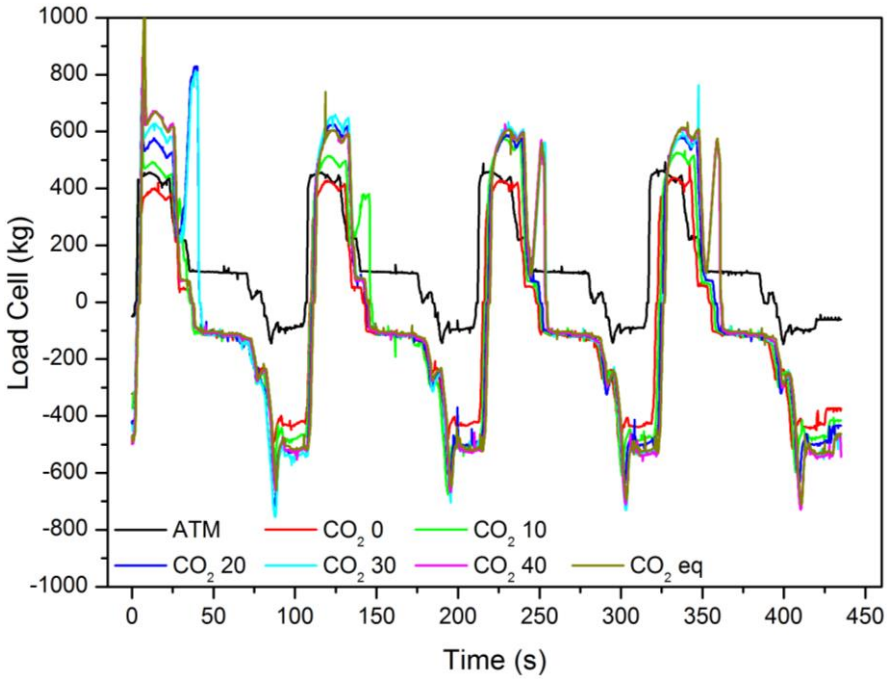

Figure 7-12: Load Cell Readings for a 4-Cycle Run Carried out in Atmospheric Conditions and Following 0, 10, 20, 30, 40 and 50 minutes of Exposure to 3.2 MPa CO_2

7.3.4 Reciprocating Dynamic Movement

As the seals are used in service their dynamic movements will shift the grease out of position and the friction they undergo will steadily increase. Whilst this is a difficult degradation mechanism to model, the Test Rig can record the increasing weight put through the load cell to induce movements in the seal. Figure 7-13 depicts the readings recorded during a 15-run cycle.

It can be seen that the required tension force to lift the seal plug increases with the number of cycles. Runs with significantly longer waiting periods than those seen in the stiction tests have been carried out for 15 cycles and the increasing required load with cycles have been calculated and reproduced below, Figure 7-14. The initial values have been removed due to excessive stiction values. All runs show an increase in friction with number of cycles.

The varying positions of the cycles are believed to be due to the greasing regime carried out before each cycle was run. Whilst every effort was made to ensure the same amount of grease was applied in the same way before each run, a build-up of grease and variation in effects is inevitable.

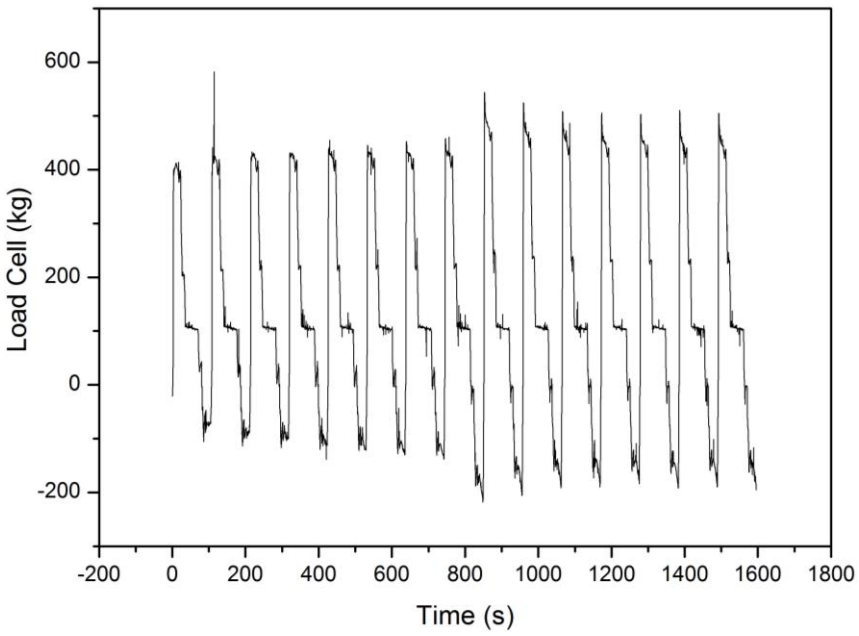

Figure 7-13: Load Cell against Time for a 15-Cycle Run carried out in Atmospheric Conditions

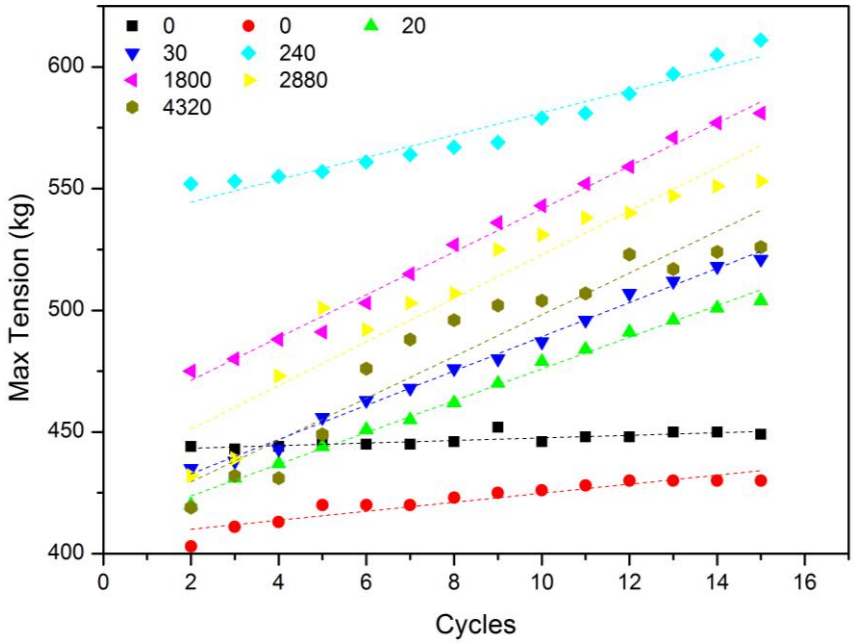

Figure 7-14: Maximum Required Tension to Induce Lift for a 15-Cycle Run carried out after 0, 20, 30, 240, 1800, 2880 and 4320 minutes of Waiting Time

7.3.5 Post-Service Investigation

Test Rig Seals and Components

Following simulated service the seals were removed for a visual inspection. Some scratch marks can be seen in Figure 7-15 that are only present on the lower seals. These scratch marks are also in line with the LRSP that has been cut into the TRPV. No flow was recorded in the LRSP which lead to a visual inspection and it was noted that the LRSP had a build-up of grease within the drilled section, Figure 7-15.

NPP Seals

The seals on the NPP are replaced at regular intervals according to the maintenance schedule. During a recent maintenance activity in late 2014 all three sets of seals (18 individual seals) were removed and sent for examination at AMEC Foster Wheeler's active metallurgy laboratory in Risley. To limit contamination the seals were kept in the lab and therefore the available testing was limited.

Visual inspection and comparison against an unused seal was deemed to provide sufficient information.

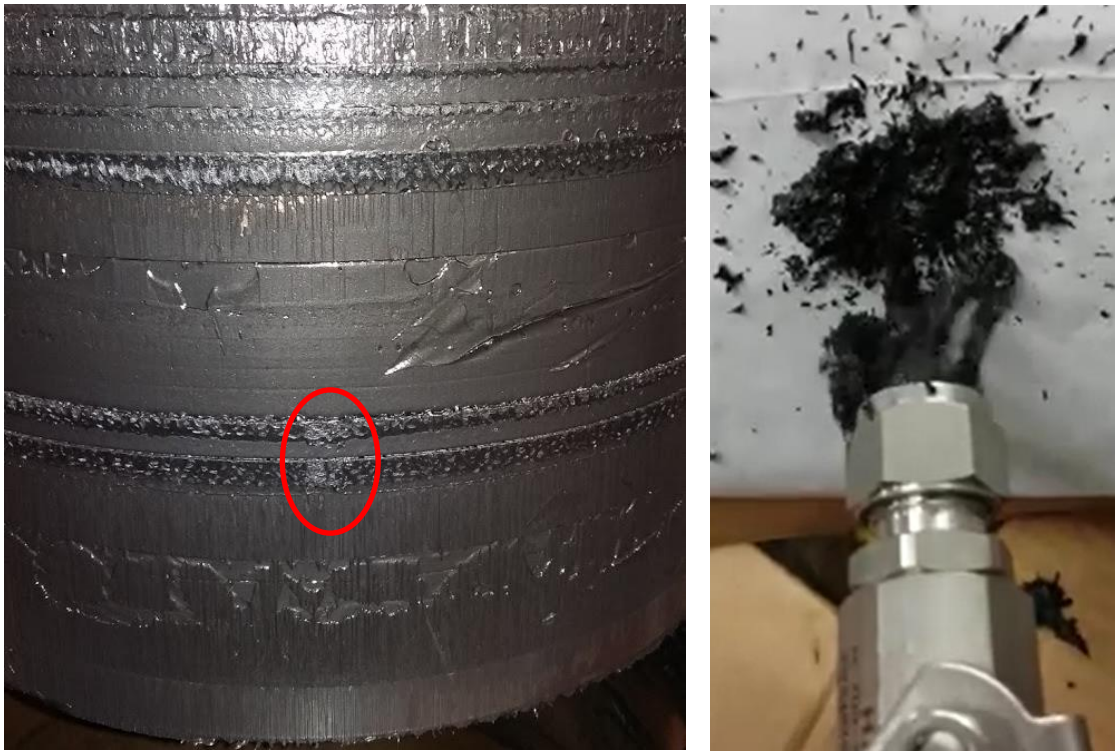

Figure 7-15: A Picture Depicting the Scratch Marks seen in the Lower Chevron Seals and the Build-up of Grease in the LRSP

All 18 seals were found to be in generally good condition with localised wear:

- fraying on contact edge with evidence of feathering
- increased visibility of brass
- thickening of grease and adherence to surface of seal
- no evidence of vacuole formation
- slight stretching in one seal – 0.5 mm variance

The height of all the seals was recorded using a digital calliper with a reproducibility of approximately 0.07 mm and the results are repeated below, Figure 7-16. It can be seen that there is not much variance in seal height with an average of 17.2 mm and a maximum range of only 0.5 mm.

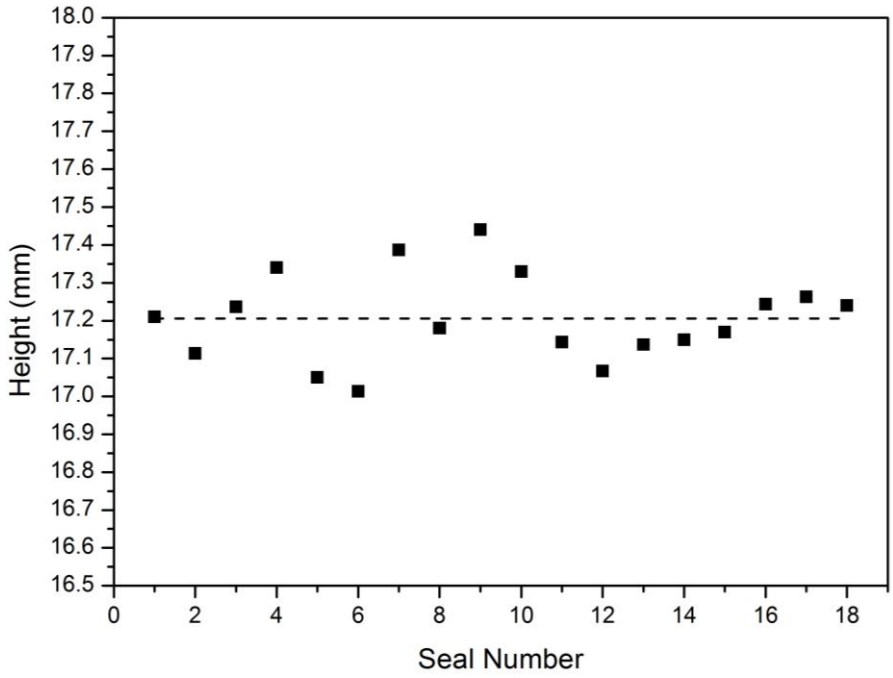

Figure 7-16: The Height of all 18 Post Service Seals

7.4 DISCUSSION

7.4.1 STICTION

The maximum tension required to initialise movement in the seals is called the stiction. The increase in stiction with waiting time has been calculated for the runs in air and the runs in pressurised CO_2 and is shown in Figure 7-17. It can be seen that the stiction increases with an exponentially decaying trend. The presence of CO_2 also appears to have little effect on the build-up of stiction. This would suggest that the stiction effects are a feature of the grease and not the seal itself.

Although these results suggest limited increase in stiction following 50 minutes of waiting time, observation of the test rig operations at longer waiting periods carried out in Section 7.3.4 suggest that stiction continues to increase and it is only the maximum capacity of the load cell that prevented these readings from being recorded.

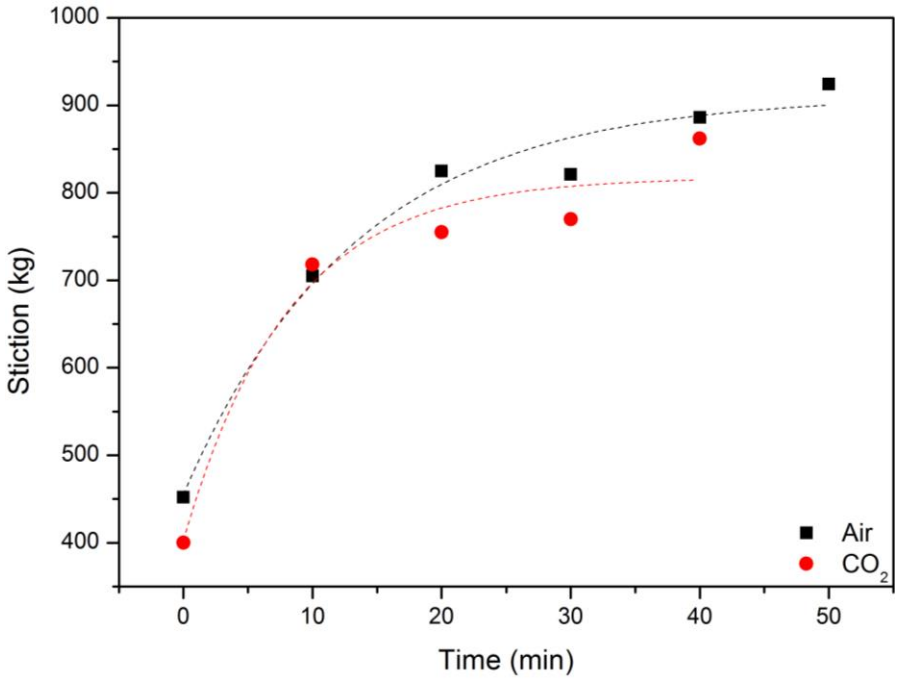

Figure 7-17: Stiction against Waiting Time in Atmospheric Conditions and in 32 bar CO_2

7.4.2 Environmental Effects

Whilst under pressurised conditions the average required tension to induce lift for each cycle was estimated and the results are shown in Figure 7-18. It can be seen that the required tension to induce lift for each cycle follows a very similar trend, an exponentially decaying increase with waiting time. This can be explained through the absorption of CO_2 into the seals and the subsequent swelling of the component. This swelling behaviour would increase the outward forces acting between the seal and the TRPV and thus a greater tension would be required to push and pull the seals into and out of their housing.

The effects appear to diminish after 50 minutes suggesting that after this amount of time the seals have reached equilibrium and thus their maximum degree of swelling. It can be seen that the required tension to lift the TRPH at each cycle of the run has increased by almost 50% of the original value. If the increase in this required tension is transferred directly to the dynamic movements of the seal then it suggests a much larger degree of friction in regular service and thus an accelerated degradation of the seals.

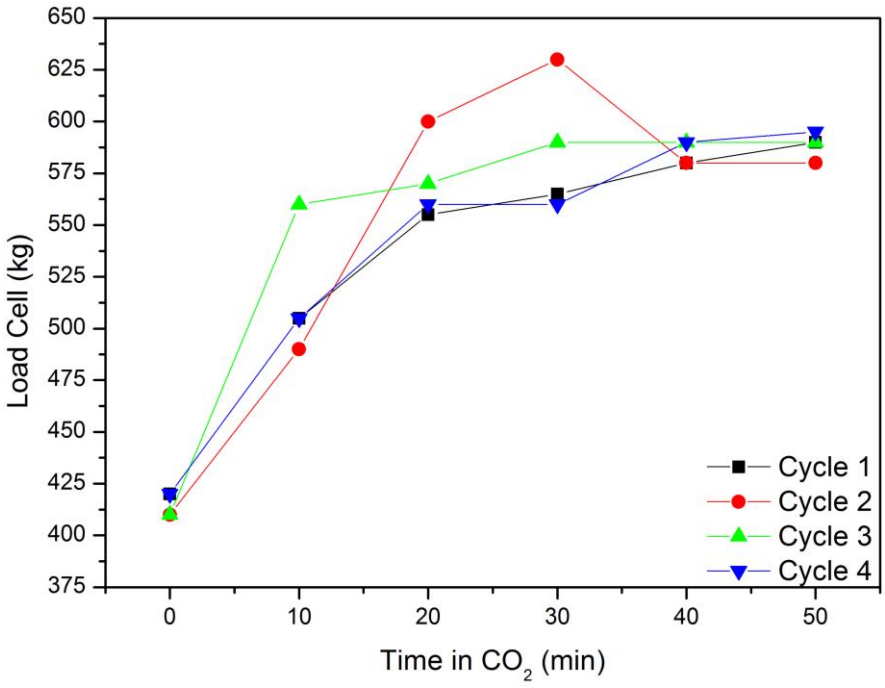

Figure 7-18: Required Tension to Induce a Lift against Exposure Time in CO2 for all Lifts in a 4-Cycle Run

7.4.3 Reciprocating Dynamic Movements

As mentioned previously there is a clear increasing trend in required tension with cycles. Fitting each 15-cycle run to a linear trend and plotting the gradient of the resultant line, the 'Increase in Friction' in $kg\ cycle^{-1}$, against the waiting time in min produces Figure 7-19.

Whilst the particular greasing regime carried out will have an effect on the increasing friction with cycles, as discussed earlier, there appears to be an increasing trend with waiting time. This shows a rather fast increase in a particular range before a consistent value is found. It is therefore suggested that as opposed to a gradual change in the increasing friction value, there is a threshold waiting time beyond which the effects become much more detrimental. This can be explained through the swiping action of the chevron seals explained in Figure 7-20. With lower waiting times the wings of the chevron design are required to overcome the stiction from the grease before they can move Figure 7-20a. However, above the threshold waiting time the stiction becomes so great that the chevron wings become deformed Figure 7-20b and as the lifting force overcomes

the stiction the wings return to their original position, and it is this action that 'swipes' the grease away from the area that is required, and thus the increasing friction with number of cycles increases rapidly and then remains constant.

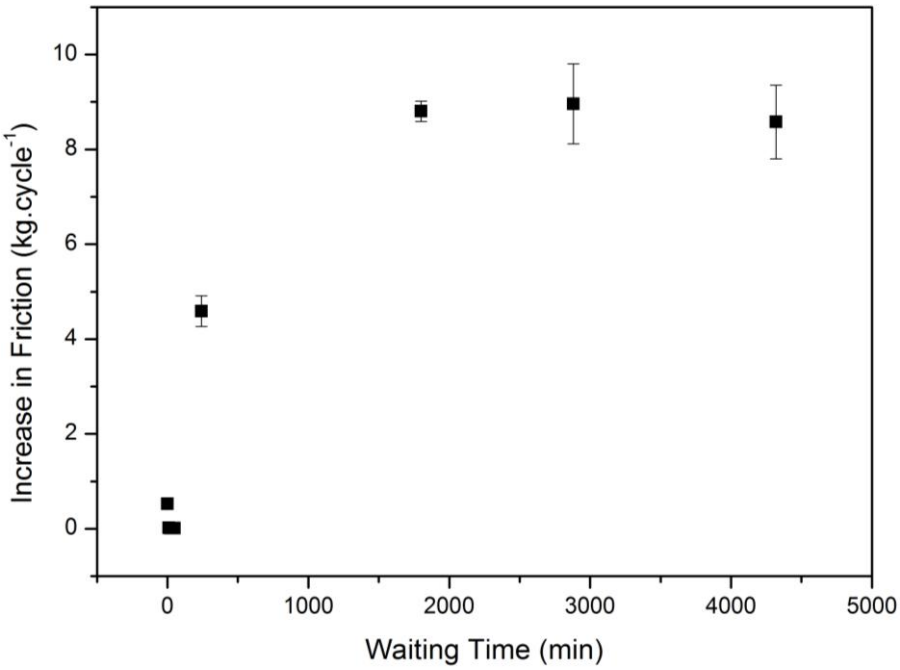

Figure 7-19: The Increase in Required Tension to Induce a Lift with Number of Cycles against Waiting Time

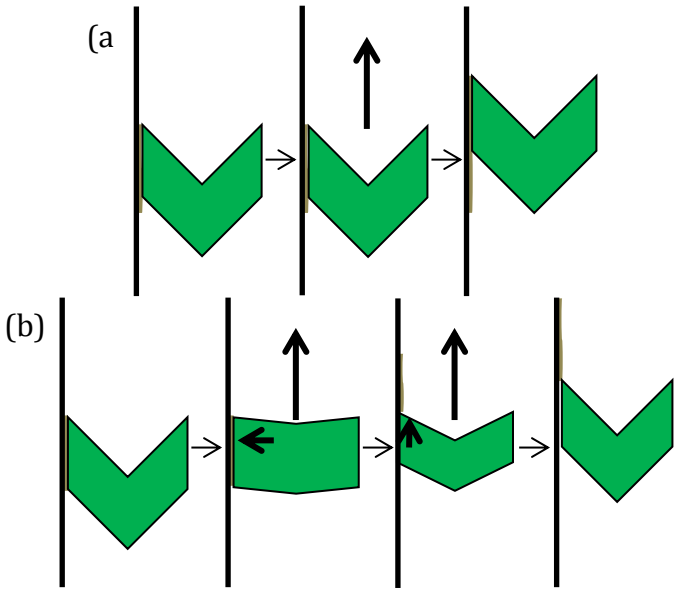

Figure 7-20: A Graphical Representation of the Initial Dynamic Movement of a Chevron Seal both (a) Below and (b) Above the Threshold Waiting Time

7.4.4 Post-Service Investigation

Due to the location of the scratch marks in the post-experimental seals it is suggested that they are the result of reciprocal movements over the drilled entry to the LRSP. The wings of the chevrons could be catching on the un-chamfered edge and scratching at the surface finish. Over time this will increase the leak rate of the seals as the damage caused will prevent this section of the seal from creating a good pressure boundary. However, this damage was not seen on the post-service seals. The post-service seals were examined before the post-experimental ones and were only compared to an un-used seal and as such there was no directed exploration for these scratch marks. A recent discussion with EDF Energy has revealed that some additional post-service seals have been sent to AMEC for further investigation and it is strongly advised that an inspection be carried out for these marks. However, it must be noted that they are only expected to appear on the lower chevron seals and, without proper record-keeping of the seals location on the Fuelling Machine, identification could prove problematic.

The build-up of grease within the LRSP on the test rig highlights a potentially severe fault with the system. The grease is known to thicken with exposure to high radiation doses as well as with pro-longed exposure to fibrous material, both of which are extremely prevalent in the Fuelling Machine. If the grease blocks the LRSP then the flowrate recorded during maintenance checks may not necessarily be an accurate representation of the leak rate past the seals and may result in a false acceptance for continued use.

The frayed edges and feathering of the fibrous material seen in the post-service seals is potentially the most detrimental piece of information gleaned from the investigation. It is evidence of the breakdown of the component and how, with continued use in this condition, the bulk material will start to breakdown. Whilst the fibres add strength to the component they inherently bring their own weaknesses and as the fibres are removed from the seals they will agglomerate in the grease and cause it to thicken and adhere to the surface of the seals. This will in turn reduce the effectiveness of the grease as a lubricant and contribute to the increase in friction and thus wear of the seals.

7.5 CONCLUSIONS

A Test Rig has been constructed that permits reciprocal dynamic movements of a piston shaft, whilst under atmospheric conditions and pressurised CO_2, to assess the long term performance of a set of chevron seals and their ability to hold a pressure boundary.

Adherence between the grease and the internal walls of the TRPV was seen as an increase in the stiction with an exponentially decaying trend against time. When the waiting period was significantly longer the increased stiction induced a swiping force in the chevrons that is believed to have removed the grease from the contact points and resulted in a much higher friction between the seals and the TRPV.

The presence of $3.2x10^6\ Pa$ pressurised CO_2 has appeared to cause the component to swell and increase the tension and compression forces required to lift and lower the seal by approximately 50%.

Repeated movements over the un-chamfered edge of the LRSP has caused some surface damage to the chevron seals that will be detrimental to its ability to contain a pressure boundary and it is strongly advised that during the next post-service chevron seal investigation, an attempt is made to locate and identify these marks on the lower chevron seals. A build up of grease within the LRSP also has the potential to greatly affect the leak rate recordings during maintenance procedures and the relative location on site should be cleaned regularly. Additionally, the fraying and feathering of the post-service seals may lead to reduced strength of the material and an increased rate of thickening in the lubricating grease.

8 CONCLUSIONS AND FUTURE WORK

8.1 CONCLUSIONS

The presence of brass wire and glass cloth in the industrial seal made calculation of T_g, IR and CO_2 absorption data particularly difficult and are believed to have been the main contributing factors in the reduced $\Delta_{M\%}$ and RF. The absolute values for all data found were therefore assessed with care and it was the change in these properties following a variety of detrimental environments and operational conditions that proved useful.

The manufacture of the industrial seal into a circular shape produced in-built stresses around the outside edge which, following surface embrittlement due to gamma ray exposure, resulted in surface defects and the initiation of micro-cracks.

It was proposed that in BA40 gamma radiation induced BDN ionisation followed by crosslinking between the vinylidene groups and *cis* C=C bonds. At higher doses both BDN and ACN monomers were ionised inducing crosslinks between C≡N and *trans* C=C. In BA50 both monomers degraded simultaneously. An increased BDN content in NBR has also been shown to increase the proclivity for crosslink clustering that reduced the dose effect and potentially increased radiation resistance in terms of physical and mechanical properties. In terms of absorption behaviour it appears a greater effect was had on the affinity of the bulk to the absorbing media due to degradation of the polar or non-polar pendants than on the formation of crosslinks hindering expansion of the molecular network.

Decompression has been shown to produce smaller bubbles in softer samples that may increase the likelihood of blistering due to the increased local strain. Step-down depressurisation appeared to have alleviated this, however, the damage done due to layer formation within the bulk was not known. The presence of $3.2x10^6\ Pa$ CO_2 has had little to no effect on the physical and mechanical properties of the samples tested and the IR spectra suggests no chemical change.

In simulated service adherence of the grease to the internal walls was evident as stiction and increased with an exponentially decaying trend against time. At significantly longer waiting periods the stiction was seen to reach such a level that the chevron wings swiped away the grease resulting in a much higher friction and increase in friction with reciprocal movements. The presence of high pressure CO_2 had limited effect on stiction but did increase the tension and compression required to lift and lower the seals by approximately 50 %. The un-chamfered edge of the LRSP had caused some surface damage to the lower seals and may have affected their ability to contain a pressure boundary. The LRSP had also built-up a blockage of grease that will thicken with loose fibres from the frayed edge of the seals and may result in significant errors during leak testing.

From this work it appears that the most deleterious effects to the industrial seal are those from the physical movements as replicated in the Test Rig, Chapter 7. The grease adherence that may result in physical wear and even abrasion to the seals surface can be alleviated through regular movements. It is also suggested that the LRSP is regularly checked and all grease is removed from the piping to ensure accurate readings during leak rate testing. A check of the lower chevron seals during maintenance procedures will also identify any damage or scoring that has resulted from the un-chamfered edge of the LRSP and increase the understanding of how this damage increases with time.

8.2 Future Work

The variety of additives and inclusions that can be used during manufacture of NBR seals and sheets combined with the proprietary knowledge of the companies have made it difficult to account particular behaviour to any particular component. If investigation into long term seal behaviour were to continue, it would be advisable to manufacture the materials in house to control what components are added and also their quantities. Each stage of the manufacture could then be tested to determine the effect any one particular component can have on the overall physical and mechanical properties. With sufficient work this would allow

a database to be created that will allow specific properties to be obtained with relative ease.

It would also be useful to design an experiment that accurately measures and records the direct sealing capacity of a sample. One possible direction this could take is the clamping of the sample between two chambers at a known distance and with a known force. The pressure in one chamber could then be raised to a set value and the flowrate past the material recorded. Changing the compression details of the sample and the pressure in the loading chamber could give a matrix of information on sealing capacities and a mathematical algorithm applied that can reduce it down to a single unit of information.

NMR has previously been used to identify the changing structure of NBR under gamma radiation and could be used to identify the effect pressurised CO_2 has on the gamma radiation-induced degradation.

A load cell with a higher maximum loading capacity could be installed on the Test Rig that will allow stiction testing to higher waiting periods. Further use of the Test Rig could also give information on appropriate greasing regimes such as how much to apply and when to apply it. The adaptability of the test rig to different environments and material loadings also means that a variety of seals could be tested for their endurance.

References

[1] Department of Energy and Climate Change, “Energy consumption in the UK,” 2015.

[2] World Nuclear Association, “World Energy Needs and Nuclear Power,” [Online]. Available: http://www.world-nuclear.org/info/Current-and-Future-Generation/World-Energy-Needs-and-Nuclear-Power/. [Accessed 18 January 2016].

[3] Hazardex, [Online]. Available: http://www.hazardexonthenet.net/global/showimage.ashx?Type=Article&ID=76134. [Accessed 18 January 2016].

[4] [Online]. Available: http://universe-review.ca/I14-03-reactorAGR.png. [Accessed 18 January 2016].

[5] R. P. Brown, T. Butler and S. W. Hawley, “Accelerated Heat Ageing Test Results,” in *Ageing of Rubber*, Shawbury, Smithers Rapra Technology, 2001.

[6] L. Achimsky, L. Audouin, J. Verdu, J. Rychly and L. Matisova-Rychla, “On a transition at 80°C in polypropylene oxidation kinetics,” *Polymer Degradation and Stability,* vol. 58, no. 3, pp. 283-289, 1997.

[7] K. T. Gillen, M. Celina and R. Bernstein, “Validation of improved methods for predicting long-term elastomeric seal lifetimes from compression stress–relaxation and oxygen consumption techniques,” *Polymer Degradation and Stability,* vol. 82, no. 1, pp. 25-35, 2003.

[8] J. B. Howard and H. M. Gilroy, “Some observations on the long-term behavior of stabilized polyethylene,” *Polymer Engineering and Science,* vol. 15, no. 4, pp. 268-271, 1975.

[9] E. Kramer and J. Koppelmann, "Measurement of oxidation stability of polyolefins by thermal analysis," *Polymer Degradation and Stability,* vol. 16, no. 3, pp. 261-275, 1986.

[10] H. J. Oswald and E. Turi, "The deterioration of polypropylene by oxidative degradation," *Polymer Engineering and Science,* vol. 5, no. 3, pp. 152-158, 1965.

[11] P. Richters, "Initiation process in the oxidation of polypropylene," *Macromolecules,* vol. 3, no. 2, pp. 262-264, 1970.

[12] J. W. Tamblyn and G. C. Newland, "Induction period in the aging of polypropylene," *Journal of Applied Polymer Science,* vol. 9, no. 6, pp. 2251-2260, 1965.

[13] M. Celina, K. T. Gillen and R. A. Assink, "Accelerated aging and lifetime prediction: Review of non-Arrhenius behaviour due to two competing processes," *Polymer Degradation and Stability,* vol. 90, no. 3, pp. 395-404, 2005.

[14] V. Langlois, L. Audouin and J. Verdu, "Thermooxidative aging of crosslinked linear polyethylene: Stabilizer consumption and lifetime prediction," *Polymer Degradation and Stability,* vol. 40, no. 3, pp. 399-409, 1993.

[15] J. Davenas, I. Stevenson, N. Celette, S. Cambon, J. L. Gardette, A. Rivaton and L. Vignoud, "Stability of polymers under ionising radiation: The many faces of radiation interactions with polymers," *Nuclear Instruments and Methods in Physics Research B,* vol. 191, no. 1-4, pp. 653-661, 2002.

[16] M. Marinović-Cincović, B. Janković, V. Jovanović, S. Samaržija-Jovanović and G. Marković, "The kinetic and thermodynamic analyses of non-isothermal degradation process of acrylonitrile–butadiene and ethylene–propylene–diene rubbers," *Composites Part B: Engineering,* vol. 45, no. 1, pp. 321-332, 2013.

[17] J. A. Hiltz, “Pyrolysis gas chromatography/mass spectrometry identification of poly(butadiene-acrylonitrile) rubbers,” *Journal of Analytical and Applied Pyrolysis* , vol. 55, no. 2, pp. 135-150, 2000.

[18] S. Chakraborty, S. Bandyopadhyay, R. Ameta, R. Mukhopadhyay and A. S. Deuri, “Application of FTIR in characterisation of acrylonitrile-butadiene rubber (nitrile rubber),” *Polymer Testing,* vol. 26, no. 1, pp. 38-41, 2007.

[19] M. Garbarczyk, W. Kuhn, J. Klinowski and S. Jurga, “Characterization of aged nitrile rubber elastomers by NMR spectroscopy and microimaging,” *Polymer,* vol. 43, no. 11, pp. 3169-3172, 2002.

[20] M. Hakkarainen, “Solid Phase Microextraction for Analysis of Polymer Degradation Products and Additives,” in *Chromatography for Sustainable Polymeric Materials*, vol. 211 of 'Advances in Polymer Science', A. Albertsson and M. Hakkarainen, Eds., Berlin, Springer Berlin Heidelberg, 2008, pp. 23-50.

[21] M. Knörgen, U. Heuert, H. Schneider, P. Bargh and W. Kuhn, “Spatially resolved and integral NMR investigation of the aging process of carbon black filled natural rubber,” *Polymer Bulletin,* vol. 38, no. 1, pp. 101-108, 1997.

[22] S. Datta, “Synthetic elastomers,” in *Rubber technologist's handbook*, vol. 1, J. R. White and S. K. De, Eds., Shawbury, Shrewsbury, Smithers Rapra Technology Limited, 2001, pp. 47-74.

[23] K. D. O. Jackson, M. J. R. Loadman, C. H. Jones and G. Ellis, “Fourier Transform Raman spectroscopy of elastomers: an overview,” *Spectrochimica,* vol. 46A, no. 2, pp. 217-226, 1990.

[24] D. J. Kohls and G. Beaucage, “Rational design of reinforced rubber,” *Current Opinion in Solid State and Materials Science,* vol. 6, no. 3, pp. 183-194, 2002.

[25] Y. Merckel, J. Diani, M. Brieu, P. Gilormini and J. Caillard, “Effect of the microsctructure parameters on the mullins softening in carbon-black filled

styrene-butadiene rubbers," *Journal of Applied Polymer Science,* vol. 123, no. 2, pp. 1153-1161, 2012.

[26] M. Davies and S. Sully, "The effect of high pressure CO2 on the mechanical properties of elastomeric materials," in *BHR Group Conference Series Publication (Fluid Sealing)*, 1997.

[27] A. E. Mathai, R. P. Singh and S. Thomas, "Transport of aromatic solvents through nitrile rubber/epoxidized natural rubber blend membranes," *Polymer Engineering and Science,* vol. 43, no. 3, pp. 704-715, 2003.

[28] L. M. Robeson, "Environmental stress cracking: A review," *Polymer Engineering and Science,* vol. 53, no. 3, pp. 453-467, 2013.

[29] H. K. Müller and B. S. Nau, Fluid Sealing Technology: Principles and Applications, vol. 117 of 'Mechanical Engineering', New York: Marcel Dekker Inc., 1998.

[30] G. P. Karpacheva, A. D. Litmanovich, G. N. Bondarenko, L. M. Zemtsov and L. B. Krentsel, "The effect of IR radiation on structurisation of butadiene-nitrile rubber," *Polymer Science Series A: Structure and Properties,* vol. 52, no. 8, pp. 787-793, 2010.

[31] V. Vijayabaskar, V. K. Tikku and A. K. Bhowmick, "Electron beam modification and crosslinking: Influence of nitrile and carboxyl contents and level of unsaturation on structure and properties of nitrile rubber," *Radiation Physics and Chemistry,* vol. 75, no. 7, pp. 779-792, 2006.

[32] T. Yasin, S. Ahmed, M. Ahmed and F. Yoshii, "Effect of concentration of polyfunctional monomers on physical properties of acrylonitrile–butadiene rubber under electron-beam irradiation," *Radiation Physics and Chemistry,* vol. 73, no. 3, pp. 155-158, 2005.

[33] R. Clavreul and L. Pellegrin, "Lifespan prediction of EPR seals under gamma radiation," *Polymer Testing,* vol. 20, no. 7, pp. 769-770, 2001.

[34] Y. Merckel, J. Diani, M. Brieu and J. Caillard, "Effects of the amount of fillers and of the crosslink density on the mechanical behavior of carbon-black filled styrene butadiene rubbers," *Journal of Applied Polymer Science,* vol. 129, no. 4, pp. 2086-2091, 2013.

[35] A. F. George, "The effect of high pressure carbon dioxide on silicone and flurocarbon seal materials," in *10th International Conference on Fluid Sealing*, Innsbruck, Austria, 1984.

[36] M. Ezrin and G. Lavigne, "Unexpected and unusual failures of polymeric materials," *Engineering Failure Analysis,* vol. 14, no. 6, pp. 1153-1165, 2007.

[37] H. T. Wang, B. R. Pan, Q. G. Du and Y. Q. Li, "The strain in the test environmental stress cracking of plastics," *Polymer Testing,* vol. 22, no. 2, pp. 125-128, 2003.

[38] G. J. Lake and A. G. Thomas, "The strength of highly elastic materials," *Philosophical Transactions of the Royal Socity of London A: Mathematical and Physical Sciences,* vol. 300, no. 1460, pp. 108-119, 1967.

[39] T. L. Smith, "Strength of elastomers - a perspective," *Polymer Engineering and Science,* vol. 17, no. 3, pp. 129-143, 1977.

[40] J. Diani, A. M. Ortega, K. Gall, S. Kasprzak and A. R. Greenberg, "On the relevance of the 8-chain model and the full-network model for the deformation and failure of networks formed through photopolymerization of multifunctional monomers," *Journal of Polymer Science Part B: Polymer Physics,* vol. 46, no. 12, pp. 1226-1234, 2008.

[41] K. A. J. Dijkhuis, J. W. M. Noordermeer and W. K. Dierkes, "The relationship between crosslink system, network structure and material properties of

carbon black reinforced EPDM," *European Polymer Journal,* vol. 45, no. 11, pp. 3302-3312, 2009.

[42] Y. Fukahori, "Mechanism of the self-reinforcement of cross-linked NR generated through the strain-induced crystallization," *Polymer,* vol. 51, no. 7, pp. 1621-1631, 2010.

[43] G. Heinrich, H. Dorschner and E. Falk, "radiation induced crosslinking of plastics for reduction of wear in textile machines applications," *Gummi Fasem Kunststoffe,* vol. 57, pp. 156-162, 2004.

[44] V. Vijayabaskar and A. K. Bhowmick, "Electron-beam modification of nitrile rubber in the presence of polyfunctional monomers," *Journal of Applied Polymer Science,* vol. 95, no. 2, pp. 435-447, 2005.

[45] M. M. Hassan, R. O. Aly, A. H. El-Ghandour and H. A. Abdelnaby, "Effect of gamma irradiation on some properties of reclaimed rubber/nitrile–butadiene rubber blend and its swelling in motor and brake oils," *Journal of Elastomers and Plastics,* vol. 45, no. 1, pp. 77-94, 2013.

[46] F. Cardona, D. J. T. Hill, P. J. Pomery and A. K. Whittaker, "A comparative study of the effects of UV- and γ-radiation on copolymers of acrylonitrile/butadiene," *Polymer International,* vol. 48, no. 10, pp. 985-992, 1999.

[47] R. H. Partridge, "Excitation Energy Transfer in Alkanes. III. Radiation Chemistry of Alkane Polymers," *The Journal of Chemical Physics,* vol. 52, no. 5, pp. 2501-2510, 1970.

[48] F. S. Ahmed, M. Shafy, A. A. Abd El-megeed and E. M. Hegazi, "The effect of γ-irradiation on acrylonitrile–butadiene rubber NBR seal materials with different antioxidants," *Materials and Design,* vol. 36, pp. 823-828, 2012.

[49] D. J. T. Hill, J. H. O'Donnell, M. C. S. Perera and P. J. Pomery, "An investigation of radiation-induced structural changes in nitrile rubber," *Journal of Polymer Science Part A: Polymer Chemistry,* vol. 34, no. 12, pp. 2439-2454, 1996.

[50] A. Mostafa, A. Abouel-Kasem, M. R. Bayoumi and M. G. El-Sebaie, "On the influence of CB loading on the creep and relaxation behaviour of SBR and NBR rubber vulcanizates," *Materials and Design,* vol. 30, no. 7, pp. 2721-2725, 2009.

[51] W. L. Holt and A. T. McPherson, "Change of volume of rubber on stretching: Effects of time, elongation and temperature," *Journal of Research of the National Bureau of Standards,* vol. 17, pp. 657-678, 1936.

[52] G. Gee, J. Stern and L. R. G. Treloar, "Volume changes in the stretching of vulcanized natural rubber," *Transactions of the Faraday Society,* vol. 46, pp. 1101-1106, 1950.

[53] L. Mullins and N. R. Tobin, "Theoretical model for the elastic behavior of filler-reinforced vulcanized rubbers," *Rubber Chemistry and Technology,* vol. 30, no. 2, pp. 555-571, 1957.

[54] H. C. Jones and H. A. Yiengst, "Dilatomer studies of pigment-rubber systems," *Rubber Chemistry and Technology,* vol. 14, no. 1, pp. 113-124, 1941.

[55] J. Ramier, L. Chazeau, C. Gauthier, L. Stelandre, L. Guy and E. Peuvrel-Disdier, "In situ SALS and volume variation measurements during deformation of treated silica filled SBR," *Journal of Materials Science,* vol. 42, no. 19, pp. 8130-8138, 2007.

[56] J.-B. Le Cam, "A review of volume changes in rubbers: the effect of stretching," *Rubber Chemistry and Technology,* vol. 83, no. 3, pp. 247-269, 2010.

[57] T. Shinomura and M. Takahashi, "Volume change measurements of filled rubber vulcanizates under stretching," *Rubber Chemistry and Technology,* vol. 43, no. 5, pp. 1025-1035, 1970.

[58] L. Mullins, "Softening of rubber by deformation," *Rubber Chemistry and Technology,* vol. 42, no. 1, pp. 339-362, 1969.

[59] J. A. Sauer and G. C. Richardson, "Fatigue of polymers," *International Journal of Fracture,* vol. 16, no. 6, pp. 499-532, 1980.

[60] C. M. Hansen, "On predicting environmental stress cracking in polymers," *Polymer Degradation and Stability,* vol. 77, no. 1, pp. 43-53, 2002.

[61] B. J. Briscoe, D. Gritsis and D. Liatsis, "The concentration and pressure dependent diffusion of carbon dioxide in nitrile rubbers," *Philosophical Transactions: Physical Sciences and Engineering,* vol. 339, no. 1655, pp. 497-519, 1992.

[62] M. S. Seehra, M. Yalamanchi and V. Singh, "Structural characteristics and swelling mechanism of two commercial nitrile-butadiene elastomers in various fluids," *Polymer Testing,* vol. 31, no. 4, pp. 564-571, 2012.

[63] C. M. Hansen, "Diffusion in polymers," *Polymer Engineering and Science,* vol. 20, no. 4, pp. 252-258, 1980.

[64] M. Huldén and C. M. Hansen, "Water permeation in coatings," *Progress in Organic Coatings,* vol. 13, no. 3-4, pp. 171-194, 1985.

[65] C. M. Hansen, "The measurement of concentration-dependent diffusion coefficients - the exponential case," *Industrial and Engineering Chemistry Fundamentals,* vol. 6, no. 4, pp. 609-614, 1967.

[66] C. M. Hansen, "Diffusion coefficient measurements by solvent absorption in concentrated polymer solutions," *Journal of Applied Polymer Science,* vol. 26, no. 10, pp. 3311-3315, 1981.

[67] G. A. Bernier and R. P. Kambour, “The role of organic agents in the stress crazing and cracking of poly (2,6-dimethyl-1,4-phenylene oxide),” *Macromolecules,* vol. 1, no. 5, pp. 393-400, 1968.

[68] A. R. Rennie and D. Tabor, “Hydrostatic pressure and long-chain organic molecule diffusion through a polymer matrix,” *Nature,* vol. 286, no. 5771, pp. 372-373, 1980.

[69] A. F. George, S. Sully and O. M. Davies, “Carbon dioxide saturated elastomers: the loss of tensile properties and the effects of temperature rise and pressure cycling,” Fluid Sealing - BHR Group, 1997.

[70] “O-Ring Failure,” Flodynamix, [Online]. Available: http://flodynamix.com/images/oring-failure-heat-explosive.jpg. [Accessed 17 September 2015].

[71] “Pressure Damage O-Ring,” Seal and Design, [Online]. Available: http://blog.sealanddesign.com/wp-content/uploads/2012/11/pressure-damage-oring-263x108.jpg. [Accessed 17 September 2015].

[72] J. Arnold, “Craze initiation during the environmental stress cracking of polymers,” *Journal of Materials Science,* vol. 30, no. 3, pp. 655-660, 1995.

[73] J. A. Jansen, “Environmental Stress Cracking - The Plastic Killer,” *Advanced Materials and Processes,* vol. 162, pp. 50-53, 2004.

[74] A. Hulme and J. Cooper, “Life prediction of polymers for industry,” *Sealing Technology,* pp. 8-12, 2012.

[75] R. P. Kambour, E. E. Romagosa and C. L. Gruner, “Swelling, crazing, and cracking of an aromatic copolyether-sulfone in organic media,” *Macromolecules,* vol. 5, no. 4, pp. 335-340, 1972.

[76] R. P. Kambour, C. L. Gruner and E. E. Romagosa, "Solvent crazing of "dry" polystyrene and "dry" crazing of plasticized polystyrene," *Journal of Polymer Science: Polymer Physics Edition,* vol. 11, no. 10, pp. 1879-1890, 1973.

[77] R. P. Kambour, C. L. Gruner and E. E. Romagosa, "Biphenol-A polycarbonate immersed in organic media. Swelling and response to stress," *Macromolecules,* vol. 7, no. 2, pp. 248-253, 1974.

[78] Y. W. Mai, "Environmental stress cracking of glassy polymers and solubility parameters," *Journal of Materials Science,* vol. 21, no. 3, pp. 904-916, 1986.

[79] J. Breen and D. J. Van Dijk, "Environmental stress cracking of PVC: Effects of natural gas with different amounts of benzene," *Journal of Materials Science,* vol. 26, no. 19, pp. 5212-5220, 1991.

[80] A. R. Berens, "Sorption of organic liquids and vapors by rigid PVC," *Journal of Applied Polymer Science,* vol. 37, no. 4, pp. 901-913, 1989.

[81] P. I. Vincent and S. Raha, "Influence of hydrogen bonding on crazing and cracking of amorphous thermoplastics," *Polymer,* vol. 13, no. 6, pp. 283-287, 1972.

[82] L. F. Henry, "Prediction and evaluation of the susceptibilities of glassy thermoplastics to environmental stress cracking," *Polymer Engineering and Science,* vol. 14, no. 3, pp. 167-176, 1974.

[83] A. N. Gent, "Hypothetical mechanism of crazing in glassy plastics," *Journal of Materials Science,* vol. 5, no. 11, pp. 925-932, 1970.

[84] H. Fujiwara, J. Yamabe and S. Nishimura, "Evaluation of the change in chemical structure of acrylonitrile butadiene rubber after high-pressure hydrogen exposure," *International Journal of Hydrogen Energy,* vol. 37, no. 10, pp. 8729-8733, 2012.

[85] Y. Guo, J. Wang, K. Li and X. Ding, "Tribological properties and morphology of bimodal elastomeric nitrile butadiene rubber networks," *Materials and Design,* vol. 52, pp. 861-869, 2013.

[86] M. Himmelsbach, W. Buchberger and E. Reingruber, "Determination of polymer additives by liquid chromatography coupled with mass spectrometry. A comparison of atmospheric pressure photoionization (APPI), atmospheric pressure chemical ionization (APCI), and electrospray ionization (ESI)," *Polymer Degradation and Stability,* vol. 94, no. 8, pp. 1213-1219, 2009.

[87] W. Buchberger and M. Stiftinger, "Analysis of Polymer Additives and Impurities by Liquid Chromatography/Mass Spectrometry and Capillary Electrophoresis/Mass Spectrometry," in *Mass Spectrometry of Polymers – New Techniques*, vol. 248 of 'Advances in Polymer Science', M. Hakkarainen, Ed., Berlin, Springer-Verlag, 2012, pp. 39-67.

[88] S. M. Reiter, W. Buchberger and C. W. Klampfl, "Rapid identification and semi-quantitative determination of polymer additives by desorption electrospray ionization/time-of-flight mass spectrometry," *Analytical and Bioanalytical Chemistry,* vol. 400, no. 8, pp. 2317-2322, 2011.

[89] J. C. J. Bart, Additives in polymers: Industrial analysis and applications, Chichester: John Wiley and Sons, 2005.

[90] P. Kusch, "Identification of organic additives in nitrile rubber materials by pyrolysis-GC–MS," *LCGC North America,* pp. 248-254, 01 March 2013.

[91] R. Rogalewicz, A. Voelkel and I. Kownacki, "Application of HS-SPME in the determination of potentially toxic organic compounds emitted from resin-based dental materials," *Journal of Environmental Monitoring,* vol. 8, no. 3, pp. 377-383, 2006.

[92] R. Schönherr, “Use of the TGA-FTIR-system for the distinction of NBR rubber with different AN content,” *KGK-Kautschuk und Gummi Kunststoffe ,* vol. 49, no. 11, pp. 737-749, 1996.

[93] G. N. Ghebremeskel and S. R. Shield, “Characterization of binary/tertiary blends of SBR, NBR and PVC by IR spectroscopy,” *Rubber World,* vol. 227, no. 4, pp. 26-30 and 46, 2003.

[94] J. F. O'Keefe, “Identification of polymers by IR spectroscopy,” *Rubber World,* vol. 230, no. 3, pp. 27-37, 2004.

[95] F. Delor, N. Barrois-Oudin, X. Duteurtre, C. Cardinet, J. Lemaire and J. Lacoste, “Oxidation of rubbers analysed by HATR/IR spectroscopy,” *Polymer Degradation and Stability,* vol. 62, no. 2, pp. 395-401, 1998.

[96] D. Tuyet-Trinh, M. Celina and P. M. Fredericks, “Attenuated total reflectance infrared microspectroscopy of aged carbon-filled rubbers,” *Polymer Degradation and Stability,* vol. 77, no. 3, pp. 417-422, 2002.

[97] S. A. Connors, A. Murray, R. M. Paroli, A. H. Delgado and J. D. Irwin, “Spectroscopic investigation into the degradation of vulcanized natural rubber museum artifacts,” in *American Chemical Society, Polymer Preprints, Division of Polymer Chemistry*, Boston, MA, USA, 1998.

[98] M. Skrifvars, P. Niemelä, R. Koskinen and O. Hormi, “Process cure monitoring of unsaturated polyester resins, vinyl ester resins, and gel coats by Raman spectroscopy,” *Journal of Applied Polymer Science,* vol. 93, no. 3, pp. 1285-1292, 2004.

[99] P. Musto, M. Abbate, G. Ragosta and G. Scarinzi, “A study by Raman, near-infrared and dynamic-mechanical spectroscopies on the curing behaviour, molecular structure and viscoelastic properties of epoxy/anhydride networks,” *Polymer,* vol. 48, no. 13, pp. 3703-3716, 2007.

[100] R. O. Carter III, M. C. Paputa Peck, M. A. Samus and P. C. Killgoar Jr., "Infrared photoacoustic spectroscopy of carbon black filled rubber: concentration limits for samples and background," *Applied Spectroscopy,* vol. 43, no. 8, pp. 1350-1354, 1989.

[101] R. O. Carter III, "The Application of Linear PA/FT-IR to Polymer-Related Problems," *Applied Spectroscopy,* vol. 46, no. 2, pp. 219-224, 1992.

[102] H. W. Schrotter and H. W. Klocker, "Raman scattering cross-sections in gases and liquids," in *Topics in Current Physics: Raman Spectroscopy of Gases and Liquids*, A. Weber, Ed., Berlin, Springer-Verlag, 1979.

[103] N. A. St John and G. A. George, "Diglycidyl amine — epoxy resin networks: Kinetics and mechanisms of cure," *Progress in Polymer Science,* vol. 19, no. 5, pp. 755-795, 1994.

[104] R. Fernández, M. Blanco, M. J. Galante, P. A. Oyanguren and I. Mondragon, "Polymerization of an epoxy resin modified with azobenzene groups monitored by near-infrared spectroscopy," *Journal of Applied Polymer Science,* vol. 112, no. 5, pp. 2999-3006, 2009.

[105] J. H. O'Donnell and D. F. Sangster, Principles of Radiation Chemistry, London: Arnold, 1970, pp. 160-169.

[106] F. T. Wall, "Statistical thermodynamics of rubber," *Journal of Chemical Physics,* vol. 10, no. 2, pp. 132-134, 1942.

[107] F. T. Wall, "Statistical thermodynamics of rubber. II," *Journal of Chemical Physics,* vol. 10, no. 7, pp. 485-488, 1942.

[108] F. T. Wall, "Statistical thermodynamics of rubber. III," *Journal of Chemical Physics,* vol. 11, no. 11, pp. 527-530, 1943.

[109] P. J. Flory and J. Rehner Jr., "Effect of deformation on the swelling capacity of rubber," *Journal of Chemical Physics,* vol. 12, no. 10, pp. 412-414, 1944.

[110] F. T. Wall and P. J. Flory, "Statistical thermodynamics of rubber elasticity," *Journal of Chemical Physics,* vol. 19, no. 12, pp. 1435-1439, 1951.

[111] H. M. James and E. Guth, "Theory of the elastic properties of rubber," *Journal of Chemical Physics,* vol. 11, no. 10, pp. 455-481, 1943.

[112] H. M. James and E. Guth, "Theory of the increase in rigidity of rubber during cure," *Journal of Chemical Physics,* vol. 15, no. 9, pp. 669-683, 1947.

[113] S. Nandi and H. H. Winter, "Swelling behavior of partially cross-linked polymers: A ternary system," *Macromolecules,* vol. 38, no. 10, pp. 4447-4455, 2005.

[114] M. Gottlieb and R. J. Gaylord, "Experimental tests of entanglement models of rubber elasticity. 2. Swelling," *Macromolecules,* vol. 17, no. 10, pp. 2024-2030, 1984.

[115] N. A. Neuburger and B. E. Eichinger, "Critical experimental test of the Flory-Rehner theory of swelling," *Macromolecules,* vol. 21, no. 10, pp. 3060-3070, 1988.

[116] Y. Zhao and B. E. Eichinger, "Study of solvent effects on the dilation modulus of poly(dimethylsiloxane)," *Macromolecules,* vol. 25, no. 25, pp. 6988-6995, 1992.

[117] G. B. McKenna and J. M. Crissman, "Temperature and crosslinking effects on the swelling of poly(isoprene) in isopiestic conditions," *Journal of Polymer Science Part B: Polymer Physics,* vol. 35, no. 5, pp. 817-826, 1997.

[118] P. R. Chatterji, "Cross-link dimensions in (gelatin-poly(acrylamide) interpenetrating hydrogel networks," *Macromolecules,* vol. 24, no. 14, pp. 4214-4215, 1991.

[119] G. B. McKenna, K. M. Flynn and Y. Chen, "Swelling in crosslinked natural rubber: Experimental evidence of the crosslink density dependence of χ," *Polymer,* vol. 31, no. 10, pp. 1937-1945, 1990.

[120] M. L. Costa, E. C. Botelho and M. C. Rezende, "Monitoring of cure kinetic prepreg and cure cycle modeling," *Journal of Materials Science,* vol. 41, no. 13, pp. 4349-4356, 2006.

[121] J. M. Barton, "The application of differential scanning calorimetry (DSC) to the study of epoxy resin curing reactions," in *Epoxy Resins and Composites I*, vol. 72 of 'Advances in Polymer Science', Berlin, Springer-Verlag, 2005, pp. 111-154.

[122] E. Papadopoulos, M. Ginic-Markovic and S. Clarke, "Reaction kinetics of polyurethane formation using a commercial oligomeric diisocyanate resin studied by calorimetric and rheological methods," *Macromolecular Chemistry and Physics,* vol. 209, no. 22, pp. 2302-2311, 2008.

[123] C. W. Cheung, J. F. Porter and G. McKay, "Sorption kinetics for the removal of copper and zinc from effluents using bone char," *Separation and Purification Technology,* vol. 19, no. 1-2, pp. 55-64, 2000.

[124] M. Ajmal, R. A. K. Rao, R. Ahmad and J. Ahmad, "Adsorption studies on Citrus reticulata (fruit peel of orange): Removal and recovery of Ni(II) from electroplating wastewater," *Journal of Hazardous Materials,* vol. 79, no. 1-2, pp. 117-131, 2000.

[125] Z. Reddad, C. Gerente, Y. Andres and P. Le Cloirec, "Adsorption of several metal ions onto a low-cost biosorbent: Kinetic and equilibrium studies," *Environmental Science and Technology,* vol. 36, no. 9, pp. 2067-2073, 2002.

[126] Y. S. Ho and G. McKay, "A Comparison of chemisorption kinetic models applied to pollutant removal on various sorbents," *Process Safety and Environmental Protection,* vol. 76, no. 4, pp. 332-340, 1998.

[127] Y. S. Ho and G. McKay, "Batch lead(II) removal from aqueous solution by peat: Equilibrium and kinetics," *Process Safety and Environmental Protection*, vol. 77, no. 3, pp. 165-173, 1999.

[128] K. Banerjee, P. N. Cheremisinoff and S. L. Cheng, "Adsorption kinetics of o-xylene by flyash," *Water Research,* vol. 31, no. 2, pp. 249-261, 1997.

[129] S. H. Lin and Y. W. Chen, "Liquid-Phase Adsorption of 1,1-Dichloro-1-fluoroethane by Various Adsorbents," *Industrial and Engineering Chemistry Research,* vol. 36, no. 10, pp. 4347-4352, 1997.

[130] Y. S. Ho and G. McKay, "The kinetics of sorption of divalent metal ions onto sphagnum moss peat," *Water Research,* vol. 34, no. 3, pp. 735-742, 2000.

[131] S. Azizian, "Kinetic models of sorption: A theoretical analysis," *Journal of Colloid and Interface Science,* vol. 276, no. 1, pp. 47-52, 2004.

[132] H. M. F. Freundlich, "Over the adsorption in solution," *Journal of Physical Chemistry,* vol. 57, pp. 385-470, 1906.

[133] I. Langmuir, "The constitution and fundamental properties of solids and liquids. Part I. Solids," *Journal of the American Chemical Society,* vol. 38, no. 11, pp. 2221-2295, 1916.

[134] C. Aharoni and M. Ungarish, "Kinetics of activated chemisorption. Part 2. Theoretical models," *Journal of the Chemical Society,* vol. 73, pp. 456-464, 1977.

[135] C. Aharoni and D. L. Sparks, "Kinetics of soil chemical reactions – A theoretical treatment," in *Rates of Soil Chemical Processes*, Madison, Soil Science Society of America, 1991, pp. 1-18.

[136] M. M. Dubinin, "The potential theory of adsorption of gases and vapors for adsorbents with energetically nonuniform surfaces," *Chemical Reviews,* vol. 60, no. 2, pp. 235-241, 1960.

[137] M. M. Dubinin, "Modern state of the theory of volume filling of micropore adsorbents during adsorption of gases and steams on carbon adsorbents," *Zhurnal Fizicheskoi Khimii,* vol. 39, pp. 1305-1317, 1965.

[138] L. V. Radushkevic, "Potential theory of sorption and structure of carbons," *Zhurnal Fizicheskoi Khimii,* vol. 23, pp. 1410-1420, 1949.

[139] J. Monika, V. K. Garg and K. Kadirvelu, "Chromium(VI) removal from aqueous system using Helianthus annuus (sunflower) stem waste," *Journal of Hazardous Materials,* vol. 162, no. 1, pp. 365-372, 2009.

[140] Whitby and Chandler Ltd., "Rubber Sheets and Rubber Components," [Online]. Available: http://whitby-chandler.co.uk/rubber-sheets-and-rubber-components.asp. [Accessed 18 January 2016].

[141] ASTM, "ASTM D6814: Standard Test Method for Determination of Percent Devulcanisation of Crumb Rubber Based on Crosslink Density," 2013.

[142] E. J. Billo, Excel for Chemists: A Comprehensive Guide, 2nd Ed. ed., New York: Wiley-VCH, 2001, pp. 223-238.

[143] Y. S. Ho, J. F. Porter and G. McKay, "Equilibrium Isotherm Studies for the Sorption of Divalent Metal Ions onto Peat: Copper, Nickel, and Lead Single Component Systems," *Water, Air and Soil Pollution,* vol. 141, pp. 1-33, 2001.

[144] D. W. Marquardt, "An Algorithm for Least-Squares Estimation of Nonlinear Parameters," *Journal of the Society for Industrial and Applied Mathematics,* vol. 11, pp. 431-441, 1963.

[145] A. Kapoor and R. T. Yang, "Correlation of equilibrium adsorption data of condensible vapours on porous adsorbents," *Gas Separation and Purification,* vol. 3, pp. 187-192, 1989.

[146] A. D. Shine, "Fitting Experimental Data to Straight Lines (Including Error Analysis)," 2006.

[147] G. Turrell and J. Corset, Raman Microscopy: Developments and Applications, London: Elsevier Academic Press, 1996.

[148] V. Vijayabaskar, V. K. Tikku and A. K. Bhowmick, "Electron beam modification and crosslinking: Influence of nitrile and carboxyl contents and level of unsaturation on structure and properties of nitrile rubber," *Radiation Physics and Chemistry,* vol. 75, pp. 779-792, 2006.

[149] J. R. Parker and W. H. Waddell, "Quantitative Characterization of Polymer Structure by Photoacoustic Fourier Transform Infrared Spectroscopy," *Journal of Elastomers and Plastics,* vol. 28, no. 2, pp. 140-160, 1996.

[150] W. West, Chemical Applications of Spectroscopy, London: Wiley and Sons Ltd, 1956.

[151] L. J. Bellamy, Advances in Infrared Group Frequencies, Moscow: Mir, 1971.

[152] H. M. Abou Zied, Z. I. Ali, T. M. Abdel Maksoud and R. M. Khafagy, "Structure-property behaviour of polyethylene exposed to different types of radiation," *Journal of Applied Polymer Science,* vol. 75, no. 2, pp. 179-200, 2000.

[153] T. Yasin, Y. Nho, S. Khan and R. Ahmad, "Effect of polyfunctional monomers on properties of radiation crosslinked EPDM/waste tire dust blend," *Radiation Physics and Chemistry,* vol. 81, no. 4, pp. 421-425, 2012.

[154] J. Coates, "Interpretation of infrared spectra: A practical approach," in *Encyclopedia of analytical chemistry*, Chichester, John Wiley and Sons Ltd., 2000.

[155] S. Chakraborty, S. Bandyopadhyay, R. Ameta, R. Mukhopadhyay and A. S. Deuri, "Application of FTIR in characterisation of acrylonitrile-butadiene rubber (nitrile rubber)," *Polymer Testing,* vol. 26, pp. 38-41, 2007.

[156] J. Mohan, Organic Spectroscopy: Principles and Applications, 2 ed., Alpha Science International Ltd, 2004.

[157] G. Helmchen, Houben-Weyl Methods of Organic Chemistry: v.b, 4 ed., Thieme Medical Publishers, 1995.

[158] Y. S. Ho, J. F. Porter and G. McKay, "Equilibrium isotherm studies for the sorption of divalent metal ions onto peat: Copper, nickel and lead single component systems," *Water Air and Soil Pollution,* vol. 141, no. 1, pp. 1-33, 2002.

[159] E. Kucukpinar and P. Doruker, "Molecular simulations of gas transport in nitrile rubber and styrene butadiene rubber," *Polymer,* vol. 47, no. 22, pp. 7835-7845, 2006.

[160] M. A. Hassan, A. Abouel-Kasem, M. A. El-Sharief and F. Yusof, "Evaluation of the material constants of nitrile butadiene rubbers (NBRs) with different carbon black loading (CB): FE-simulation and experimental," *Polymer,* vol. 53, no. 17, pp. 3807-3814, 2012.

[161] B. J. Briscoe and S. Zakaria, "Interaction of CO2 gas with silicone elastomer at high ambient pressures," *Journal of Polymer Science: Part B: Polymer Physics,* vol. 29, no. 8, pp. 989-999, 1991.

[162] G. K. Fleming and W. J. Koros, "Dilation of polymers by sorption of carbon dioxide at elevated pressures. 1. Silicone rubber and unconditioned polycarbonate," *Macromolecules,* vol. 19, no. 8, pp. 2285-2291, 1986.

[163] G. B. McKenna, K. M. Flynn and Y. Chen, "Swelling in crosslinked natural rubber: experimental evidence of the crosslink density dependence of χ," *Polymer,* vol. 31, no. 10, pp. 1937-1945, 1990.

[164] W. Zhao, L. Yu, X. Zhong, Y. Zhang and J. Sun, "Radiation vulcanization of hydrogenated acrylonitrile butadiene rubber (HNBR)," *Journal of Applied Polymer Science,* vol. 54, no. 9, pp. 1199-1205, 1994.

[165] R. K. Sinnot, Chemical Engineering Design, 4th Ed. ed., Oxford: Elsevier Butterworth-Heinemann, 2005.

[166] Ram Charan, "NBR rubber: Its classification and selection criteria," Chennai, 2012.

[167] J. Davenas, I. Stevenson, N. Celette, S. Cambon, J. L. Gardette, A. Rivaton and L. Vignoud, "Stability of polymers under ionising radiation: The many faces of radiation interactions with polymers," *Nuclear Instruments and Methods in Physics Research B,* vol. 191, no. 1-4, pp. 653-661, 2002.

EDF Internal Documents

[E1] YET TO BE PUBLISHED – Dungeness B Power Station Fuel Route Workbook Number 3: Fuel, Fuel Plug Units, Control Rods, the New Fuel Preparation Room and New Fuel Transfer Room, 22 February 2011, British Energy

[E2] YET TO BE PUBLISHED – Dungeness B Power Station Fuel Route Workbook Number 4: Fuelling Machine, 22 February 2011, British Energy

[E3] EPD/DNB/REP/0060/097 – The Routine Off-Load Refuelling Safety Case Head Document – Section 4 Pressure Boundary / Containment Integrity, July 1997, D. R. Blythe

[E4] E/EAN/BRBB/0004/DNB/03 – Dungeness B Power Station Review of Absorbed Doses to Fuelling Machine Cables, Seal Plug Seals, and Nose Unit Seals and Buffer Store 21 Air Eliminators, 4 June 2003, P. Symons

[E5] DMV/01/10/11563 – Dungeness B Nuclear Power Station MV-01 Assembly of Seal Plug Upper Chevron Seal

[E6] DMV/01/10/11403 – Dungeness B Nuclear Power Station MV-01 Assembly of Seal Plug Detail of Spacer

[E7] DMV/01/10/11569 – Dungeness B Nuclear Power Station MV-01 Assembly of Seal Plug Detail of Grinding Ring

[E8] DMV/01/10/11575 – Dungeness B Nuclear Power Station MV-01 Assembly of Seal Plug Detail of Split Ring

[E9] DMV/01/10/11573 – Dungeness B Nuclear Power Station MV-01 Assembly of Seal Plug Detail of Backing Ring

[E10] DMV/01/10/11571 – Dungeness B Nuclear Power Station MV-01 Assembly of Seal Plug Detail of Lantern Ring

[E11] BEG/SPEC/ENG/TGN/005 – Technical Guidance Note 005 – Guidance for the Selection, Assurance, Procurement, Storage and Installation of Elastomer Seals for Nuclear Plant Applications, April 2010, P. F. Disley

[E12] DMV/01/11/10995 – Dungeness B Nuclear Power Station MV-01 Nose Unit Detail of Inner Sleeve

[E13] DMV/01/10/11383 – Dungeness B Nuclear Power Station MV-01 Assembly of Seal Detail of Seal Plug Centre

[E14] E/ES/BRBB/0021/DNB/11 – Dungeness B Power Station Specification for the Endurance Testing of the Dungeness B Fuelling Machine Winch Input Shaft Seals, September 2011, P. Tudor

[E15] DNB/PIOI/10/02/01/44/20 Revision 018 – Monthly/30 Day Nose Unit Primary Seal(s), Back-Up Seal(s) and Seal Plug Chevron Seal Leak Testing, February 2012

[E16] FRO/REP/CGBC/005/DNB/07 – Assessment of Fuelling Machine Pressure Boundary Duty Cycles, December 2007, D. Blythe